

Klemens  
Lautenbach

*Dissertation*

# High Speed Data Multiplexer for the Belle II Pixel Detector

Search for an Exotic Resonance  
at the  $D^{*0}\bar{D}^{*0}$  Threshold in  
Charged  $B$  Meson Decays

High Speed Data Multiplexer  
for the Belle II Pixel Detector

&

Search for an Exotic  
Resonance at the  $D^{*0}\bar{D}^{*0}$   
Threshold in Charged  $B$   
Meson Decays



JUSTUS-LIEBIG-



UNIVERSITÄT  
GIESSEN

# High Speed Data Multiplexer for the Belle II Pixel Detector

&

## Search for an Exotic Resonance at the $D^{*0}\bar{D}^{*0}$ Threshold in Charged $B$ Meson Decays

INAUGURALDISSERTATION

*zur Erlangung des Doktorgrades am*

FACHBEREICH MATHEMATIK UND INFORMATIK,  
PHYSIK, GEOGRAPHIE

*der*

JUSTUS-LIEBIG-UNIVERSITÄT GIEßEN

*vorgelegt von*

KLEMENS LAUTENBACH

*aus Oberweid*

Gießen 2020

Aus dem II. Physikalischen Institut

Dekan: Prof. Dr. Kai-Thomas Brinkmann

Gutachter: apl. Prof. Dr. Jens Sören Lange AR

Gutachterin: Prof. Dr. Claudia Höhne

# Selbstständigkeitserklärung

Hiermit versichere ich, die vorgelegte Thesis selbstständig und ohne unerlaubte fremde Hilfe und nur mit den Hilfen angefertigt zu haben, die ich in der Thesis angegeben habe. Alle Textstellen, die wörtlich oder sinngemäß aus veröffentlichten Schriften entnommen sind, und alle Angaben die auf mündlichen Auskünften beruhen, sind als solche kenntlich gemacht. Bei den von mir durchgeführten und in der Thesis erwähnten Untersuchungen habe ich die Grundsätze gute wissenschaftlicher Praxis, wie sie in der Satzung der Justus-Liebig-Universität zur Sicherung guter wissenschaftlicher Praxis' niedergelegt sind, eingehalten. Gemäß § 25 Abs. 6 der Allgemeinen Bestimmungen für modularisierte Studiengänge dulde ich eine Überprüfung der Thesis mittels Anti-Plagiatssoftware.

---

Datum

---

Unterschrift



# Danksagung



Während den Jahren meiner Promotion und den Monaten, in denen diese Dissertation erarbeitet wurde, war es mir vergönnt viele Leute kennenzulernen und, während anstrengender Zeiten, auf den Rückhalt vieler, altbekannter Menschen aus dem Freundes-, Familien-, und Arbeitsumfeld bauen zu können. All diesen möchte ich an dieser Stelle danken.

Allen voran danke ich meinem Betreuer apl. Prof. Dr. Sören Lange, der mir immer mit Rat und Tat zur Seite gestanden hat und mir ermöglichte, im Laufe meiner Promotion, an vielen internationalen Konferenzen teilzunehmen. Auch Herrn Prof. Dr. Wolfgang Kühn, der mich schon während der Bachelor und Masterarbeit mitbetreute, gilt großer Dank. Viel Dank gebührt auch jedem einzelnen Mitglied der AG Kühn/Höhne, für die immer tolle Arbeitsatmosphäre, die wissenschaftlichen Diskussionen und sommerlichen Grillnachmittage. Besonders hervorheben möchte ich hier meinen Bürokollegen Leonard Koch, der mir bei so mancher Fragestellungen mit seiner Expertise weiterhelfen konnte und mit dem ich einige schöne Konferenzreisen, die immer mit einem kleinen Abenteuer (Novosibirsk, Liechtenstein, Japan, etc.) verknüpft waren, unternehmen konnte. Großer Dank gilt auch meinen Kollegen Thomas Geßler, Simon Reiter und Dennis Getzkow, welche mir bei Fragestellungen im Zusammenhang mit der PXD DAQ immer eine große Hilfe waren und mit denen ich viele schöne Tage auf Strahlzeiten und in Japan verbrachte.

A big thanks also to all Belle II collaboration members, especially the ones I had the pleasure to get to know a bit better in my times in Japan and on conferences throughout Europe and Germany.

Weiterer Dank gilt den administrativen Kräften der AG Kühn/Höhne für ihre oftmals unbürokratische und schnelle Hilfe. Also many thanks to the administrative forces at the KEK research facility in Tsukuba, who helped me out with the one or the other problem during my stays in Japan - *Arigatou gozaimasu.*

Vielen Dank auch an meinen Freundes- und Bekanntenkreis, sowie den Mitgliedern meiner WG, die mir in mühseligen Zeiten immer mit erheitern- den Worten oder erlebnisreichen Wochenenden die Arbeit einfacher machten.

Abschließend möchte ich meiner gesamten Familie, allen voran meinen Großeltern, ganz herzlich danken. Ihr habt mich immer unterstützt und mir den nötigen Rückhalt in sämtlichen Lebenslagen gegeben. Das Jahr 2020 der Coronapandemie, das für viele ein Schrecken war, bot für mich viele schöne und produktive Monate in meiner Heimat auf, in denen ich nicht nur diese Thesis verfassen konnte, sondern es mir auch vergönnt war viel Zeit mit der Familie in Wald und Flur zu verbringen. Dafür bin ich sehr dankbar.



# Contents

<b>I Motivation</b>	<b>7</b>
I.1. High Speed Data Multiplexer for the Belle II Pixel Detector . . . . .	7
I.2. Search for an Exotic Resonance at the $D^{*0}\bar{D}^{*0}$ Threshold in Charged $B$ Meson Decays . . . . .	9
<b>II Theoretical Introduction</b>	<b>11</b>
II.1. The Standard Model of Particle Physics . . . . .	11
II.1.1 The Standard Model Lagrangian . . . . .	13
II.1.1.1 The Kinematic Term of the Standard Model Lagrangian . . . . .	14
II.1.1.2 The Electromagnetic and the Weak Force . . . . .	14
II.1.1.3 The Strong Force . . . . .	15
II.1.1.4 The Higgs Field . . . . .	16
II.1.1.5 The Yukawa Coupling . . . . .	16
II.1.1.6 The Unitary Triangle and $CP$ -Violation . . . . .	17
II.2. Physics at the Belle II Experiment . . . . .	20
II.2.1 $CP$ Violation Measurements . . . . .	20
II.2.1.1 Coherent $B^0 - \bar{B}^0$ Mixing . . . . .	24
II.2.1.2 Flavor Tagging . . . . .	25
II.3. Theoretical Introduction to the $X(4014)$ . . . . .	31
II.3.1 Charmonium Spectroscopy . . . . .	31
II.3.2 Exotic Charmonia . . . . .	34
II.3.2.1 Hadro-Quarkonium . . . . .	35
II.3.2.2 Tetraquarks . . . . .	35
II.3.2.3 Hybrids . . . . .	36
II.3.2.4 Hadronic Molecules . . . . .	36
II.3.2.5 Glueballs . . . . .	37
II.3.2.6 Threshold Effects . . . . .	37

II.3.3	The X(3872) . . . . .	37
II.3.4	X(4014) - A Partner State to the X(3872) Favoring a Molecular Description . . . . .	39
<b>III</b>	<b>The Belle II Experiment</b>	<b>47</b>
III.1.	SuperKEKB - An Asymmetric $e^+e^-$ -Collider . . . . .	47
III.2.	Belle II - A Precision Frontier Particle Detector . . . . .	51
III.2.1	The Vertex Detector - VXD . . . . .	52
III.2.1.1	The Pixel Detector - PXD . . . . .	52
III.2.1.2	The Silicon Vertex Detector - SVD . . . . .	58
III.2.2	The Central Drift Chamber - CDC . . . . .	59
III.2.3	Particle Identification . . . . .	60
III.2.3.1	Time of Propagation Counter - TOP . . . . .	61
III.2.3.2	Aerogel Ring-Imaging Cherenkov Detector - ARICH . . . . .	62
III.2.4	The Electromagnetic Calorimeter - ECL . . . . .	62
III.2.5	$K_L^0$ and $\mu$ Detection - KLM . . . . .	62
III.3.	Belle II Trigger and Data Acquisition System . . . . .	64
III.3.1	Trigger System . . . . .	64
III.3.2	Data Acquisition System . . . . .	65
III.3.3	The PXD DAQ System . . . . .	66
III.3.3.1	The ONSEN Data Reduction System . . . . .	69
III.4.	The Belle II Analysis Framework - BASF2 . . . . .	76
III.4.1	Simulation and Reconstruction in basf2 . . . . .	77
III.4.2	Conditions Data Base . . . . .	78
III.4.3	The Belle to Belle II Framework - b2bii . . . . .	78
III.4.4	Example for a Simulation and Reconstruction Chain with basf2 and b2bii . . . . .	79
<b>IV</b>	<b>High Speed Data Multiplexer for the Belle II Pixel Detector</b>	<b>81</b>
IV.1.	New Output Option via 10 GbE ATCA-Switch . . . . .	81
IV.1.1	Local Link Combiner - IP Core Development . . . . .	84
IV.1.2	Adjustments in Slow Control . . . . .	85
IV.2.	Laboratory Tests . . . . .	87
IV.2.1	Data Integrity Test . . . . .	87
IV.2.2	Results for Data Rate Test . . . . .	89
IV.2.3	Results for Long-Term Stability Test . . . . .	89
IV.3.	Remaining Issues . . . . .	91

---

---

<b>V Simulation of a Resonant Structure at the <math>D^{*0}\bar{D}^{*0}</math> threshold in B decays at Belle II</b>	<b>93</b>
V.1. Introductory Remarks on the Reconstruction Strategy . . . . .	93
V.2. Reconstruction on Signal Monte Carlo . . . . .	94
V.2.1 Impact of Beam Background Processes on the Reconstruction . . . . .	97
V.2.2 Selection Cuts for Final State Particles . . . . .	99
V.2.3 $\pi^0$ Reconstruction . . . . .	102
V.2.4 $K_S^0$ Reconstruction . . . . .	109
V.2.5 $D^0$ Reconstruction . . . . .	111
V.2.6 $X(4014)$ Reconstruction . . . . .	116
V.2.7 $B^\pm$ Reconstruction . . . . .	118
V.2.7.1 Best Candidate Selection . . . . .	120
V.2.8 Background Estimation . . . . .	123
V.3. Impact of the Pixel Detector on the Analysis . . . . .	125
V.4. Fitting Strategy . . . . .	127
V.4.1 Signal . . . . .	130
V.4.2 Combinatorial Background . . . . .	130
V.4.3 Generic Background . . . . .	131
V.4.4 Testing for Signal Bias with Toy-MC Study . . . . .	133
V.4.5 Combined Fit to the $X(4014)$ Invariant Mass Distribution Using the Maximum Likelihood Approach . . . . .	134
V.4.6 Significance Calculation . . . . .	135
V.4.6.1 Shape Dependent Model . . . . .	135
V.4.6.2 Shape Independent Model . . . . .	137
V.4.7 Outlook for a Discovery with Future Belle II Data Sets . . . . .	139
V.5. Data and MC Comparison for Belle II . . . . .	141
V.5.1 Comparison of Final State Particles in MC and Data . . . . .	142
V.5.2 Comparison of $\pi^0$ in MC and Data . . . . .	143
V.5.3 Comparison of $D^0$ in MC and Data . . . . .	145
V.5.4 Comparison of Kinematical $B^\pm$ Variables in MC and Data . . . . .	146
<b>VI Search for an Exotic Resonance at the <math>D^{*0}\bar{D}^{*0}</math> Threshold in Charged <math>B</math> Meson Decays at Belle</b>	<b>149</b>
VI.1. Simulation of the $X(4014)$ at Belle Monte-Carlo . . . . .	149
VI.1.1 Comparison with the Belle II Simulation . . . . .	150
VI.2. $B^\pm$ Reconstruction . . . . .	152
VI.3. Data and MC Comparison for Belle . . . . .	153
VI.3.1 Comparison of Final State Particles in MC and Data . . . . .	154

---

VI.3.2	Comparison of $\pi^0$ in MC and Data . . . . .	155
VI.3.3	Comparison of $D^0$ in MC and Data . . . . .	157
VI.3.4	Comparison of $B^\pm$ in MC and Data . . . . .	158
VI.4.	Exploiting the Reconstruction Strategy on the $X(3872) \rightarrow D^0 \bar{D}^0 \pi^0$ Reference Channel in Belle Data. . . . .	159
VI.4.0.1	2D Fitting Strategy for Higher Signal Signifi- cance . . . . .	162
VI.4.1	Comparison of Extracted $X(3872)$ Properties with Pub- lished Numbers . . . . .	167
VI.5.	Unblinding of Data in the $X(4014)$ Signal Region . . . . .	168
<b>VII</b>	<b>Summary and Outlook</b> . . . . .	<b>173</b>
VII.1.	Alternative Output for the Belle II Pixel Detector DAQ . . . . .	173
VII.2.	Search for an Exotic Resonance at the $D^{*0} \bar{D}^{*0}$ Threshold in Charged $B$ Meson Decays . . . . .	174
VII.2.1	Simulation of a Resonant Structure at the $D^{*0} \bar{D}^{*0}$ threshold in $B$ decays at Belle II . . . . .	174
VII.2.2	Search for an Exotic Resonance at the $D^{*0} \bar{D}^{*0}$ Thresh- old in Charged $B$ Meson Decays at Belle . . . . .	176
<b>VIII</b>	<b>Appendix A</b> . . . . .	<b>179</b>
VIII.1.	Fitting Parameters of Belle II Signal MC Fits . . . . .	179
VIII.1.1	Fits to Intermediate Resonances . . . . .	179
VIII.1.1.1	$\pi^0$ from $D^0$ . . . . .	179
VIII.1.1.2	$\pi^0$ from $X(4014)$ Fit . . . . .	180
VIII.1.1.3	$D^0 \rightarrow K^\pm \pi^\mp$ Fit . . . . .	181
VIII.1.1.4	$D^0 \rightarrow K^\pm \pi^\mp \pi^0$ Fit . . . . .	182
VIII.1.1.5	$D^0 \rightarrow K^\pm \pi^\mp \pi^\pm \pi^\mp$ Fit . . . . .	183
VIII.1.1.6	$D^0 \rightarrow K_S^0 \pi^\pm \pi^\mp$ Fit . . . . .	184
VIII.1.1.7	$D^0 \rightarrow K^\pm K^\mp$ Fit . . . . .	185
VIII.1.2	Fits to the $D^0$ Resonances <b>Without PXD</b> . . . . .	186
VIII.1.2.1	$D^0 \rightarrow K^\pm \pi^\mp$ Fit . . . . .	186
VIII.1.2.2	$D^0 \rightarrow K^\pm \pi^\mp \pi^0$ Fit . . . . .	187
VIII.1.2.3	$D^0 \rightarrow K^\pm \pi^\mp \pi^\pm \pi^\mp$ Fit . . . . .	188
VIII.1.2.4	$D^0 \rightarrow K_S^0 \pi^\pm \pi^\mp$ Fit . . . . .	189
VIII.1.2.5	$D^0 \rightarrow K^\pm K^\mp$ Fit . . . . .	190
VIII.1.3	Fits to Variables of the Final $B^\pm$ Meson List . . . . .	191
VIII.1.3.1	Fit to the $\Delta E$ Signal Distribution . . . . .	191
VIII.1.3.2	Fit to the $\Delta E$ Signal Distribution Without PXD . . . . .	192

---

VIII.1.3.3	Fits to the $D^0\bar{D}^0\pi^0\pi^0$ Invariant Mass Signal Distribution . . . . .	193
VIII.1.4	Signal Event Estimation . . . . .	199
VIII.1.5	Invariant Mass Distributions of the $\Gamma = 3$ MeV Data Set	199
VIII.1.6	Fits to the Invariant Mass Distribution of the Combi- natorial Background . . . . .	201
VIII.1.7	Fit to the Invariant Mass Distribution of the Generic Background . . . . .	207
VIII.2.	TOY MC Study . . . . .	208
VIII.3.	Discovery Maps . . . . .	209
VIII.4.	Data/MC Comparison for Belle II . . . . .	212
VIII.4.1	$K^\pm$ Data/MC Comparison . . . . .	212
VIII.4.2	$\pi^\pm$ Data/MC Comparison . . . . .	213
VIII.4.3	$K^\pm, \pi^\pm$ Efficiency and Fake Rate in Belle II MC . . . . .	214
VIII.4.4	$K_S^0$ Data/MC Comparison . . . . .	214
VIII.4.5	$\pi^0$ from $D^0$ Data/MC Comparison . . . . .	215
VIII.4.6	$\pi^0$ from $X(4014)$ Data/MC Comparison . . . . .	217
VIII.4.7	$D^0 \rightarrow K^\pm\pi^\mp$ . . . . .	219
VIII.4.8	$D^0 \rightarrow K^\pm\pi^\mp\pi^0$ . . . . .	221
VIII.4.9	$D^0 \rightarrow K^\pm\pi^\mp\pi^\pm\pi^\mp$ . . . . .	223
VIII.4.10	$D^0 \rightarrow K_S^0\pi^\pm\pi^\mp$ . . . . .	225
VIII.4.11	$D^0 \rightarrow K^\pm K^\mp$ . . . . .	227
VIII.4.12	$B^\pm$ List Variables . . . . .	229
<b>IX</b>	<b>Appendix B</b> . . . . .	<b>231</b>
IX.1.	Fitting Parameters to Belle Signal MC Fits . . . . .	231
IX.1.1	Fits to Intermediate Resonances . . . . .	231
IX.1.1.1	$\pi^0$ from $D^0$ . . . . .	231
IX.1.1.2	$\pi^0$ from $X(4014)$ Fit . . . . .	232
IX.1.1.3	$D^0 \rightarrow K^\pm\pi^\mp$ Fit . . . . .	234
IX.1.1.4	$D^0 \rightarrow K^\pm\pi^\mp\pi^0$ Fit . . . . .	235
IX.1.1.5	$D^0 \rightarrow K^\pm\pi^\mp\pi^\pm\pi^\mp$ Fit . . . . .	236
IX.1.1.6	$D^0 \rightarrow K_S^0\pi^\pm\pi^\mp$ Fit . . . . .	237
IX.1.1.7	$D^0 \rightarrow K^\pm K^\mp$ Fit . . . . .	238
IX.1.2	Fits to Variables of the Final $B^\pm$ Meson List for the $X(3872)$ Analysis . . . . .	239
IX.1.2.1	Fit to the $\Delta E$ Signal MC Distribution . . . . .	239
IX.1.2.2	Fit to the $M_{BC}$ Signal MC Distribution . . . . .	240

IX.1.2.3	Fit to the MCtruth-matched $X(3872)$ Invariant Mass Signal MC Distribution . . . . .	241
IX.1.2.4	Fit to the $\Delta E$ Combinatorial Background Distribution . . . . .	242
IX.1.2.5	Fit to the $M_{BC}$ Combinatorial Background Distribution . . . . .	243
IX.1.2.6	Fit to the $X(3872)$ Combinatorial Background Invariant Mass Distribution . . . . .	244
IX.1.2.7	Fit to the $\Delta E$ of the Generic Background (Including Non-Resonant) . . . . .	245
IX.1.2.8	Fit to the $M_{BC}$ Distribution of the Generic Background (Including Non-Resonant) . . . . .	246
IX.1.2.9	Fit to the $M(D^0 \bar{D}^0 \pi^0)$ Invariant Mass Distribution of the Generic Background . . . . .	247
IX.1.2.10	Fit to the $M(D^0 \bar{D}^0 \pi^0)$ Invariant Mass Distribution of the Non-Resonant Background . . . . .	248
IX.2.	Data/MC Comparison for Belle . . . . .	249
IX.2.1	$K^\pm$ Data/MC Comparison . . . . .	249
IX.2.2	$\pi^\pm$ Data/MC Comparison . . . . .	250
IX.2.3	$K^\pm, \pi^\pm$ Efficiency and Fake Rate in Belle MC . . . . .	251
IX.2.4	$K_S^0$ Data/MC Comparison . . . . .	251
IX.2.5	$\pi^0$ from $D^0$ Data/MC Comparison . . . . .	252
IX.2.6	$\pi^0$ from $X(4014)$ Data/MC Comparison . . . . .	254
IX.2.7	$D^0 \rightarrow K^\pm \pi^\mp$ . . . . .	256
IX.2.8	$D^0 \rightarrow K^\pm \pi^\mp \pi^0$ . . . . .	258
IX.2.9	$D^0 \rightarrow K^\pm \pi^\mp \pi^\pm \pi^\mp$ . . . . .	260
IX.2.10	$D^0 \rightarrow K_S^0 \pi^\pm \pi^\mp$ . . . . .	262
IX.2.11	$D^0 \rightarrow K^\pm K^\mp$ . . . . .	264
IX.2.12	$B^\pm$ List Variables for the $X(3872)$ Decay . . . . .	266
IX.2.13	$B^\pm$ List Variables for the $X(4014)$ Decay . . . . .	271
IX.3.	$X(3872)$ 2D Fit PDF . . . . .	276

**Bibliography**

## I.1 High Speed Data Multiplexer for the Belle II Pixel Detector

The Belle II Experiment is located at the asymmetric electron-positron-collider SuperKEKB in Tsukuba, Japan. The innermost vertexing detector, the Pixel Detector (PXD), has to cope with data rates of up to 20 GB/s when the collider reaches its design Luminosity of  $8 \cdot 10^{34}$  cm<sup>2</sup>/s. Those data rates arise from the high trigger frequency of  $\approx 30$  kHz and the expected PXD occupancy of  $\approx 3\%$ , due to the short distance to the Interaction Point (IP), where the electron and positron beams cross.

In order to handle these high trigger and data rates, a dedicated Data Acquisition (DAQ) system for the PXD, which runs in parallel to the Belle II DAQ system, was developed. The system is based upon Field Programmable Gate Array (FPGA) technology, embedded on custom designed Compute Node (CN) boards fulfilling the Advanced Telecommunications Computing Architecture (ATCA) standard. This system, the ONline Selection Nodes (ONSEN), receives pixel data from the Data Handling Hybrid (DHH) system, which directly reads out the PXD. Data arriving at the ONSEN system are selected according to interesting physics events by an external trigger decision from the High Level Trigger (HLT), combining the information of all Belle II detectors except the PXD. Depending on these trigger information, which contain so-called Regions Of Interest (ROI), a selection of pixels on the PXD surface, which belong to a reconstructed particle trajectory, are filtered and send further to the Event Builder 2 (EVB2), which builds the full Belle II event. All other pixels are discarded. This way, a physically sensible data reduction of a factor of  $\approx 30$  is achieved.

The default design of the ONSEN-EVB2 data link is based upon 32 optical fiber cables, transmitting the data via SiTCP - an FPGA implementation

of the TCP protocol. This output scheme is right now running stable at the experiment, where only 16 of 32 cables are needed until the upgrade of the PXD in 2022. As soon as more cables are needed, the output option becomes vulnerable and needs more maintenance, due to the 32 optical fibers. To reduce this amount of cables, a new output strategy was developed in this thesis. It combines the outgoing data stream of four ONSSEN modules to one and transmits the data via one 10 Gigabit Ethernet (GbE) cable to the EVB2. This way, the data receiving on the EVB2 can be simplified, the maintenance of 32 cables is brought down to one and the resources of the SiTCP transmitter on the ONSSEN FPGAs can be spared. In this thesis, the firmware for such an alternative output option was developed, the ONSSEN Slow Control (SC) was adjusted and tests for the new output option were performed.

## I.2 Search for an Exotic Resonance at the $D^{*0}\bar{D}^{*0}$ Threshold in Charged $B$ Meson Decays

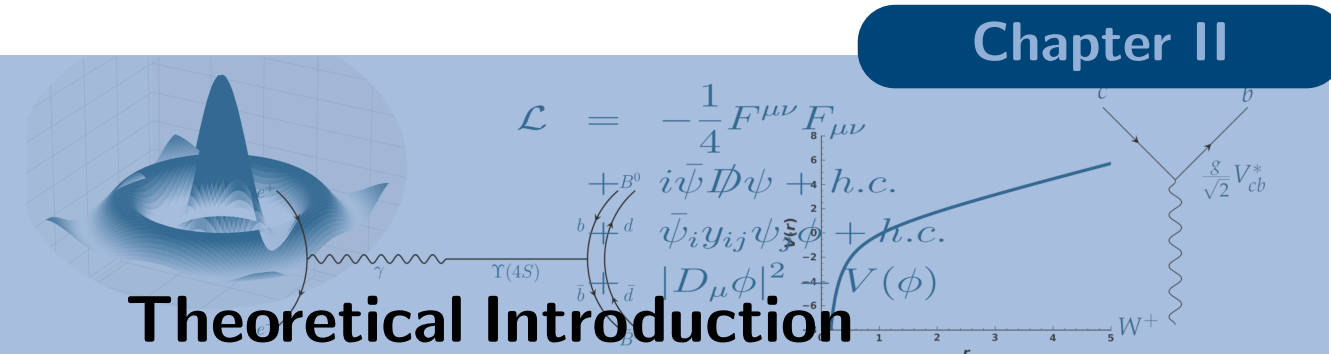
Charmonium spectroscopy has been a vivid field in particle physics since the discovery of the  $c$ -quark in 1974 as a constituent of the  $J/\Psi$  meson. Throughout the decades many new resonances with charm quarks have been discovered. In particular, states of a charm quark and an anti-charm quark, called charmonium, fitted well into a level-scheme, comparable to the one of positronium, dependent on the mass and  $J^{PC}$  quantum numbers of the discovered state. Until 2003, all new states were already predicted by theory and fit in the assumption of such a bound state, until the Belle Experiment discovered a new, narrow resonance - the  $X(3872)$  - in  $B \rightarrow J/\Psi\pi^+\pi^-$  decays.

Due to the decay mode, in which it was discovered, the  $X(3872)$  had clearly charm quarks among its constituents but did not fit into the charmonium level-scheme. For the first time, a resonance, which could only be explained with four quarks as constituents, was observed. The discovery attracted a high level of interest from both, the experimental and theoretical community, and numerous papers trying to explain the nature of that state, and predicting new, likewise states, were published in the following years.

New discoveries in the exotic-state regime, like the  $\Psi(4040)$ ,  $Y(4360)$  and  $Y(4660)$ , strengthened the theories, which explained those states as real resonance, rather than glue-balls or threshold-effects. In 2013, a first charged state - the  $Z_c(3900)$  - was discovered and added to the growing level-scheme of charmonia, now including also all the non-predicted but discovered exotic states.

One theoretical model, which is nowadays one of the most prominent, describes many of these states as hadronic molecules. A bound state of two Mesons interacting via one-pion exchange. As a consequence of heavy quark spin symmetry, those states would have partner states with higher mass and total angular momentum ( $J$ ). In case of the  $X(3872)$ , which is close to the  $D^{*0}\bar{D}^0$  threshold, the predicted resonance, which would be a strong argument for the molecular model, is predicted near the  $D^{*0}\bar{D}^{*0}$  threshold. In this thesis, a simulation of this resonance is performed on Belle II Monte Carlo and the discovery potential for various different width and branching

fraction scenarios in three different data sets is estimated. The reconstruction strategy used for the Belle II simulation is then verified on the rediscovery of the  $X(3872)$  reference channel in  $711 \text{ fb}^{-1}$  of Belle data. At the end of this thesis, the reconstruction is also performed for the  $X(4014)$  search on the full Belle data set.



# Theoretical Introduction

**T**HIS chapter gives an overview of the theoretical base underlying modern particle physics and, in particular, of the physics of interest for the Belle II Experiment and the analysis of this thesis. A first section focuses on the forces and particles described in the Standard Model (SM) starting with a brief introduction on fundamental particles and their categorization before introducing the most relevant terms of the SM Lagrangian and the implications on Charge conjugation and Parity (CP) violation. The second section explains briefly the method of CP-violation measurement at Belle II. In the last section of this chapter, a theoretical introduction to a possible  $X(3872)$  partner state at the  $D^{*0}\bar{D}^{*0}$  threshold is given, which is covering the history of conventional charmonium spectroscopy as well as exotic-state searches.

## II.1 The Standard Model of Particle Physics

**P**ARTICLE physics is the study of elementary particles, point-like objects which are - at least for what science knows so far - not further dividable. To describe those particles and the interactions between them, a successful theoretical framework, the SM, was developed throughout the last decades beginning in the middle of the 20<sup>th</sup> century with the work of Yang and Mills [1], Glashow [2] and Weinberg and Salam [3]. From those first publications, the SM became more and more accurate and promising with every experimental validation or new observation it could describe, such as the discovery of the weak neutral current in 1973 [4]. The core element of the SM are Quantum Field Theories (QFT), theoretical frameworks combining classical field theories, quantum mechanics and special relativ-

ity. A large variety of those has been developed in the past years on top of the two most fundamental QFTs - Quantum Chromo Dynamics (QCD) and Quantum Electro Dynamics (QED). Formally, QED and QCD are a unified quantum field theory with an underlying  $SU(3)_c \times SU(2)_L \times U(1)_Y$ <sup>1</sup> gauge group<sup>2</sup>. This unified theoretical building is essential to describe three out of the four forces in nature:

- **Strong Force:** binding nucleons in atomic cores, described by QCD
- **Weak Force:** responsible for the nuclear  $\beta$ -decay, described by QED
- **Electromagnetism:** governing all kinds of electromagnetic interaction, described in QED

The missing, and for us most "visible" force, gravitation, is not described in the SM at all. By construction, the existence of a force-carrying particle for gravitation is valid in the SM, but the description of phenomena taking into account all four forces is not possible within the SM. Since distances and time evolution are taking action on very small scales and masses, the effect of gravitation is suppressed by many orders of magnitude and can therefore be ignored. All elementary particles and the forces described in the SM are shown in II.1.

In figure II.1, particles are structured in Quarks (blue), Leptons (red) and Gauge-Bosons (yellow). Leptons and Quarks are commonly referred to as Fermions,  $Spin = 1/2$  particles building up the matter surrounding us, whereas the Gauge-Bosons, which arise from excitations in the associated gauge fields and carry the forces, are Bosons with integer spin. The gluon ( $g$ ) mediates the strong force, the photon ( $\gamma$ ) the electromagnetic force and  $W^\pm$  and  $Z^0$  are carrying the weak force. The Higgs-Boson (H) is not mediating any force in the SM but, instead, responsible for the acquisition of mass. In the SM, this mechanism is implemented through spontaneous symmetry breaking, a phenomenon introduced by a complex scalar field with non-zero vacuum expectation value<sup>3</sup>, referred to as the Higgs-Field.

---

<sup>1</sup>where  $c$  is the color charge,  $L$  the chiral symmetry and  $Y$  the hyper-charge

<sup>2</sup>A field theory with an invariant Lagrangian being under local transformations. First gauge-theory by W. Pauli in 1941 [5]

<sup>3</sup>The average expected value of an operator acquires in vacuum, e.g. state with lowest possible energy

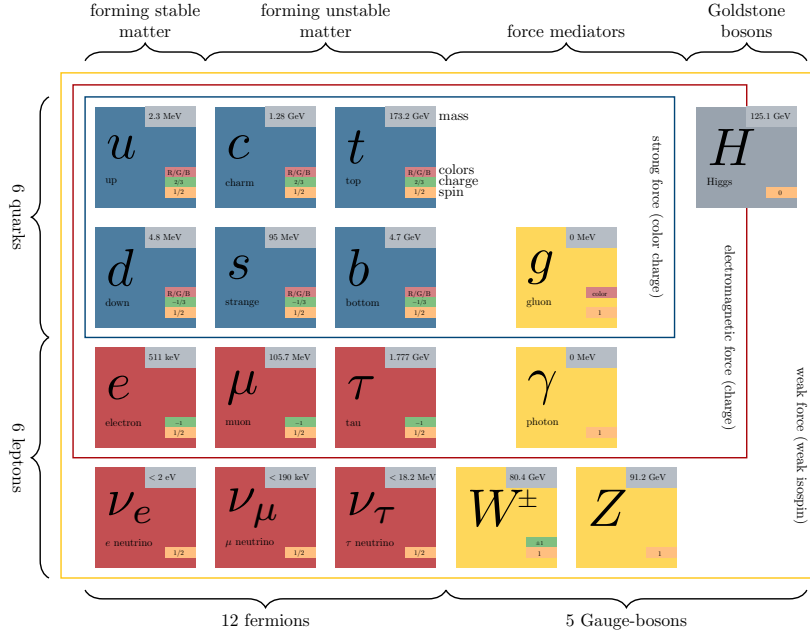


Figure II.1: A schematic overview of the fundamental constituents of the Standard Model of Particle Physics.

### II.1.1 The Standard Model Lagrangian

THE mathematical description of the theories unified in the SM is provided by the Lagrangian formalism:

$$\mathcal{L}_{SM} = \mathcal{L}_{Kinetic} + \mathcal{L}_{EW} + \mathcal{L}_{QCD} + \mathcal{L}_{Higgs} + \mathcal{L}_{Yukawa} \quad (1)$$

Each term of the SM Lagrangian is briefly discussed in the following section.

### II.1.1.1 The Kinematic Term of the Standard Model Lagrangian

In the first term,  $\mathcal{L}_{Kinetic}$ , the self-interactions of the gauge bosons are described. It can be written as

$$\mathcal{L}_{Kinetic} = -\frac{1}{4}B_{\mu\nu}B^{\mu\nu} - \frac{1}{2}tr(W_{\mu\nu}W_{\mu\nu}) - \frac{1}{2}tr(G_{\mu\nu}G^{\mu\nu}), \quad (2)$$

where traces ( $tr$ ) run over  $SU(2)$  and  $SU(3)$  indices of  $W$  and  $G$  respectively.  $B_{\mu\nu}$  represents the gauge-field tensor of the weak hyper charge.

### II.1.1.2 The Electromagnetic and the Weak Force

The second term,  $\mathcal{L}_{EW}$ , describes the electroweak unification of the SM which corresponds to the symmetry group  $U(1) \times SU(2)_L$ <sup>4</sup> and can be written as

$$\mathcal{L}_{EW} = \sum_i \bar{\psi}_i \gamma^\mu (i\partial_\mu - \frac{1}{2}g'Y_W B_\mu - \frac{1}{2}g\tau W_\mu^a)\psi_i \quad (3)$$

The sum in the above equation is running over  $\psi_i$  indicating left-handed fermion doublets described as Dirac spinors which connect to the vector representation of the Lorentz group through the Dirac matrices  $\gamma_\mu$ . A kinetic term for the fermion is introduced by the derivatives  $\partial_\mu$ ,  $g'$  and  $g$  are coupling constants to the electromagnetic and weak fields respectively. The weak hyper charge,  $Y_W$ , generator of the  $U(1)$  group acting on the  $U(1)$  gauge field  $B_\mu$ , is defined by the equation  $Q = I_3 + \frac{Y_W}{2}$  with  $Q$  being the electric charge and  $I_3$  the third component of the weak isospin. The infinitesimal generators of the  $SU(2)$  group, the Pauli matrices  $\tau$ , contain the isospin charges of particles interacting with the weak force as their eigenvalues. The gauge bosons, arranged in a weak Isospin triplet  $W_\mu^a$  ( $a = 1, 2, 3$ ) and a singlet  $B_\mu$ , represent the mediators of the electromagnetic and the weak force. This is called the **electroweak unification** [3, 6].

The electromagnetic interaction is mediated via photons ( $\gamma$ ) which couple to the electric charge, hence neutral particles do not take part. Since the photon itself is mass less and carries no charge, the range of the electromagnetic interaction becomes infinite.

---

<sup>4</sup>L indicates a coupling only to left-handed fermions

The weak force is mediated by the charged  $W^\pm$  and the neutral  $Z^0$  bosons. Since the  $W^\pm$  originates from the  $SU(2)$  group, which is depending on chiral symmetry, it is maximal charge and parity-violating; it only couples to left-handed particles and right-handed anti-particles. So far, the exchange of  $W^\pm$  bosons is the only source of flavor changing processes in the SM which can couple an up-type quark to a down-type quark and a lepton to its corresponding neutrino. In the lepton sector, those flavor changes are limited to the individual families, whereas in the quark-sector flavor changes can be introduced over family borders.

The interaction via the neutral current mediated by the  $Z^0$  is similar to the electromagnetic interaction. In principle, a flavor change via the  $Z^0$  is not forbidden in the SM but highly suppressed via the GIM mechanism [6]. Due to the large masses of  $W^\pm$  and  $Z^0$ , the weak interaction is very short-ranged but has similar coupling strength as the electromagnetic interaction.

### II.1.1.3 The Strong Force

To describe the strong interaction in the SM, the  $\mathcal{L}_{QCD}$  term is introduced as

$$\mathcal{L}_{QCD} = \sum_j \bar{\psi}_j \gamma^\mu (i g_s G_{A,\mu} T_{A,ij} - m \delta_{ij}) \psi_j, \quad (4)$$

where  $g_s$  is the coupling constant of the strong force,  $G_{A,\mu}$  the gluon field,  $T_a$  the generator of the  $SU(3)$  symmetry and the mass  $m$ . The indices  $i$  and  $j$  are running from 1 to 3 and indicate the color/anti-color<sup>5</sup> carried by quarks and gluons. Since the underlying symmetry group ( $SU(3)$ ) is non-abelian, the gluons are always carrying color and anti-color, allowing them to interact among themselves. The quarks do only carry either color, in case of a quark and anti-color, in case of an anti-quark.

All particles shown in II.1 are elementary and do therefore not divide into other particles nor do they decay. Nevertheless, the SM predicts many more states of combinations of those particles, the so-called Hadrons, bound by the strong force. Hadrons are further divided in Mesons, integer spin particles composed of quark and anti-quark, and Baryons, particles with  $(2n + 1)/2$  spin composed of 3 quarks or anti-quarks. All of these objects are colorless states, which means, that the net-color combines to a white state. Up to now, no observed states are featuring a net-color charge! The SM explains

---

<sup>5</sup>The color/anti-color quantum numbers have values red, green and blue ( $r, g, b$ ) and anti-red, anti-green and anti-blue ( $\bar{r}, \bar{g}, \bar{b}$ ) respectively

this with the **confinement** [7, 8], due to which no free quarks can be observed and only bound states are allowed. Other states, such as 4 or 5-Quark bound states, are also possible within the SM. A first one of those new states, the  $X(3872)$ , was found in 2003 at the Belle Experiment [9] and later validated by BaBar [10] and BESIII [11]. A theoretical introduction to those states and especially the possible  $X(4014)$  resonance, which is one topic of this thesis, is given in II.3.

#### II.1.1.4 The Higgs Field

The kinetic contribution of the Higgs-boson and its interactions with the other force-carriers are described in the Higgs-term of the SM-Lagrangian.

$$\mathcal{L}_{Higgs} = [(\partial_\mu - igW_\mu^a t^a - ig'Y_\phi B_\mu)\phi]^2 + \mu^2\phi^\dagger\phi - \lambda(\phi^\dagger\phi)^2, \quad (5)$$

where  $\partial_\mu$  is the kinetic term,  $g$  and  $g'$  are the coupling constants of the weak and electromagnetic force respectively. The complex scalar Higgs field denoted in  $\phi = \frac{1}{\sqrt{2}} \begin{pmatrix} \phi^+ \\ \phi^0 \end{pmatrix}$ , with  $+$  and  $0$  indicating the electric charge. By choosing  $\lambda > 0$  and  $\mu^2 > 0$ , the mechanism of spontaneous symmetry breaking can be used and the  $W^\pm$  and  $Z^0$  bosons acquire their masses.

#### II.1.1.5 The Yukawa Coupling

The acquisition of quark masses, as a result of the interaction with the Higgs-field, is described in the Yukawa term of the SM-Lagrangian.

$$\mathcal{L}_{Yukawa} = G_u^{ij}\bar{U}_L\phi^0U_R - G_u^{ij}\bar{D}_L\phi^-U_R + G_d^{ij}\bar{U}_L\phi^+D_R + G_d^{ij}\bar{D}_L\phi^0D_R \quad (6)$$

In the above equation, the right-handed quark fields (indexed with  $R$ ) couple to the left-handed (indexed  $L$ ) quark fields via the scalar fields  $\phi$ . The Yukawa couplings  $G_{u,d}^{ij}$  are complex  $3 \times 3$  matrices with indices  $i, j = 1, 2, 3$  denoting the quark generations and  $u, d$  denoting up-type ( $u$ ) or down-type ( $d$ ) quarks.

Since the scalar Higgs fields  $\phi$  have a non-zero vacuum expectation value ( $v^0$ ), the mass matrices for up-type ( $MU_{ij}$ ) and down-type ( $MD_{ij}$ ) quarks, wick can be written as:

$$MU_{ij} = \frac{1}{\sqrt{2}}G_u^{ij}v^0 \quad \text{and} \quad MD_{ij} = \frac{1}{\sqrt{2}}G_d^{ij}v^0 \quad (7)$$

get, via diagonalization with the unitarity matrices  $TU_{L,R}, TD_{L,R}$ , non-zero entries on their main diagonal. Those matrices also transform the left-handed ( $U_L$ ) and right-handed ( $U_R$ ) quark fields from their weak eigenstate basis to the mass eigenstate basis. When expressing the interaction of quarks with the gauge fields in terms of the mass eigenstates, instead of the weak eigenstates, the term for the neutral current stays invariant while the charge current term changes. This is the foundation of the GIM mechanism and the reason for the absence of flavor changing neutral currents - at tree level - in the SM.

When expressing the charged currents in the mass eigenstates ( $M$ ),

$$\begin{aligned} I_V^+ &= \bar{U}_L \gamma^\nu D_L = \bar{U}_L^M \gamma^\nu T U_L T D_L^\dagger D_L^M \\ I_V^- &= \bar{D}_L \gamma^\nu U_L = \bar{D}_L^M \gamma^\nu T D_L T U_L^\dagger U_L^M \end{aligned} \quad (8)$$

the transformation matrices  $TU_L T D_L^\dagger$  can be expressed as the unitary Cabibbo-Kobayashi-Maskawa (CKM) matrix  $V_{CKM}$ .

$$V_{CKM} = \begin{pmatrix} V_{ud} & V_{us} & V_{ub} \\ V_{cd} & V_{cs} & V_{cb} \\ V_{td} & V_{ts} & V_{tb} \end{pmatrix} \quad (9)$$

When comparing the charged current interaction of quarks with its charge and parity (CP) conjugated<sup>6</sup> counterpart, one observes that only if  $V_{CKM_{ij}}^* = V_{CKM_{ji}}$  is satisfied the interactions are equal. As Kobayashi and Maskawa demonstrated in 1973 [12], the CKM quark-mixing matrix contains a complex phase, if there are at least three or more quark generations. This phase causes an inequality in the matrix elements  $i, j$  of the  $V_{CKM}$  compared to the ones of  $V_{CKM}^*$ , which is the only source of CP violation in the SM.

### II.1.1.6 The Unitary Triangle and CP-Violation

The charged current interactions, mediated by the  $W^\pm$  bosons, couple the up and down-quark types via the corresponding matrix element  $ij$  of the CKM matrix. Examples for this are shown in Fig. II.2.

In the Feynman diagrams, the matrix elements  $V_{ij}$  contain the coupling strength of the charged weak boson, the  $W^\pm$ , to the individual quark flavors. To visualize this strength, which is strongly dependent on the quark

---

<sup>6</sup>charge conjugate C : exchange of all internal quantum numbers, e.g. transforms particle in anti-particle

parity conjugate P : reverses handedness of particle, e.g. left-handed to right-handed

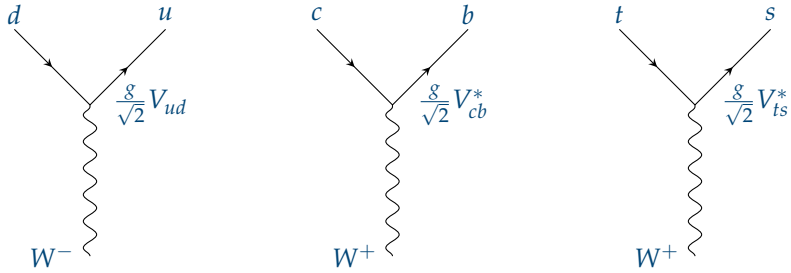


Figure II.2: The Feynman diagrams above show the transformation of  $d \rightarrow u$ ,  $c \rightarrow b$  and  $t \rightarrow s$ . During the transition, a  $W^\pm$  boson is exchanged and couples to the quarks via the matrix element  $V_{ij}$  of the CKM matrix.  $g$  denotes the coupling constant of the strong interaction.

families of the mixing quarks, a schematic coupling diagram is shown in Fig. II.3 The lines indicate the strength of the  $W^\pm$  coupling between different quark flavors, or, in other words, the probability for a transition among them. Coupling strength decreases in line thickness.

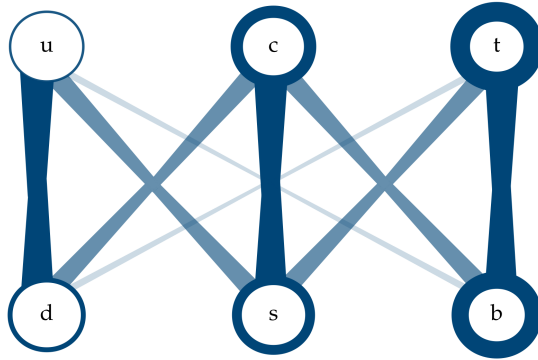


Figure II.3: Visualization of the CKM matrix elements as interaction lines between quark families. Thick, dark blue lines indicate strong coupling, while thinner, lighter blue lines indicate decreasing CKM couplings. Transitions of quarks belonging to the same family  $((u, d), (c, s), (t, b))$  are CKM favored!

As already stated before, the CKM matrix fulfills the unitarity conditions,

---

e.g.  $V_{CKM}^\dagger V_{CKM} = \mathbb{1}$ , which can be expressed as:

$$\sum_i (V_{CKM})_{ij} (V_{CKM})_{ik}^* = \delta_{jk} \quad \text{and} \quad \sum_j (V_{CKM})_{ij} (V_{CKM})_{kj}^* = \delta_{ik} \quad (10)$$

Those conditions can be rewritten to six equations with a vanishing sum of the CKM matrix elements  $\delta_{ij}$ :

- $V_{ud}^* V_{us} + V_{cd}^* V_{cs} + V_{td}^* V_{ts} = 0$
- $V_{ud} V_{cd}^* + V_{us} V_{cs}^* + V_{ub} V_{cb}^* = 0$
- $V_{us}^* V_{ub} + V_{cs}^* V_{cb} + V_{ts}^* V_{tb} = 0$
- $V_{td} V_{cd}^* + V_{ts} V_{cs}^* + V_{tb} V_{cb}^* = 0$
- $V_{td} V_{ud}^* + V_{ts} V_{us}^* + V_{tb} V_{ub}^* = 0$
- $V_{ud} V_{ub}^* + V_{cd} V_{cb}^* + V_{td} V_{tb}^* = 0$

All these equations can be interpreted as triangles in the complex plane. To have an understanding of how strong CP violation is in the CKM matrix, the angles of these triangles are measured. Unfortunately, not all of them can be used. In Fig. II.3 the coupling strength among quark flavors is indicated as lines of different thickness. The numerical decrease between the coupling strength of thick lines and thin lines is skipping a few orders of magnitude. For the first four equations above, this results in a distorted triangle with tiny angles, which are very hard to measure. For the last two equations, the matrix elements  $V_{ij}$  all have the same magnitude leading to "normal" triangles with bigger angles. Of particular interest for  $B$ -factories, where the produced  $B$  mesons contain a bottom ( $b$ ) quark, is the triangle given by the last, blue equation, which contains  $b$  quark transitions in all terms. In Fig. II.4 this triangle is shown and some of the measurable decay channels are indicated.

The angles of that triangle are named  $\alpha$ ,  $\beta$  and  $\gamma$ <sup>7</sup> and are related to the matrix elements of the CKM matrix as follows.

$$\alpha = \arg\left(-\frac{V_{td} V_{tb}^*}{V_{ud} V_{ub}^*}\right), \quad \beta = \arg\left(-\frac{V_{cd} V_{cb}^*}{V_{td} V_{tb}^*}\right), \quad \gamma = \arg\left(-\frac{V_{ud} V_{ub}^*}{V_{cd} V_{cb}^*}\right) \quad (11)$$

---

<sup>7</sup>This is the Belle naming convention, at BaBar they are named  $\phi_1 = \beta$ ,  $\phi_2 = \alpha$ ,  $\phi_3 = \gamma$ .

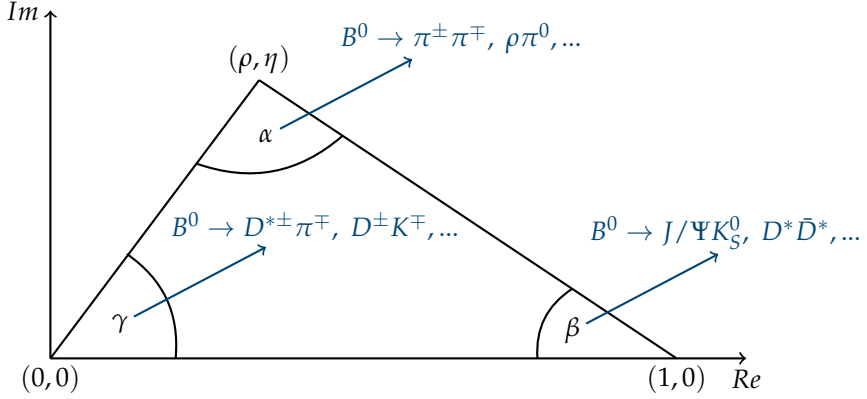


Figure II.4: The unitary triangle in the complex plain, the angles  $\alpha, \beta, \gamma$  are indicated with corresponding decay modes which can be measured at  $B$ -factories.

## II.2 Physics at the Belle II Experiment

**I**N this section an overview on the main physics phenomena - measurement of CP-violation - which will be targeted at the Belle II experiment is given.

### II.2.1 CP Violation Measurements

**T**HE SM differentiates between two types of CP-violation - direct and indirect. Direct CP-violation is resulting in different branching fractions of a particle and its CP conjugated counterpart due to different decay amplitudes, i.e.  $|A_f/\bar{A}_f| \neq 1$ , with  $f$  being a CP eigenstate. It is the only source of CP-violation in decays of charged mesons. For charged  $B$  mesons, the direct CP-asymmetry,  $A_{CP}^{dir}$ , can be expressed as the difference in decay rates between  $B^+$  and  $B^-$  normalized to their total rate.

$$A_{CP}^{dir} = \frac{Br(B^- \rightarrow f^-) - Br(B^+ \rightarrow f^+)}{Br(B^- \rightarrow f^-) + Br(B^+ \rightarrow f^+)} \quad (1)$$

An example Feynman diagram for direct CP-violation in  $B$  decays is given in Fig. II.5. It shows the decay  $B_d^0 \rightarrow K^+ \pi^-$ , which CP asymmetry has been measured by LHCb to be  $-0.074 \pm 0.33 \pm 0.008$  [13]

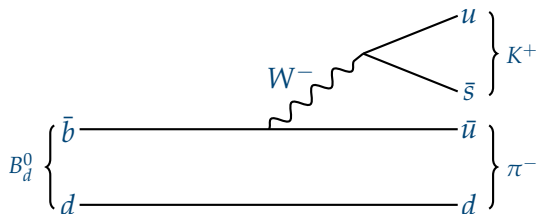


Figure II.5: Feynman diagram of the decay  $B_d^0 \rightarrow K^+ \pi^-$ .

Indirect CP-violation evolves from meson mixing and was first discovered in the Kaon system. A meson, consisting of quark and anti-quark, is produced with definite quark flavors but propagates with a distinct mass. The eigenstate of the propagation can be a superposition of different flavor eigenstates, hence a flavor eigenstate, different from the initial one, can be observed after a time of propagation  $t$ . This change in flavor eigenstate can be expressed as an oscillation of a particle into its own anti-particle and back. In Fig. II.6 such an oscillation is shown for the example of  $B^0 - \bar{B}^0$  and  $B_s^0 - \bar{B}_s^0$  mixing.

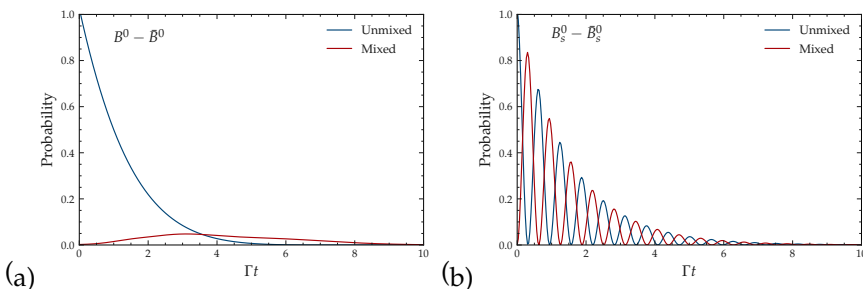


Figure II.6: Oscillation probabilities for the unmixed (blue) and mixed (red) in dependence of the decay time for the  $B^0$  (a) and  $B_s^0$  (b) system.

In case of the  $B_s^0$  system the mixing frequency is much higher<sup>8</sup> due to the stronger CKM-coupling between the  $b$  and the  $s$  quark contained in the meson. For the  $B^0$  mixing, the matrix element is much smaller since the flavor change has to skip two quark generations.

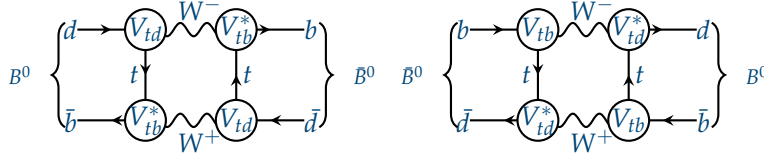


Figure II.7: Feynman diagram of the  $B^0 - \bar{B}^0$  mixing.  $V_{ij}$  indicates the participating CKM matrix element.

Focusing on the  $B^0$  mixing, Fig.II.7, the mass eigenstates can be expressed as

$$B_L = p|B^0\rangle + q|\bar{B}^0\rangle \quad \text{and} \quad B_H = p|B^0\rangle - q|\bar{B}^0\rangle \quad (2)$$

With indices  $L$  and  $H$  denoting the light and heavy eigenstate respectively. When the parity operator  $P = -(-1)^L$  is applied to  $B^0$  a negative sign is introduced<sup>9</sup>

$$P|B^0\rangle = -|\bar{B}^0\rangle \quad (3)$$

the same applies to  $\bar{B}^0$ . When additionally applying the charge operator  $C$ , particle and anti-particle are exchanged, so the  $CP$  conjugate of  $B_L$  and  $B_H$ , whilst holding  $q$  and  $p$ , gives

$$\begin{aligned} CP(p|B^0\rangle + q|\bar{B}^0\rangle) &= -(p|B^0\rangle + q|\bar{B}^0\rangle) \quad \text{and} \\ CP(p|B^0\rangle - q|\bar{B}^0\rangle) &= (p|B^0\rangle - q|\bar{B}^0\rangle). \end{aligned} \quad (4)$$

The above transformation shows that the mass and  $CP$  eigenstate of  $B^0$  meson are identical, which implies, that a once determined  $CP$  eigenstate would also propagate in that configuration and could not be measured with another value at a later time. A measurable  $CP$ -violation can thus only be

<sup>8</sup>Can only be measured at LHCb due to larger boost of the  $B_s^0$  system

<sup>9</sup> $L$  being the angular momentum, 0 in case of  $B^0$

introduced if  $|p| \neq |q|$ . This effect is called indirect CP violation.

In 1981 Bigi and Sanda published a paper in which they propose to investigate a combined effect of direct and indirect CP-violation in the  $B$  meson system [14]. This effect can be observed when a coherent meson system decays into the same final state. In case this final state,  $f$ , is a CP eigenstate, the magnitude of CP-violation can be expressed as

$$\lambda_{CP} = \frac{q}{p} A_f \bar{A}_f \quad (5)$$

This mixing-induced CP-violation can be expressed as time dependent asymmetry

$$A_{CP}(t) = \frac{\Gamma(\bar{P}^0(t) \rightarrow f) - \Gamma(P^0(t) \rightarrow f)}{\Gamma(\bar{P}^0(t) \rightarrow f) + \Gamma(P^0(t) \rightarrow f)}, \quad (6)$$

which can be rewritten to [15](p.31)

$$A_{CP}(t) = \frac{S_{CP}^{mix} \sin(\Delta Mt) - C_{CP}^{dir} \cos(\Delta Mt)}{\cosh(\Delta \Gamma t/2) - A_{\Delta \Gamma} \sinh(\Delta \Gamma t/2)}, \quad (7)$$

with

$$S_{CP}^{mix} = \frac{2\text{Im}(\lambda_{CP})}{1 + |\lambda_{CP}|^2}, \quad C_{CP}^{dir} = \frac{1 - |\lambda_{CP}|^2}{1 + |\lambda_{CP}|^2} \quad \text{and} \quad A_{\Delta \Gamma} = \frac{2\text{Re}(\lambda_{CP})}{1 - |\lambda_{CP}|^2} \quad (8)$$

For  $S_{CP}^{mix}$ ,  $C_{CP}^{dir}$  and  $A_{\Delta \Gamma}$  also applies

$$|S_{CP}^{mix}|^2 + |C_{CP}^{dir}|^2 + |A_{\Delta \Gamma}|^2 = 1. \quad (9)$$

To measure the mixing-induced and direct CP-violation, the parameters  $S_{CP}^{mix}$  and  $C_{CP}^{dir}$  can be used respectively. The parameter  $|A_{\Delta \Gamma}|$  introduces another observable for neutral meson systems. In  $B^0$  decays it is negligible due to the low oscillation frequency, which simplifies the expression for the time-dependent amplitude  $A_{CP}(t)$  to

$$A_{CP}(t) = S_{CP}^{mix} \sin(\Delta Mt) - C_{CP}^{dir} \cos(\Delta Mt) \quad (10)$$

$S_{CP}^{mix}$  and  $C_{CP}^{dir}$  are directly accessible from the oscillation amplitudes of proper decay times for flavor tagged decays<sup>10</sup>. If all amplitudes contributing

---

<sup>10</sup>The flavor of the first  $B$  decay is tagged, detailed explanation in next chapter.

to a decay carry the same weak phase, one finds  $|A_{f_{CP}}| = |\bar{A}_{f_{CP}}| = |\lambda_{f_{CP}}| = 1$ . In that case, no direct CP-violation occurs and the mixing induced CP-violation is related to the CKM matrix elements involved in the mixing.

### II.2.1.1 Coherent $B^0 - \bar{B}^0$ Mixing

To measure the mixing induced CP-violation in  $B^0$  decays at Belle II, a coherent  $B^0 - \bar{B}^0$  mixing is mandatory, allowing the analyst to flavor-tag one of the initial  $B^0$  candidates. The  $B$  mesons, produced in  $e^+e^- \rightarrow (4S) \rightarrow B\bar{B}$ , are evolving coherently, starting from a well-defined quantum entangled state<sup>11</sup>.

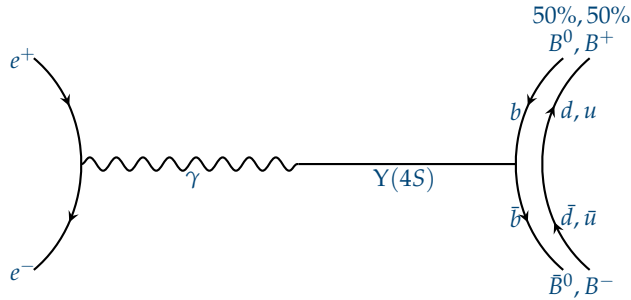


Figure II.8: Production of  $B$  mesons at SuperKEKB.

The quantum entangled  $B$  states shown in Fig. II.8, are examples of the Einstein-Podolsky-Rosen effect [16]. In the  $e^+e^-$  collisions at Belle II, a virtual photon is produced, which, due to its energy sitting directly at the  $Y(4S)$  mass, forms an  $Y(4S)$  with quantum numbers  $J^{PC} = 1^{--}$ . This  $Y(4S)$  state is the first bottomonium-state above the open-bottom threshold, thus  $M(Y(4S)) > M(B\bar{B})$ , which makes the decay to a  $B$  meson system possible. Due to the open-bottom decay, which accounts for 96% of the  $Y(4S)$  decays, the  $Y(4S)$  decay rate is much higher than from its lower mass relatives.

---

<sup>11</sup> $N$  particles form a quantum entangled state, if the state, as one, is well defined, rather than its components alone.

### II.2.1.2 Flavor Tagging

A tag on the flavor can be set once one of the two  $B$  is decayed into a flavor specific<sup>12</sup> final state. Since the  $B$  system is quantum entangled, one can conclude that the other  $B$ , which decays later, **must**, at the time of decay, be the anti-particle of the tagged  $B$ . In Fig. II.10 such a decay is shown. The tagged  $B$  meson  $B_{tag}$  is decaying via the semi-leptonic decay  $B^0 \rightarrow D^- l^+ \nu_l$ , a flavor specific decay of the  $B^0$  **but not** the  $\bar{B}^0$ . In this example, the tagged  $B^0$  defines the flavor of the other  $B$  meson to be  $\bar{B}^0$ , at the time of decay. From that moment on, the  $\bar{B}^0$  is propagating as individual, flavor oscillating particle until it decays - either as  $B^0$  **or**  $\bar{B}^0$ .

If the decay happens to be a CP eigenstate, like  $J/\Psi K_S^0$  in the example, CP-violation measurements in the interference of decay and mixing can be done. In the article published by Bigi and Sanda, they concluded that the decay  $B^0/\bar{B}^0 \rightarrow J/\Psi K_S^0$ , often referred to as *golden channel*, is a very promis-

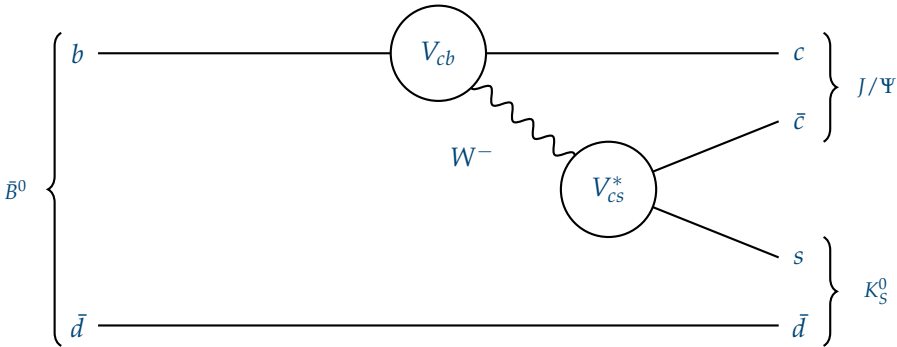


Figure II.9: Golden channel decay.

ing candidate to measure time-dependent CP-violation for the  $\sin(2\beta)$  angle (Fig. II.4). To measure time-dependent CP violation, it is crucial to have a precise determination of the decay time difference  $\Delta t$  between the two  $B$  meson decays,  $B_{tag}$  and  $B_{reco}$ . In the production process Fig. II.8, the  $B$  mesons are produced at rest, if the  $Y(4S)$  has momentum zero - in that case no decay time difference could be measured.

<sup>12</sup>A flavor combination only possible for either  $B$  or  $\bar{B}$

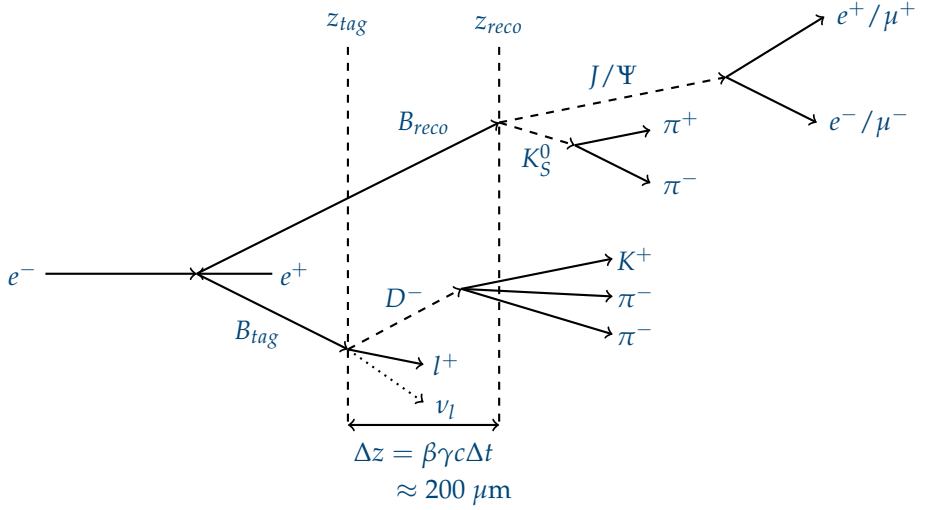


Figure II.10: Flavor tagging scheme for the measurement of time dependent CP-violation at Belle II.

A non-zero  $Y(4S)$  momentum can be transferred, if the  $e^+e^-$ -collider has asymmetric energies between both rings. In case of Belle and Belle II, the electron beam has, in respect to the positron beam, a higher energy leading to a boost of the produced  $B$  meson system. If the boost is strong enough, and a good vertexing is applied, one can calculate the decay time difference  $\Delta t$  via  $\Delta t = \Delta z / \beta\gamma c$ , with  $\beta\gamma$  being the boost of the center of mass frame,  $c$  the speed of light and  $\Delta z$  the vertex resolution in beam direction. In the former Belle experiment, a silicon-strip vertex detector<sup>13</sup> performed the vertexing. For Belle II an additional vertex detector, based on single pixels instead of strips, was installed. It allows for vertex resolutions of  $\approx 20 \mu\text{m}$  in  $z$  direction [11, p. 16] which is, compared to the former Belle vertex resolution of  $\approx 100 \mu\text{m}$  in  $z$  [17], a huge increase and will give rise to high precision measurements of  $B$  meson decay vertices.

In 2001 Belle and Babar published two papers which showed CP-violation in the *golden channel* of the  $B$  meson system [18, 19]. To measure CP-violation, Eq. 6 is exploited. The important parameter is  $\lambda_{CP}$ , which, via Eq. 5, is con-

<sup>13</sup>Explanation to the upgraded Belle II version in the experimental chapter.

nected to the coefficients  $q$  and  $p$  of the  $B$  meson mixing Eq. 2. In the SM, the fraction  $q/p$  can be expressed as

$$\frac{q}{p} = \frac{V_{td}V_{tb}^*}{V_{td}^*V_{tb}} \quad (11)$$

which can be derived from the Feynman diagrams in Fig. II.7 ([20], p.304). Since the final state,  $J/\Psi K_S^0$ , is dominated by the  $b \rightarrow c\bar{c}s$  transition and the neutral Kaon mixing, Fig. II.11, the matrix elements involved are known and the decay amplitudes can be expressed as

$$\frac{\bar{A}_f}{A_f} = \eta_f \frac{V_{cb}V_{cs}^*}{V_{cb}^*V_{cs}} \frac{V_{cd}V_{cd}^*}{V_{cd}^*V_{cd}} \quad (12)$$

with  $\eta_f$  being the CP eigenvalue of the final state;  $-1$  for  $K_S^0$  and  $+1$  for  $K_L^0$ . The  $V_{cs}$  and  $V_{cs}^*$  elements cancel and, with Eq. 5,  $\lambda_{CP}$  can be written as

$$\lambda_{CP} = \eta_f \frac{V_{td}V_{tb}^*}{V_{td}^*V_{tb}} \frac{V_{cb}V_{cd}^*}{V_{cb}^*V_{cd}} \quad (13)$$

Using the rules for the  $arg$  function, and the definition for  $\beta$  in Eq. 11, the above equation can be rewritten as

$$\lambda_{CP} = \eta_f e^{-2i\beta} = \eta_f \cos(2\beta) - i\eta_f \sin(2\beta) \quad (14)$$

This allows the calculation of the CP asymmetry with Eq. 10. The terms  $S_{CP}^{mix}$  and  $C_{CP}^{dir}$  are defined in Eq. 8. Since  $C_{CP}^{dir} = (1 - |\lambda_{CP}|^2)/(1 + |\lambda_{CP}|^2)$ , the direct CP violation term vanishes,  $C_{CP}^{dir} = 0$ , and only the mixing induced CP-violation,  $S_{CP}^{mix} = \eta_f \sin(2\beta)$ , does not vanish. With Eq. 10, the time-dependent CP asymmetry is expressed as

$$A_{CP}(t) = \eta_f \sin(2\beta) \sin(\Delta Mt). \quad (15)$$

The measurable quantities of Eq. 15 are  $A_{CP}(t)$  and  $\sin(\Delta Mt)$ ,  $\eta_f$  is defined by the  $K_S^0$

final state as  $+1$ , which allows the calculation of the  $\beta$  angle and the magnitude of the corresponding CKM matrix elements. The measurement of the  $\beta$  angle was, for Belle as well as for BaBar, a huge success and let, in 2008, to the Nobel prize for Makoto Kobayashi and Toshihide Maskawa for their work on the CKM mechanism and CP violation from 1973 [12].

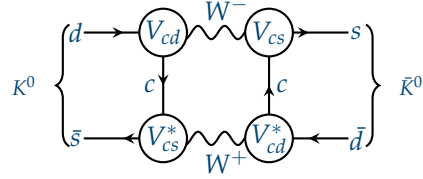


Figure II.11: Mixing in the neutral Kaon system.

In Fig. II.12 the latest Belle measurements on time depended CP violation, using the full  $711 \text{ fb}^{-1}$  Belle data set, is shown. The CKM-fitter group<sup>14</sup> uses the published measurements from various experiments and combines them in an annual report on the different CKM triangles. In Fig. II.13 the most recent update of the bespoken triangle is shown. The fitted values of this triangle are:

$$\begin{aligned}
 A &= 0.8235^{+0.0056}_{-0.014} \quad , \quad \lambda = 0.224837^{+0.000251}_{-0.000060} & (16) \\
 \bar{\rho} &= 0.1569^{+0.0102}_{-0.0061} \quad , \quad \bar{\eta} = 0.3499^{+0.0079}_{-0.0065} \\
 \alpha &= 86.4^{\circ+4.5}_{-4.3} \quad , \quad \beta = 22.56^{\circ+0.47}_{-0.40} \quad , \quad \gamma = 65.80^{\circ+0.94}_{-1.29}
 \end{aligned}$$

with  $A$ ,  $\lambda$ ,  $\bar{\rho}$  and  $\bar{\eta}$  the parameters of the Wolfenstein parametrization<sup>15</sup>.

If the triangle closes at the tip, i.e.  $\alpha + \beta + \gamma = 180^\circ$ , no New Physics<sup>16</sup> (NP), originating from CP violation, is expected. A not closing triangle instead will favor a contribution of NP to the CP violation mechanism in the SM.

<sup>14</sup>Group of researches presenting annual reports and fits for the CKM triangles.

<sup>15</sup>A commonly used parametrization of the CKM matrix by Lincoln Wolfenstein [21].

<sup>16</sup>Commonly used term to refer to physics outside the Standard Model

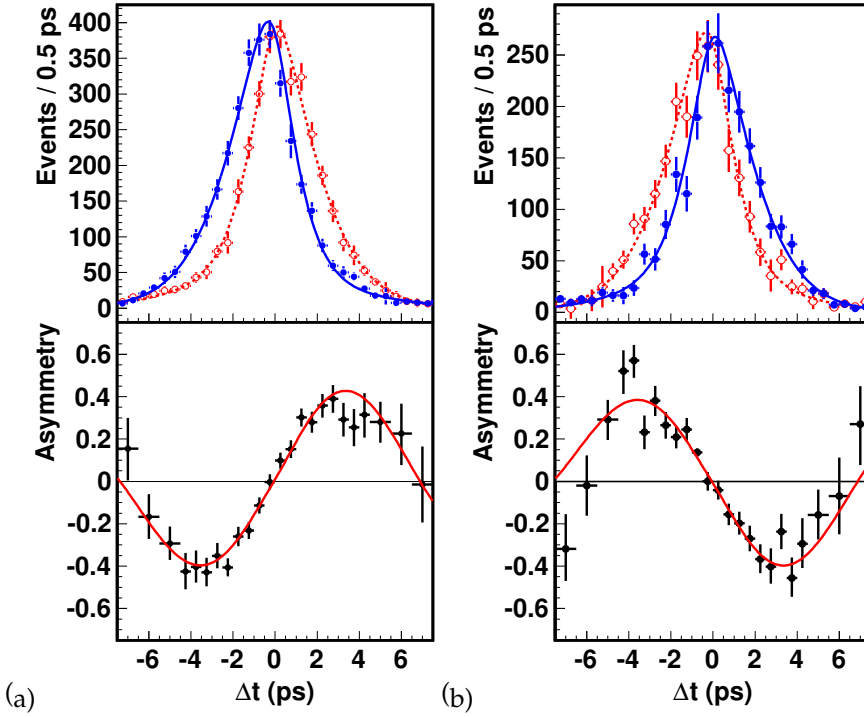


Figure II.12: Measurements of time-dependent CP asymmetry with the full Belle data set, taken from [22]. Plot (a) shows the decay  $B \rightarrow K_S^0 J/\Psi$ , a CP-odd final state, while (b) shows the CP-even  $B \rightarrow K_L^0 J/\Psi$  final state. The top plots show the decay rates, with  $B_{tag} = B^0$  in red and  $B_{tag} = \bar{B}^0$  in blue. In the bottom plots the asymmetry is shown, which allows the extraction of  $\sin(2\beta)$ .

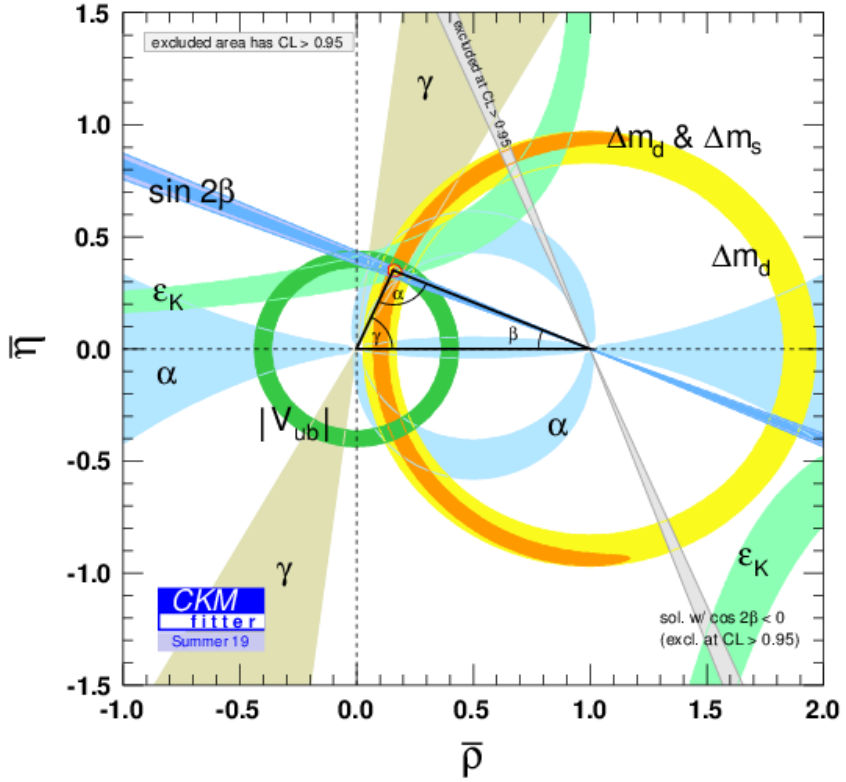


Figure II.13: Graphical representation of one of the unitary triangles, spanned by the angles  $\alpha$ ,  $\beta$ ,  $\gamma$ . The CKM parameters,  $\alpha$ ,  $\beta$ ,  $\gamma$ ,  $\bar{\rho}$ ,  $\bar{\eta}$  are fitted and errors are indicated as colored areas [23].

## II.3 Theoretical Introduction to the X(4014)

THIS section will give an introduction to the underlying theoretical framework of the potential X(4014) - one topic of this thesis project. It will start with a short overview on charmonium spectroscopy before briefly summarizing some of the unexpected exotic states found in the charmonium spectrum. The theoretical descriptions of those states, which are still under discussion, are presented thereafter. A more detailed description will be given on the X(3872), an exotic charmonium resonance which could be a partner state to the potential X(4014). The section will conclude with a discussion on the X(4014) itself, taking into account recent theoretical considerations.

### II.3.1 Charmonium Spectroscopy

CHARMONIUM spectroscopy investigates the energy spectrum of charmonia, meson states with charm and anti-charm ( $c\bar{c}$ ) content. Like the positronium spectrum, bound states of electrons and positrons, charmonia can occupy different mass states through certain combinations of their spin and orbital momentum. In Fig. II.15, the level scheme of charmonium is illustrated. The y-axis shows the mass while the x-axis is made up of columns for different quantum numbers  $J^{PC}$ . In Fig. II.14, the production of charmonium in a charged  $B$  meson decay is shown.

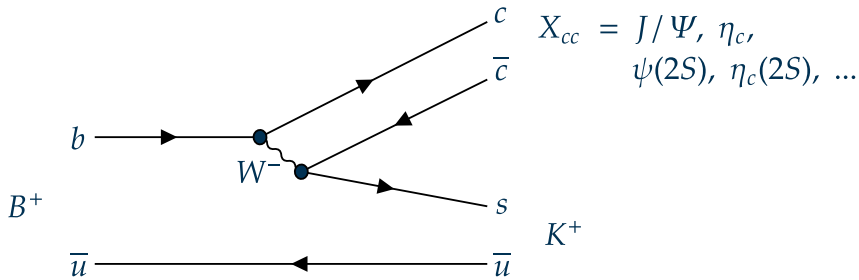


Figure II.14: Feynman diagram of  $c\bar{c}$  production in charged  $B$  meson decays.



A more detailed approach includes also a term for spin-spin interaction, like shown below (taken from [25]):

$$V(r) = \frac{4}{3} \frac{\alpha_s}{r} + kr + \frac{32\pi\alpha_s}{9m_c^2} \delta_\sigma(r) \vec{S}_c \cdot \vec{S}_{\bar{c}}, \quad (2)$$

Here,  $\delta_{sigma} = (\sigma/\sqrt{\pi})^3 e^{-\sigma^2 r^2}$ , represents the spin-spin hyperfine interaction. The parameters,  $\alpha_s$ ,  $m_c$ ,  $k$  and  $\sigma$ , are fitted from experimental data. Besides this spin-spin interaction, a spin-orbit interaction can be added, leading to more precise predictions, especially in the higher mass regions of the charmonium spectrum.

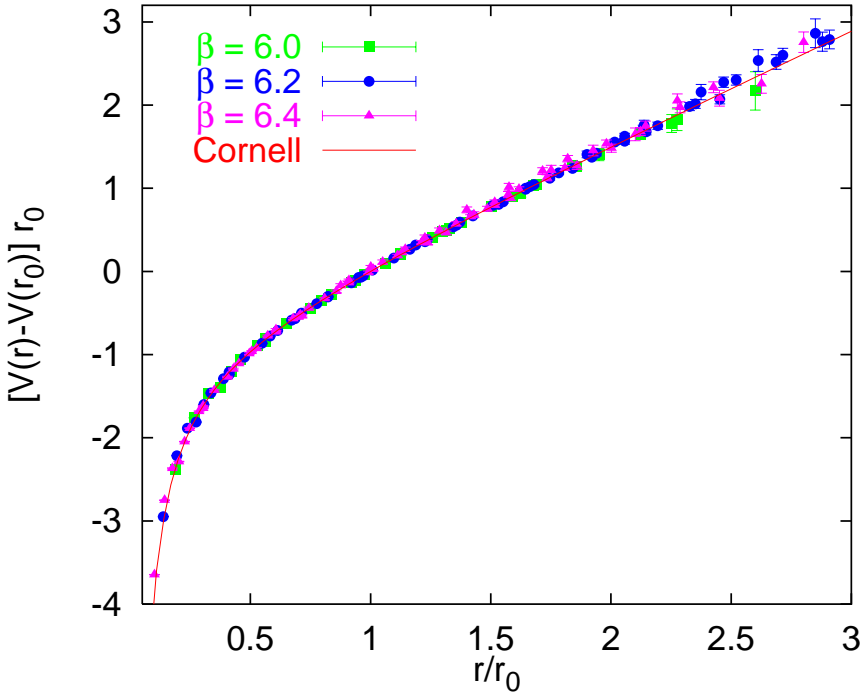


Figure II.16: Cornell potential vs. lattice QCD calculations for different couplings of  $\beta = 3/(2\pi\alpha_s)$  [26], p. 71.

A more sophisticated way of describing charmonia and their spectrum is lattice QCD<sup>17</sup>, which can predict the quark anti-quark potential in good agreement with the Cornell potential [26], as shown in Fig. II.16. However, when calculating the charmonium spectrum, the simple approach of the Cornell potential shows a more precise agreement to the experimentally discovered states than calculations done on the lattice [25], [28].

### II.3.2 Exotic Charmonia

UNTIL 2003 many of the conventional charmonium states, indicated in black in Fig. II.15, were discovered, when the discovery of a completely unforeseen new state was published by Belle - the  $X(3872)$ . In the publication [9], the Belle collaboration measured a narrow resonance in the invariant mass spectrum of  $J/\Psi\pi^+\pi^-$  in the decay  $B^+ \rightarrow J/\Psi\pi^+\pi^-K^+$ . The  $X(3872)$ , as it was named, does not match the expectations of a charmonium resonance above the  $D^0\bar{D}^{*0}$  threshold, which should have shown a much broader width<sup>18</sup>. Many more of those so-called charmonium-like states have been discovered since then. In 2013 a first charged charmonium like state, the  $Z(3900)$ , was discovered at BES III [29]. The resonance was observed in the  $J/\psi\pi^\pm$  invariant mass spectrum in  $e^+e^- \rightarrow \pi^+\pi^-J/\psi$  and, if interpreted as a particle, has unusual characteristics since it carries charge and couples to charmonium. All of these new states, especially the charged ones, can not be explained by a  $c\bar{c}$  content only. Over the years a commonly, accepted nomenclature has been developed. All neutral, non-vector states are called  $X$ , the vector states<sup>19</sup> are called  $Y$  and the charged states  $Z$ , all followed by their mass in brackets. A selection of articles, discussing those new states, can be found in [9, 10, 30, 31, 32, 33].

What makes those states special, compared to normal charmonia with a  $c\bar{c}$  content only, is their relatively long lifetime (narrow width), their decay rates to charmonia above the open-charm threshold<sup>20</sup> and that they are not predicted by quark models. For the  $Z$ -states the difference to  $c\bar{c}$ -only states is even more strict, since mesons consisting of quark and anti-quark

---

<sup>17</sup>A non-perturbative approach for solving QCD theory of quarks and gluons on a grid, the so called lattice [27].

<sup>18</sup>Particle width  $\Gamma$  is anti-proportional to the particle life-time  $\tau$ .

<sup>19</sup>States with a spin equal to one, so  $J^{PC} = 1^{--}$ .

<sup>20</sup>Normal charmonia above the  $D\bar{D}$  threshold decay dominantly in  $D\bar{D}$ , like the  $\Psi(3770)$  with  $Br(\Psi(3770) \rightarrow D\bar{D}) = 93\%$  [7].

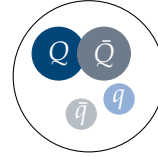
of the same flavor can never be charged. To understand the nature of those XYZ-states, the theory community came up with various ideas to describe their inner composition, which are briefly summed up in the following. The schematic drawings for each of the different theories are indicating a light quark ( $u, d$ ) as small circle labeled  $q(\bar{q})$  and the heavy quarks  $c, b$  as big circles labeled  $Q(\bar{Q})$ .

### II.3.2.1 Hadro-Quarkonium

Since all new charmonium states were seen in decays to a conventional  $c\bar{c}$  state plus mesons containing lighter quarks ( $u, d$ ) [34], it was concluded that a possible way to describe those states is a central, heavy quarkonium state ( $c\bar{c}$ ) with a cloud of light quarks surrounding it. The hadro-quarkonium picture would explain naturally the surviving of the compact  $c\bar{c}$  state and the radiated light mesons ( $\pi^\pm, \pi^0$ ), in the final state of the decay. In [35],

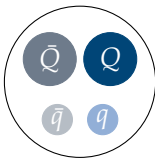
this model was successfully applied to  $Y(4260)$ ,  $Y(4360)$ ,  $Y(4660)$  and  $Z(4430)$ . However, there are also drawbacks for the Hadro-Quarkonium picture, e.g. when studying the  $Z(3900)$  [36]. In this paper, the expected dominance of the  $Z(3900)$  decay to  $J/\Psi\pi^+\pi^-$  could not be shown, since the  $D\bar{D}$

decay, which is suppressed in the hadro-quarkonium picture, has an unexpected high rate. In general, one can conclude that the measurements of high rates for open-charm decays disfavor a Hardo-Quarkonium picture.



### II.3.2.2 Tetraquarks

Tetraquarks can be thought of as strongly bound states of four quarks, which internally form a system of compact diquarks ( $qQ$  and  $\bar{q}\bar{Q}$ ). In [37], a so-called double-well potential model was proposed to explain the inner



structure and distance between the diquarks. This assumption can explain why exotic states prefer to decay in open-flavor mesons<sup>21</sup> instead to quarkonia. In the tetraquark framework, this property of many exotics can only be enabled if a constituent of the diquark tunnels through the barrier to enable a decay in two mesons (which always contain quark and anti-quark).

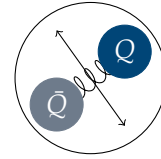
<sup>21</sup>Mesons with different quark flavors inside, e.g.  $D^0(c\bar{u})$

Since the possibility of tunneling is highly suppressed for the heavy quarks, the favored decays to open-charm arise naturally. To calculate the internal structure of tetraquarks, one can also use a Dyson-Schwinger/Bethe-Salpeter approach as discussed in [38]. In that work, the amplitudes are discussed as heavy-light meson-meson, hadro-charmonium and diquark-antidiquark operators. This way the different internal configurations can be discriminated against each other and a dominant component can be found. For both attempts, a  $cq\bar{q}c$  and a  $cs\bar{s}c$  quark content, they find the heavy-light meson-meson component to be dominant. The  $X(3872)$  is calculated with  $3916 \pm 74 \text{ MeV}/c^2$  and a  $cs\bar{s}c$  state is predicted at  $4068 \pm 61 \text{ MeV}/c^2$ .

### II.3.2.3 Hybrids

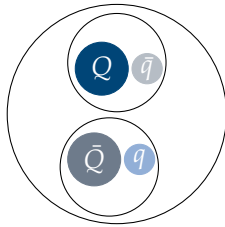
Hybrids consist of a quark anti-quark pair with an excited gluon, which introduces an additional degree of freedom compared to ordinary mesons. There are plenty of different models describing hybrids, e.g. bag-model [39], the flux-model [40], a Coulomb-gauge theory [41] and also a

non-relativistic effective field theory model called Born-Oppenheimer [42]. A model using lattice QCD calculations predicts the lightest charmonium hybrid around the mass of 4.2 GeV, which was associated with the  $Y(4260)$  state [43].



### II.3.2.4 Hadronic Molecules

Hadronic molecules are conventional meson states bound by one-pion exchange, which was already postulated in 1994 [44]. Even though, one-pion exchange was already proposed as a binding possibility before exotic



states were discovered, the potential of this coupling is still not known very well. However, there are some statements about the hadronic-molecule, which can be made without understanding the underlying potential in detail. One consequence of a molecular structure is setting limits on the size of the molecule. For a molecular interpretation of the  $X(3872)$ , with a binding energy of about 200 keV, a size of at least  $10 \text{ fm}^{22}$  is expected [45], p. 16. Many proper-

---

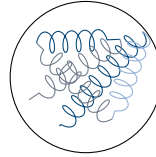
<sup>22</sup>Approximately 12 times the charge radius of a proton.

ties of exotic states, like the X(3872) or the Y(4230), are in good agreement with the hadronic molecule model. A detailed and comprehensive work on hadronic molecules, their potential and predictions can be found in [46].

### II.3.2.5 Glueballs

Glueballs are not considered as feasible states for the charmonium-like exotics, but might be an explanation for exotic states decaying to a broader variety of flavor final states<sup>23</sup>.

They are completely composed of gluons underlying their self-interactions. For a detailed description of glueballs and their properties see [47].



### II.3.2.6 Threshold Effects

Some XYZ states are found close to kinematical thresholds for e.g. meson anti-meson production. Such an threshold opening of an additional partial cross section can produce a peak-like structure, so-called "cusps", in the total cross section, as all particle cross sections are coupled by unitarity. Such an interpretation as a kinematical effect would mean, that XYZ states are not resonances [48]. However, cusps should have a width of larger than 10 MeV, thus states such as the very narrow X(3872) can not be interpreted in such a way.

## II.3.3 The X(3872)

THE first XYZ candidate, was the X(3872) discovered by Belle in 2003 [9], later also observed by BaBar in 2005 [10] and many other experiments later on. In Fig. II.17, the X(3872) invariant mass spectrum for different decay channels and experiments is shown. Since its discovery (Fig. II.17, a), the X(3872) has been seen as well in B decays (Fig. II.17 c BaBar, d Belle), radiative transition from the Y(4260) [11], as well as in proton anti-proton collisions at LHCb (Fig. II.17, b). Due to the many experiments, which observed the X(3872) in various decay channels, the description as a threshold effect is very unlikely, in fact, the X(3872) is one of the best candidates for a molecular description.

---

<sup>23</sup>Charmonium-like exotics show a strong binding to  $c\bar{c}$  flavored final states.

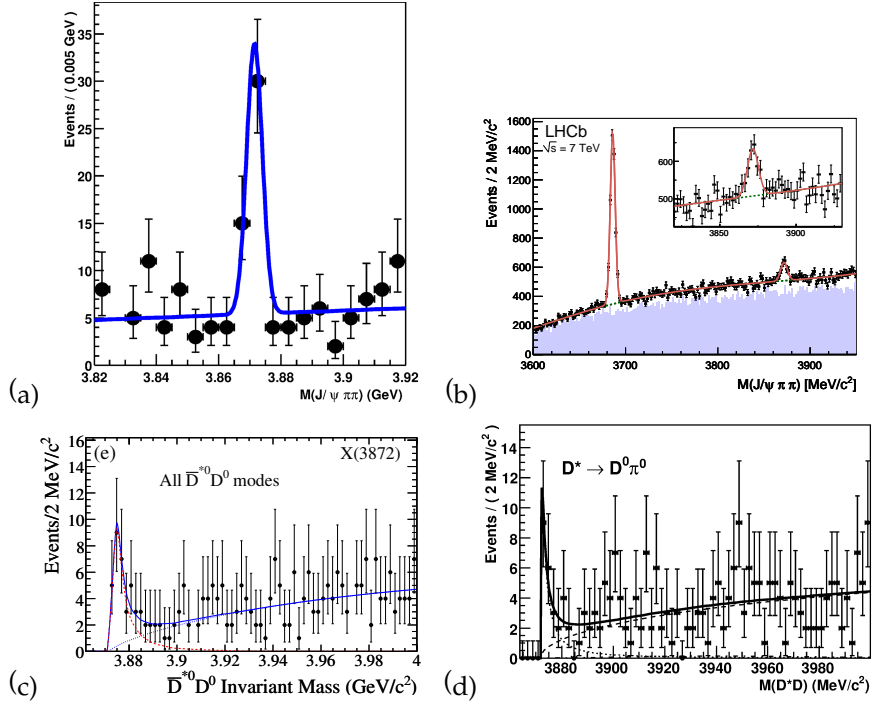


Figure II.17: Examples for observed  $X(3872)$  peaks in the invariant mass spectrum  $J/\Psi\pi^\pm\pi^\mp$  from Belle (a) [9], LHCb (b) [49] and in the  $D^*\bar{D}$  spectrum from Belle (c) [50](e) and BaBar (d) [51].

In 2013, LHCb performed an amplitude analysis determining the correlations between  $B^+ \rightarrow X(3872)K^+$ , where  $X(3872) \rightarrow J/\Psi\pi^+\pi^-$ , in which they determined the quantum number to be  $J^{PC} = 1^{++}$  [52]. Even though its mass cannot be distinguished from the  $D^0\bar{D}^{*0}$  threshold, the width of the  $X(3872)$  is surprisingly small. As published in [53], an upper limit of  $\Gamma < 1.2$  MeV within a 90% CL, could be reached for the decay to  $J/\Psi\pi^+\pi^-$ .

### II.3.4 X(4014) - A Partner State to the X(3872) Favoring a Molecular Description

IN Ref. [54, 55] the X(3872) is described as a molecular bound state of two mesons. Following the proposed effective field theory (EFT) approach, a  $J^{PC} = 2^{++}$  s-wave  $D^{*0}\bar{D}^{*0}$  bound state is predicted. Since the  $D^{*0}$  is representing an excited  $D^0$  state in terms of angular-momentum excitation, the two resonances have a strong relation with the  $D^{*0}$  and the  $D^0$ . Due to those relations, one can also picture the X(4014) as a  $J^{PC}$  triplet state with resonant formations satisfying three different angular momentum excitations.

$$X(4014) = \begin{cases} J = 0 : & D^0\bar{D}^0\pi^0\pi^0 \text{ OR } D^0\bar{D}^0\gamma\gamma \text{ OR } D^{*0}\bar{D}^0\gamma \\ J = 1 : & D^0\bar{D}^0\pi^0\gamma \text{ OR } D^{*0}\bar{D}^0\pi^0 \\ J = 2 : & D^{*0}\bar{D}^{*0} \text{ OR } D^0\bar{D}^0\gamma\gamma \text{ OR } D^{*0}\bar{D}^0\gamma \end{cases}$$

Parity and Charge quantum numbers,  $P$  and  $C$  respectively, are :

$$\begin{aligned} D^0 &= 0^- \\ \bar{D}^0 &= 0^- \\ D^{*0} &= 1^- \\ \bar{D}^{*0} &= 1^- \\ \pi^0 &= 0^{-+} \end{aligned}$$

In this thesis the  $J^{PC} = 0^{++}$  state made up by  $D^0\bar{D}^0\pi^0\pi^0$  is exploited only! The reasons for that are discussed as foreword to the analysis section.

In [56], it is argued, that the XYZ states cannot originate from a purely kinematic effect near the threshold. The authors state, that the most likely scenarios for describing those new states are *Hadro – Quarkonia*, *Tetraquarks* and *Hadronic Molecules*. Tab. II.1 shows charmonium-like resonance calculated for the *Tetraquark* and *Hadronic Molecule* models of the internal structure.

In [57], hadronic molecules from  $D^{(*)}$  and  $\bar{D}^{(*)}$  mesons were already pre-

	Mass [GeV/c <sup>2</sup> ]	Taken from	Candidate
Tetraquark	3870	[57]	X(3872)
	3871	[58]	X(3872)
	3916	[38]	X(3872)
	4051	[58]	X(4014)
	4068	[38]	X(4014)
Hadronic Molecule (HQSS)	4012	[54]	X(4014)
	4015	[57]	X(4014)

**Table II.1:** Table showing mass predictions for the X(3872) and X(4014) from different theory approaches.

dicted. The mechanism to describe the binding of such molecular states could be given by the one-pion exchange potential, providing a binding energy of a few MeV and thus bound states close to the  $D\bar{D}^*$  and  $D^*\bar{D}$  thresholds. Due to symmetry arguments the molecule wave function can be written as:

$$|\Psi\rangle = \frac{1}{\sqrt{2}}(|D\bar{D}^*\rangle + |D^*\bar{D}\rangle)$$

And a general form of a one-pion exchange potential for a  $J^{PC} = 0^{++}$  state<sup>24</sup> as [57]:

$$V_{0^{++}}(r) = -\gamma V_0 \left[ \begin{pmatrix} 1 & 0 \\ 0 & \frac{-1}{2} \end{pmatrix} \cdot C(r) + \begin{pmatrix} 0 & \sqrt{\frac{1}{2}} \\ \sqrt{\frac{1}{2}} & 1 \end{pmatrix} \cdot T(r) \right]$$

$$C(r) = \frac{e^{-m_\pi r}}{m_\pi r}$$

$$T(r) = C(r) \left[ 1 + \frac{3}{m_\pi r} + \frac{3}{(m_\pi r)^2} \right]$$

With the pion mass  $m_\pi$ , the molecule radius  $r$  and a factor  $\gamma$ , which describes the strength of the spin-isospin coupling and can be approximated with 6 for the  $D^*\bar{D}^*$  ( $I = 0, S = 0$ ) case.  $C(r)$  and  $T(r)$  are the cen-

<sup>24</sup>The potential X(4014) state discussed in this thesis.

tral and the tensor part of the potential, respectively, and the constant term  $V_0 \approx 1.3$  MeV. The potential is found to be attractive for quantum numbers  $J^{PC} = 0^{-+}, 1^{++}$  for molecular states formed by a pseudoscalar and a vector meson, and  $J^{PC} = 0^{++}, 0^{-+}, 1^{+-}, 2^{++}$  for molecular states formed by two vector mesons. In Fig. II.18 a feynman diagram showing the decay of a  $B^\pm$  to such resonant states is shown. Depending on the  $D$  meson combination,  $D^0\bar{D}^0$  or  $D^{*0}\bar{D}^{*0}$ , an X(3872) or X(4014) is formed.

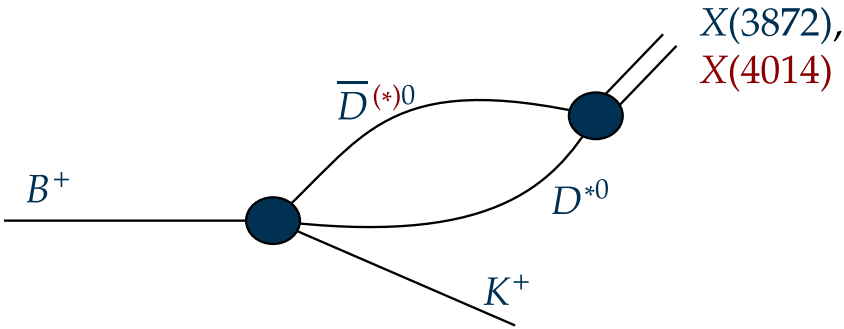


Figure II.18: Feynman diagram of the decay of a charged  $B$  meson to an  $D^0\bar{D}^0$  (blue) or  $D^{*0}\bar{D}^{*0}$  (red) resonant state identified as hadronic molecule.

The X(3872) or X(4014) could also be described as *Tetraquarks*. In such a model, the constituents of the resonance do not have to be considered as color neutral objects bound by pion exchange, as is the case for the hadronic molecule, but can consist of four quarks without any requirements on the two-quark subsystem to be color neutral. In case of a tetraquark, the color neutrality can be achieved by the combination of the pairwise interactions of the four constituents, i.e. with an Hamiltonian approach:

$$H = \sum_{i=1}^4 \left( m_i + \frac{\vec{p}_i^2}{2m_i} \right) + \sum_{j \neq i}^4 V(\vec{r}_{ij})$$

Where  $m_i$  and  $p_i$  are the mass and the momentum of the quark, respectively and  $V(\vec{r}_{ij})$  represents the two-body interaction. Binding energies are determined by the color configuration of the quarks. For the  $q\bar{q}$  system, a repulsive potential is formed in the case of different colors, the potential is attrac-

tive in the case of same colors. In case of the  $qq$  system, the color factors have different sign, i.e. attractive potential for different colors and repulsive potential for same colors. The form factors are taken from [60, p. 38, 39 ] and for better visualization listed in Tab. II.2.

	same color	different color
$qq$	$2/3$	$-4/3$
$q\bar{q}$	$-8/3$	$1/3$

**Table II.2:** Table showing the form factors for the tetraquark potential in case of  $qq$  and  $q\bar{q}$  dependent on the color charge configuration. Negative sign for attractive potential, positive for repulsive.

As can be noticed, the potential in case of a  $q\bar{q}$  has double the strength of that formed by a  $qq$  setup.

In Fig. II.19, the connected (left) and disconnected (right) tetra quark model type is shown. For the disconnected type the potential can be written as [59]:

$$V_{disco}(r) = -\frac{4}{3}\alpha_s \left( \frac{1}{r_{13}} + \frac{1}{r_{24}} \right) + k(r_{13} + r_{24})$$

With  $k \approx 1 \text{ GeV/fm}$  being the string constant as introduced in 1. In case of the connected type, the potential is [59]:

$$V_{conn}(r) = -\frac{4}{3}\alpha_s \left( \left( \frac{1}{r_{12}} + \frac{1}{r_{34}} \right) + \frac{1}{2} \left( \frac{1}{r_{13}} + \frac{1}{r_{14}} + \frac{1}{r_{23}} + \frac{1}{r_{24}} \right) \right) + k'L_{min}$$

With a modified string constant  $k'$  and the minimum total flux tube length  $L_{min}$ <sup>25</sup>.

A potential minimum can be achieved by both configurations, settling

---

<sup>25</sup>Cylindrical tube area created by gluon interaction in QCD. When considering the second term in the Cornell potential ( $kr$ ) 1, the fluxtube breaks for larger  $r$  and two shorter tubes are formed - confinement.

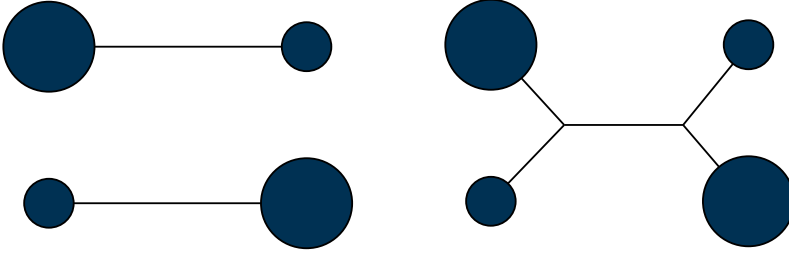


Figure II.19: Variations of tetraquark models. Connected type on the left and disconnected type on the right. Large circles represent heavy quarks, small circles light quarks.

the lowest lying tetraquark state at [60, p. 39]:

$$V_{min}(r) = \min(V_{conn}(r) \cdot V_{disco}(r))$$

For both variations, and all configurations of  $q$  and  $\bar{q}$  for that specific configuration, the same spin-spin forces apply, leading to a repulsive term of  $+1/2$  for  $S = 1$  and an attractive term of  $-3/2$  for  $S = 0$ . They lead to only fully anti-symmetric di-quarks [61]. Colored quark configurations like  $(qq)(\bar{q}\bar{q})$  and  $(q\bar{q})(q\bar{q})$  are possible candidates to form bound states. For the potentials describing  $(qq)(\bar{q}\bar{q})$  configurations, the di-quarks are not point like but instead have form factors,  $F_1(r)$  and  $F_2(r)$ , that are accounted for by

$$V_C(r) = -\frac{4}{3}\alpha_s \frac{F_1(r) \cdot F_2(r)}{r},$$

a Coulomb-type part of the potential [58]. Tetraquarks are a many body system and therefore not easy to solve from a theoretical point of view. Possible approaches are now briefly discussed.

### QCD Sum Rules

Originally proposed in [62], QCD sum rules can be applied to calculate tetraquarks with heavy quarks ( $c, b$ ) as constituents. A two-point quark correlation function can be written as:

$$\Pi_{quark}(q^2) = \int_{2m_Q^2}^{\infty} ds \frac{\rho(s)}{s - q^2}$$

With the momentum transfer  $q^2$ , the mass of the heavy quark  $m_Q$ , the center of mass energy  $s$  and a spectral function of a hadron,  $X$ ,  $\rho(s)$ . This spectral function corresponds on an experimental level to the cross section  $\sigma(e^+e^- \rightarrow X)$  and can be described as a resonant lineshape function of  $s$ , e.g. a Breit-Wigner [63] (Sec. , Eq. V.2).

For a hadron, the upper equation can be written as:

$$\Pi_H(q^2) = \frac{2f_X^2 m_X^8}{m_X^2 - q^2}$$

With the hadronic decay constant  $f_X$  and  $m_X$  the mass of the unknown hadron, or, in case of an exotic resonance, the mass of the tetraquark. With the ansatz  $\Pi_{quark} = \Pi_H$ , the unknown mass  $m_X$  can be calculated [60, p.39 ].

### Diquark Clustering

This approach reduces the 4-body problem to a 2-body problem, by using di-quark anti-di-quark interactions in the form  $(Qq)(\bar{Q}\bar{q})$ , in case of a heavy tetraquark. In that case, also spin-spin and spin-orbit interactions can be included in the Lagrangian. Possible states are shown in Tab. II.3 summarized from [64] and [65].

The model shows quantum numbers, like  $1^{-+}$  in Tab. II.3, which are forbidden in normal quarkonia and therefore might provide a proof of the tetraquark nature on experimentally observed states [60, p.40 ].

$\left  (S_{Qq} \times S_{\bar{Q}\bar{q}})_S \right\rangle$	$L = 0$	$L = 1$
$ (0 \times 0)_0\rangle$	$0^{++}$	$1^{--}$
$ (1 \times 1)_0\rangle$	$0^{++}$	$1^{--}$
$1/\sqrt{2} \cdot ( (1 \times 0)_0\rangle +  (0 \times 0)_1\rangle)$	$1^{++}$	$0^{--}, 1^{--}, 2^{--}$
$1/\sqrt{2} \cdot ( (1 \times 0)_0\rangle -  (0 \times 0)_1\rangle)$	$1^{+-}$	$0^{-+}, 1^{-+}, 2^{-+}$
$ (1 \times 1)_1\rangle$	$1^{+-}$	$0^{-+}, 1^{-+}, 2^{-+}$
$ (1 \times 1)_2\rangle$	$2^{++}$	$1^{--}, 2^{--}, 3^{--}$

**Table II.3:** Spectrum of the  $L = 0$  and  $L = 1$  tetraquark states calculated from the  $(Qq)(\bar{Q}\bar{q})$  model, in accordance to their spin wave function  $\left| (S_{Qq} \times S_{\bar{Q}\bar{q}})_S \right\rangle$ . With  $S_{Qq}$ ,  $S_{\bar{Q}\bar{q}}$  and  $S$ , denoting the di-quark spin, the anti-di-quark spin, and the total spin, respectively.

Another picture on the nature of this state, is given by exploiting the model of heavy quark spin symmetry (HQSS). It describes a symmetry of an EFT, which is in good approximation to QCD, in defined kinematic regions, i.e. in systems where the heavy quark interacts predominantly by soft gluon<sup>26</sup> exchange. As a consequence, the heavy quark is approximately on-shell<sup>27</sup> leading to a vanishing component of the velocity fluctuation. In that case, the velocity is no longer a degree of freedom, but instead a conserved quantity [66]. As a result of this theory, applied on a potential X(4014), the binding energy would be similar to the one of the X(3872) and thus in the order of  $M(D^{*0}) - M(D^0) \approx 140$  MeV. A mass splitting of 140 MeV/c<sup>2</sup> would favor a molecular description of the X(4014), as well as the X(3872), since other models are postulating a much smaller mass splitting of  $\sim 30$  MeV/c<sup>2</sup> (Godfrey-Isgur quark model [67]),  $\sim 40$  MeV/c<sup>2</sup> (quark model with screened potential [68]) and  $\sim 70$  MeV/c<sup>2</sup> (tetraquark model [69]).

In [54], the X(3872) is considered as a molecular hadronic state. The paper predicts four molecular partner states to the X(3872) using the EFT and HQSS. The  $D^{*0}\bar{D}^{*0}$  partner state is predicted with a mass of  $4012 \pm 3$  MeV/c<sup>2</sup> when the one pion exchange (OPE) potential is not considered in the calculation. If the OPE is taken into account the mean value increases to 4015 MeV/c<sup>2</sup>. In the analysis of this thesis, a mass value of 4014 MeV/c<sup>2</sup>

<sup>26</sup>Can be thought of as connecting "string" between the quarks. Energy stored in a soft gluon is too small to break this string and force a decay.

<sup>27</sup>Momentum fluctuates around the mass in the order of  $\Lambda_{QCD}$ .

will be simulated.

The existence of the  $X(4014)$  might be contingent on the size of HQSS violations. Those violations could arise from the finite charm quark mass, which is added as a correction to the heavy quark limit potentials (leading order potential) of the  $X(3872)$  and  $X(4014)$  states.

$$\Phi_{m_Q=m_c}^{LO} = \Phi_{m_Q=\infty}^{LO} \cdot \left(1 + \mathcal{O}\left(\frac{\Lambda_{QCD}}{m_c}\right)\right)$$

With a charm quark mass of  $m_c \approx 1.5 \text{ GeV}/c^2$  and  $\Lambda_{QCD} \approx 200 \text{ MeV}/c^2$ , the correction is in the order of 15 % violation of HQSS. Within this uncertainty, the prediction of the  $X(4014)$  as  $2^{++}$  partner state to the  $X(3872)$ , is robust with respect to the theoretical error source [p. 7][54]. As a conclusion, Nieves and Valderrama consider the  $X(4014)$  as the most robust and model independent state of their calculations and express their confidence in the existence of such a state, which is taken as motivation for the studies performed in this thesis.

# The Belle II Experiment

**T**HE Belle II experiment is hosted at the High Energy Research Facility (KEK) in Tsukuba, Japan. Its predecessor, the Belle experiment, was running from 1999 until 2010. The data collected during that time is subject to many important results in the field of particle physics, especially in flavor and CP violation studies, published by the Belle collaboration. In 2010 people decided the upgrade of the collider, KEKB, as well as the Belle detector. This chapter will give a brief summary of this upgrade, which had its first, successful commissioning run in 2018.

## III.1 SuperKEKB - An Asymmetric $e^+e^-$ -Collider

**T**HE collider hosting the Belle II experiment, SuperKEKB, is an upgrade of the former KEKB collider which provided the beams for the Belle experiment. SuperKEKB is situated in the same tunnel and uses many of the old components of KEKB. The main improvement, compared to its predecessor, is the increase in design luminosity by a factor of 40 to  $8 \cdot 10^{35} \text{ cm}^{-2} \text{ s}^{-1}$ , which will allow the Belle II experiment to collect a data set of about  $50 \text{ ab}^{-1}$ . This section is briefly introducing the main changes needed in order to meet the upgrade specifications. A detailed description can be found in [70].

In Fig. III.1 a sketch of the SuperKEKB accelerator and its supporting facilities is shown. The rings, with a circumference of 3016 m each, are referred to as Low-Energy-Ring for positrons (LER) and High-Energy-Ring for electrons (HER) storing beams of 3.6 A ; 4 GeV and 2.62 A ; 7 GeV, respectively. Due to the asymmetric energies, the Center of Mass (CM) system is

not at rest in the laboratory frame, but is boosted by a factor of  $\beta\gamma = 0.28$ , which allows a better identification of the displaced vertex of the  $B$ -mesons. Its predecessor Belle had a boost of 0.42, to correct for this decrease a much better vertexing is needed, which is why Belle II will compose the vertex detector as a combination of silicon strips and pixels.

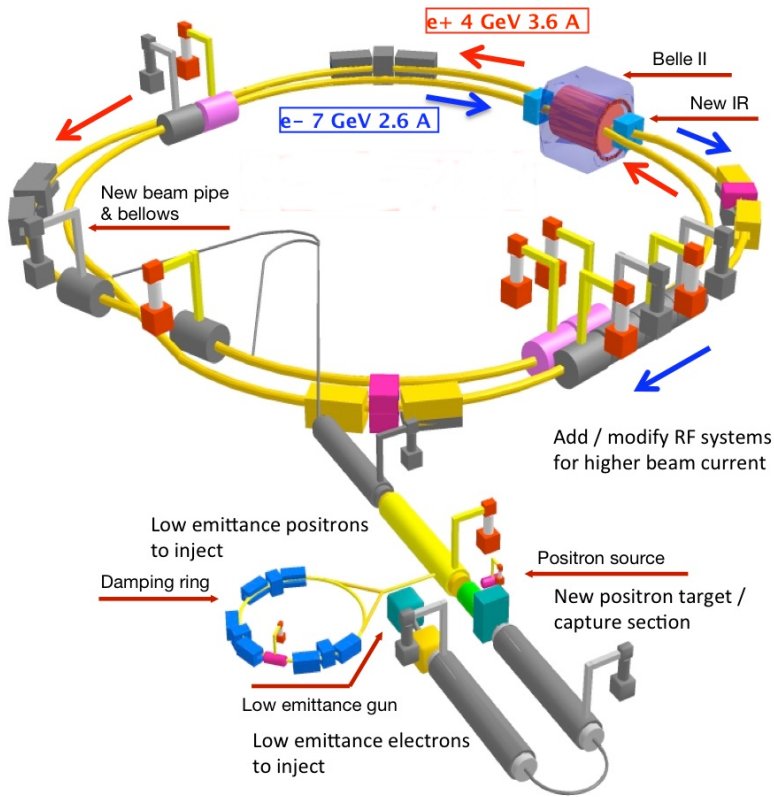


Figure III.1: Sketch of the SuperKEKB collider.

As the emittance of the positron behind the source is not small enough to fulfill the injection requirement, their emittance is improved by factor  $\approx 2$  in the damping ring.

Electrons are produced by a new RF-gun irradiating a photo cathode with short-pulsed laser photons. After being accelerated to 7 GeV in the linac, they are dumped to the HER. For positron production the former KEKB thermionic RF electron gun is used. It provides a 3.3 GeV electron beam which, after being shot on a tungsten target and causing bremsstrahlung, converts to an electron positron pair. This procedure leads to an high emittance positron beam which is accelerated to 1 GeV and directed to a damping ring which reduces the emittance and further accelerates the positrons to 4 GeV before they are stored in the LER.

The most important upgrade to achieve the luminosity goal is the **nano-beam scheme**. A schematic illustration is shown in Fig. III.2. The technique aims at an extreme decrease in vertical beam size directly at the interaction point, leading to an increase in luminosity. For the interaction of two flat beams with equal size, the luminosity is defined as

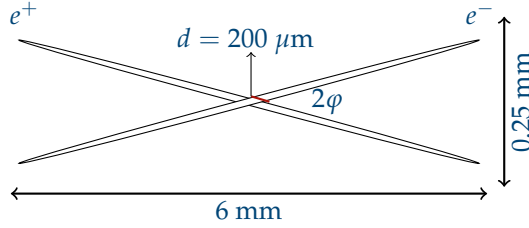


Figure III.2: Illustration of the nano-beam-scheme.

$$\mathcal{L} = \frac{\gamma_{\pm}}{2er_e} \frac{R_L}{R_{\zeta_y}} \frac{I_{\pm}\zeta_{y,\pm}}{\beta_{y,\pm}^*} \quad (1)$$

with parameters for positrons and electrons marked with + and – respectively. The first fraction consists of constants only;  $\gamma$  the Lorentz factor,  $r_e$  the classical electron radius and  $e$  the electron charge and the second term shows a reduction factor close to one. The only adjustable parameters are in the last fraction; the beam current  $I$ , the beam-beam parameter  $\zeta_y$ , which describes the force acting on a particle in the potential of a colliding bunch, and the vertical  $\beta$ -function  $\beta_y^*$ .

The  $\beta$ -function is linked to the vertical size  $\sigma_y$  of a Gaussian shaped particle beam in

$$\sigma_y = \sqrt{\epsilon\beta_y^*} \quad (2)$$

Considering the equations in 1 and 2, a decrease in vertical beam size is directly leading to an increase in luminosity.

The squeezing of the beam is done with quadropol magnets along the beam pipe. A final focusing magnet (QCS) provides a significant decrease in vertical beam size down to  $270 \mu\text{m}$  for the LER and  $410 \mu\text{m}$  for the HER. The luminosity can not be arbitrary increased by this method and is always constrained by the bunch length  $\sigma_z$ , introducing a hard limit of  $\beta_y^* > \sigma_z$  with a bunch length of  $\sigma_z = 5 \text{ mm}$  in beam direction.

In order to correct for this effect, the nano-beam scheme uses a finite angle  $\varphi$  for the beam crossing, decreasing the effective cross section of the beams to  $d = \sigma_x / \varphi$  with  $\sigma_x$  being the horizontal beam spread. The constrained for the beta function is then given by  $\beta_y^* > d$ . Taking into account the design value for the crossing angle of  $\varphi = 41.5 \text{ mrad}$  and a horizontal beam size of  $\sigma_x = 7.75 \mu\text{m}$ , the effective crossing length goes down to  $d = 200 \mu\text{m}$ , which provides a 25 times smaller constrained than the  $\sigma_z = 5 \text{ mm}$  given by the bunch length.

The nano beam scheme will allow SuperKEKB to reach the design luminosity goal of

$$\mathcal{L} = 8 \cdot 10^{35} \text{ cm}^{-2}\text{s}^{-1}, \quad (3)$$

which is 40 times the instantaneous luminosity of its predecessor Belle<sup>1</sup>. Expecting a similar run time of Belle II, a total integrated luminosity of  $50 \text{ ab}^{-1}$  will be collected.

---

<sup>1</sup>Belle luminosity record reached  $2.11 \cdot 10^{34} \text{ cm}^{-2}\text{s}^{-1}$  in 2009, link active on 24.01.2020. <https://cerncourier.com/a/kekb-breaks-luminosity-record/>

## III.2 Belle II - A Precision Frontier Particle Detector

**T**HIS section will focus on the Belle II detector which is located at the interaction point of the SuperKEKB collider. The full detector consists of 6 subsystems which are cylindrically arranged around the interaction point of SuperKEKB, with a forward extension in the boost direction  $+z$ . Due to its barrel shaped design, Belle II covers a total acceptance of  $2\pi$  in the azimuthal plane  $\phi$ , and  $17 < \theta < 150$  in the polar plane. Figure III.3 shows an illustration of the Belle II detector. A brief overview of the individual sub-detectors is given in the next sub-chapters.

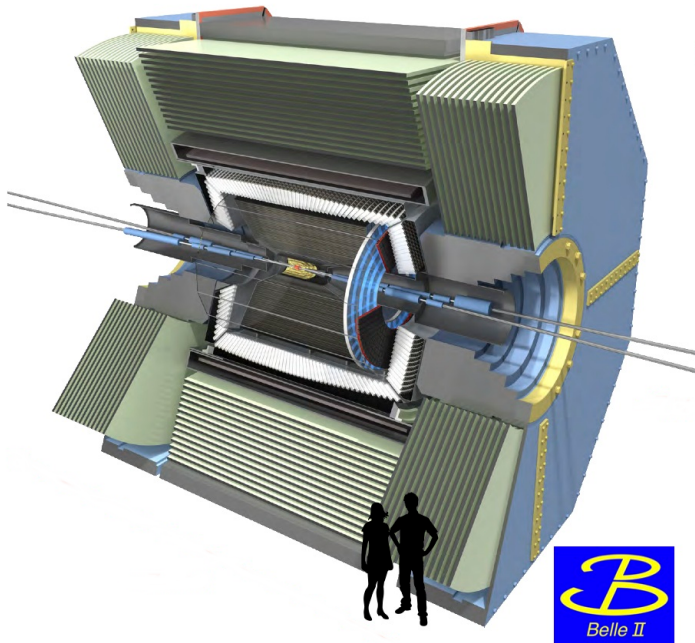


Figure III.3: Sketch of the Belle II detector with two persons for size comparison.

### III.2.1 The Vertex Detector - VXD

IN Sec. II.1.1.6 the method to measure CP-violation in  $B$ -meson decays is discussed. One of the crucial parameters for this measurement is the difference in life time of the two  $B$ -mesons, which is calculated from the spatial separation of the decay vertices. In order to measure these vertices with high precision, Belle II upgraded and extended the former Belle Silicon Vertex Detector (SVD) with a DEpleted P-channel Field Effect Transistor (DEPFET) Pixel Detector (PXD). The two together make up the Vertex Detector (VXD), which provides a  $20\ \mu\text{m}$  resolution in  $z$  direction [70, p. 16]. A sketch is shown in Fig. III.4.

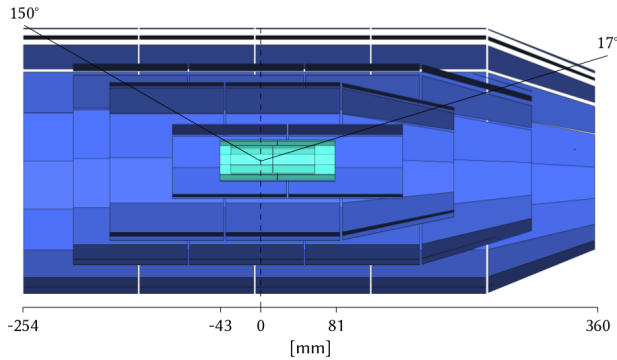


Figure III.4: Sketch of the Belle II VXD, in blue the SVD and in turquoise the PXD.

#### III.2.1.1 The Pixel Detector - PXD

The Belle II Pixel Detector (PXD) is the innermost detector and contributes two of the six layers to the VXD. It is composed of 40 modules (half-ladders) arranged in two layers with 16 and 24 half-ladders respectively. The first layer is surrounding the IP at 14 mm distance, the second layer at 22 mm. Each module hosts a sensitive area composed of DEPFET pixels [71], and ASICs<sup>2</sup> for the readout attached to the supporting structure. Due to its location at very small radii around the IP of a high luminosity machine, the PXD has to handle large backgrounds. Before giving a short overview of the detection technique and the readout, the relevant background contributions

---

<sup>2</sup>Application-Specific Integrated Circuit, a single task specific chip.

are explained and their implications for the detector and readout design is compiled.

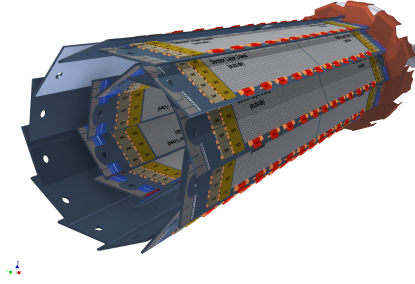


Figure III.5: Sketch of the Belle II PXD, by the DEPFET collaboration.

### Background Contributions

The relevant background processes for the PXD as referred in [72] can be categorized by their origins:

- Beam-induced processes, and
- Luminosity-induced processes

Beam-induced processes originate within the two beam separately and **not** from their collisions. A Gaussian shaped beam-bunch in a particle accelerator is losing charge, i.e. particles, during its turns in the beam line. A beam-lifetime  $\tau$  can be defined by taking into account the typical time scale of each process contributing to the charge loss.

$$\frac{1}{\tau} = \frac{1}{\tau_{\text{Touschek}}} + \frac{1}{\tau_{\text{Beam-Gas}}} + \frac{1}{\tau_{\text{Synchrotron}}} \quad (1)$$

When particles cross the bunch borders due to such processes, they will collide with the beam pipe and cause particle showers which then, if happening in the range of a detector, cause signals superimposing the physics process as background. The Touschek effect, an intra-bunch scattering of two electrons or positrons, is one of the most relevant processes causing beam background. The effect is proportional to the inverse beam size, which

is very small due to the nano-beam scheme. Another process which reduces the beam-life and contributes to the background is the beam-gas scattering, happening when beam particles escape the bunch and interact with residual gas molecules in the pipe. The third component in Eq. 1 denotes the synchrotron radiation, a photon emission due to acceleration of charged particles. In case of the particle beams at SuperKEKB it is produced by electrons or positrons getting deflected in the magnetic field of the quadropole magnets which focus the beams before the IP.

Luminosity induced processes are caused by QED interactions of electrons and positron, hence they are caused by the beam collisions directly. Due to their direct dependency on the instantaneous luminosity, their rate

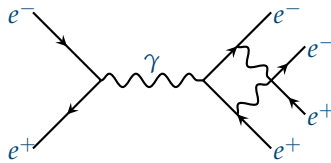


Figure III.6: Two-photon process in  $e^+e^-$  collisions.

can be expected to be 40 times higher than at Belle. The dominant source of luminosity induced background is expected to be two-photon processes. They originate by the QED process  $e^+e^- \rightarrow e^+e^-\gamma\gamma \rightarrow e^+e^-e^+e^-$ , which is also indicated in Fig. III.6. The low energetic electron positron pair originating from the  $\gamma\gamma$  interaction is curling in the magnetic field leaving only hits in the PXD. A

second source of background from QED processes is the Bhabha scattering. Electrons and positrons from the colliding beams do not annihilate but scatter ( $e^+e^- \rightarrow e^+e^- + n\gamma$ ). The scattered particles are then leaving the interaction region under very small angles and convert in the beam pipe to secondary particles producing hits in the PXD.

In [72] the expected fractions of background events to the total amount of fired PXD pixels, the *occupancy*, is simulated. An adapted and simplified table, for all processes and inner (L1) and outer (L2) layer, is shown in Tab. III.1. In total, the background sources add up to 1.74 % occupancy of the PXD, considering a hardware limit, of 3 %, the PXD should operate effectively in the expected environment. However, when taking into account the 30 kHz design trigger rate, the expected PXD data rate is about 20 GB/s, which must be handled by a dedicated DAQ system and a fast readout with buffering and data reduction capacities.

Background source	L1 occupancy [%]	L2 occupancy [%]
Two-photon	0.89	0.29
Bhabha	0.2	0.05
Synchrotron	0.1722	0.0919
Touschek	0.019	0.0156
Beam-Gas	0.009102	0.0055
Total	1.29	0.45

Table III.1: Summary of the individual background sources dominating the PXD occupancy, taken from [72].

### Detection Technique - The DEPFET Pixel

The underlying detector technology for the Belle II PXD is the depleted field-effect transistor (DEPFET). It is used for a particle physics experiment the first time in Belle II and is also considered one of the options for the International Linear Collider (ILC) [73]. An important motivation for choosing this detection technology was given by the thickness of the sensitive area. For the measurements done at Belle II a very good vertex resolution is needed, hence the multiple scattering of particles inside the detection layer of the PXD needs to be as small as possible. The DEPFET technology can be thinned down to 75  $\mu\text{m}$ , enough to neglect the impact of multiple scattering on the vertexing.

In Fig. III.7, a sketch of a DEPFET pixel is shown. The main part consists of a silicon soil (bulk) grounded on a positive contact and topped with a p-channel Metal Oxide Semiconductor Field Effect Transistor (MOSFET). Due to the positive grounding plate, the bulk region of the DEPFET becomes fully depleted, i.e. free of unbound electrons, in return, the p-doped ground plate acquires a negative potential. When a charged particle ionize the silicon soil, it creates an electron-hole pair. The "positively charged" will drift to the ground plate while the electrons accumulate beneath the 'FET gate' in the 'internal gate', which modulates the potential of the FET gate. If the gate is active, the drain current, which is directly proportional to the created electrons during ionization, can be measured. Once the drain current is measured and the amplified signal is sent down the data acquisition chain, the electrons in the 'internal gate' must be cleared for the next measurement. This is done by applying a positive potential to the 'clear gate', causing the

electrons to drift there and free the 'internal gate' for a new readout cycle.

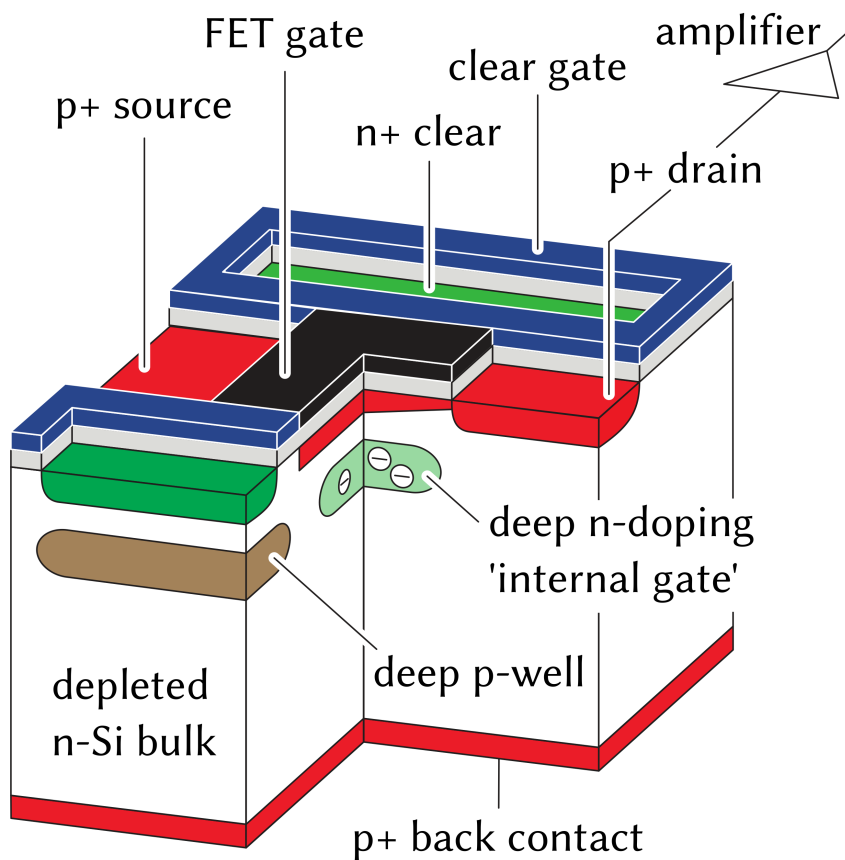


Figure III.7: Sketch of a DEPFET pixel.

## Module Design

Each of the 40 PXD modules is composed of a supporting structure, carrying the ASICs and a sensitive area with 768 DEPFET pixels in a row and 250 in a column, giving a total of 7'680'000 pixels for the whole PXD. On the inner layer, pixels have a side-length of  $55\ \mu\text{m}$  and  $60\ \mu\text{m}$  while the pixels for the outer layer measure  $70\ \mu\text{m}$  and  $80\ \mu\text{m}$ , leading to a module length of 68 mm and 85 mm for inner and outer layer respectively. Each module has a width of 15.4 mm, perpendicular to the beam direction, with a sensitive area thinned down to  $75\ \mu\text{m}$ , covering 12.5 mm of that width. The active length is 44.8 mm and 61.44 mm for inner and outer layer respectively. The  $420\ \mu\text{m}$  thick supporting structure is covering the rest of the area and hosts the readout ASICs as well as the connection to the Kapton cable, a flexible printed circuit for voltage supply, operation signal control and data transfer. In Fig. III.8, a schematic view of a DEPFET module is shown.

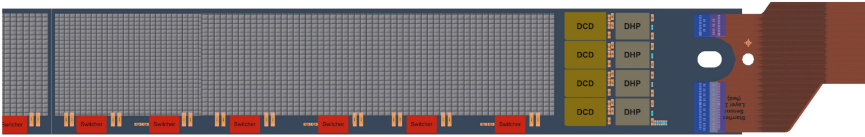


Figure III.8: Illustration of a PXD module, by the DEPFET collaboration.

## Readout

The readout of the pixel matrix is performed via three types of ASICs, the SWITCHER [74], the Data Handling Processor (DHP) [75] and the Drain Current Digitizer (DCD) [76]. The DCD represents an ADC with the specific feature that it digitizes an electrical current rather than an electrical voltage. All three are mounted on the supporting structure of a PXD module (Fig. III.8) and communicate with the back-end electronics via the Kapton cable. Each module hosts six SWITCHERs controlling the readout timing of 32 rows<sup>3</sup> by driving their gate and clear voltages. The current from 250 column lines, produced by an ionizing particle, is then read out and digitized from the DCDs which are mounted at the end of each sensor. All DCDs are connected to their own DHP, which stores the digitized pixel data in a ring-

<sup>3</sup>The sensor is electrically divided in row-groups of four, making 192 logical rows (32 for every SWITCHER) and 1000 logical columns.

buffer, always containing the data from a complete sensor readout cycle up to the current row. When a trigger arrives, the data for the event are read out. After pedestal subtraction all pixels with a non-zero charge value are framed as a DHP data package and send out to the data acquisition.

### III.2.1.2 The Silicon Vertex Detector - SVD

The outermost 4 layers of VXD compose the SVD, whose basic units are double sided silicon strip sensors, mounted onto ladders which are grouped in 4 layers. Each sensor consists of one side of highly p-doped stripes in direction of the beam and highly n-doped stripes perpendicular to it. The stripes are separated by a n-doped bulk region which is ionized by charged, traversing particles. Due to the ionization of the bulk silicon, electron-hole pairs are generated with electrons and holes drifting to the closest, oppositely charged strip. An external trigger-signal, sent from the global DAQ, triggers the readout of those strips. Generated signals are amplified by an APV25 chip on the sensor and transmitted to the Flash ADC<sup>4</sup>, outside the highly radiative area. The Flash ADC shapes and digitizes the analog signals which are then transmitted on an optical data link to the global DAQ.

A common problem for silicon strip detectors arises from their geometrical construction. Due to the perpendicular arranged strips, the detector is producing so called *ghost hits*.

Those hits occur naturally, when a charged particle crosses the detector. So if  $n$  particles cross the detector at the same time,  $n$  p-doped and  $n$  n-doped strips will send a signal. The DAQ has to send out all of those signals, since every hit could have been the real particle. Due to that problem, the SVD will suffer large backgrounds the closer it is to the IP. One way to tackle this problem is a pixel detector closer to the IP. This was the option chosen for Belle II. Due to the combination of strip and pixel detectors, manufacturing costs could be saved and the final product still fulfills the requirements for a precise vertex separation.

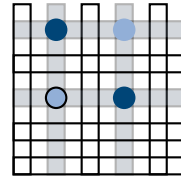


Figure III.9: Schematic picture of two ghost hits (light blue) and two real hits (dark blue) on the SVD.

---

<sup>4</sup>Analog Digital Converter

### III.2.2 The Central Drift Chamber - CDC

**S**URROUNDING the VXD, the Central Drift Chamber (CDC) is the outermost tracking detector and the third detector counting from the IP outwards. It consists of 14366 sense wires which are divided in eight, alternating arranged super layers. Each super layer consists of six (the innermost has eight) layers of sense wires which divide into axial layers, with wires parallel to the beam pipe, and stereo layers which are tilted at angles between  $-74$  and  $70$  mrad.

The CDC volume, which expands from 160 cm to 1130 cm in radial direction and 2.4 m in beam direction, is filled with a gas mixture of 50 % helium and 50 % ethane. This gas is ionized by charged particles traversing the CDC with a trajectory bend in the magnetic field. The electric field between the wires causes liberated electrons to drift towards the sense wires, which produces an electrical signal. From the signal timing and the drift velocity, the distance of the electron origin, e.g. the particle trajectory can be calculated. In the plane perpendicular to the beam pipe, the trajectory can be fitted as a circle. To get the slope in  $z$ -direction, of the typical track-helix, the stereo wires are used.

Since charged particles bend in the magnetic field, the CDC can determine their momentum via the bending radius. Another important particle quantity, which can be determined via information provided by the CDC, is the energy loss per length,  $dE/dx$ . When a particle crosses the CDC, it deposits a small amount of its energy in each layer it activates by ionizing the gas. The mean energy loss along the particles trajectory can then be used to determine  $dE/dx$ . To have a first separation on the particle type, the correlation of the momentum and the energy loss is used.

### III.2.3 Particle Identification

THE particle identification at Belle II is divided into two sub detectors. The bigger one, the Time of Propagation Counter (TOP), is surrounding the CDC in the barrel region, while the Aerogel Ring-Imaging Cherenkov detector (ARICH) is covering the endcap parts in plus and minus  $z$ -direction. The underlying detection method for both detectors is the Cherenkov effect [77]. Charged particles moving in a medium with a speed faster than the speed of light emit Cherenkov radiation. The angular distribution of the emitted light is given by

$$\Theta = \arccos(1/\beta n), \quad (2)$$

with  $\Theta$  the angle between the particles flight path and the wave-front constructed by the interfering photons (Fig. III.10),  $\beta = v/c$  the particle speed in units of the vacuum speed of light and  $n$  the refractive index of the medium. The cone of the wave front which is schematically shown in Fig. III.10, is detected as a circle at a distance  $d$ . From the refractive index  $n$ , and the known distance  $d$  one can calculate the particle speed by measuring  $r$ .

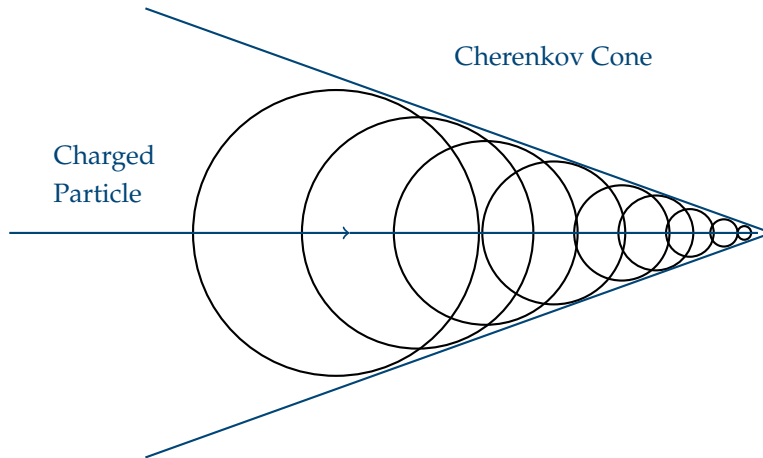


Figure III.10: Illustration of a particle generating Cherenkov light.

### III.2.3.1 Time of Propagation Counter - TOP

The TOP detector consists of 16 quartz bars with size  $2700 \text{ mm} \times 450 \text{ mm} \times 20 \text{ mm}$  placed around the CDC. All borders of those bars, except one, are completely reflecting the Cherenkov light emitted by particles traversing the quartz, Fig. III.11. At the reflective edge of each quartz bar a prism is expanding the detectable area to 51 mm. For detection, 32 micro-channel plate photo multiplier tubes (MCP-PMTs), arranged in two rows at the end of the prism are used. A mirror attached to the opposite site of the quartz reflects the Cherenkov light towards the detection end. Wave fronts which arrive under the same angle get focused.

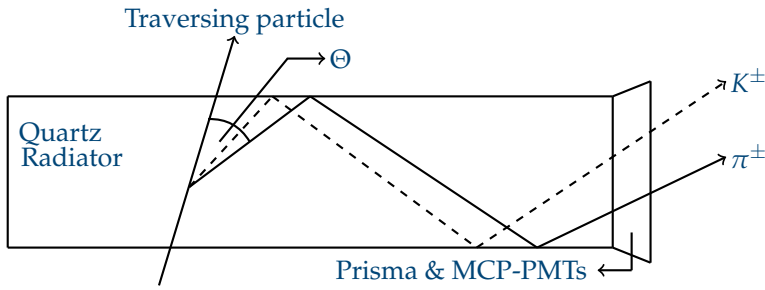


Figure III.11: Illustration of a particle crossing the TOP detector.

Due to the high timing resolution of the MCP-PMTs of 50 ps, the time between bunch crossing and detection of Cherenkov light can be measured. This time corresponds to the sum of the particles travel time to the detector and the Cherenkov light propagation in the quartz. When relating the Cherenkov information to the CDC tracking information, a calculation on the position and angle, under which the particle hit the TOP-quartz, can be done. The outcome is compared to a prediction, done under the assumption of the particle being a kaon or a pion, which defines the likelihood of the measured particle. In the final reconstruction, the likelihood-ratio  $\eta_L = L_i / \sum L_i$ , where  $i$  stands for the particle hypothesis, is calculated and associated to the particle candidate.

### III.2.3.2 Aerogel Ring-Imaging Cherenkov Detector - ARICH

The ARICH is located on the forward-endcap of the Belle II detector, closing the CDC. Its main component, the Aerogel radiator, is arranged in a radial structure divided in tiles at a distance of 167 cm from the IP, covering the angular area from  $14^\circ$  to  $43^\circ$ . To get a better focus of the Cherenkov light, the Aerogel layers have different refractive indices of 1.055 and 1.065. The produced light is detected by 540 hybrid avalanche photo detectors (HAPDs), each divided in  $12 \times 12$  matrices and placed 20 cm apart from the outer Aerogel layer.

### III.2.4 The Electromagnetic Calorimeter - ECL

THE final state products of  $B$  meson decays consist to approximately 3% of neutral particles like  $\pi^0$ ,  $K^0$  or  $\gamma$  leading to a high number of photons in a wide energy range between 20 MeV and 4 GeV. A high-resolution electromagnetic calorimeter (ECL) is therefore a substantial part of the Belle II detector. For the Belle II ECL most parts of the Belle ECL are reused, major changes are only affecting the readout system. The detection principle is based on scintillating<sup>5</sup> crystals made up from caesium-iodide doped with thallium CsI(Tl) which are read out by photodiodes and digitized by Flash ADCs. The ECL is build up from 6624 crystals in the barrel, 1216 in the forward and 1040 in the backward region. Besides its main task to detect and differentiate electrons and photons, the ECL, together with the CDC, is the main trigger source of Belle II.

### III.2.5 $K_L^0$ and $\mu$ Detection - KLM

ALL Belle II sub detectors explained in the last sections are surrounded by a 1.5 T magnetic field sourced by a cylindrical magnet coil surrounding the ECL. The yoke, composed of alternating iron plates and detection layers, serves as magnetic flux return and outermost detector for long-living neutral kaon and muon detection - the KLM. In the barrel part, an azimuthal region of  $45^\circ < \Theta < 125^\circ$  is covered. By adding the endcaps, the KLM reaches an angular coverage of  $20^\circ < \Theta < 155^\circ$ . In the outer layers the detection is done with electrode Resistive Plate Chambers (RPCs) [78] while the inner part and the endcaps, which suffers much more from the high rates, are readout by Silicon Photo Multipliers (SiPMs) [79].

---

<sup>5</sup>Particles traversing a scintillating material excite the atoms, which radiate a photon when falling back to the ground state.

Kaons, with a relatively large lifetime, initiate hadronic showers when reaching the iron plates between the detection layers, which are then detected by the RPCs or SiTCPs. In case of muons traversing the KLM, the CDC track will be extrapolated to the KLM using a pion hypothesis. The outermost KLM layer is then checked for the hit postulated by the pion hypothesis. If this hit is present, the track reconstruction is then started again at the entry point of the KLM with a muon hypothesis. Based on the Kalman filtering technique [80], a likelihood for the track being a muon is calculated, leading to a detection efficiency of 90 % in the momentum range of 1.0 GeV/c to 3.0 GeV/c [79].

### III.3 Belle II Trigger and Data Acquisition System

**I**N this section an overview of the Belle II trigger and Data Acquisition (DAQ) system is given. A first sub-chapter gives a brief discussion on the trigger system, which is split up in two levels, the Level 1 (L1) and Level 2 (L2) trigger, before the overall global DAQ system is shortly summarized. A broader overview is then given on the PXD DAQ system, which is subject to minor updates developed for this thesis.

#### III.3.1 Trigger System

**T**HE Belle II trigger system uses information from the outer detectors, mainly the CDC and ECL. Interesting physics processes from simulation are compared to the topology and deposited energy of recorded events and, if a matching event is found, a trigger signal will be issued. Almost all interesting events contain at least two good tracks, reconstructed by the CDC, originating from a region close to the IP and electron/photon energy clusters deposited in the ECL. Additional trigger sources are timing informations from ARICH and TOP as well as muon identification from KLM. The trigger signals from the different sub detectors are then collected by the Global Decision Logic (GDL), which makes a final trigger decision based upon the incoming data. If this decision is positive the L1 trigger signal is issued and distributed through the Frontend Timing Switches (FTSW) [81]. The basic components of this trigger are the event number<sup>6</sup>, the run number<sup>7</sup>, the sub-run number<sup>8</sup>, the experiment number<sup>9</sup> and a 64-bit trigger type word where the trigger setup is encoded.

The expected trigger rate is a combination of  $B$  meson events from  $Y(4S)$  decays (960 Hz), hadronic production from continuum  $e^+e^-$ -annihilation into  $q\bar{q}$  pairs undergoing hadronization process (2.2 kHz) or  $\mu$  and  $\tau$  pair production (1280 kHz), giving a total expected rate of around 20 kHz. For the design of the DAQ system, a safety margin of 10 kHz was added.

---

<sup>6</sup>32-bit incremented for each L1 trigger

<sup>7</sup>14-bit, incremented for each new run after stop of the DAQ

<sup>8</sup>8-bit, incremented for a minor sub detector change without stopping the run

<sup>9</sup>10-bit, incremented after major detector or accelerator changes

### III.3.2 Data Acquisition System

ALL Belle II sub-detectors, except the PXD, have, apart from their individual Front End Electronics (FEE), a similar readout scheme, which delivers the L1-triggered data via the Belle2-Link<sup>10</sup> (b2link) to several Common Pipeline Platform for Electronics Readout (COPPER) boards [83]. The COPPER boards receive their data from multiple FEE devices of the sub-detectors and the trigger from the FTSW. A sub-event is build on each COPPER board which is then further transmitted to the sub-detector readout PC (ROPC) where the sub-events of one sub-detector are combined (event-builder 0).

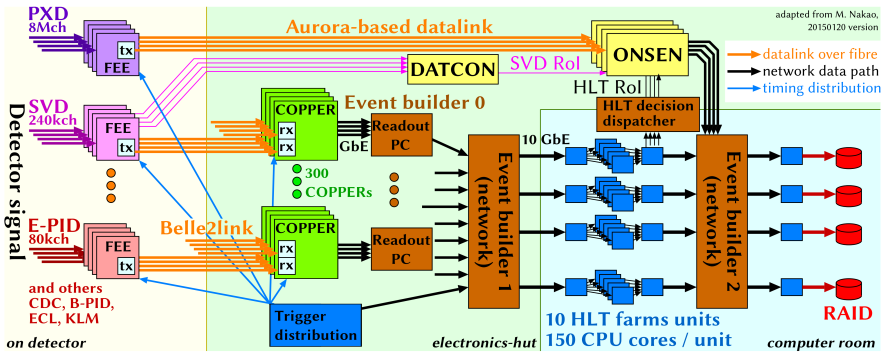


Figure III.12: Simplified schematic overview of the global Belle II DAQ system.

The data from all ROPCs is then transmitted via Ethernet to the Event-Builder 1 (EB1) PC farm, where the sub-events from the individual, outer detectors are combined to a single event package. At this stage the data rate from all outer detectors is estimated to be around 2.5 GB/s, which is further transmitted via 10 GbE to the High Level Trigger (HLT) [84] system. The combined information from all sub-detectors, except the PXD, is used to perform a full event reconstruction with tracking using CDC and SVD hits. Due to the complex calculations the processing time can last up to 5 seconds, depending on the event topology. On the average, a processing time of 1 second is expected. The output rate of the HLT is estimated to be around 10 kHz, a factor 3 reduction compared to the total expected input data. After event reconstruction the HLT transmits trigger packets to the

<sup>10</sup>Unified Belle II transfer protocol for data and slow control [82].

PXD DAQ and the full event package to the Event Builder 2 (EB2), up to which the data stream of all outer-detectors (including SVD) and the PXD data stream were completely separated. On the EB2, the data from **all** sub-detectors are combined and further transmitted to permanent storage.

### III.3.3 The PXD DAQ System

**T**HE PXD DAQ has to cope with high trigger rates and, due to the detector location very close to the beam pipe, high occupancies of the sensitive area. As discussed in the previous chapter, the expected trigger rate is 30 kHz and the maximum occupancy 3 %. The zero-suppressed pixel data format, in which data is encoded by the DHP, foresees 16-bit to represent a double row plus 16-bit for each column and ADC<sup>11</sup> value. With the expected occupancy, one can expect on average  $500 \cdot 0.03 = 15$  pixel per double row, summing up to  $15 \cdot 16 = 240$  bit. Including the 16-bit row header,  $(240 + 16)/8 = 32$  bytes are needed for 15 pixels, giving an average of  $\approx 2.5 \frac{\text{bytes}}{\text{pixel}}$ . Extrapolating this number for the whole PXD, gives an estimated average data rate of  $3 \% \cdot 7'680'000 \cdot 2.5 \text{ bytes} \cdot 30 \text{ kHz} \approx 17.3 \text{ GB/s}$ . While propagating through the DAQ chain, the pixel data will be reformatted and metadata<sup>12</sup> information, such as checksums and module numbers, will be added. Including this metadata information and adding a safety margin, a conservative estimation of  $\approx 20 \text{ GB/s}$  is done. Comparing this to the combined data rate of all other detectors, which is about a factor 10 lower, it becomes clear that the unified readout scheme cannot be applied to the PXD and therefore a complete new readout concept is needed.

The readout of the module ASICs, namely the DHP, is done by the Data Handling Hybrid (DHH) system [85]. It consists of customized developed boards with a Field Programmable Gate Array (FPGA) and DDR3 memory as their main component. In Fig. III.13, a schematic overview of the PXD DAQ system with focus on the DHH is given. As can be seen, the Data Handling Engine (DHE) receives the data from the FEE (namely the DHP) of one PXD module via four 1.5 Gbps optical cables, which are routed through a patch panel to connect to the Kapton cable coming from the module. Besides receiving the pixel data, the DHE also routes the slow control and configuration signals to the DHP, DCD and SWITCHER chips on the

---

<sup>11</sup>8-bit for charge encoding.

<sup>12</sup>Metadata contains global information on a specific event, such as experiment number, run number and event number.

module. After a complete event was received, the DHE reformats the DHP data and places an additional start and end frame, which includes, among other data, the module (DHE) number<sup>13</sup> and a timing tag, to the data stream.

The DHE data stream is then transmitted via 5 x 6.125 Gbps links using the Xilinx AURORA protocol [86] to the Data Handling Concentrator (DHC). Before data are sent out further down the DAQ chain, an additional header and trailer is added and a 5-to-4 multiplexing is performed. The output uses AURORA link layer protocol at a link bandwidth of 6.125 Gbps. Another module, the Data Handling Isolator (DHI), is receiving trigger and clock signals and communicates the DHH status via slow control. All of the previous mentioned modules, five DHEs, one DHC and one DHI, are plugged into an Advanced Telecommunications Computing Architecture (ATCA) board, which completes one of eight DHH modules. To compensate for the different data rates from inner and outer PXD modules, a load-balancing is applied. It foresees a connection of always two inner forward modules (high occupancy) with three outer backward modules (low occupancy) per DHC. In this way, an equal data output per DHC is ensured.

---

<sup>13</sup>6-bit identification number for a PXD module. 1-bit for inner or outer layer, 1-bit for forward or backward module and 4-bit counting up the module number in  $\phi$  direction.

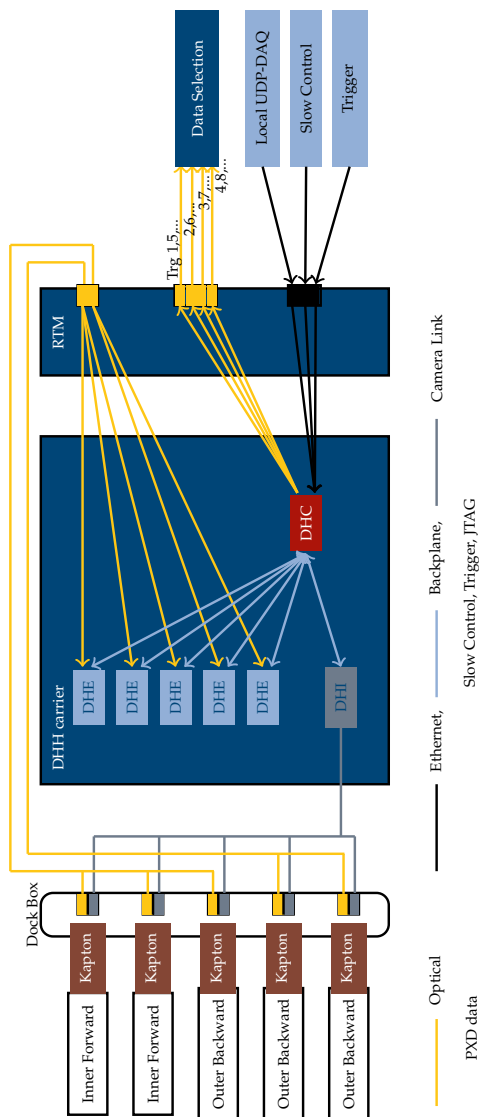


Figure III.13: Schematic overview of one DHH module.

### III.3.3.1 The ONSEN Data Reduction System

To reduce the PXD data of  $\approx 20$  GB/s before the transfer to EB2 and permanent storage, a data reduction has to be performed. This is done on the Online Selection Node (ONSEN) system, an ATCA and FPGA based, modular DAQ system. Before giving an overview of the internal architecture, the underlying data filtering mechanism is discussed.

#### Data Reduction - ROI

The data reduction for the PXD is based on two stages. As a first step, the data will be reduced, like for all other detectors, according to the HLT decision. This is done by a 1-bit flag in the HLT data stream, forcing the ONSEN system to discard the flagged event, which does not parse any of the HLT trigger lines, leading to a reduction of the non-interesting background processes by a factor of 3. The second step is performed for each PXD module separately, instead for complete event. During processing time, the HLT calculates the back-projection of the reconstructed tracks, including SVD hits, on to the surface of the PXD. Around the intersection point of this track with the PXD module, the HLT defines a so-called Region Of Interest (ROI). This rectangular shaped area, with height and length according to the uncertainty of the interpolated track intersection, defines the region in which PXD hits are kept. All hits (or clusters) outside those ROI are discarded from the upstream data to EB2. In addition to the ROIs calculated by the HLT, a second, independent system is calculating ROIs for ONSEN - the Data Acquisition Tracking and Concentrator Online Node (DATCON) [87]. The FPGA based DATCON system is composed of two different modules for input/preprocessing and calculation/output purposes. In contrast to the HLT, the DATCON is performing its calculations exclusively on SVD data. During data processing, a Hough transformation [88] is performed including the four SVD layers and the, IP as constraints for a track. The DATCON ROIs are then transmitted to ONSEN and merged with the ones from HLT. If DATCON found a track inside an HLT-rejected event, the data is not kept. If a DATCON ROI is placed outside an HLT ROI, the pixels inside are kept. An illustration of the ROI mechanism can be seen in Fig. III.14.

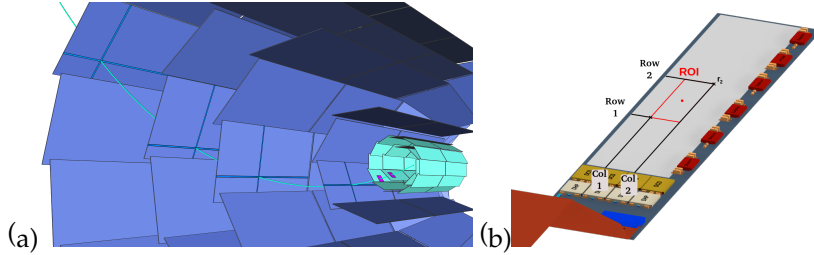


Figure III.14: A track is extrapolated back to the PXD surface (a) and a corresponding ROI on a PXD module (b).

### The ONSSEN Hardware Platform

Below, the previously elaborated requirements for the ONSSEN data reduction system are compiled:

- Input data rate up to 6.125 Gbps
- Input trigger rate up to 30 kHz
- Input bandwidth 20 GB/s
- Output bandwidth 700 MB/s
- Parallel processing
- Data buffering for up to 5 seconds
- Ethernet and optical data transmission
- Slow control accessibility

The development of an ATCA/FPGA based system with modular architecture was found to be the most suitable strategy. The main work on this system was done in [89]. A general scheme of the ONSSEN system can be found in Fig. III.15.

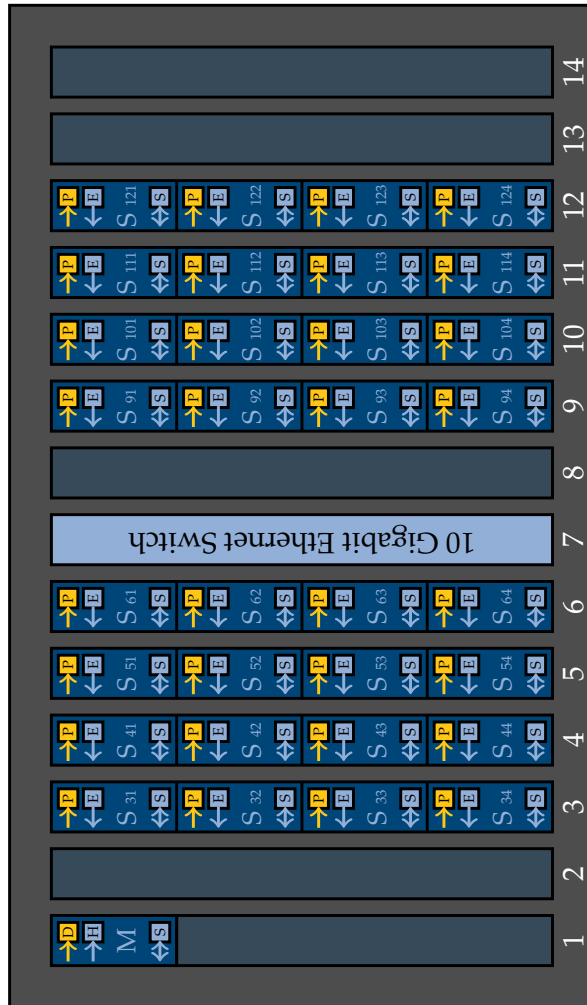


Figure III.15: Illustration of the ONSEN system. A 14 slot ATCA shelf (dark gray) is equipped with 9 carrier boards containing sub module FPGA cards (dark blue). Yellow fields indicate data transfer via AURORA, light blue fields data transfer via Ethernet.

The ONSSEN system consists of 9 carrier boards, of which each can host up to 4 daughter boards. Together they make up the Compute Node (CN) [90] which was developed by the Institute of High Energy Physics (IHEP) in Beijing and Giessen University. A first iteration of the CN was developed and realized as a single board with five Xilinx Virtex 5 FPGAs for the PANDA experiment<sup>14</sup>.

The whole system is hosted in an ATCA shelf providing a shelf manager using the Intelligent Platform Management Interface (IPMI) standard for power management and sensor readout. All 14 slots of the shelf are connected via full-mesh backplane<sup>15</sup>, guaranteeing data rates of up to 3.125 Gbps. On the back side, each slot can be extended with a Rear Transition Module (RTM), featuring ports for Ethernet, USB, as well as JTAG<sup>16</sup> connection. After it was chosen as hardware platform for the Belle II PXD DAQ, its architecture was redesigned and is now realized as carrier board hosting one Xilinx Virtex 4 FPGA, the Compute Node Carrier Board (CNCB), with up to four Advanced Mazanine Cards (AMC) hosting a Xilinx Virtex 5 FPGA, called the xTCA-based FPGA Processor (xFP). The xFP cards are connected to the CNCB via the AMC connector at the end of the docking bay, allowing data transmission between the xFP and CNCB FPGAs via six Multi Gigabit Transceivers (MGT) and twelve bi-directional Low Voltage Differential Signal (LVDS) links. Since the ONSSEN system has to buffer the incoming pixel data until the HLT decision arrives, each xFP card hosts two 2 GB DDR2 SDRAM modules. Each xFP card receives data via the AURORA or TCP protocol over optical fibers or Ethernet cables. For a flexible adjustment this was realized by two SFP+ cages at the front of each xFP, which connect to the MGT of the FPGA. The cages can be equipped either with optical fiber or RJ45 Ethernet adapters. In addition, a fixed RJ45 port for Slow Control purposes and a miniUSB universal asynchronous receiver/transmitter (UART) port for debugging is installed. To program the FPGA upon power up, a 4 MiB<sup>17</sup> Xilinx Platform Flash chip, capable of storing the firmware, is installed. Board operation via Slow Control (SC) is performed on a PowerPC 440 (PPC) CPU with Ethernet MAC included.

---

<sup>14</sup>A planned fixed target physics experiment for proton anti-proton collisions at the Facility for Antiproton and Ion Research (FAIR) in Darmstadt, Germany.

<sup>15</sup>All boards can communicate via bi-directional backplane channels.

<sup>16</sup>Joint Test Action Group, IEEE-Standard 1149.1

<sup>17</sup>Mebibyte, 1 MiB = 2<sup>20</sup> Byte

The CNCB's Xilinx Virtex 4 FPGA provides 16 bi-directional LVDS links with line rates of up to 600 Mbps, which are connected to the xFP cards, four links per docking bay. A PowerPC 405 CPU with Ethernet MAC is providing access for slow control. The connection to the PPC is realized via a RJ45 connector on the pluggable RTM.

A Complex Programmable Logic Device (CPLD) can be accessed via the IPM Controller (IPMC) chip, which is connected to the shelf manager. The CPLD allows the programming of the whole shelf upon power-cycle, or re-programming of individual CNCBs and their xFPs with the corresponding firmware, stored in the each card's flash chip, on demand. 16 3.125 Gbps serial MGT transceivers connect the CNCB to the fabric channels<sup>18</sup> of the full-mesh backplane of the shelf, allowing data transfer among all FPGAs in the system. In addition, a GbE line connects the CNCB to the backplane's base-channel for support of Ethernet connection from each slot to the central Ethernet switch of the shelf.

#### The ONSSEN Firmware Architecture

The proposed data reduction scheme with ROIs is implemented in four firmware projects running on the ONSSEN system. Two, the merger and selector project, are designed to run on the xFP FPGA, the other two, the merger-switch and selector-switch, are designed for the CNCB FPGAs. In Fig. III.16, a simplified schematic of those projects and the data transfer inside them is shown.

The incoming DATCON ROIs are received via AURORA and written to the internal xFP memory. The storage address in the memory and the trigger number are saved in a Look-Up Table (LUT). HLT ROIs, which need more processing time and therefore arrive later, are directly send to the merger-core, while the trigger number is used to retrieve the memory address of the corresponding DATCON ROIs. This address is forwarded to the reader-core, which reads-back the DATCON ROIs from internal storage and forwards it to the merger-core. ROIs get merged according to trigger number and sorted by increasing DHE number, before they are transmitted to the AURORA-core. It parses the merged ROIs via the bi-directional GT11 links on the AMC-CNBC interface to the receiving side AURORA-core on the merger-switch. Since the pixel data, received from the DHH, is

---

<sup>18</sup>Composed of four bi-directional links between two boards.



distributed in packets of DHE-ID<sup>19</sup>, the merger-switch has to perform a distribution to the corresponding selector-switch. This is done before transmitting the data, via eight instantiations of the AURORA-core driving the MGT links, to the selector-switch unit. Arrived on the selector-switch, the ROIs are separated according to their trigger number. Each selector (per selector-switch) receives pixel data in packets of  $Trg\#\%4$ , i.e.  $Trg\#_{sel1} = 1, 5, \dots$ ,  $Trg\#_{sel2} = 2, 6, \dots$ ,  $Trg\#_{sel3} = 3, 7, \dots$ ,  $Trg\#_{sel4} = 4, 8, \dots$ . On the other AURORA input link, the selector AMC receives pixel data matching in DHE-ID and Trigger Number to the ROIs received by the selector switch. Pixel data gets written to the on-board memory and the address pointer is saved in a LUT. Once the matched ROI data stream arrives, it gets forwarded to the pixel-filter. The trigger number from the ROI data is used to locate the memory address pointer and transfer it to the reader. Once the pixel data is read back from memory, it is transmitted to the pixel-filer, where the ROI selection is performed - only pixels inside an ROI are kept. On this stage data are reduced by a factor of 30, factor 3 reduction from HLT decision for the global event and a factor 10 by ROI selection. The pixel data stream is then propagated to the outgoing AURORA-core which is connected to the boards SFP+ transceivers. Each transceiver<sup>20</sup> connects via optical fiber to the EVB2, where the data is matched with the combined sub-detector data stream from EVB1.

---

<sup>19</sup>5 DHE-IDs, i.e. PXD modules, two inner-forward and 3 outer backward, per selector AMC.

<sup>20</sup>In total 32, one for each selector-AMC.

## III.4 The Belle II Analysis Framework - BASF2

The Belle II Analysis Framework (basf2), is a complex arrangement of analysis and data processing tools, input/output modules and data base records [91]. It is used for online data processing on the HLT, as well as for offline reprocessing, e.g. the production of *skimmed*<sup>21</sup> data samples for analysis, and individual analysis performed by the user.

The framework with its modular architecture is developed on top of ROOT<sup>22</sup> [92], the modules are mainly written in C and C++, Python scripts are used for steering. An examples is shown in Fig III.17.

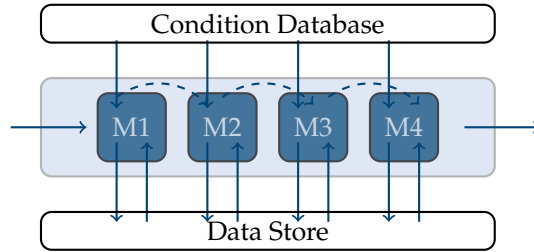


Figure III.17: Schematic data flow in a basf2 steering script. Each module, M1 to M4, has read and write access to the data store and can read from the condition database. The input data is modified according to the modules, by applying constraints from the condition database or interacting with other data received from the data store. The last module is usually saving the modified data to disk.

All class defining objects (data types, nTuples<sup>23</sup>, calibration, etc.), that are stored in the data store, are ROOT-based objects which are either stored permanently in \*.root files, or temporarily, event-wise in the ring buffer until each module in the steering chain has performed its task. Some modules, especially for reprocessing of the RawData<sup>24</sup> for analysis purposes, need calibration input to set important parameters, e.g. magnetic field strength in a particular run for tracking. Those modules do not only access the data

---

<sup>21</sup>Preselection of a particular physics process, e.g. continuum or *B* meson production for fast analysis.

<sup>22</sup>Commonly used analysis framework developed at the European Organization for Nuclear Research (CERN)

<sup>23</sup>ROOT based objects containing variables for each entry in an event

<sup>24</sup>Digitized, unprocessed data from the detectors

store but also the condition database, which contains all important detector/machine parameters for each recorded run. For analysis tasks, the last module in a steering chain is usually the `RootOutputModule`, which writes the analyzed `nTuples` or `RawData` to a `*.root` file.

### III.4.1 Simulation and Reconstruction in `basf2`

THE data for simulation and reconstruction purposes, for MC as well as for real data, are stored in `TTree` inside a `.root` file. Those trees contain detector, particle and meta data variables which are structured event-wise in C++ data types. The only mandatory object, `EventMetaData`, contains all relevant meta information, like run number, experiment number and event number, of a certain data set.

In case of performing a simulation, the raw data, stored for each detector in several branches of the `TTree`, is read by the `RootInputModule`. For each event a module chain, like defined in the python steering script, is then processed. The hit, cell and cluster based detector information is first unpacked by dedicated unpacker modules for each Belle II sub detector. The unpacker converts those informations into digit objects<sup>25</sup>, which are used by several tracking and reshaping algorithms to build higher level data objects such as tracks and clusters. During this intermediate processing step, the raw detector data information is discarded, which can reduce the event size by a factor of 40. The final outcome of the simulation and reconstruction process chain are particle information data such as charge, four momenta, energy and event-shape variables, which can then be used by the individual analyst for physics analysis.

For charged particles the track reconstruction is a crucial processing step during simulation and reconstruction. Track parameters and errors are extracted from detector level information given by the Belle II tracking devices CDC and VXD. The unpacked digits of those devices are processed by dedicated tracking modules using the Kalman filter fit technique [93], which takes into account multiple scattering effects and energy loss in the detector material for the track reconstruction. The particle momenta can then be measured from the reconstructed tracks, while the energy is determined from

---

<sup>25</sup>In case of MC simulations, the digit objects are written out by a detector specific digitizer module using the detector response simulated by GEANT4.

ECL and KLM clusters, which are associated with the track. Algorithms, which are mainly linked to the ARICH and TOP detector, perform particle identification based on likelihood ratios, comparing a given particle hypothesis with the actual measurement. Stable particles<sup>26</sup> can then be combined to form common vertices and therefore originate from a reconstructed, intermediate mother particle. For the reconstruction of those intermediate states, basf2 provides a large variety of vertex fitters and algorithms dealing with neutral candidates. By combining the final (stable) particles to intermediate states and those states to the next higher one, the analyst can reproduce a defined decay chain until reaching the  $B$  meson<sup>27</sup>. Informations for each reconstructed particle are stored as variables in the particle list, which is then written out for each candidate in an event to the final \*.root file for analysis purposes.

### III.4.2 Conditions Data Base

THE condition data base collects all variables which define the conditions of a run. Those data are stored as payloads which reproduce the change of detector and machine<sup>28</sup> specific variables over time, on a run dependent basis. An ensemble of these payloads is combined after a certain integrated luminosity goal in a Global Tag (GT). During reconstruction of the data, the GT is assigned to the script and, by matching the EventMetaData of a specific run to the run and experiment numbers in the GT, the correct condition variables are transferred to the reconstruction algorithm.

### III.4.3 The Belle to Belle II Framework - b2bii

TO analyze Belle and Belle II data convenient within the same framework, the Belle to Belle II Framework (b2bii) [94] was developed. The Belle data are stored as RawData, as well as final reprocessed, so-called mDST, files. A conversion of Belle RawData to the basf2 format would be in principle possible, but, due to the different detector layouts, parameters and backgrounds, a very difficult task. Another approach is the conversion of mDST files to the basf2 format, in this case most of the data are already detector independent.

---

<sup>26</sup>Here stable refers to all particles living long enough to cross through the whole detector.

<sup>27</sup>In case of an  $Y(4S)$  on-resonance analysis.

<sup>28</sup>Refers to the collider specific variables, for example the size of the beam spot or the collision angle under which the beams interact at the IP.

To ensure a correct working conversion in a first step, MC samples produced in the Belle Analysis Framework (basf) were analyzed and compared to converted samples analyzed in basf2. In a second step also physics analysis performed by the Belle collaboration were redone within the b2bii and basf2 frameworks and the output compared. A working conversion is therefore taken as granted in this work.

### III.4.4 Example for a Simulation and Reconstruction Chain with basf2 and b2bii

IN the last part of this section, two flow charts are shown, which illustrate the python steering files used for simulation (III.18) and reconstruction (III.19) of data or MC.

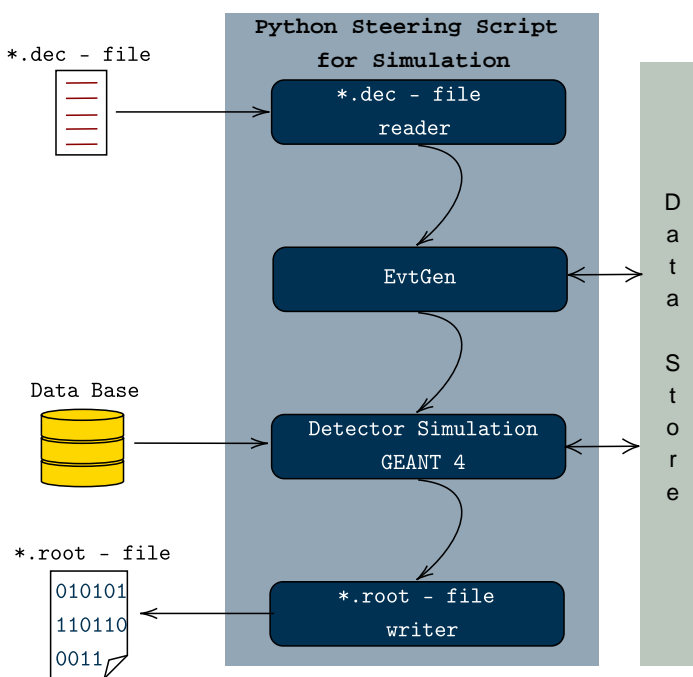


Figure III.18: Schematic data flow in a basf2 steering script used for generating signal MC root-files.

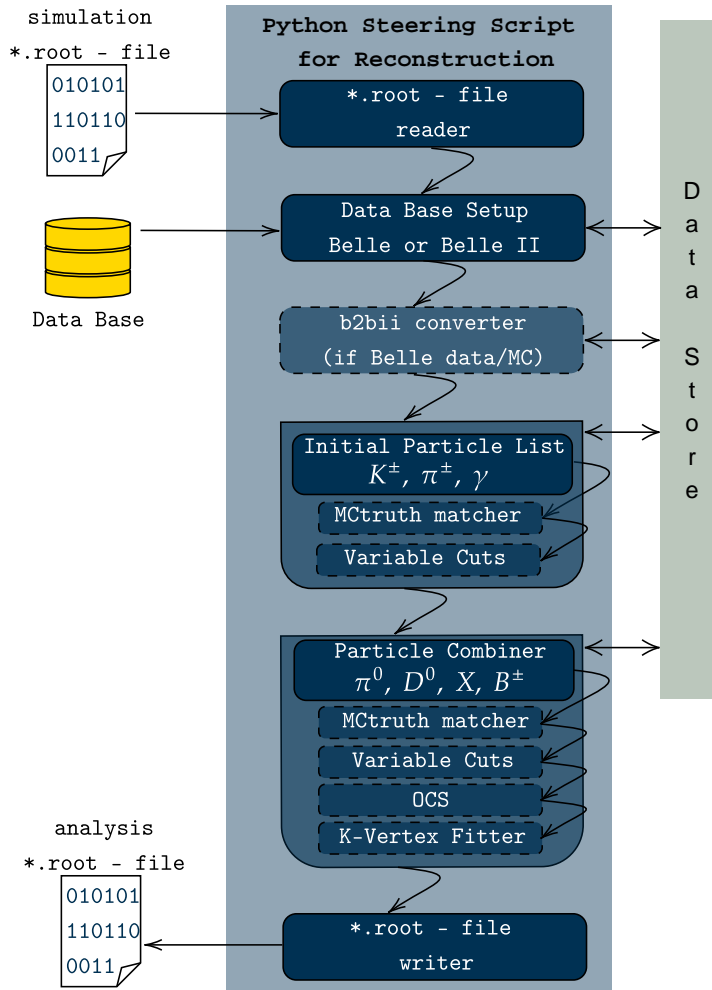


Figure III.19: Schematic data flow in a basf2 steering script used to reconstruct particles from a given data or MC file for Belle or Belle II. The light blue boxes with dashed borders indicate optional steps in the reconstruction chain. After processing, this script produces an analysis root-file which is then used to visualize or perform calculations within Jupyter-Notebooks and Python analysis code.

# High Speed Data Multiplexer for the Belle II Pixel Detector

**I**N this chapter the developments towards an alternative output for the pixel detector DAQ, in particular the ONSEN system, as well as its implications for slow control are discussed. The developed code was tested under realistic conditions in the laboratory, but is so far not used at the final experiment. At the end of the chapter, the test results are discussed and the missing steps in order to implement it at the experiment are outlined.

## IV.1 New Output Option via 10 GbE ATCA-Switch

**T**HE current data-flow scheme of the ONSEN system is described in Sec. III.3.3.1 and illustrated in Fig. III.16. In this option, the ROI selected pixel data is transmitted via 32 optical fiber cables to the EVB2. This option works, but was considered unpractical for two reasons:

- 32 cables, i.e. 64 connectors between ONSEN and EVB2.
- FPGA resources of the selector AMC project.

Since the standard option is working well and was implemented first, on ONSEN and EVB2 side, and tested during test-beams, this project did not have a high priority but could contribute to an almost maintenance free cabling and better use of resources on the selector AMC. Due to polluted cable connectors or broken/defect cables between ONSEN and EVB2 the data transmission could suffer from a large number of error points, i.e. cables. A smarter solution, which needs only one cable connection, can improve this situation. Since, for the current solution, the SiTCP-core on the selector-AMC needs a lot of FPGA resources, a project omitting this core for the EVB2 transmission, would be smaller and more flexible, if future upgrades are

needed. A possible upgrade could be the instantiation of a second RAM controller on the selector AMC to get access to the full 4 GB memory. In that case, the buffered pixel data could be doubled, leading to higher data retention, higher data rates, or additional functionality. Also other features like online event checks for pixel cluster parameters could be possible.

To pursue this option, the filtered pixel data, transmitted from the selector-AMC, had to be redirected back to the selector-switch. Here, the four incoming AMC data streams are merged and send out via SiTCP to the 10 GbE ATCA-Switch, which is connected to the EVB2. For the data transmission between selector-AMC and selector-switch, the same links as for sending and receiving ROIs are used. The transmitting AURORA-core on the selector-switch had to be extended by the instantiation of four receiving ports. On the selector-AMC a transmitting port was added to the AURORA-core. Assuming equally saturated data links between DHC and ONSEN, each selector-AMC has to cope with  $625 \text{ MB/s}^1$ , at most. After pixel filtering, and therefore a data reduction of factor 30, the output data rate of one selector-AMC is expected to be slightly above  $20 \text{ MB/s}$  and therefore, even with the incoming ROI data stream, not saturating the LVDS links between selector-AMC and selector-switch. The data stream of one selector-switch,  $\approx 80 \text{ MB/s}$ , is still well below the limit of GbE and a transmission via the backplane GbE to an ATCA switch possible. For the  $\approx 640 \text{ MB/s}$  data transmission to EVB2, an ATCA-switch with 10 GbE up-link was tested and installed. In Fig. IV.1 the internal data flow for the 10 GbE output option is shown.

---

<sup>1</sup>Estimated 20 GB/s PXD data split up on 32 ONSEN links.

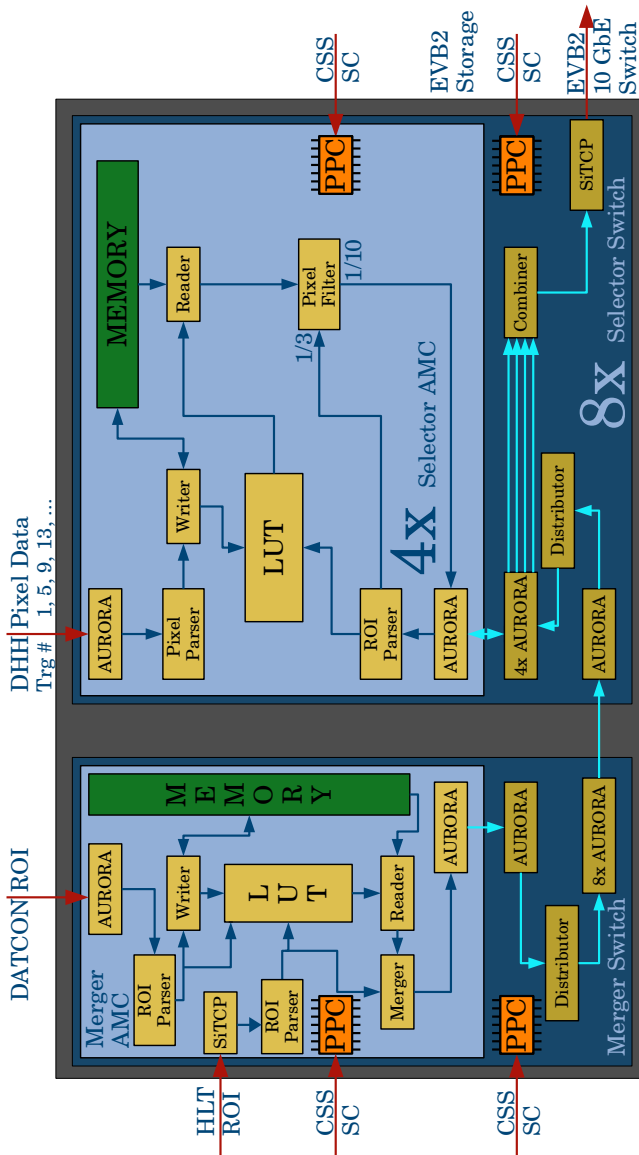


Figure IV.1: Simplified illustration of the internal logic of the ONSEN system including the 10 GbE data output option, developed as part of this thesis.

## IV.1.1 Local Link Combiner - IP Core Development

TO merge the incoming data streams from the selector-AMCs on the selector-switch, a dedicated IP-core was developed for this thesis - the `ll_combiner`. It receives the incoming, ROI-filtered pixel data stream from four selector-AMCs and combines them to a single output stream to be propagated to the selector-switch SiTCP output. For data transmission between individual cores on the FPGA, the Xilinx LocalLink (LL) interface standard is used [95]. It is defined by a number of signals for the point-to-point data transfer, between source and destination IP-core, of data frames. Each frame consists of an arbitrary number of bytes aligned as 32-bit data words. When a data frame is transmitted from the source IP-core, the number of valid bytes are defined and whether the transmitted word is a at the start or the end of the data frame. During any clock cycle<sup>2</sup> the receiving LL can stop accepting the data. This will trigger the source to send the data again in the next clock cycle. This mechanism generates back pressure, that can cascade down to the initial, data receiving interface.

In case of the `ll_combiner`, five LL interfaces are instantiated; four incoming for the data coming from the selector-AMC and one outgoing for the combined data stream to SiTCP. An internal entity, the `ll_muxer`, defines those LL connectors as block of six data ports. Source and destination ready ports define the state of a receiving or transmitting LL, start-of-frame and end-of-frame ports indicate whether a data frame has just begun or ended, a data port (32-bit vector) saves the data word which was just transmitted during the current clock cycle. The last port is connected to the system clock, which defines the frequency with which the state machine, the ports and the signals are processed. A synchronizing state machine runs, with every rising clock edge<sup>3</sup>, through enabling and forwarding signals, which enable an incoming LL from the selector-AMC or force that LL to forward data to its data port. All incoming LLs are addressed by the state machine when the source and destination ready ports have the correct values and the enable/forward signal of that LL is set, until the end-of-frame signal is received. After a complete state machine cycle, the LL of all attached selector-AMCs are read out and forwarded to the `ll_combiner` LL output.

---

<sup>2</sup>Data processing cycle during which all internal FPGA signals are read out in parallel and operations are processed

<sup>3</sup>Cllocking pulse rising from 0 to 1.

## IV.1.2 Adjustments in Slow Control

IP-cores developed for the ONSSEN project are connected to SC via the on-board Ethernet interface operated by the xFP's PPC. A Linux system for the two different PPC models (PPC 405 for CNCB and PPC 440 for xFP FPGAs) is compiled from source. During start-up, the Linux also provides the data-base entries for the FPGA registers which should be accessible by SC. The mapping of these hardware registers to readable software data-base entries is done by the Experimental Physics and Industrial Control System (EPICS) [96], an open-source software framework developed for the integration and control of large computer networks which give operation control and feedback, i.e. detector response. The EPICS framework as well as dedicated extensions and user-specific, so called Input-Output Controllers (IOC), programs are compiled for the corresponding PPC Linux and integrated in the systems initial ram file system<sup>4</sup>. Process Variables (PVs) are defined as variable type, e.g. string, float, integer,..., inside the IOCs data base section. If the PV is reading out or writing to registers in the FPGA, it is mapped to the register inside its defining code block. PVs are commonly read out every second but also other read-out cycles are programmable, as well as triggered readouts upon request.

To display the various PVs and assure an easy-as-possible operation of the system, a Graphical User Interface (GUI) is necessary. The Belle II Experiment uses Control System Studio (CSS) [97] for that purpose. CSS is an eclipse-based set of programs and tools to monitor large scale systems and is widely used in experimental physics. The program's editor is an easy to use, GUI-based workspace, allowing a user to quickly design a custom control panel for a dedicated purpose. Buttons, readout-files, temperature scales and other tools for visualization or control can be linked to EPICS PVs, giving easy control and a clear overview to the user.

The ONSSEN system is operated via several CSS OPIs and the EPICS IOCs. A few of them are responsible for the visualization of data transfer between the individual ONSSEN boards, as well as the ingoing data from the DHH, HLT and DATCON and the outgoing data stream to EVB2. In Fig. IV.2 the CSS-GUIs for the selector-AMC and the selector-switch are shown. Changes on these OPIs as well as the underlying IOCs had to be made in

---

<sup>4</sup>A compact file archive holding data which is necessary for the system start.

order to visualize the changes made for the 10 GbE data output option on firmware level. A set of new PVs for counting of ingoing and outgoing data frames and 32-bit words was defined and mapped to the FPGA registers.

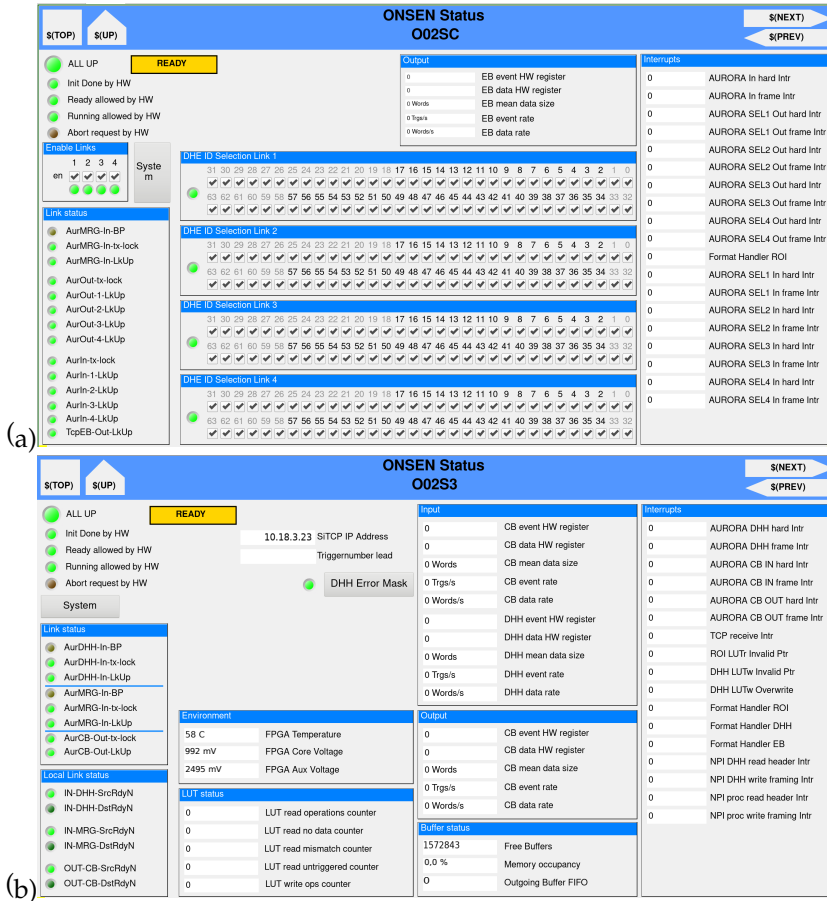


Figure IV.2: CSS control panel OPI for the selector-switch (a) and the selector-AMC (b). The current state, "READY", indicates that the system is configured, all values are initialized and the in- and outgoing connections are established (indicated as green LEDs). The data taking can start at demand.

## IV.2 Laboratory Tests

**T**O test the developed IP-core and new data routing via the 10 GbE switch including SC via EPICS, a dedicated laboratory test bench was set up at Giessen. Since, at this stage, no DHH unit was vacant to be placed at the Giessen laboratory, it had to be simulated. The DHH data packets were simulated on PC with a fixed geometrical pixel shape and charge value per module. Data packets were then sent to a stand alone xFP card, which received the DHH data via SiTCP from PC and transmitted it via AURORA on optical fiber to the ONSSEN selector-AMC. Due to the low bandwidth possible with this transmission option, only the data integrity could be tested with this setup. To test the data rates and long time transmission stability, simple data packets were generated directly on the selector-AMC and transmitted to the CNCB which further transmitted them via backplane Ethernet to the 10 GbE shelf-switch connected to a receiving PC. By exploiting both methods, a comprehensive test could be done, even though essential hardware components for the full DAQ chain were missing.

### IV.2.1 Data Integrity Test

**T**O test for the data integrity of the alternative routing via the 10 GbE switch, DHH data was generated on PC. A dedicated C++ program was written for that purpose. In order to check consistency of the data flow, i.e. compare the in and outgoing data streams, the simulated pixel<sup>5</sup> and ROI data was split and transmitted to the DHE-simulator AMC, as well as dumped to hard-disk. That way, it was possible to compare the online selected pixel data from the ONSSEN with the offline selected data after applying the ROI filter on PC. Fig. IV.3 shows the generated pixel pattern before (a) and after (b) ROI selection, with ROIs indicated as blue-shaded area. For simplicity and illustration reasons the ROIs are chosen to be fixed rectangular tiles covering half of the sensor, thus an ROI reduction factor of 2, instead of 10, is applied. The HLT decision, which would give an additional factor of 3 reduction, is not simulated, since the firmware part responsible for this operation is inside the merger-AMC and is therefore not touched by the firmware changes. To compare the outcome of the test, the generated pixel pattern (Fig. IV.3 (a)) was selected according to the ROIs, on PC, and compared with the outgoing - and online selected - data stream from ONSSEN.

---

<sup>5</sup>Simulated pattern with occupancy of 2.1 %

For each generated DHE-ID, 10 in total, the online reduced pattern received from ONSEN was subtracted from the offline selected pattern. All hit maps showed zero entries and therefore the test was successful.

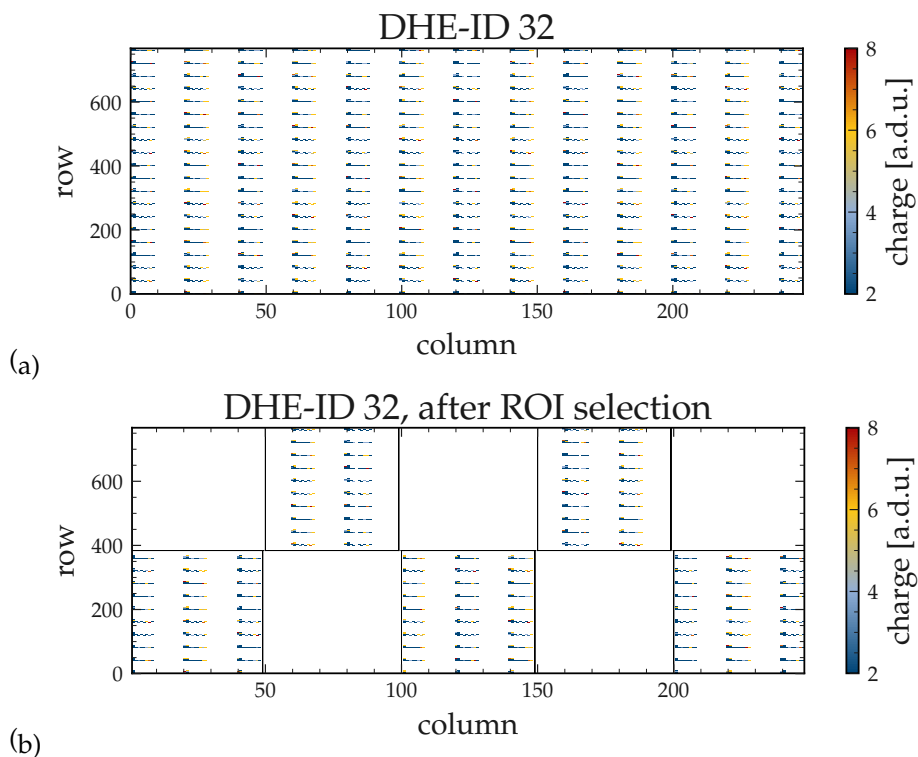


Figure IV.3: Pixel pattern used for the data integrity test for module with DHE-ID 32.

### IV.2.2 Results for Data Rate Test

DU<sup>E</sup> to the lack of hardware in Giessen, a full system test with DHH and ONSEN could not be established and the stable data transmission via the MGT links between AMC and CNCB, as well as the backplane connection from the CNCB to the 10 GbE shelf-switch had to be tested differently. For this purpose a dedicated firmware project for the selector-AMC was developed. Since the selector-CNCB, as well as the developed combiner-core, are not checking for the data format of the ingoing data stream from the selector-AMC<sup>6</sup>, the simplest approach for such a project was pursued. The new project consists mainly of generator-core and AURORA-core. Data are generated in the generator-core and transmitted to the CNCB via the AURORA-core. To check the consistency of data and for possible errors during transmission, a fixed number of  $\sim 2000$  bytes was generated, always framed between a Start-of-Frame and an End-of-Frame Word and every new event starting with the common ONSEN 32 bit magic-word<sup>7</sup> "0xCAFEBABE". This way it was possible to check for transmission errors in the AURORA-core<sup>8</sup> and to count the in and outgoing events on the selector-CNCB. A successful test should show conclusive numbers on the in and outgoing event counters. As an important result, an output data rate of 950 MB/s was achieved, close to the theoretical 10 GbE limit. Fig. IV.4 (a) shows that achieved data rate as a function of time.

### IV.2.3 Results for Long-Term Stability Test

Besides the conclusive numbers on in- and outgoing data, also the long-term stability of data processing was tested. The processed data transmitted via the 10 GbE shelf-switch to a 10 GbE network interface on PC was recorded by a small program, which extracted the number of events per second and the transferred data size per second. While receiving, the data was again checked for integrity, by comparing the first word with the standard ONSEN magic-word "0xCAFEBABE" and counting the ingoing, previously fixed bytes until the next magic-word. The whole test was performed with 8 full equipped selector-CNCB cards<sup>9</sup>, running for almost 3 days, showing no

---

<sup>6</sup>This is done on merger-AMC and selector-AMC only

<sup>7</sup>Signature for the start of a new frame displayed in hexadecimal numbers

<sup>8</sup>Transmission errors are divided as `Hard` and `Frame` errors. Framing errors occur when the frame is broken or not fully transmitted, hard errors occur when a link is shortly dropped and transmission broken.

<sup>9</sup>Four selector-AMC per selector-CNBC

drops in data or trigger rate, as well as no data integrity errors during transmission. In Fig. IV.4 two plots, showing the total data rate received from all 8 selector-CNCB boards (a) and from one individual board (b).

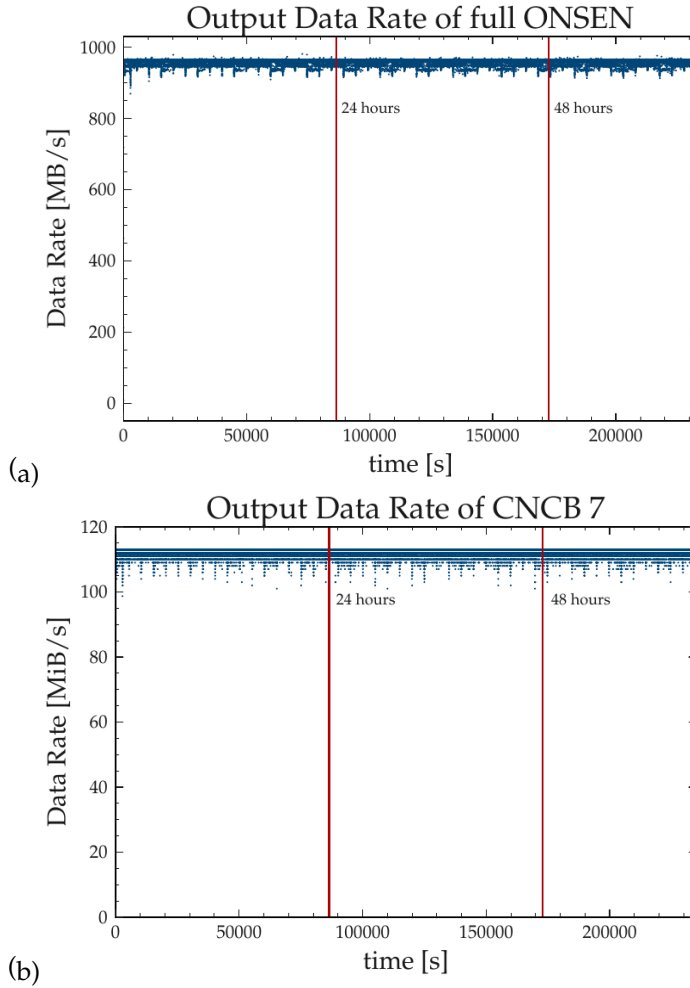


Figure IV.4: Combined data rate of 8 selector-CNCB cards (a) and data rate of single selector-CNCB nr. 7 (b).

## IV.3 Remaining Issues

The tests done so far were the most comprehensive and conclusive tests possible with a restricted setup. To have complete prove of a working 10 GbE solution for the ONSSEN system, a test with the full PXD DAQ chain at KEK in Japan would be required. This can only be done during the downtime period of the machine in the summer month<sup>10</sup>. For such a test, the receiving side, the Event Builder 2, would have to be modified in order to accept data via one cable and 8 links, instead of 32 cables and links. Also an additional, re-framing-feature could be implemented to the `ll_combiner`. Such a re-framing would allow the CNCB to re-frame the four data packets received by the four selector-AMCs and combine them in one data packet. To do so, the length of the data packets in each selector-AMC frame would have to be stored and added together for the final length of the data packet transmitted to the EVB2. Depending on the size of the individual frames, this could be an issue leading to back pressure in the system. When testing with the current architecture, the Slow Control GUIs and IOCs would have to be updated and merged with the ones from the standard output architecture.

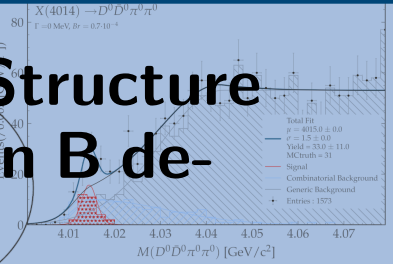
---

<sup>10</sup>Earliest in summer 2021



$$\chi_{\text{BCS}}^2 = \left(\frac{\Delta M_{D_1^0}}{\sigma_{M_{D_1^0}}}\right)^2 + \left(\frac{\Delta M_{D_2^0}}{\sigma_{M_{D_2^0}}}\right)^2 + \left(\frac{\Delta E}{\sigma_{\Delta E}}\right)^2 + \left(\frac{\Delta M_{\pi^0}}{\sigma_{\pi^0}}\right)^2$$

# Simulation of a Resonant Structure at the $D^{*0}\bar{D}^{*0}$ threshold in B decays at Belle II



**I**N this chapter, the  $X(4014)$  resonance is simulated with EVTGEN [98] and reconstructed with a GEANT4-based [99] simulation of the Belle II detectors. The data is analyzed within the basf2 framework and its underlying ROOT externals. All plots and fits to the data are done in jupyter-notebooks, exploiting python3 libraries like pandas, RooFit and matplotlib.

## V.1 Introductory Remarks on the Reconstruction Strategy

**I**N preparation of the simulation, the work done by N. Zwahlen and T. Aushev on the search for the  $X(3872)$  resonance at Belle [100] has been studied. For this work, the authors studied the decay  $B \rightarrow X(3872)(DD^*)K$  by using both  $D^{*0}$  decays; to  $D^0\gamma$  and to  $D^0\pi^0$ . In their reconstruction they used photons with an energy greater than 30 MeV in the barrel and 50 MeV in the forward/backward part of the Belle electromagnetic calorimeter. Due to the limited data set of Belle ( $711 \text{ fb}^{-1}$ ) and the, compared to Belle II, worse photon reconstruction, this was necessary in order to see a peaking structure in the beam constraint mass, as well as the invariant mass spectrum<sup>1</sup>. For the final result, they fitted both spectra, once in the signal region and once for the sidebands. This two-dimensional fit lead to a significant signal strength of  $7.3 \sigma$  with  $22 \pm 7.6$  events in the peak. Since the width of the  $X(4014)$  was predicted to be larger than the one of its  $D^0D^{*0}$ -threshold partner state  $X(3872)$  [101], and the pole of the  $X(4014)$  resonance might be above or below the  $D^{*0}\bar{D}^{*0}$  threshold, we do not use the  $D^{*0} \rightarrow D^0\gamma$  channel. The reasons for this are explained in the next chapter.

<sup>1</sup>Crucial selection parameters for  $B$ -meson decays in  $B$ -factories. Explained in Sec. V.2.7

## V.2 Reconstruction on Signal Monte Carlo

THE data sets produced for simulated Monte Carlo (MC) samples for the signal simulation study have been produced and analyzed with the software version release-03-02-04 of the Belle II Analysis Framework. The simulated signal sample consists of  $10^5$  events of charged  $B$  meson pairs, where one meson decays to the  $X(4014)K^\pm$  signal channel, and the other one decays generically. This sample has been used to optimize the signal event reconstruction.

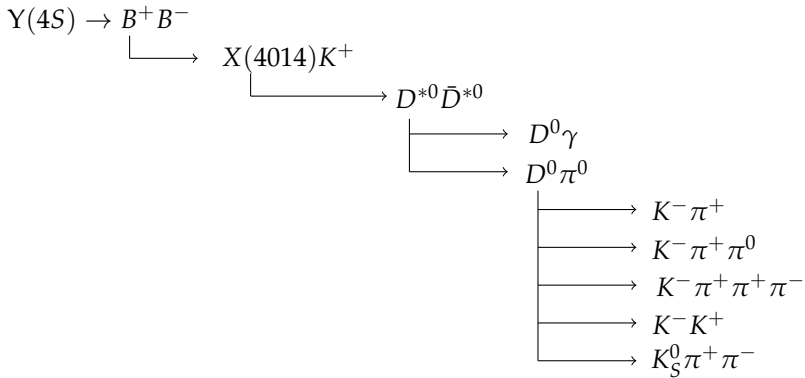


Figure V.1: Decay chain used for the above-threshold decay in charged  $B$  decays. The  $D^0$ -channels add up to 30% of the total branching fraction.

In the first attempt, the decay chain shown in V.1 is investigated. Both decays of the  $D^{*0}$ , to  $D^0\gamma$  and to  $D^0\pi^0$  final states, are exploited. For the reconstruction procedure a mass and vertex constraint fit on the  $D^0$ , as well as on the  $D^{*0}$  candidates is performed. Two of the  $D^{*0}$  candidates are then combined to form an  $X(4014)$ , which, together with a  $K^\pm$  allows to reconstruct the signal  $B^\pm$  meson candidate. To suppress a large amount of background contamination,  $B^\pm$  candidates are selected in the  $\Delta E - M_{bc}$  plane. The surviving  $B^\pm$  undergo a best candidate selection (BCS) which selects the best candidate per event. Fig. V.2 shows the final selection of candidates with a mass vertex constraint fit on both,  $D^0$  and  $D^{*0}$ , Fig. V.3 shows the reconstructed distribution without a mass vertex constrained fit to the  $D^{*0}$  candidates.

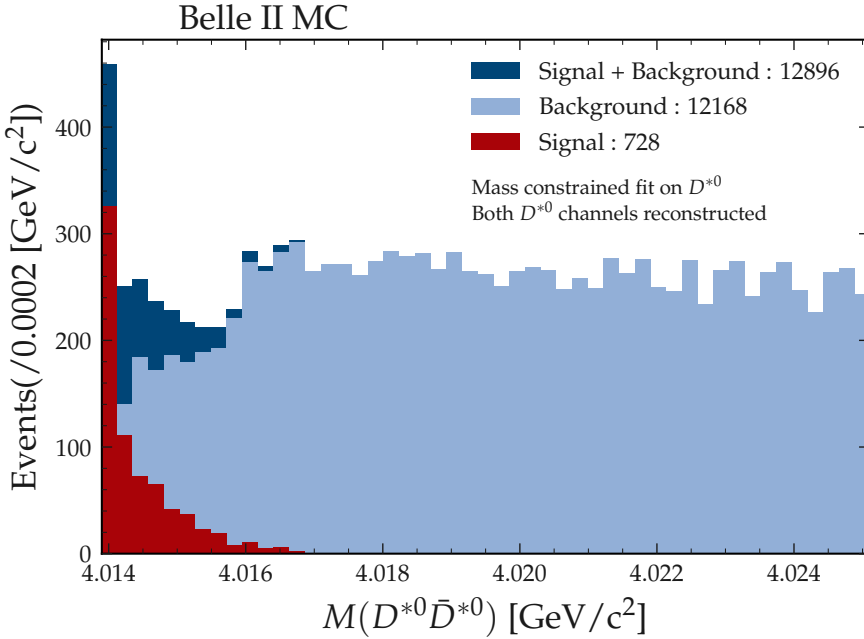


Figure V.2: Distribution of  $D^{*0}\bar{D}^{*0}$  invariant mass spectrum after final selection of  $B^{\pm}$  candidates. A mass vertex constraint fit on  $D^0$  and  $D^{*0}$  was applied.

As can be seen from the plot in Fig. V.2, the reconstruction with a mass vertex constrained fit on the  $D^{*0}$  candidates is not feasible for invariant masses below the  $D^{*0}\bar{D}^{*0}$  threshold. Due to the mass vertex constraint fit, all candidates in the  $D^{*0}$  list will be set to have the nominal PDG mass of  $2.007 \text{ GeV}/c^2$ , thus any value below  $4.014 \text{ GeV}/c^2$ , for the  $X(4014)$  invariant mass, is therefore not accessible. In case the  $X(4014)$  is a hadronic bound state with a mass pole slightly below the  $D^{*0}\bar{D}^{*0}$  threshold, the analysis strategy would be blind to an observation.

When applying the mass vertex constraint fit only to the  $D^0$ , but not to the  $D^{*0}$  candidates, the signal peak can not be distinguished from the combinatorial background and the reconstruction efficiency drops below 0.4 %, as can be seen in Fig. V.3. It is clear that also this strategy will not lead to

any meaningful result.

A new strategy, excluding the decay  $D^{*0} \rightarrow D^0\gamma$ , is depicted as decay chain in Fig. V.4. Here, the  $X(4014)$  is generated and reconstructed directly in  $D^0\bar{D}^0\pi^0\pi^0$  without reconstructing the intermediate  $D^{*0}$  resonances. The advantage, compared to the first decay chain above, is that the analysis gets sensitive to the  $X(4014)$ , also if the pole is situated below the  $D^{*0}\bar{D}^{*0}$  threshold. The performed simulation and the analysis on Belle data in chapter VI, are based on this decay chain!

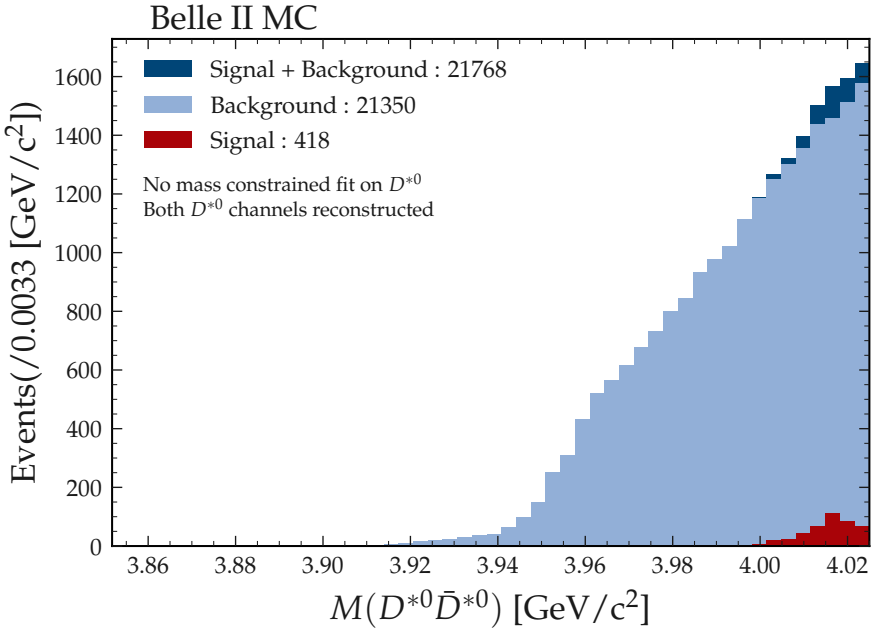


Figure V.3: Distribution without the a mass vertex constrained fit on the  $D^{*0}$  candidates.

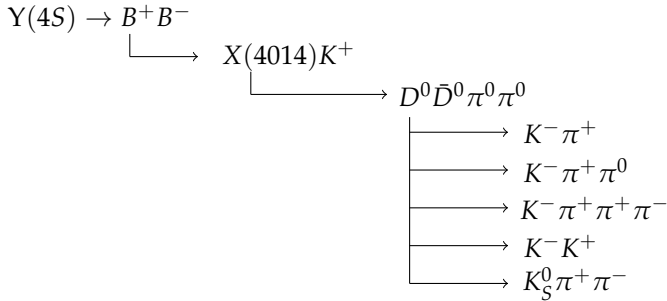


Figure V.4: Decay chain used for the below-threshold decay in charged  $B$  decays, leaving out the intermediate  $D^{*0}$  and its decay to  $D^0 \gamma$ .

### V.2.1 Impact of Beam Background Processes on the Reconstruction

**I**N Tab. III.1, the different background sources for luminosity-induced and beam-induced background processes are shown. To check whether the impact of those processes on the  $B^\pm$  reconstruction can be neglected or not, the MC sample was simulated with and without beam background. The individual steps of reconstruction are discussed in detail in the next sections. Here, a final selection of  $B^\pm$  candidates of the two MC samples is shown and the main source of beam background is evaluated.

In Fig. V.5, the amount of total reconstructed  $B^\pm$  candidates for MC samples with and without beam background is shown. It can be noticed that the number of total reconstructed candidates almost doubles in case of simulated beam backgrounds. The number of MCtruth-matched<sup>2</sup> candidates is with 5 % slightly higher in case of no simulated beam background. It is clear that a better reconstruction method is needed to suppress the huge amount of candidates stemming from beam backgrounds. To do so, the number of signal and background candidates on the decay channels of the  $X(4014)$  are evaluated individually - per reconstructed channel - as shown in Fig. V.6.

<sup>2</sup>Particles, which are correctly reconstructed, after simulating the interaction with the Belle II detector, according to the information provided at MC particle generation level.

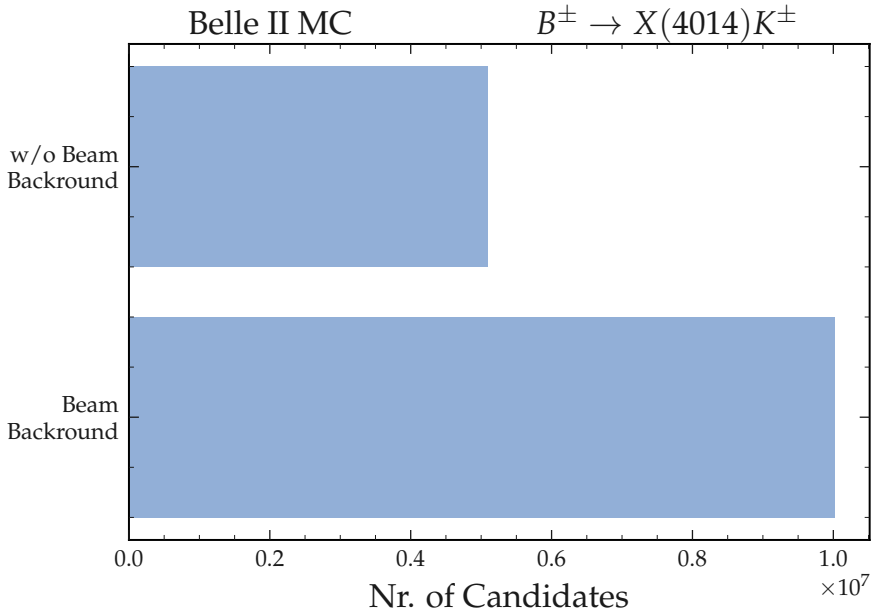


Figure V.5: Total number of reconstructed  $B^\pm$  candidates for the MC sample with (lower) and without beam background (upper) in a data set of  $10^6$  events.

The strongest growth, and by far dominating backgrounds, stem from channels where at least one of the  $D^0$  decays to the  $K^\pm \pi^\mp \pi^0$  final state. Thus the  $\pi^0$  reconstruction and background suppression for beam background  $\pi^0$  is crucial. The second strongest gain is coming from the  $K^\pm \pi^\mp \pi^\pm \pi^\mp$  final state due to the large combinatorics. In the following sections the method to suppress the relevant beam backgrounds for  $\pi^0$ ,  $D^0$  and  $X(4014)$  is explained.



should originate within  $|dz| < 3 \text{ cm}^3$  from the Interaction Point (IP) and satisfy an impact parameter<sup>4</sup> of  $|d0| < 0.5 \text{ cm}$  (Fig V.7). Rectifying plots are shown in Fig. V.8. Using tighter cuts on the particleID decreases the overall reconstruction efficiency of the X(4014) significantly. Most of the background is later discarded by selecting the best candidate. The gain in purity by introducing a higher value for the particle-ID is negligible compared to the loss in reconstruction efficiency. Photons are selected to meet the standard Belle II efficiency 50 % photon list:

- CDC acceptance :  $0.296706 < \theta < 2.61799$ ,
- forward ECL :  $E > 50 \text{ MeV}$  **or** barrel ECL :  $E > 30 \text{ MeV}$  **or** backward ECL :  $E > 50 \text{ MeV}$ ,
- $clusterE1E9^5 > 0.3$  **or**  $E > 100 \text{ MeV}$ , and
- $|clusterTiming| < clusterTimingError$  **or**  $E > 100 \text{ MeV}$

The common value used in many other analysis, to suppress large parts of the beam background, is 100 MeV. Since the mass of the X(4014) is expected to be very close to, or exactly at, the  $D^{*0}\bar{D}^{*0}$  threshold, the free energy in the decay is around

$$Q = M(X(4014)) - 2 \cdot M(D^0) - 2 \cdot M(\pi^0) = 18 \text{ MeV}$$

only - an average of 4.25 MeV per daughter. In this case, the  $\pi^0$  from the X(4014) decay can be expected to have almost zero momentum leading to two very low energetic photons in the decay.

---

<sup>3</sup>z: distance in beam direction

<sup>4</sup>Distance to the point of closest approach in  $r - \phi$  plane with respect to the vertex

<sup>5</sup>Central crystal and surrounding  $9 \times 9$  matrix Energy

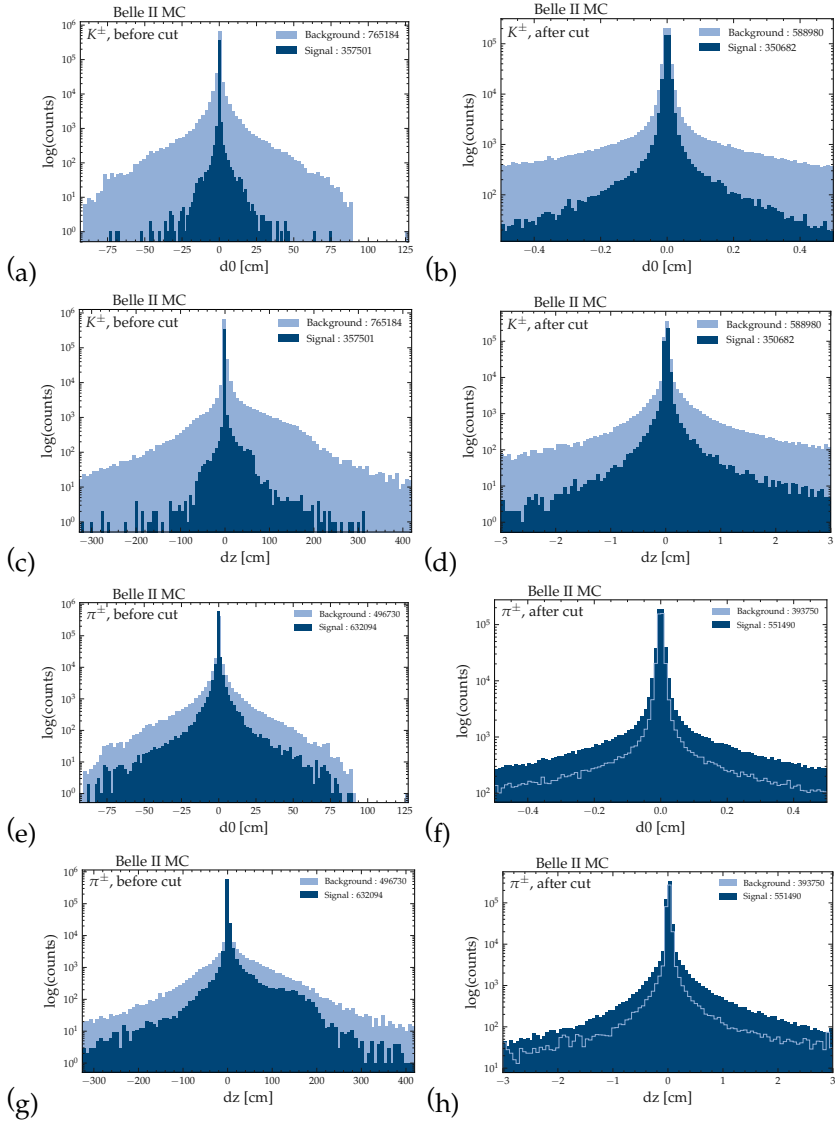


Figure V.8: Distance from IP in z-direction ( $dz$ ) and impact parameter ( $d0$ ) distributions of  $K^\pm$  and  $\pi^\pm$  for signal (dark blue) and background (light blue), before and after the selection.

### V.2.3 $\pi^0$ Reconstruction

NEUTRAL pions mainly decay to two photon final states with a branching fraction (Br) larger than  $Br > 98\%$  [102]. In Tab. III.1, the different processes dominating the Belle II beam background were shown. Due to these processes, it is expected (and was shown in Fig. V.6) to see large combinatorial backgrounds in the reconstruction of  $\pi^0 \rightarrow \gamma\gamma$ . In this section, the selections to increase the purity of the  $\pi^0$  samples are described. The photons which have passed the primary selection are combined to form  $\pi^0$  candidates. Due to the loose selection, a large contamination from combinatorial background is observed and it is crucial to disentangle the origins of the  $\pi^0$ s.

- $\pi^0$  from wrong combinatorics,
- $\pi^0$  from the other  $B^\pm$  decay,
- $\pi^0$  from  $D^0$ , and
- $\pi^0$  from  $X(4014)$ .

This background is dominated by real neutral pions not originating from the signal decay, except for fake candidates which are produced due to random photon combinatorics passing all the  $\pi^0$  reconstruction selections. The information regarding the identity of the generated mother particle can be retrieved in the simulation and then be used to construct a dedicated background suppression strategy for  $\pi^0$  from wrong combinatorics.

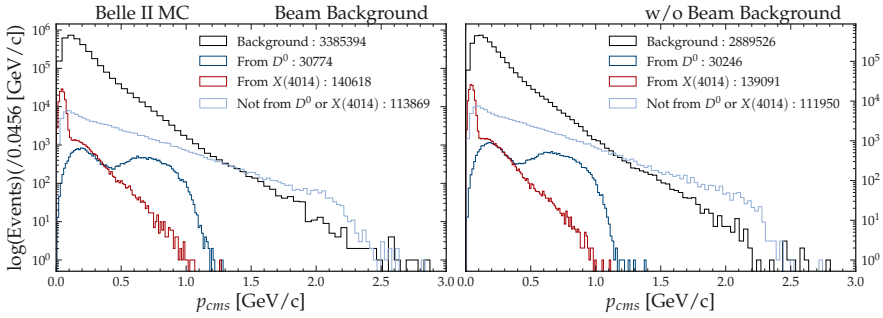


Figure V.9: Left:  $\pi^0$  momentum in CMS for a signal MC sample including beam background. Right: A signal MC sample without beam background.

In Fig. V.9, the momentum in the  $\pi^0$  center of mass frame (CMS) ( $p_{\pi^0}^{cms}$ ) is shown for the different sources listed above. On the left of Fig. V.9,  $p_{\pi^0}^{cms}$  is shown for an MC sample including beam background, on the right without simulated beam background.

Fig. V.9 shows a peaking structure for  $\pi^0$  from  $X(4014)$  in the low momentum,  $p_{\pi^0}^{cms} < 0.11$  GeV/c, region, while  $\pi^0$  stemming from  $D^0$  have higher momenta in CMS. This separation on  $p_{\pi^0}^{cms}$  is used to disentangle  $\pi^0$  candidates from  $D^0$  ( $p_{\pi^0}^{cms} > 0.11$  GeV/c) and  $X(4014)$  ( $p_{\pi^0}^{cms} < 0.11$  GeV/c).

To have a better signal to background discrimination, the decay

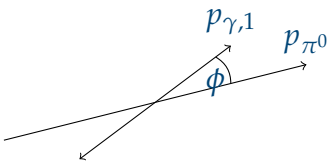


Figure V.10: Decay angle  $\phi$  in the mother's rest frame.

kinematics of the  $\pi^0$  decay are evaluated. In a 2-body decay, the decay products are emitted back to back, i.e.  $180^\circ$ , in the rest frame of the mother particle. If the mother particle is unpolarized, i.e.  $spin = 0$ , like the  $\pi^0$ , the decay axes in the mother's rest frame, with respect to the mother's momentum vector, is distributed isotropically Fig. V.10. As can be seen in Fig. V.12, the decay angle  $\phi$  is isotropically distributed for MCtruth-matched  $\pi^0$  and has peaking structures at forward and backward angles

for  $\pi^0$  identified as a background  $\pi^0$  from wrong combinatorics.

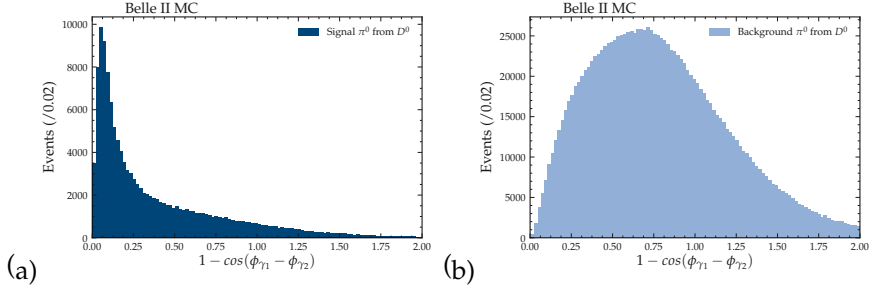


Figure V.11:  $1 - \cos(\phi_{\gamma_1} - \phi_{\gamma_2})$  distribution for signal (a) and background (b)  $\pi^0$  from  $D^0$ .

A better purity of the  $\pi^0$  sample is achieved by an online candidate selection (OCS), which runs during the event reconstruction on an event-by-event basis. For each candidate in the event,  $1 - \cos(\phi_{\gamma_1} - \phi_{\gamma_2})$  is calculated and  $\pi^0$ s are ordered in increasing value of this quantity Fig. V.11.

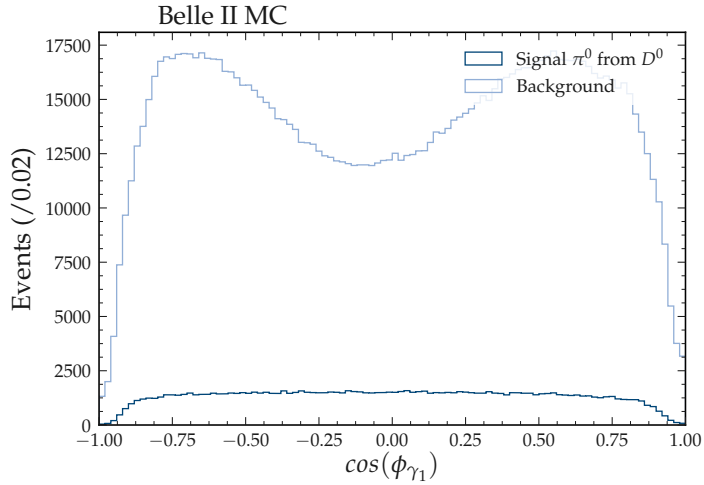


Figure V.12: Distribution of the decay angle  $\phi$  of the first photon in the decays of  $\pi^0$  stemming from  $D^0$ .

In Fig. V.13, the signal and background candidates as well as the  $S/\sqrt{S+B}$  ratio (all normalized to one) is shown in dependence of  $\chi_{rank}^2$ . This value indicates the ranking position of a particle inside one event in dependence of  $1 - \cos(\phi_{\gamma_1} - \phi_{\gamma_2})$ , the selection criteria shown in Fig. V.11. The larger  $1 - \cos(\phi_{\gamma_1} - \phi_{\gamma_2})$  is, the more likely the candidate is a background candidate and thus will have a higher ranking in  $\chi_{rank}^2$ . The best 15 candidates per event are kept, which results in keeping 90 % of the signal events and rejecting  $\approx 35$  % of the background.

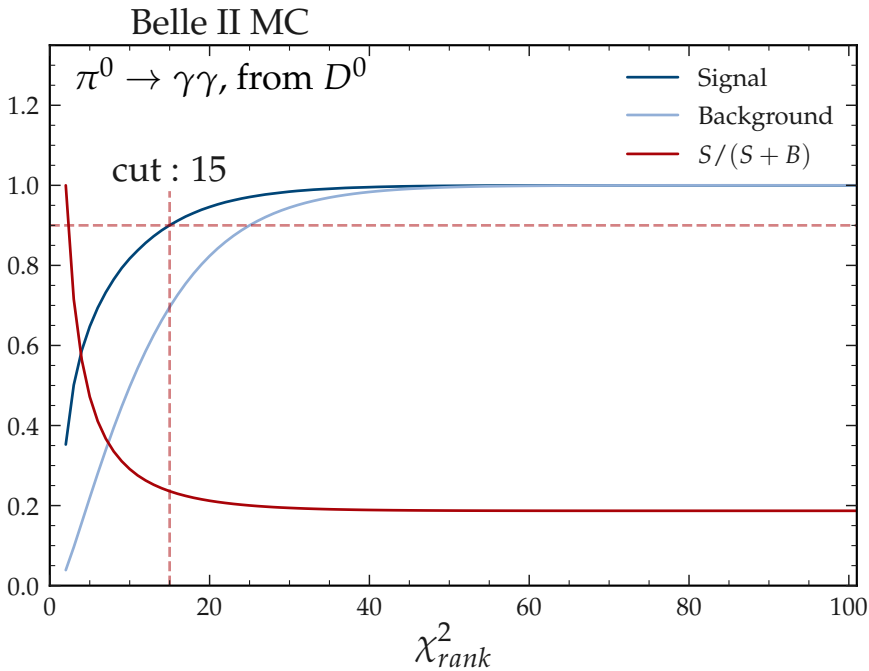


Figure V.13: Selection cut on the number of  $\pi^0$  candidates kept per event. The y-axis is normalized to one.

For  $\pi^0$ s originating from  $D^0$  mesons, a mass distribution as shown in Fig. V.14 is obtained. The signal is fitted with the sum of a Crystal Ball shape function and a Gaussian function. For the background a first order polynomial is used.

$\pi^0$ s originating from  $X(4014)$  are, in addition to the  $p_{\pi^0}^{cms}$  selection from Fig. V.9, reconstructed with a photon energy of less than 0.12 GeV. Like in the previous discussed reconstruction of  $\pi^0$  originating from  $D^0$ , an online candidate selection during reconstruction is applied. The distribution of the decay angle  $\phi$  in the case of a low momentum  $\pi^0$  from the  $X(4014)$  is shown in Fig. V.15.

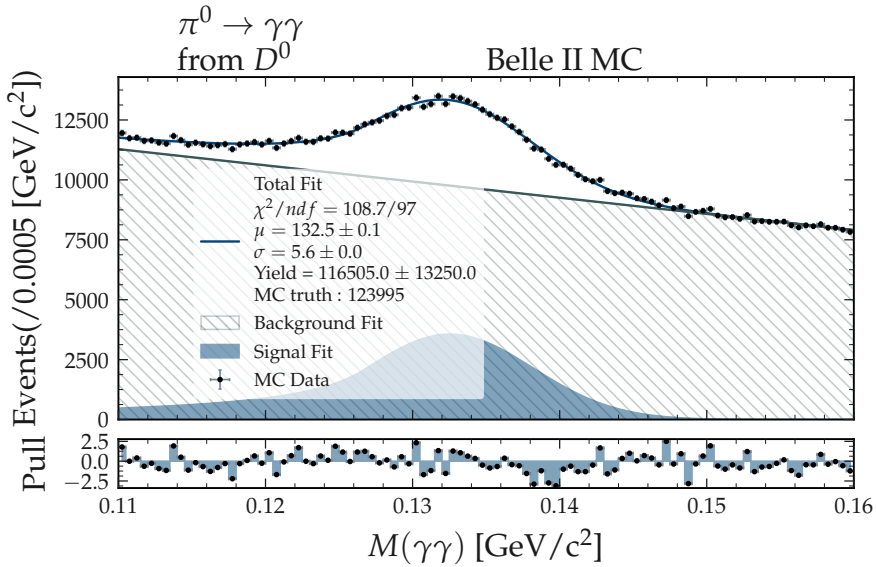


Figure V.14: Invariant mass of  $\pi^0$ s stemming from  $D^0$ s. The dashed area shows the background fitted with a first-order polynomial. For the signal fit (blue area) a Crystal Ball and a Gaussian is used. The total fit is shown as blue line.

Since in that case the photons have a rather low energy, the combinatorial background is peaking in the center. For signal candidates the angle is still distributed rather isotropically.

For the online candidate selection, the sum of the decay angles  $\phi$ , of both photons, and the center of mass momentum of the neutral pion is used. Candidates in the same event are ranked ( $\chi_{rank}^2$ ) according to their increasing value in this summed up quantity and the best 11 are kept. In Fig. V.16 the impact of the online selection on the reconstruction efficiency and back-

ground rejection is shown. It can be observed, that a selection of 11  $\pi^0$  candidates per event keeps 90 % of the signal events and suppresses  $\approx 35$  % of the background. Due to the loose selection of the photons, the reconstructed mass distribution becomes broad. Fig. V.17 shows the invariant mass distribution of the  $\pi^0$  candidates surviving the selection discussed above. The signal is fitted with the sum of a Crystal Ball shaped function and a Gaussian function while the background is modeled by a first order polynomial.

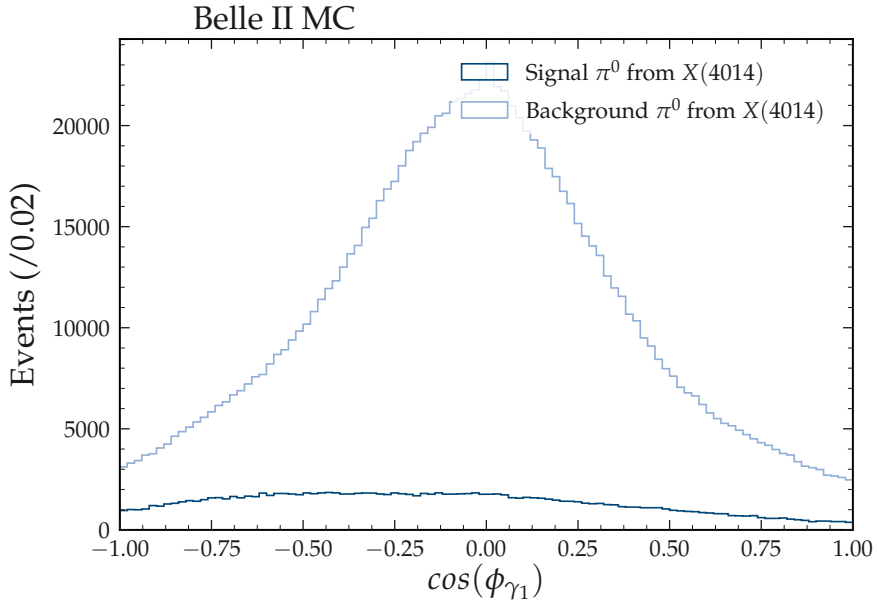


Figure V.15: Decay angle  $\phi$  of the first photon in the mother-particles rest frame for signal candidates in dark-blue and background candidates in light-blue.

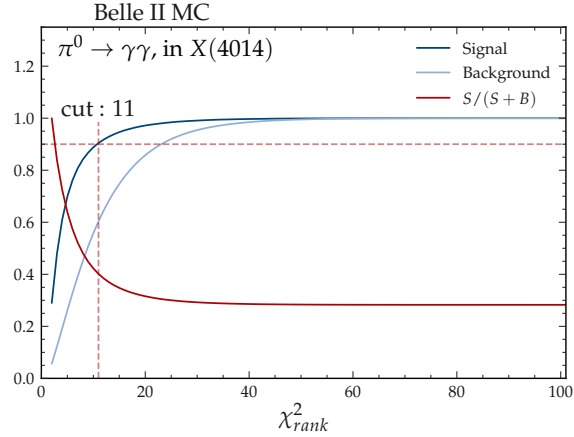


Figure V.16: Candidate selection of the  $\pi^0$  stemming from  $X(4014)$ . The y-axis is normalized to one.

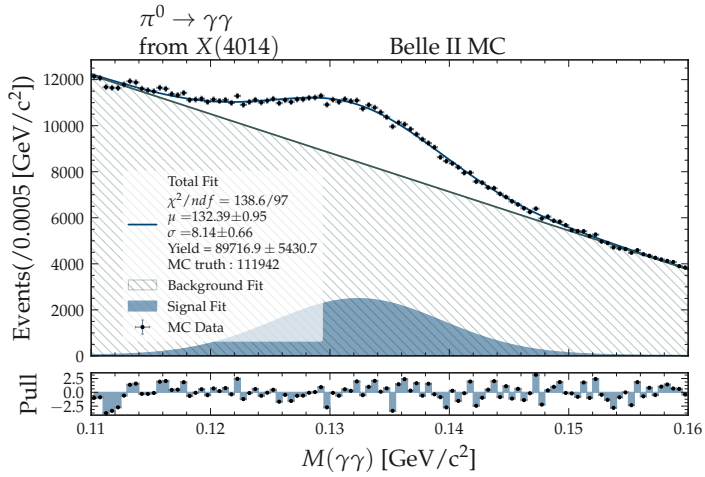


Figure V.17: Fit to the invariant mass distribution of  $\pi^0$  originating from  $X(4014)$ . The dashed area shows the background events which are fitted by a first order polynomial. The blue area shows the signal candidates fitted by the sum of a Crystal Ball shaped function and a Gaussian. The total fit is indicated as dark-blue line.

## V.2.4 $K_S^0$ Reconstruction

THE reconstruction of  $K_S^0$  is done by selecting only two tracks identified as oppositely charged pions with an invariant mass window of 0.45 GeV/c<sup>2</sup> to 0.55 GeV /c<sup>2</sup>. In addition, an algorithm already used for the Belle analysis framework is exploited. It combines different selection criteria which are shown below and compiles them to a binary variable, *goodBelleKshort*, for selection.

- $d\phi = \arccos\left(\frac{(dx \cdot px) + (dy \cdot py)}{dr \cdot \sqrt{px^2 + py^2}}\right)$ , with  $dx, dy, dr$  being the distance to the IP in  $x, y, r$  respectively
- $d\rho = \min(\text{abs}(d0_{\pi^+}), \text{abs}(d0_{\pi^-}))$ , with  $d0$  the impact parameter explained in V.7
- $dz_{\pi^+ - \pi^-} = dz_{\pi^+} - dz_{\pi^-}$ , with  $dz_{\pi^\pm}$  the distance in z-direction from the fitted track to the IP
- $p$ , the magnitude of the  $K_S^0$  4-momentum

The parameters explained above are sorted in three categories (*low, mid, high*):

- *low* :  $p < 0.5$  and  $\text{abs}(dz_{\pi^+ - \pi^-}) < 0.8$  and  $d\rho > 0.05$  and  $d\phi < 0.3$
- *mid* :  $p < 1.5$  and  $p > 0.5$  and  $\text{abs}(dz_{\pi^+ - \pi^-}) < 1.8$  and  $d\rho > 0.03$  and  $d\phi < 0.1$  and  $dr > 0.08$
- *high* :  $p > 1.5$  and  $\text{abs}(dz_{\pi^+ - \pi^-}) < 2.4$  and  $d\rho > 0.02$  and  $d\phi < 0.03$  and  $dr > 0.22$

A candidate satisfying one of those categories is flagged with *goodBelleKshort* == 1, the rest with 0. In Fig. V.18, the  $K_S^0$  invariant mass is plotted before and after the selection. A background reduction of 99% is reached while 88% of the signal candidates are kept.

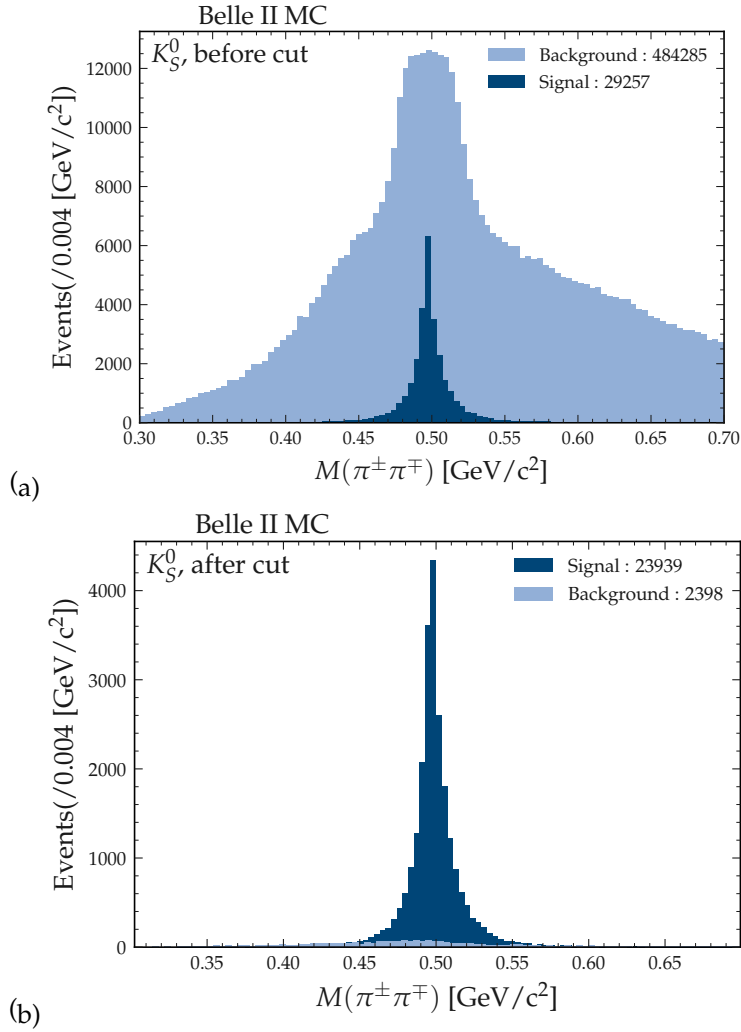


Figure V.18:  $K_S^0$  candidates before (a) and after (b) the selection with *goodBelleKshort*.

A mass-constrained vertex fit is applied to the candidates which are further used to reconstruct the  $D^0$  in the  $K_S^0\pi^\pm\pi^\mp$  channel.

### V.2.5 $D^0$ Reconstruction

NEUTRAL  $D$  mesons are reconstructed in the decay channels listed in Fig. V.4. The reconstructed  $D^0$  candidates are required to have an invariant mass within  $1.7 < M < 2.1$  GeV/ $c^2$ . This mass window also includes a larger sideband area to find the optimal region to fit the  $D^0$  mass distributions. In case of the  $D^0 \rightarrow K^\pm \pi^\mp \pi^0$  and  $D^0 \rightarrow K^\pm \pi^\mp \pi^\pm \pi^\mp$  channels, an online candidate selection is used to reduce the combinatorial background. Due to the contamination from the beam-induced background processes producing photons, the number of multiple candidates in the  $D^0 \rightarrow K^\pm \pi^\mp \pi^0$  is strongly increasing since random photons can be picked up to form a  $\pi^0$  (combinatorial background, see Sec. V.2.3). In case of the  $D^0 \rightarrow K^\pm \pi^\mp \pi^\pm \pi^\mp$  the effect is mitigated but still not negligible as for the other decay channels. In both cases the particle likelihoods of  $K^\pm$  and  $\pi^\pm$ , as well as the absolute value of the impact parameter,  $|d0|$ , and the longitudinal distance from the IP along the beam,  $|dz|$ , are taken into account. For the  $D^0 \rightarrow K^\pm \pi^\mp \pi^0$  channel, in addition, a selection on the  $\pi^0$  invariant mass is used.

The formulas to calculate the ranking parameter ( $\chi_{rank}^2$ ) for a reconstructed candidate according to the above defined online selection are shown below:

- $K^\pm \pi^\mp \pi^\pm \pi^\mp$  decay :  $\chi_{rank}^2 = \chi_{base} = \Sigma|d0|_{K,\pi} + \Sigma|dz|_{K,\pi} + \Sigma pID_{K,\pi}$
- $K^\pm \pi^\mp \pi^0$  decay :  $\chi_{rank}^2 = \chi_{base} + \left( \frac{M_{\pi^0} - M_{\pi^0}^{pdg}}{\sigma_{\pi^0}^2} \right)^2$

The last term of the first equation above is summing over all *kaonID* and *pionID* indicated as  $pID_{K,\pi}$ . In both cases, particles in one event are ordered in ascending  $\chi_{rank}^2$ -value. The result is shown in Fig. V.19 where the number of signal and background events, as well as the ratio  $S/(S+B)$ , is plotted against the  $\chi_{rank}^2$ -value ordering.

The  $\chi_{rank}^2$ -value that minimizes the background and maximizes the signal, is situated at the turn-around-point of the red function, or, in other words, at the maximum distance between the signal and background curve. The best purity of the final  $X(4014)$  sample can be achieved by selecting candidates with a ranking value smaller or equal than the above defined optimal one.

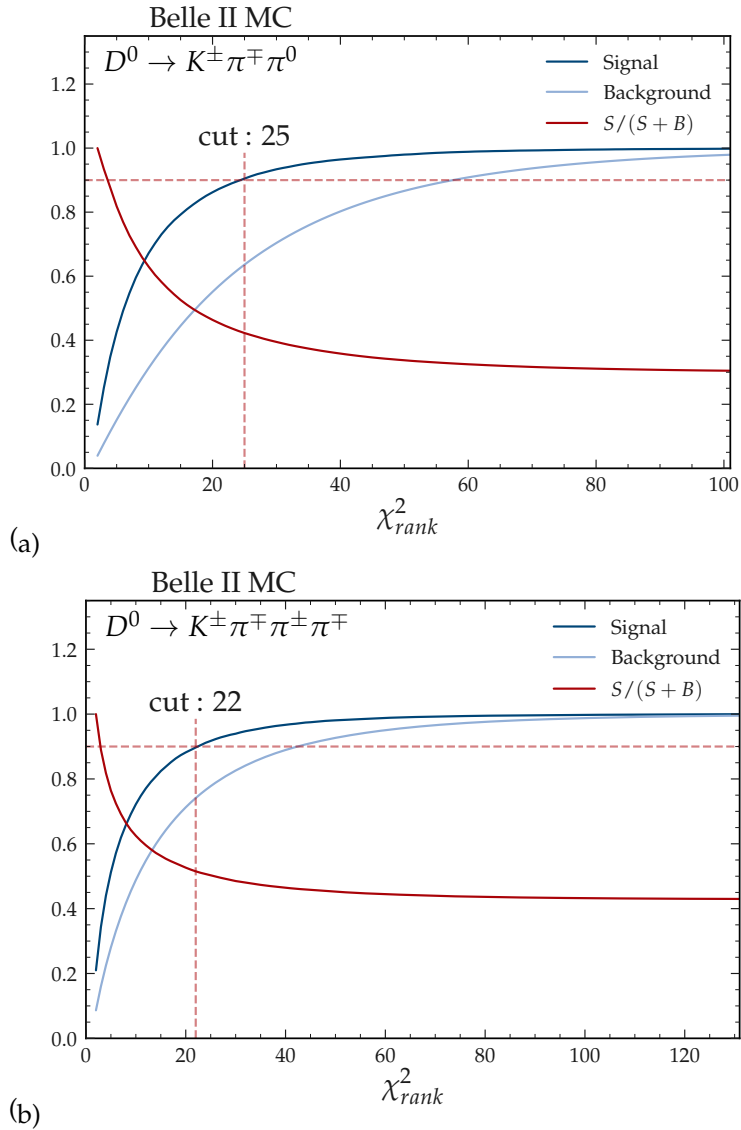


Figure V.19: Selection of candidates based on the  $\chi$ -value for  $D^0 \rightarrow K^\pm \pi^\mp \pi^0$  (a) and  $D^0 \rightarrow K^\pm \pi^\mp \pi^\pm \pi^\mp$  (b).

Since the reconstruction efficiency in that case lowers to 0.6%, and the expected maximal branching fraction of  $10^{-4}$  is very low, the selection is done with a  $\chi$ -value of 25, in case of  $D^0 \rightarrow K^\pm \pi^\mp \pi^0$  and 22 in case of  $D^0 \rightarrow K^\pm \pi^\mp \pi^\pm \pi^\mp$ . Those values are determined by keeping 90% of the signal  $D^0$ , which levels the  $X(4014)$  reconstruction efficiency at around 1%.

For the other decay channels,  $K^\pm \pi^\mp$ ,  $K_S^0 \pi^\pm \pi^\mp$  and  $K^\pm K^\mp$ , this technique is not applied. In Fig. V.20 to V.22, the fitted invariant mass spectra for all  $D^0$  channels are shown. The blue area shows the signal part of the distribution while the dashed gray area shows the background. In dark-blue the total fit is shown. The fits to all  $D^0$  channels are performed with a first or second order Polynomial for the background and a sum of two Gaussian's or Crystal-Ball plus Gaussian<sup>6</sup> for the signal contribution. All fit parameters can be found in the attachments in Tab. VIII.5 to VIII.13. The fitted widths and masses do all agree with the PDG values and the calculated signal yield contains the number of MCtruth-matched candidates within a  $3\sigma$  region. For further reconstruction, the  $D^0$  candidates are selected within a  $3\sigma$  region around the mean. Below, a table comparing some relevant numbers is shown. The mean and width of the distribution is calculated via

$$\mu = \sqrt{f_{G1} \cdot \mu_{G1}^2 + (1 - f_{G1}) \cdot \mu_{G2}^2}$$

and

$$\sigma = \sqrt{f_{G1} \cdot \sigma_{G1}^2 + (1 - f_{G1}) \cdot \sigma_{G2}^2}$$

with  $f_{G1}$  being the fraction of candidates fitted to the first Gaussian, the sum of Gaussians is normalized to one. Tab. V.1 lists the most important parameters for  $D^0$  reconstruction. The efficiencies  $\eta_{reco}$  and  $\eta_{sel}$  are defined as:

$$\eta_{reco} = \frac{MCtruth}{Generated} \quad \text{and} \quad \eta_{sel} = \frac{MCtruth}{Reconstructed}$$

---

<sup>6</sup> $D^0 \rightarrow K^\pm \pi^\mp \pi^0$  channel

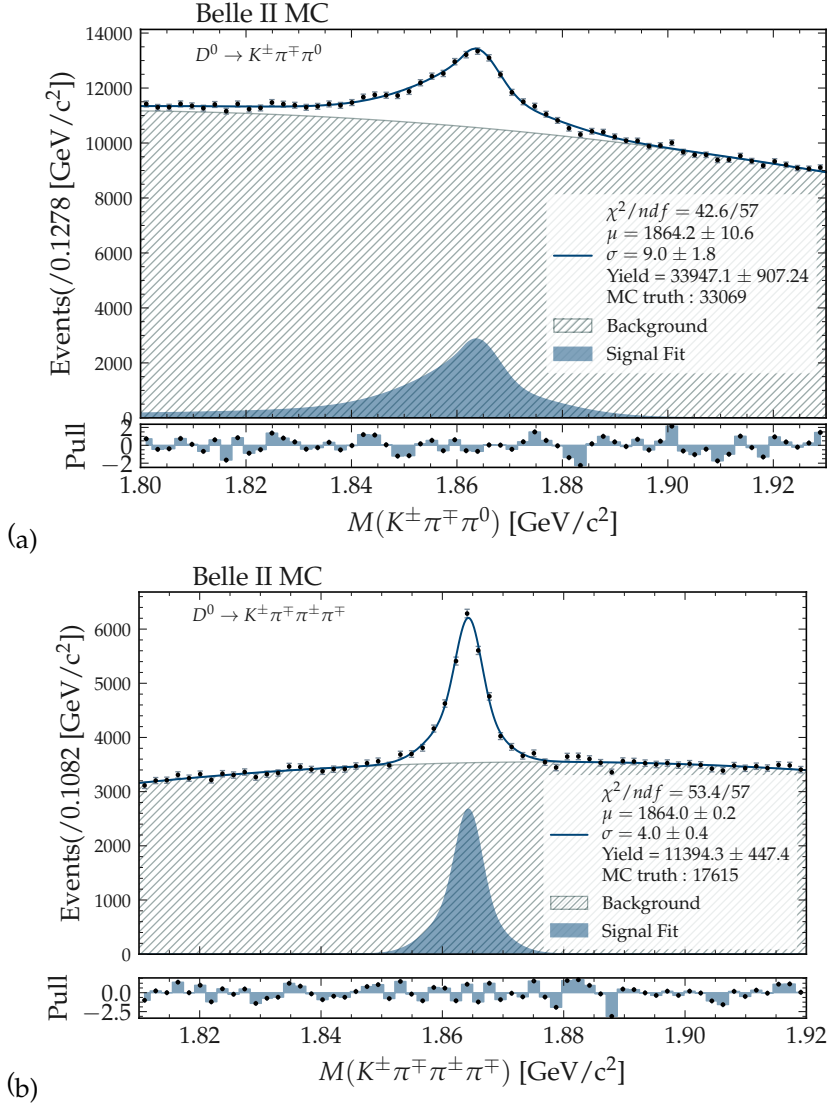


Figure V.20: Fit to the  $D^0$  invariant mass spectra for the  $K^\pm \pi^\mp \pi^0$  decay (a) and the  $K^\pm \pi^\mp \pi^\pm \pi^\mp$  decay (b).

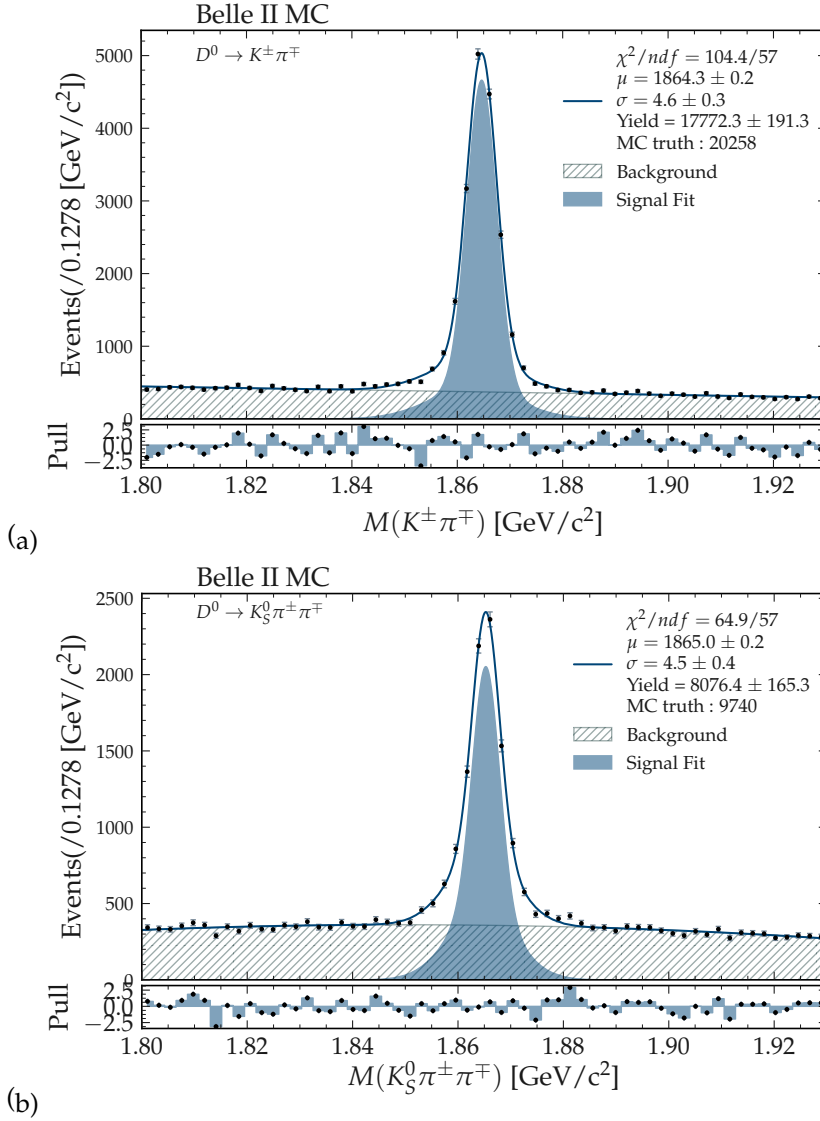


Figure V.21: Fit to the  $D^0$  invariant mass spectra for the  $K^\pm \pi^\mp$  decay (a) and the  $K_S^0 \pi^\pm \pi^\mp$  decay (b).

$D^0 \rightarrow$	$K^\pm \pi^\mp$	$K^\pm \pi^\mp \pi^0$	$K \pi^\mp \pi^\pm \pi^\mp$	$K_S^0 \pi^\pm \pi^\mp$	$K^\pm K^\mp$
Fitted-Yield	17776	33947	11394	8076	15387
MCtruth	20258	33069	17615	9740	19050
Width [MeV]	4.6	9.0	4.0	4.5	3.8
Mass [MeV/ $c^2$ ]	1864.3	1864.2	1864.0	1865.0	1864.2
$\eta_{reco}$ [%]	60.3	27.4	25.5	30.0	57.2
$\eta_{sel}$ [%]	55.1	5.9	8.1	38.2	55.2

Table V.1: Table summarizing the fitted  $D^0$  parameters on signal MC.

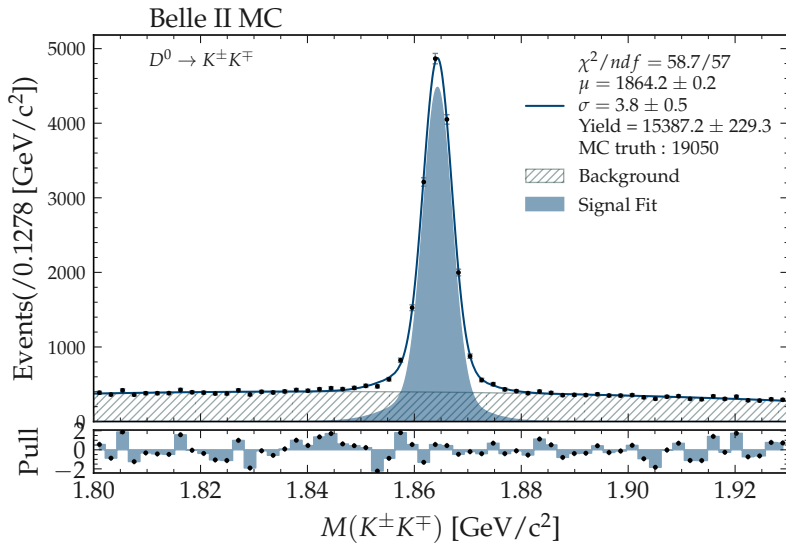


Figure V.22: Fit to the  $D^0$  invariant mass spectrum for the  $K^\pm K^\mp$  decay.

## V.2.6 $X(4014)$ Reconstruction

The  $X(4014)$  is reconstructed from two  $D^0$  and two  $\pi^0$  candidates. The latter are taken from a dedicated list for  $\pi^0$ s from the  $X(4014)$  decay. At this stage of the reconstruction, the combinatorics is already very high and leads to an average number of 9851  $X(4014)$  candidates per event. To reduce this

multiplicity the same technique as for the reduction of wrong combinatorics in the  $\pi^0$  and  $D^0$  lists is applied. In case of the  $X(4014)$ , the  $\chi^2$  calculation is performed as shown below.

$$\chi^2 = \left( \frac{\Delta M_{D_1^0}}{\sigma_{M_{D^0}}} \right)^2 + \left( \frac{\Delta M_{D_2^0}}{\sigma_{M_{D^0}}} \right)^2 + \left( \frac{\Delta M_{\pi_1^0}}{\sigma_{\pi^0}} \right)^2 + \left( \frac{\Delta M_{\pi_2^0}}{\sigma_{\pi^0}} \right)^2$$

For the width of the  $D^0$ ,  $\sigma_{D^0}$ , the average width from all channels weighted according to the number of MCtruth reconstructed candidates for that channel, 5.8 MeV is taken. The width of the  $\pi^0$  candidates,  $\sigma_{\pi^0} = 8.14$  MeV is shown in Fig. V.17. The  $\chi_{rank}^2$  distributions for the reconstructed  $X(4014)$  candidates are shown separately for background and signal in Fig. V.23. It can be noticed, that the signal candidates are distributed on the very left side towards smaller values of the  $\chi_{rank}^2$ -ranking parameter of the event, while background events show larger tails at higher values of the  $\chi_{rank}^2$  distribution.

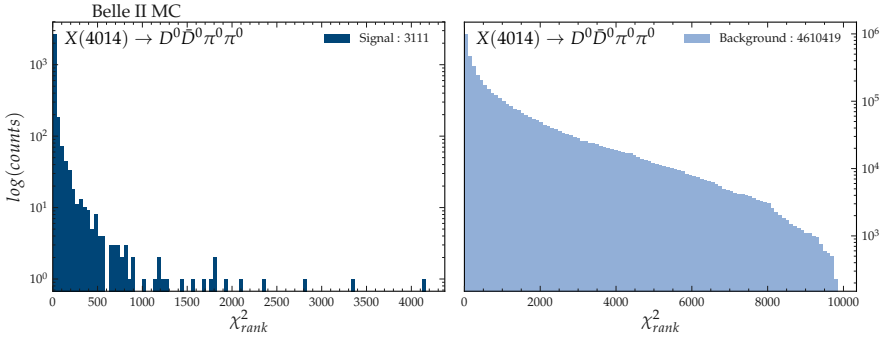


Figure V.23: Distribution of the  $\chi^2$ -ranking per event for signal candidates (left) and background candidates (right).

The separation power of the  $\chi_{rank}^2$  parameter is used to reject background and define a selection that returns 90 % of the signal efficiency, corresponding to 92 candidates of the OCS reconstructed  $X(4014)$

## V.2.7 $B^\pm$ Reconstruction

A mass-constrained vertex fit is applied to all  $D^0$  candidates before they are combined to a single particle list for further reconstruction. In each event, a pair of  $D^0$  candidates resulting from the mass-constrained fits is combined with two neutral pions to form an  $X(4014)$  candidate, which is required to come from a charged  $B$  meson decay. The  $B$  meson candidate is reconstructed from its decay to  $X(4014)$  and a charged kaon. To suppress the large contribution coming from the combinatorial background, further selections exploiting the kinematic variables typical for  $B$  meson reconstruction are devised. The impact of this suppression on the invariant mass spectrum of the  $X(4014)$  candidates is also studied.

For pre-selection, a mass window of  $3.9 < M < 4.1$  GeV/ $c^2$  for the  $X(4014)$  is applied and a beam constrained mass of  $M_{bc} > 5.2$  GeV/ $c^2$  for the  $B^\pm$  is requested. The beam(-energy) constrained mass is a quantity often used at  $B$ -factories to discriminate the on-resonant<sup>7</sup> produced  $B$ -Mesons from candidates which might be formed in continuum. Mathematically it is expressed as  $M_{bc} = \sqrt{(\frac{\sqrt{s}}{2})^2 - p_B^{*2}}$ .  $\frac{\sqrt{s}}{2}$  denotes the energy of the beam in the center of mass frame of the  $Y(4S)$  resonance and  $p_B^*$  the momentum of the  $B$  candidate in the  $Y(4S)$  CMS. Since the  $Y(4S)$  decays to the two-body  $B\bar{B}$  state, the expected value of  $M_{bc}$ , for correctly reconstructed  $B$  candidates, peaks around 5.28 GeV/ $c^2$  – the  $B$ -meson mass. Another important kinematic variable used for analysis at  $B$ -factories is the energy difference  $\Delta E = E_B - E_{beam}$ ,  $E_B$  denotes the  $B$ -candidates energy in CMS frame of the  $Y(4S)$ . In case of a correct reconstructed  $B$ -meson,  $\Delta E$  should peak around zero.

In the two dimensional  $\Delta E - M_{bc}$  space, the correctly reconstructed  $B$  candidates populate a small, very distinct area while most of the combinatorial background and events not coming from  $B$  meson decays are distributed over the whole plane. Fig. V.24 shows the distribution of the signal MC sample  $\Delta E - M_{bc}$  space divided in signal and background events. The signal area, in which a good signal retention efficiency and background suppression is achieved, is determined as  $\Delta E < 0.01$  GeV and  $M_{bc} > 5.272$  GeV/ $c^2$ .

---

<sup>7</sup>Candidates originating from the  $Y(4S)$  resonance.

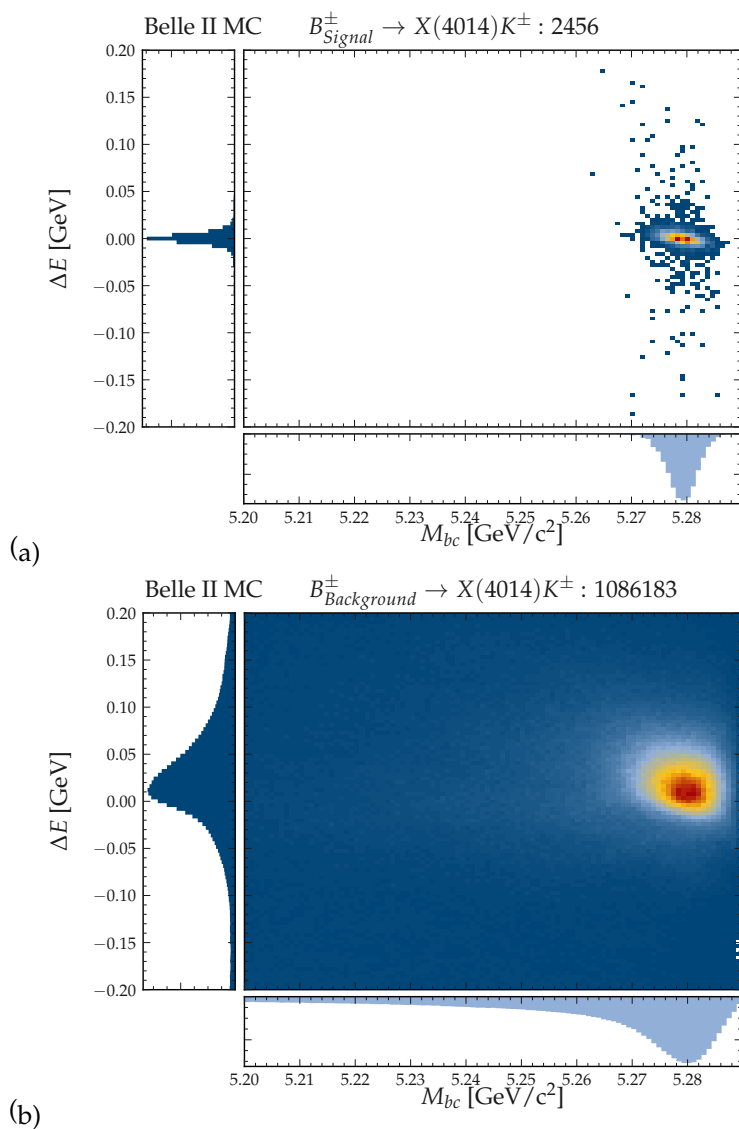


Figure V.24: Signal (a) and combinatorial background (b)  $B^{\pm}$  candidates before selection of the  $\Delta E - M_{bc}$  signal area.

### V.2.7.1 Best Candidate Selection

In Fig. V.25, the  $X(4014)$  candidates, as first daughter of the  $B^\pm$  list, which survive the selection, are shown for six different simulated widths. Due to the various combinatorics, an average multiplicity of 9.4 candidates per event is observed, thus, among those, a best candidate has to be selected.

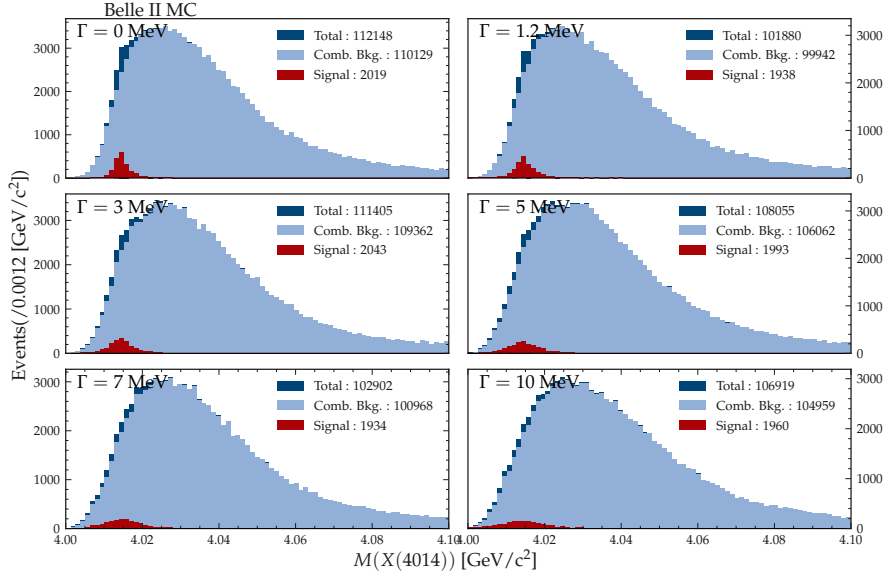


Figure V.25:  $X(4014)$  invariant mass distribution for six different simulated widths after selection of  $B^\pm$  candidates in  $\Delta E - M_{bc}$  space.

As there are multiple candidates per event, a best candidate selection (BCS) is applied, which enhances the signal to background ratio drastically and therefore leads to a much better differentiation between signal and background. For all  $B^\pm$  candidates in the  $\Delta E - M_{bc}$  signal region a  $\chi_{BCS}^2$  value according to the formula in Eq. V.1 is calculated. Only the candidate with the smallest  $\chi_{BCS}^2$  value per event is kept - all others are discarded. The first five, dominant terms of the BCS formula are taken from [103]. In addition, the selection includes terms for all Kaon and Pion particleIDs as well as their  $d0$  and  $dz$  resolutions in the decay chain.

$$\chi_{BCS}^2 = \left( \frac{\Delta M_{D_1^0}}{\sigma_{M_{D^0}}} \right)^2 + \left( \frac{\Delta M_{D_2^0}}{\sigma_{M_{D^0}}} \right)^2 + \left( \frac{\Delta E}{\sigma_{\Delta E}} \right)^2 + \left( \frac{\Delta M_{\pi^0}}{\sigma_{\pi^0}} \right)^2 + |d0_i| + |dz_i| + (1 - pID_i) \quad (1)$$

Eq. V.1: Formula of the best candidate selection to determine the best  $B^\pm$  candidate per event.

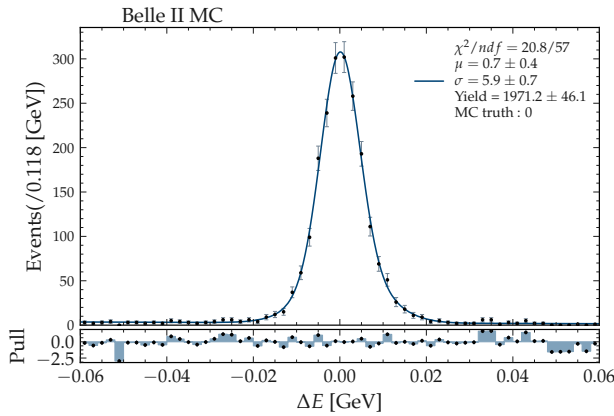


Figure V.26: Fitted  $\Delta E$  distribution of the MCtruth-matched  $B^\pm$  candidates for a simulated  $X(4014)$  width of 0 MeV. The Fit was performed with two Gaussians, parameters are listed in Tab. VIII.25.

The first two terms select  $D^0$  produced in the  $X(4014)$  decay and calculate their mass-difference to the PDG-mass in units of their reconstructed resolution. Since the  $D^0$  widths are varying over the different decay modes, the individual width for each mode, instead of the mode-average, is used. Candidates are further selected with the deviation of their  $\Delta E$  value from the resolution obtained from fitting the  $\Delta E$  distribution for MCtruth-matched candidates in the  $M_{BC} - \Delta E$  signal-window Fig. V.26.

The impact of the different simulated  $X(4014)$  widths is found to be negligible on the resolution of the  $\Delta E$  distribution. Therefore, the same value of the  $\Delta E$  resolution, fitted from the signal sample with a 0 MeV generated  $X(4014)$  width is used for all the BCS.

An additional term calculates the  $\pi^0$  mass difference of the intermediate  $D^{*0} \rightarrow D^0\pi^0$  decay, to its nominal value in units of the obtained  $\pi^0$  width shown in Fig. V.17. After applying the  $M_{bc} - \Delta E$  selection and finding the best candidate for each event, the invariant mass of the  $X(4014)$  candidates for all six simulated widths is plotted in Fig. V.27. An average signal reconstruction efficiency of around 1 % and a purity<sup>8</sup> around 9 % is achieved for the signal sample.

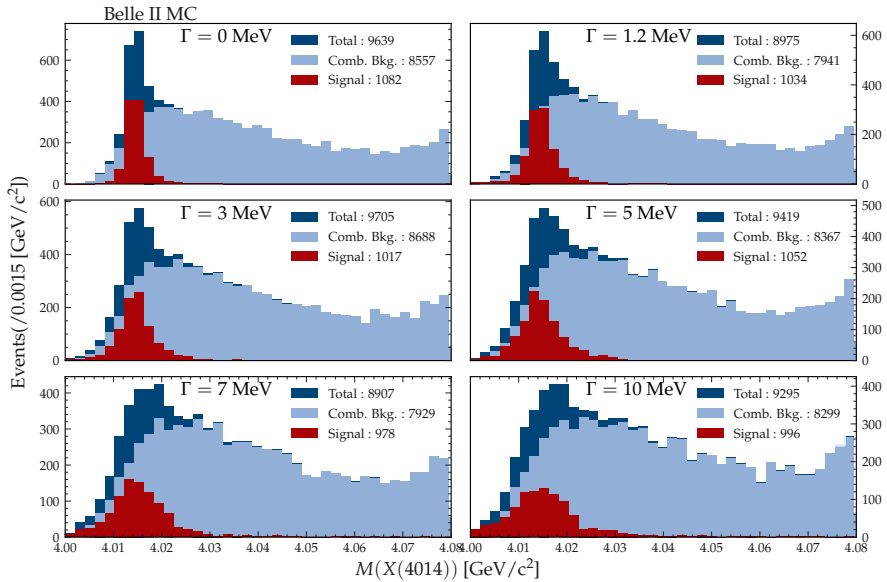


Figure V.27: Invariant mass of the  $X(4014)$  candidates after  $\Delta E - M_{bc}$  signal window selection and best candidate selection. Signal in red, combinatorial background in light blue and combined data in dark blue.

<sup>8</sup>MC-truth matched signal candidates after the final selection and BCS divided by the number of combinatorial background candidates surviving the final selection and BCS.

## V.2.8 Background Estimation

SO far only the beam background processes, as shown in Tab. III.1 and the combinatorial background contribution coming from the signal MC were included in the simulation. In the real physics experiment various other background sources will occur, which have to be taken into account as well – hereinafter referred to as generic background. In this section, those components are listed and scaled for different data sets in terms of integrated luminosity. The backgrounds simulated in this study are taken from the official Belle II MC 12 campaign, which include also the simulation of the beam-induced background conditions.

Generic backgrounds split up in: *charged*, *mixed*,  $c\bar{c}$ ,  $d\bar{d}$ ,  $u\bar{u}$ ,  $s\bar{s}$  and  $\tau\bar{\tau}$  and correspond to an integrated luminosity of  $\simeq 2 \text{ ab}^{-1}$  for the full MC12 campaign. The *charged* and *mixed* components originate from generic decays of charged and neutral  $B$  mesons, continuum hadronization process from  $e^+e^- \rightarrow q\bar{q}$  is contained in the  $c\bar{c}$ ,  $d\bar{d}$ ,  $u\bar{u}$  and  $s\bar{s}$  background components. The  $\tau\bar{\tau}$  component also arises from continuum  $e^+e^-$  annihilations. As working hypothesis to evaluate the expected signal yields, the signal branching fraction analyzed in the decay chain described in Fig. V.1 is estimated from the measured branching fraction for  $B^\pm \rightarrow X(3872)K^\pm$ ,  $X(3872) \rightarrow D^0\bar{D}^0\pi^0 = (1.0 \pm 0.4) \cdot 10^{-4}$  taken from the PDG [104]. For the complete MC12 generic background, a number of

$$N = \mathcal{L}_{int} \cdot 1.1 \text{ nb} \cdot 0.5 \cdot 0.5 \cdot 0.3 \cdot 10^4 \approx 16500$$

signal events was reconstructed for the full  $2 \text{ ab}^{-1}$  generic MC sample.

In the above formula  $1.1 \text{ nb}$  correspond to the cross section of  $Y(4S) \rightarrow B\bar{B}$ . Since only the charged  $B$  mesons are reconstructed, an additional factor of 0.5 was included to correct for the 50% of  $Y(4S)$  which decay to a neutral  $B$  meson pair. The decay table shown in V.4 is based on five  $D^0$  decays which add up to  $\approx 30\%$  of the total  $D^0$  decays. A factor of 0.3 is introduced to correct for the  $D^0$  decays missing in the reconstruction. The second factor of 0.5 corrects for the  $D^{*0} \rightarrow D^0\gamma$  decay, which is not taken into account for the reconstruction.

To have an estimate on the discovery potential, the simulation is performed for different scenarios of the resonant  $X(4014)$  manifestation and

three different simulated data sets of  $711 \text{ fb}^{-1}$  (the Belle data set),  $2 \text{ ab}^{-1}$  and  $14 \text{ ab}^{-1}$ . Due to the limited size of the generic MC12 sample, the  $14 \text{ ab}^{-1}$  data set was generated in RooFit as TOY-MC data modulated by the Probability Density Function (PDF) used to fit the  $2 \text{ ab}^{-1}$  generic background sample. Further explanations on that are discussed in Sec. V.4.3.

Since the actual width is not known, six different signal samples with varying input width of 0, 1.2<sup>9</sup>, 3, 5, 7 and 10 MeV are simulated. A plot showing the fitted width of the reconstructed  $X(4014)$  for each sample against its simulated width on the x-axis is shown in Fig. V.28.

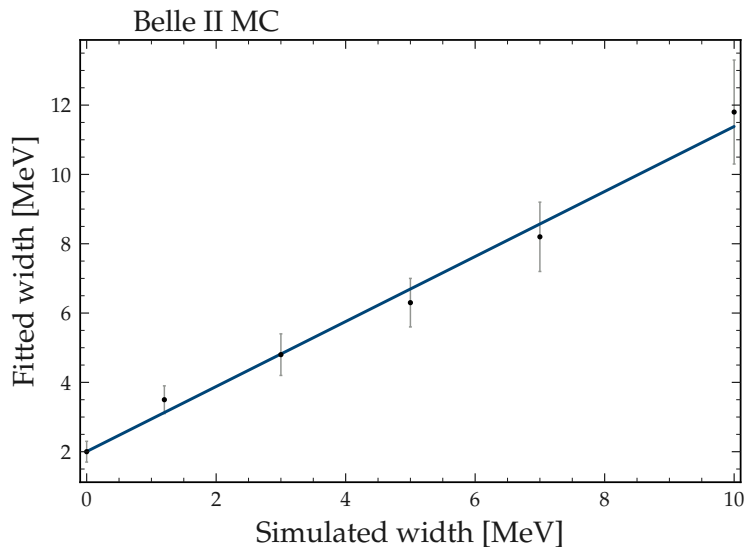


Figure V.28: Fitted width vs. simulated input width of the  $X(4014)$  resonance, fitted with a linear function.

The fits for obtaining the signal width are performed on the MCtruth-matched candidates only. A Breit Wigner convoluted with a Gaussian detector resolution function is used (Eq. V.2). Corresponding plots and fit parameters are shown in Fig. VIII.13 to VIII.18 and Tab. VIII.27 to VIII.32 in the appendix.

---

<sup>9</sup>Upper limit on the  $X(3872)$  width [105].

$$\begin{aligned}
 BW(M; \Gamma) &= \frac{1}{(M - M_0) - i\Gamma/2}, \quad G(M; \mu, \sigma) = \frac{1}{\sigma\sqrt{2\pi}} \cdot e^{-\frac{1}{2}\left(\frac{M-\mu}{\sigma}\right)^2} \\
 V(M; \sigma, \Gamma) &= BW(M; \Gamma) \otimes G(M; \mu, \sigma) \\
 &= \int_{-\infty}^{\infty} G(M'; \sigma) BW(M - M'; \Gamma) dM'
 \end{aligned}$$

Eq. V.2: A Breit-Wigner and a Gaussian function are convoluted to build the signal PDF.

The six different signal samples are then mixed with generic backgrounds corresponding to three different integrated luminosities of  $711 \text{ fb}^{-1}$  (the Belle data set),  $2 \text{ ab}^{-1}$  and  $14 \text{ ab}^{-1}$ . Ten different branching fractions of  $0.1 \cdot 10^{-4}$  to  $10^{-4}$  were considered and a signal sample matching the corresponding number of expected  $X(4014)$  resonances was reconstructed. In total the simulation was performed for 180 different scenarios<sup>10!</sup> The number of expected signal events  $N_i$  for a certain data set  $\mathcal{L}_i$  and branching fraction  $\mathcal{B}_i$  is shown in Tab. VIII.19 in the appendix.

### V.3 Impact of the Pixel Detector on the Analysis

**S**INCE a part of this thesis is dedicated to a new data output for the PXD and the Giessen group is heavily involved in the PXD collaboration, the impact of the PXD on the search for exotic resonances, specifically for the  $X(4014)$ , is discussed in this chapter. Since many of the exotic charmonium resonances are decaying to charmonium states like  $D^0$  or  $D^{*0}$ , which further decay to pions and kaons, the PXD and its vertexing abilities play a major role in the reconstruction efficiency and resolution of these states.

In this chapter, the analysis on the  $X(4014)$  signal sample featuring a simulated width of 0 MeV is performed again without the presence of the PXD in the Geant 4 simulation. This way a comparison between the reconstruction efficiency and resolution of the individual  $D^0$  decay channels, as

---

<sup>10</sup>10 branching fractions  $\times$  6 widths  $\times$  3 data sets.

Chapter V. Simulation of a Resonant Structure at the  $D^{*0}\bar{D}^{*0}$  threshold in  $B$  decays at Belle II

well as the final reconstruction efficiency of the  $B^\pm$  mesons can be made.

$D^0 \rightarrow$	$K^\pm \pi^\mp$	$K^\pm \pi^\mp \pi^0$	$K \pi^\mp \pi^\pm \pi^\mp$	$K_S^0 \pi^\pm \pi^\mp$	$K^\pm K^\mp$
<b>without PXD</b>					
Fitted-Yield	17651	38122	11449	8611	15734
MCtruth	20131	33125	17688	9578	18871
Width [MeV]	4.5	13.1	4.8	5.8	4.5
Mass [MeV/ $c^2$ ]	1864.3	1863.3	1864.6	1865.1	1864.2
$\eta_{reco}$ [%]	59.2	26.4	24.8	29.5	56.0
$\eta_{sel}$ [%]	54.4	5.9	8.0	36.5	54.7
<b>with PXD</b>					
Fitted-Yield	17772	33947	11394	8076	15387
MCtruth	20258	33069	17615	9740	19050
Width [MeV]	4.6	9.0	4.0	4.5	3.8
Mass [MeV/ $c^2$ ]	1864.3	1864.2	1864.0	1865.0	1864.2
$\eta_{reco}$ [%]	60.3	27.4	25.5	30.0	57.2
$\eta_{sel}$ [%]	55.1	5.9	8.1	38.2	55.2
<b>Changes in %</b>					
Width	+2	-32	-17	-23	-16
$\eta_{reco}$	+0.9	+1	+0.7	+0.5	+1.2
$\eta_{sel}$	+0.6	-	+0.1	+1.7	+0.5

Table V.2: Table summarizing the  $D^0$  fit parameters on signal MC for a simulation without PXD (top), including PXD (middle) and the parameter changes in % (bottom). Positive changes are indicated in blue.

In Tab. V.2, the reconstruction efficiency ( $\eta_{reco}$ ), purity ( $\eta_{sel}$ ), mean mass values and width are shown for a  $X(4014)$  signal MC sample without (top) and with PXD (middle) in the simulation. The bottom part of the table shows the change in % in  $\eta_{reco}$ ,  $\eta_{sel}$  and the resolution of the individual  $D^0$  decay channels. Positive changes<sup>11</sup> are indicated in blue colors. Since the reconstruction of signal MC was performed with an earlier version of the Belle II analysis framework, release-03-02-04, the particle identification based on likelihood ratios for different particle hypothesis (*kaonID* and *pionID* variables) is not yet optimal and needs further improvement and a better calibration. For later releases, a higher efficiency and better resolution is expected, when including the PXD to the reconstruction. However, for the resolution of the  $D^0$  resonances, a significant decrease in almost all channels

<sup>11</sup>Decrease in width and increase in efficiency and purity.

can be observed. All corresponding plots and fit parameters can be found in Sec. VIII.1.2 of the appendix.

For the final reconstruction efficiency and purity of the  $B$  meson, an increase of  $\approx 10\%$ , when including the PXD, is achieved.

## V.4 Fitting Strategy

**I**N this section the fitting procedure for the  $X(4014)$  invariant mass fit is discussed. First, the different components contributing to the final invariant mass distribution after the BCS according to the simulation are shown and the PDFs to fit them are introduced. At the end of the section, the total PDF is described as composed by the combination of the individual components for signal, combinatorial background and generic background.

Before unblinding the final data samples for extracting the signal yields according to the fitting procedure discussed in this chapter, the two methods to compute the signal yield significance;

- Method 1 : Shape dependent model
- Method 2 : Shape independent - cut and count - model

are described and the underlying maximum log-likelihood mechanism is explained.

Before investigating the individual components, a combined picture of the invariant mass distribution is analyzed. As it can be noted from Fig. V.29, the signal contribution to the total invariant mass distribution of the reconstructed  $X(4014)$  is, due to the low reconstruction efficiency of around 1 % and total purity of

$$\eta_{sel,tot} = \frac{N_{sig}}{N_{sig} + N_{combBkg} + N_{genBkg}} \approx 0.5 \%$$

very small, a peak hunting would thus be diluted by the high background contribution.

To further reject the generic background, a final selection on the free energy of the  $X(4014)$  decay is applied.

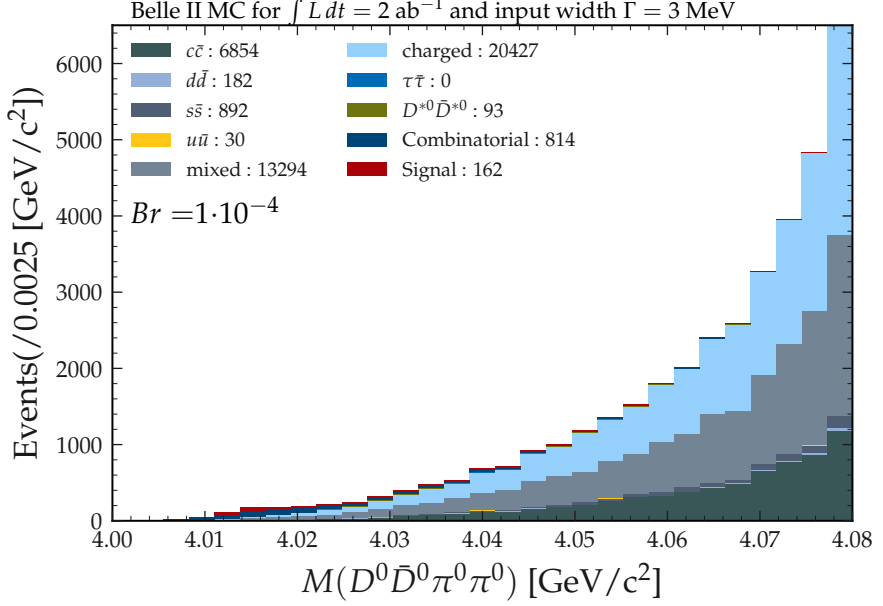


Figure V.29: Example distribution for an assumed width of  $\Gamma = 3$  MeV and a branching fraction of  $Br = 10^{-4}$  of the  $X(4014)$  invariant mass after BCS including all relevant signal and background components.

The resonant  $X(4014) \rightarrow D^0\bar{D}^0\pi^0\pi^0$  decay will generate, dependent on the actual pole of the potential  $X(4014)$ , a tight window for the energy left in the decay. For an assumed pole directly at the  $D^{*0}\bar{D}^{*0}$  threshold, the free energy is calculated as:

$$\begin{aligned}
 Q &= M(X(4014)) - M(D^0) - M(\bar{D}^0) - M(\pi^0) - M(\pi^0) \\
 &= 4014 \text{ MeV}/c^2 - 2 \cdot 1864.83 \text{ MeV}/c^2 - 2 \cdot 134.98 \text{ MeV}/c^2 \\
 &= 14.38 \text{ MeV}/c^2
 \end{aligned}$$

Since the free energy  $Q$  is directly correlated with the quantity under investigation, i.e. the fitted mass  $M(X(4014))$ , a tight selection on that value

can bias the final data set. In order to prevent that, a larger phase space window of  $Q < 40 \text{ MeV}/c^2$  is applied. As can be seen from Fig. V.30, the number of generic background events decreases drastically from 23945 with  $Q < 100 \text{ MeV}$  to 4068 with  $Q < 40 \text{ MeV}$ . A selection, accepting only events with  $Q < 40 \text{ MeV}$  will therefore purify the sample. In appendix, Fig. VIII.20, an example plot for the  $X(4014)$  invariant mass (including all components), assuming a width of 3 MeV and the 10 different branching fractions taken into account, is shown.

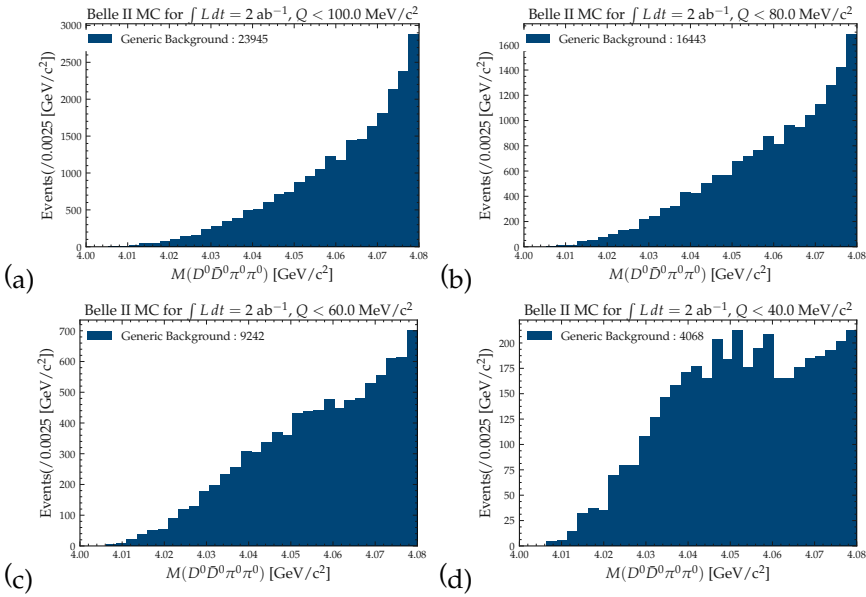


Figure V.30: Generic background contribution to the total  $M(X(4014))$  invariant mass spectrum. (a) with  $Q < 100 \text{ MeV}$ , (b)  $Q < 80 \text{ MeV}$ , (c)  $Q < 60 \text{ MeV}$  and (d)  $Q < 40 \text{ MeV}$  - the final selection value.

### V.4.1 Signal

As discussed in the last chapter, the signal component is fitted with a Breit-Wigner convoluted with a Gaussian. In Fig. V.31, the fitted distribution for the final  $X(4014)$  selection, corresponding to the  $14 \text{ ab}^{-1}$  data set, with a simulated width of 3 MeV is shown. For the scenarios with other simulated width, the plots are shown in appendix VIII.1.3.3 (Fig. VIII.13 to VIII.18). The fits are applied to the simulated samples equivalent to  $14 \text{ ab}^{-1}$  integrated luminosity.

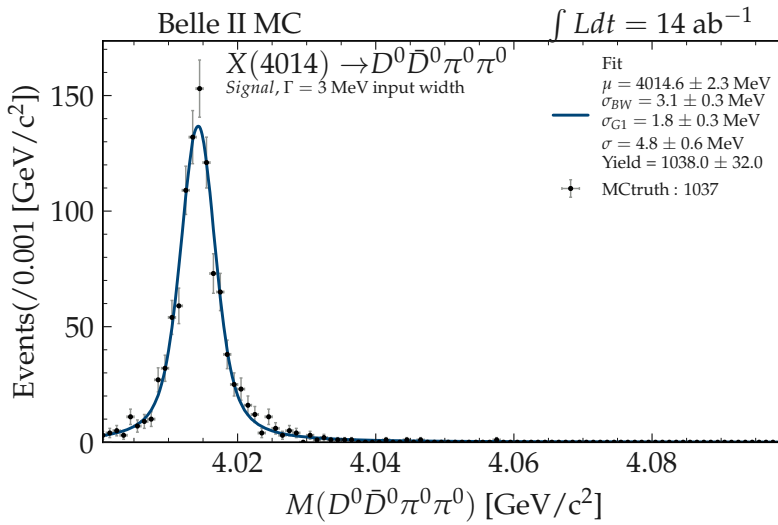


Figure V.31: Example fit for the MC-truth-matched  $X(4014)$  invariant mass distribution to a simulated  $\Gamma = 3 \text{ MeV}$  input width, corresponding to a  $14 \text{ ab}^{-1}$  data set, assuming a signal branching fraction of  $10^{-4}$ .

### V.4.2 Combinatorial Background

For the combinatorial background, i.e. the background originating from the second, generically decaying  $B$  meson in the signal sample, the sum of a Bifurcated Gaussian function and a Gaussian function is used. This parametrization allows to mimic the steeply rising tail on the right of the distribution, as well as the long tail towards higher masses on the left. An example fit for a simulated signal width of 7 MeV is shown in Fig. V.32. All fits

to the combinatorial background contribution for different simulated signal widths and the corresponding parameters are shown in appendix VIII.1.6 Fig. VIII.21 to VIII.26 and Tab. VIII.33 to VIII.38 respectively.

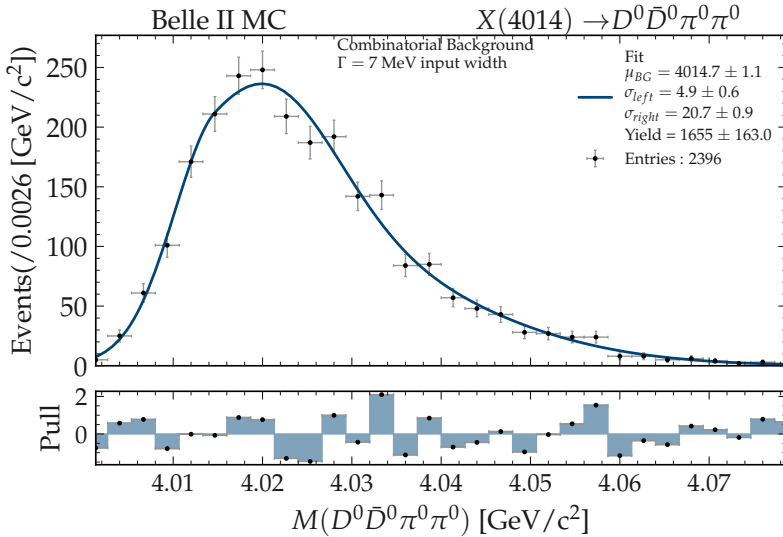


Figure V.32: Fit to the combinatorial background contribution to the  $X(4014)$  invariant mass for a sample with 7 MeV simulated signal width.

### V.4.3 Generic Background

Generic background originates from  $B^\pm$  and  $B^0$  decays from the  $Y(4S)$  resonance and includes also the non-resonant contribution from the  $B^\pm \rightarrow D^{*0} \bar{D}^{*0} \pi^0 \pi^0$  decay, that has a branching fraction ( $Br = 1.12 \pm 0.13$ ) much larger than the one expected for the resonant channel. This non-resonant contamination is suppressed by requiring the free energy of the  $X(4014)$  decay to be smaller than  $q < 40 \text{ MeV}$ . In Fig. V.33 the generic background sample for an integrated luminosity of  $2 \text{ ab}^{-1}$  is fitted with a Bifurcated Gaussian, showing a steep rising tail on the left and a flat tail on the right side of the distribution. Tab. VIII.39 in appendix shows the fit parameters. The shape parameters obtained from fitting the  $2 \text{ ab}^{-1}$  background sample are used to generate a  $14 \text{ ab}^{-1}$  TOY-MC sample according to the generic back-

ground PDF. The number of events in the TOY-MC sample was estimated with the number of events in the  $2 \text{ ab}^{-1}$  sample times  $\frac{14 \text{ ab}^{-1}}{2 \text{ ab}^{-1}} = 7$ . The TOY-MC generation is done in RooFit using as parent distribution the above mentioned PDF with parameters fixed to the values fitted on the  $2 \text{ ab}^{-1}$  simulation. The more statistics, the smaller the deviation of each generated data point to the input PDF.

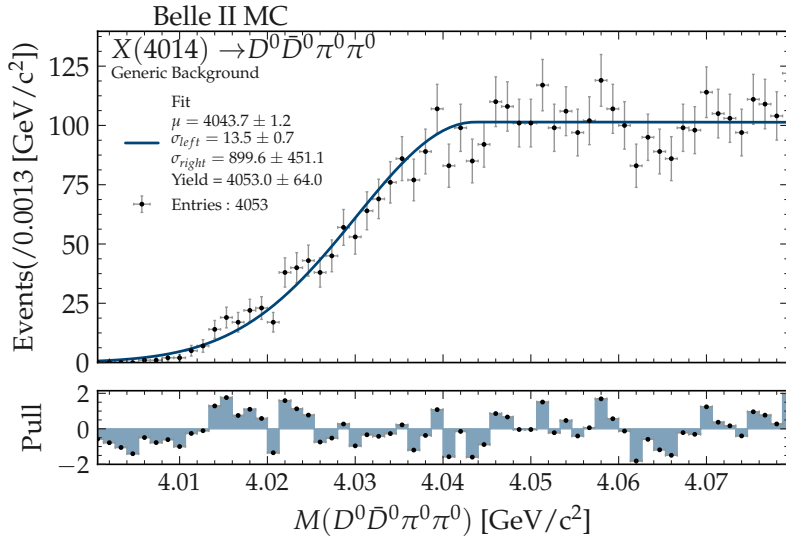


Figure V.33: Fit to the generic background component of the  $X(4014)$  invariant mass spectrum after BCS and  $Q < 40 \text{ MeV}$  selection.

#### V.4.4 Testing for Signal Bias with Toy-MC Study

The TOY-MC generation is also used to test for a signal yield bias of the combined PDF. After fitting the individual components as described above, the total PDF is constructed as sum of the three individual PDFs, with shape parameters taken and fixed to the ones from the individual fits.

The RooFit TOY-MC algorithm generates  $n_{evt}$  events per sample, according to the input PDF, and performs the fit. This is done for  $n_{exp}$  experiments, i.e. different generated data sets. Initial yields for signal, combinatorial background and generic background are chosen before generation and the fits are performed with floating values between  $-10^6$  and  $10^6$  for the yields of the individual components. After fitting all  $n_{exp}$  samples, each fitted yield is saved and the values are plotted in a histogram which should show a Gaussian distribution around the input yield value. Another check is the pull distribution of the fitted yields against their input yield. It should follow a Gaussian shape with a width compatible with one and peaking at zero. In Fig. VIII.28, both distributions are shown for an expected  $X(4014)$  width of  $\Gamma = 7$  MeV. The number of generated events was chosen as  $n_{evt} = 5000$  and the number of experiments was set to  $n_{exp} = 1000$ . The generated signal yield was set to 169. In a second try the signal yield was set to 0 to be sure no bias is caused. The corresponding plots are shown in VIII.2 of the appendix.

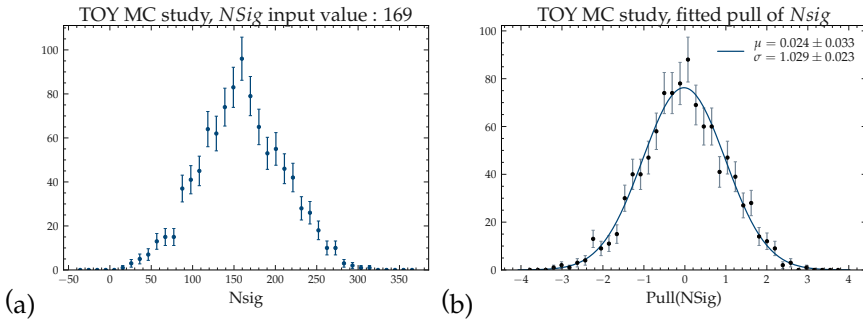


Figure V.34: Verification of an unbiased signal yield extraction for the total PDF with TOY-MC. Left plot (a) shows the distribution of the extracted signal yield. Right plot (b) shows the pull distribution.

### V.4.5 Combined Fit to the $X(4014)$ Invariant Mass Distribution Using the Maximum Likelihood Approach

After fitting the individual simulated components of the  $X(4014)$  invariant mass distribution and checking the total PDF for a signal yield bias, the fits to the final data sets are performed.

In total 360 fits were performed, one per each of the 6 different input widths, the 10 assumed branching fractions, the 3 luminosity scenarios and the 2 strategies for the final signal yield extraction and significance computation. All fits are performed in RooFit using the maximum likelihood method, which is now briefly explained.

For a given data set  $x_1, \dots, x_N$ , with  $N$  events measuring the statistically independent measurement  $x_i$ , the probability density function can be written as  $f(x; \vec{\alpha})$ . The parameter space,  $\vec{\alpha} = (\alpha_1, \dots, \alpha_m)$ , with unknown values, defines the set of parameters needed to describe the PDF. The combined PDF for the observed values of  $x$  is given by the likelihood function:

$$L(x; \vec{\alpha}) = \prod_{i=1}^N f(x_i; \vec{\alpha})$$

The maximum likelihood for the parameters  $\alpha_i$  is reached by a set of parameters with the values  $\hat{\alpha}_i$ , for which the likelihood function has a global maximum. For practical reasons, the searched parameter set  $\hat{\alpha}_i$  is often found by using the logarithm of the likelihood function,  $\log L(x; \vec{\alpha})$ , and search the minimum of the negative log-likelihood function

$$-\log(L(x; \vec{\alpha})) = -\sum_{i=1}^N \log(f(x_i; \vec{\alpha}))$$

The global minimum can be found if it doesn't occur on the boundaries of the parameter space  $\vec{\alpha}$  and the partial derivative of the negative log-likelihood function for each parameter  $\alpha_i$  is equal to zero. In most cases, the minimum of the negative log-likelihood can not be found analytically and must therefore be calculated numerically. The numerical formalism behind those calculations need a deeper understanding in numerical mathematics and should therefore not be further explained here.

## V.4.6 Significance Calculation

To check whether a statistically significant signal can be found for a certain  $X(4014)$  scenario in the simulated data sets, the invariant  $D^0\bar{D}^0\pi^0\pi^0$  distribution is fitted with the total PDF, using the unbinned maximum likelihood method. The two fitting strategies, the shape dependent and the shape independent, which are explained below, will result in a significance, in units of Gaussian standard deviations, which is used to determine the discovery potential of the simulated Belle II data sets.

### V.4.6.1 Shape Dependent Model

In case of the shape dependent model, the fit is performed twice per  $X(4014)$  scenario sample. Once with the total PDF including signal and background components and once with the background hypothesis only. In this thesis, it is called shape dependent due to the fact that the whole distribution is exploited and the fit can arrange its shape in the signal, as well as the sideband region. After performing both fits, the log-likelihood are used to calculate the significance with:

$$\sigma = \sqrt{2 \cdot (\ln(S + B) - \ln(B))}$$

In the above equation  $\ln(S + B)$  denotes the signal plus background hypothesis fit and  $\ln(B)$  the background hypothesis only. Fig. V.35 shows two example fits to the  $D^0\bar{D}^0\pi^0\pi^0$  invariant mass distribution with the total PDF exploiting the shape dependent significance method.

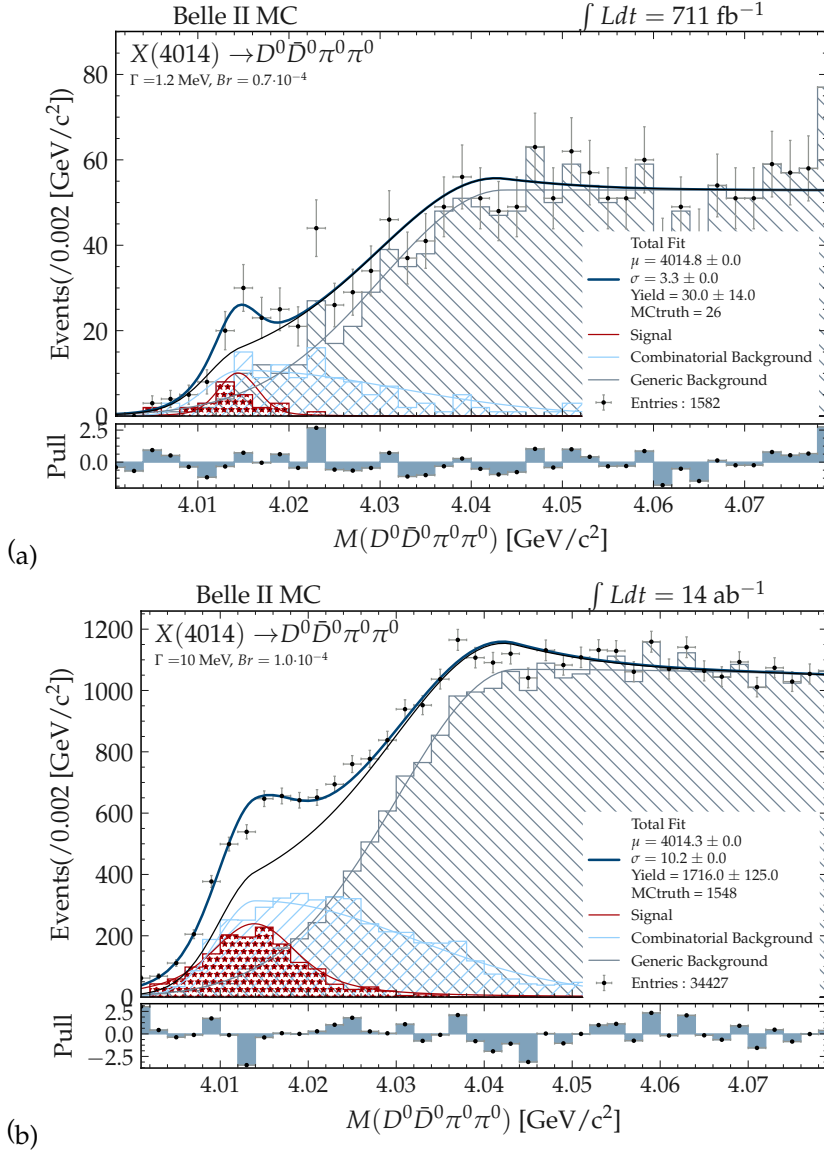


Figure V.35: Fit of the total PDF to the  $\Gamma = 1.2 \text{ MeV}$ ,  $Br = 0.7 \cdot 10^{-4}$  and  $711 \text{ fb}^{-1}$  sample (a) and to the  $\Gamma = 10 \text{ MeV}$ ,  $Br = 1 \cdot 10^{-4}$  and  $14 \text{ ab}^{-1}$  sample (b).

### V.4.6.2 Shape Independent Model

The shape independent model is exploiting only the sideband region of the invariant mass distribution. To do so, the data points in the signal region between  $4.01 < M(D^0\bar{D}^0\pi^0\pi^0) < 4.025$  MeV are not included in the fit. The sidebands, left and right of the signal region, are fitted with the background hypothesis PDF only. The fitted function is then integrated over the signal region to extract the number of expected events populating the signal region when only the background PDF is fitted - this is referred to as null-hypothesis. To calculate a significance, the null-hypothesis is compared to the actual number of observed events in the signal region of the data sample, this is done via the  $p$ -value. For an expected, known background  $b^{12}$ , calculated by the integral of the null-hypothesis over the signal region, the  $p$ -value is given by:

$$p = \sum_{n=n_{obs}}^{\infty} f(n;b)$$

where

$$f(n;b) = \frac{b^n e^{-b}}{n!}$$

is the poissonian distribution to obtain  $n$  events for an expectation value of  $b$ . This number can be converted in a significance  $\sigma$  in units of Gaussian standard deviations by:

$$\int_{\sigma}^{\infty} \frac{1}{2\sqrt{\pi}} e^{-t^2/\sigma} dt = p$$

The  $p$ -value are calculated for the number of events extracted from the null-hypothesis and the observed number of events in the data sample. Subtracting them gives the total  $p$ -value, when comparing background only estimation and observed events. Two example fits for this strategy are shown in Fig. V.36.

---

<sup>12</sup>Since the expected background for the process  $B^{\pm} \rightarrow D^0\bar{D}^0\pi^0\pi^0$  is standard model only, the background distribution is well known.

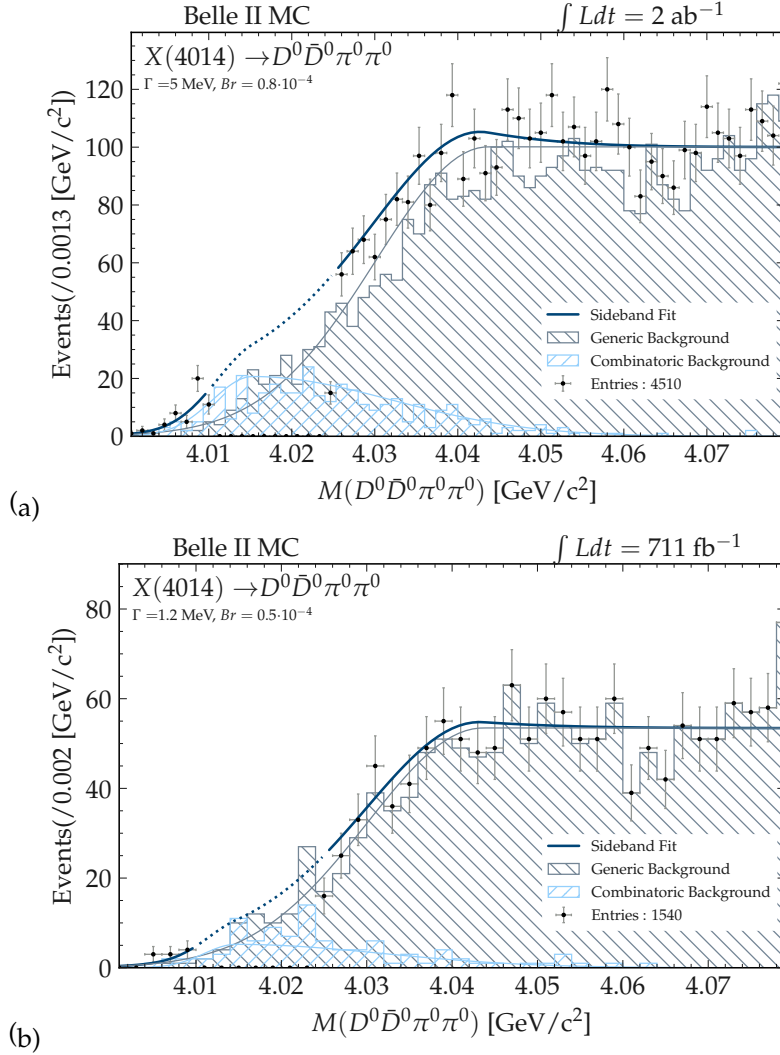


Figure V.36: Sideband fit to the  $D^0\bar{D}^0\pi^0\pi^0$  invariant mass distribution excluding the events in the signal region for the  $\Gamma = 5$  MeV,  $Br = 0.8 \cdot 10^{-4}$  and  $2 \text{ ab}^{-1}$   $X(4014)$  scenario (a) and the  $\Gamma = 1.2$  MeV,  $Br = 0.5 \cdot 10^{-4}$  and  $711 \text{ fb}^{-1}$  scenario (b).

### V.4.7 Outlook for a Discovery with Future Belle II Data Sets

To check whether the search for the  $X(4014)$  can be successful with the different data sets ( $711 \text{ fb}^{-1}$ ,  $2 \text{ ab}^{-1}$  and  $14 \text{ ab}^{-1}$ ) and scenarios for the  $X(4014)$ s branching fraction and expected widths, the significances calculated like explained in the last two sections, are illustrated in dependence of the input width, branching fraction and fitting method (shape-dependent or shape-independent). The errors shown in those plots take into account the fitting errors only. They are calculated as the largest difference from the significance calculated from fixing the shape parameters to the mean value extracted by the individual fits, to the significance calculated by fit were the shape parameters are fixed to the mean plus or minus the error of the shape values from the individual fits. In Fig. V.37 and V.38, two example maps for a data set of  $2 \text{ ab}^{-1}$  using the shape-dependent and shape-independent significance calculation respectively, are shown. All maps are shown in Fig. VIII.30 to VIII.32 in VIII.3.

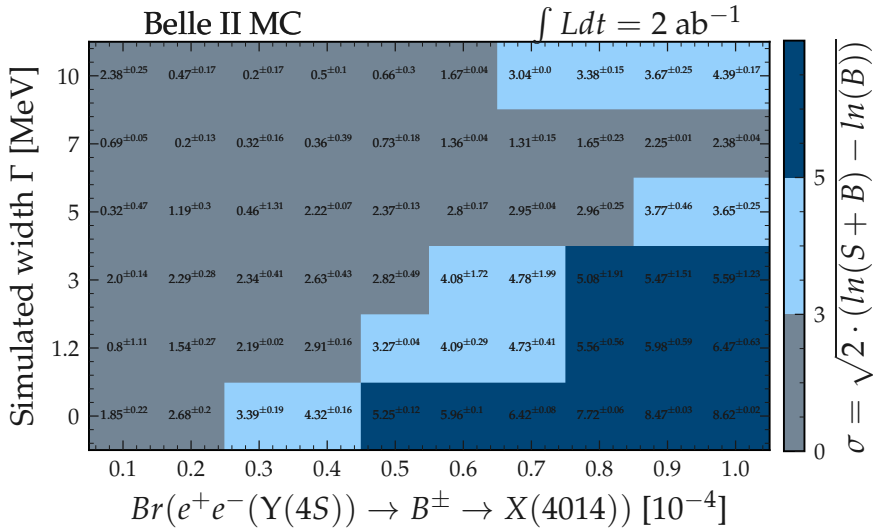


Figure V.37: Significance map of the  $2 \text{ ab}^{-1}$  data sample calculated via the shape-dependent fitting model.

As can be seen from the example maps for the  $2 \text{ ab}^{-1}$  sample, the number of scenarios with a significance greater  $3\sigma$  or  $5\sigma$  increases in the shape-independent model for data sets with small statistics. This is due to the fact that here only the number of events inside the signal window is used to calculate the significance. In case of the shape-dependent model also the accuracy of the fitting shape inside the signal region is taken into account. Since the Bifurcated Gaussian, used for the combinatorial background PDF, can also mimic a broader peaking structure, the significance gets lower when comparing it to a fit including the signal PDF. For a large statistic data set, like the simulated  $14 \text{ ab}^{-1}$ , the shape-dependent model will become more effective due to a better pronounced peaking structure compared to the combinatorial background.

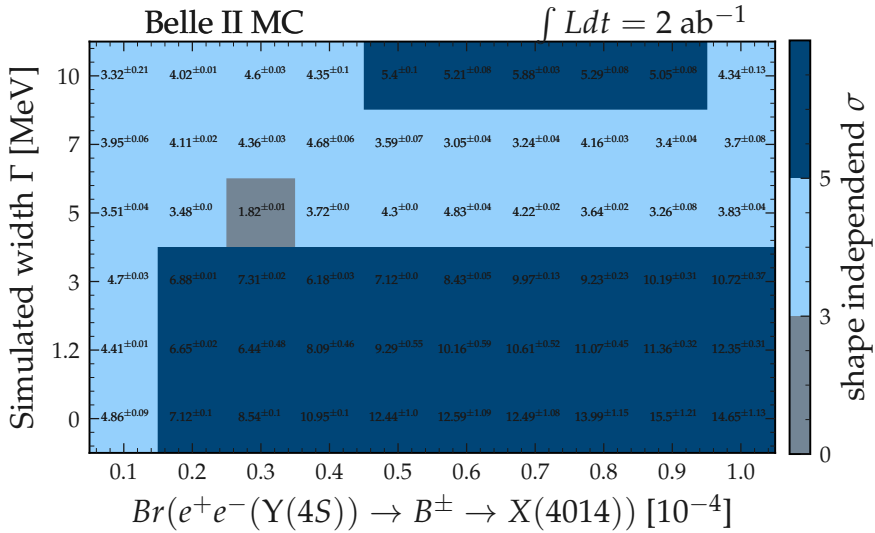


Figure V.38: Significance map of the  $2 \text{ ab}^{-1}$  data sample calculated via the shape-independent model.

Considering all scenarios taken into account, it can be concluded that with larger statistics Belle II will be able to discover the  $X(4014)$  resonance, if it exists. The discovery potential is, apart from larger data sets, also strongly correlated with the width and branching fraction of the resonance. In the worst case scenario, considering a width of  $\Gamma = 10 \text{ MeV}$  and a branching

fraction of  $Br = 10^{-5}$ , a sample of at least  $2 \text{ ab}^{-1}$  is needed, while an analyzed sample of  $14 \text{ ab}^{-1}$  with no significant peak will exclude the existence of the  $X(4014)$  in almost all scenarios taken into account for this study.

## V.5 Data and MC Comparison for Belle II

The current available data set of the Belle II experiment<sup>13</sup> is not sufficient to perform a search on the potential  $X(4014)$ . However, the presented strategy shall be used on larger Belle II data sets in a few years from now. To check whether a principal agreement between the accessible Belle II data and MC is given, this section is dedicated to the comparison of data and MC for Belle II. A comparison of all final state particle variables used for this analysis, as well as all reconstructed intermediate resonances is made. At the end of the section, the  $\Delta E$  and  $M_{bc}$  variables in use to select the final  $X(4014)$  candidates are compared. The comparison plots for all variables are shown in the appendix under VIII.4.

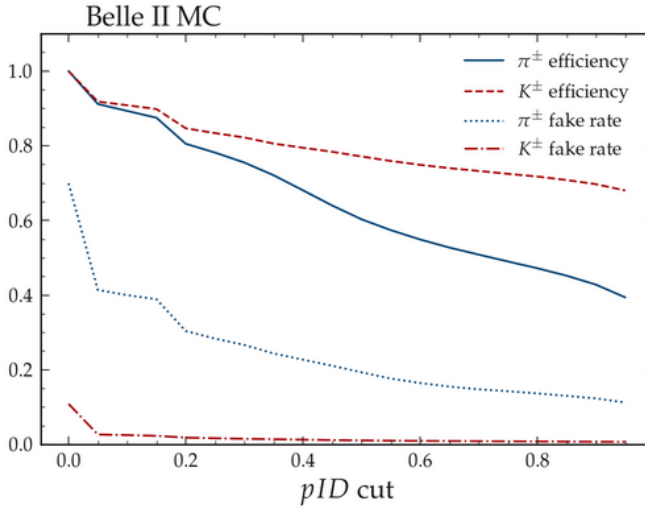


Figure V.39: Efficiencies and fake-rates for  $K^\pm$  and  $\pi^\pm$  reconstruction with different values of *particleID*

---

<sup>13</sup>  $\approx 10 \text{ fb}^{-1}$  of processed data in September 2020.

The *particleID* selection criteria of  $kaonID > 0.1$  and  $pionID > 0.05$  were, like in the whole analysis, also used for the data/MC comparison. Fig. V.39 shows the efficiencies and fake-rates for  $K^\pm$  and  $\pi^\pm$  reconstruction when demanding an increasing *particleID*.

The efficiency in this case is defined as MCtruth-matched candidates surviving a certain *particleID* selection divided by the number of total reconstructed candidates. Fake-rate is defined as MCtruth matched candidates of the other opponent particle type<sup>14</sup> kept after applying the *particleID* selection divided by the number of correct, demanded particles. Since the efficiency curves drop already quite significantly at small values, while the  $\pi^\pm$  fake-rate stays at a level above 20 % over almost all the range, one can conclude, that the particle identification at Belle II is working, but still needs some tuning to gain higher efficiencies and lower fake-rates at increasing *particleID* selection values.

For all plots shown in this section the MC is scaled according to  $L_{Data}/L_{MC}$ , where  $L_{Data}$  is the offline measured data luminosity over a certain run range and  $L_{MC}$  is the calculated luminosity of reconstructed MC. To calculate those values, the MC samples,  $u\bar{u}, d\bar{d}, s\bar{s}, c\bar{c}, \tau\bar{\tau}, mixed$  and  $charged$ , where reconstructed independently. The number of total events generated per reconstructed MC sample was taken to calculate  $L_{MC}$  via:

$$L_{MC}^i = \alpha_i \cdot N_{gen}^i$$

With  $i \in \{u\bar{u}, d\bar{d}, s\bar{s}, c\bar{c}, \tau\bar{\tau}, mixed, charged\}$ ,  $N_{gen}$  the number of generated events per sample and  $\alpha$  the cross section factor in nb per sample<sup>15</sup> [106].

## V.5.1 Comparison of Final State Particles in MC and Data

The final state reconstruction of  $K^\pm$  and  $\pi^\pm$  is performed with experiment 10, run 3860 with an integrated luminosity of  $\int Ldt = 8830.66 \text{ nb}^{-1}$ . In Fig. V.40 the distribution of the *pionID* for  $\pi^\pm$  and  $dz$  for  $K^\pm$  is shown as

---

<sup>14</sup>In case of  $K^\pm, \pi^\pm$  and vice versa.

<sup>15</sup> $\alpha_{u\bar{u}} = 1.61, \alpha_{d\bar{d}} = 0.4, \alpha_{s\bar{s}} = 0.38, \alpha_{c\bar{c}} = 1.3, \alpha_{\tau\bar{\tau}} = 0.919, \alpha_{mixed} = 0.51, \alpha_{charged} = 0.54$

points with error-bars for data and as stacked histogram for MC. The inset plot shows the ratio of data/MC in each bin.

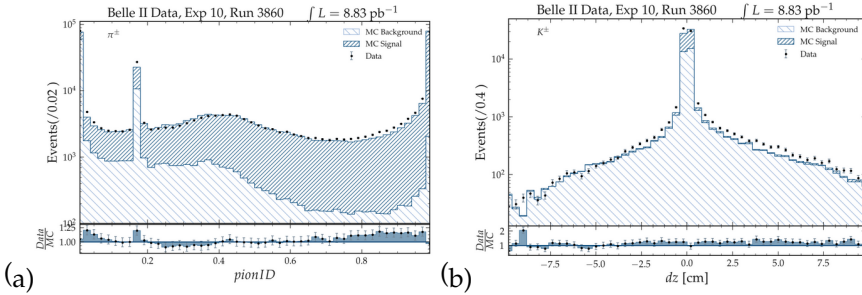


Figure V.40: Data/MC comparison for  $\text{pionID}$  of  $\pi^\pm$  (a) and  $dz$  for  $K^\pm$  (b).

For both plots, as for all others in VIII.4.1 and VIII.4.2, the overall shape seems to be in good agreement between data and MC. For higher values in  $\text{pionID}$  and over the whole range of  $dz$ , a discrepancy of 10 – 20 % can be observed in the inset plot.

## V.5.2 Comparison of $\pi^0$ in MC and Data

In Fig. VI.4 and VI.5, the comparison of the  $\gamma\gamma$  invariant mass spectrum for  $\pi^0$  candidates, stemming from  $D^0$  and  $X(4014)$  respectively is shown.

As can be seen from the plots in Fig. VI.4 and VI.5, the mass of the  $\pi^0$  is slightly shifted towards lower values for data. Apart from that, the overall shapes, as well as the number of candidates, are in good agreement between data and MC. In Tab. VIII.1 and Tab. VIII.3 of the appendix, the fit results of the data and MC fits to the  $\gamma\gamma$  invariant mass spectrum for  $\pi^0$  candidates stemming from  $D^0$  and  $X(4014)$  are shown respectively. For the candidates stemming from  $D^0$ , the agreement in these parameters between data and MC fits is within the error bars. Due to the large, low momentum fraction in the  $\pi^0$  reconstruction where candidates stem from the  $X(4014)$ , a larger discrepancy within  $3\sigma$  of the errors between data and MC can be seen.

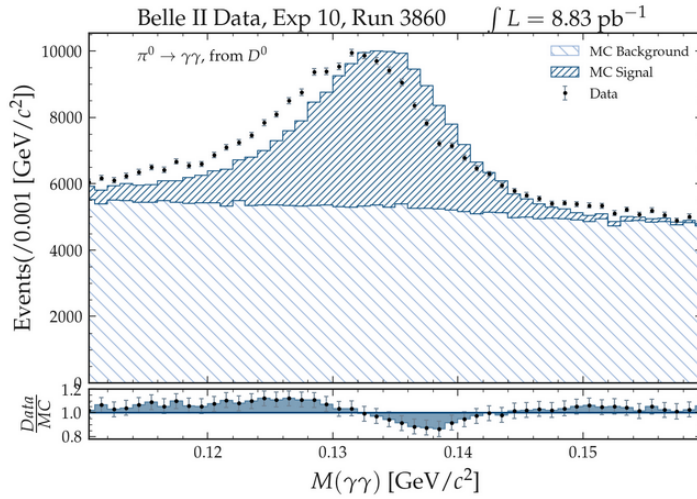


Figure V.41: Data/MC comparison of the  $\gamma\gamma$  invariant mass for  $\pi^0$  candidates stemming from  $D^0$ .

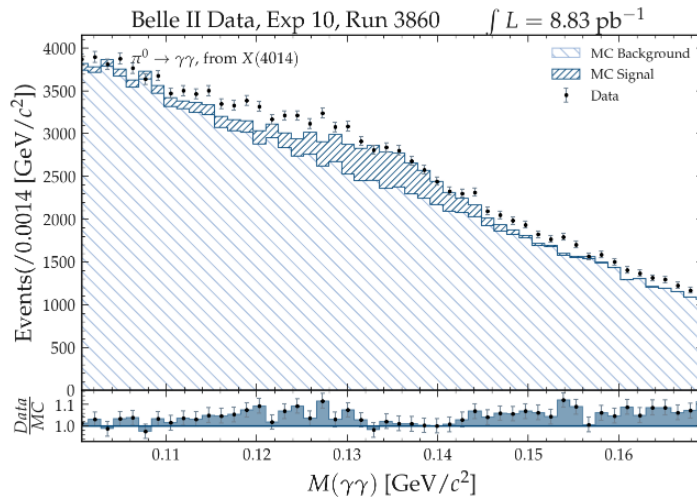


Figure V.42: Data/MC comparison of the  $\gamma\gamma$  invariant mass for  $\pi^0$  candidates stemming from  $X(4014)$ .

### V.5.3 Comparison of $D^0$ in MC and Data

Comparing plots and fitting values of  $D^0$  candidates can be seen in Sec.VIII.1.1.6 to VIII.1.1.7. An example plot for the comparison between data and MC in the  $D^0 \rightarrow K^\pm K^\mp$  channel is shown in Fig. V.43. The mass peak is shifted slightly towards smaller values for data, which is also seen for the other channels. Still, the fitted values in VIII.13 are in good agreement when comparing data to MC and the fitted mass of each channel on data is within the errors of the MC fitted peak.

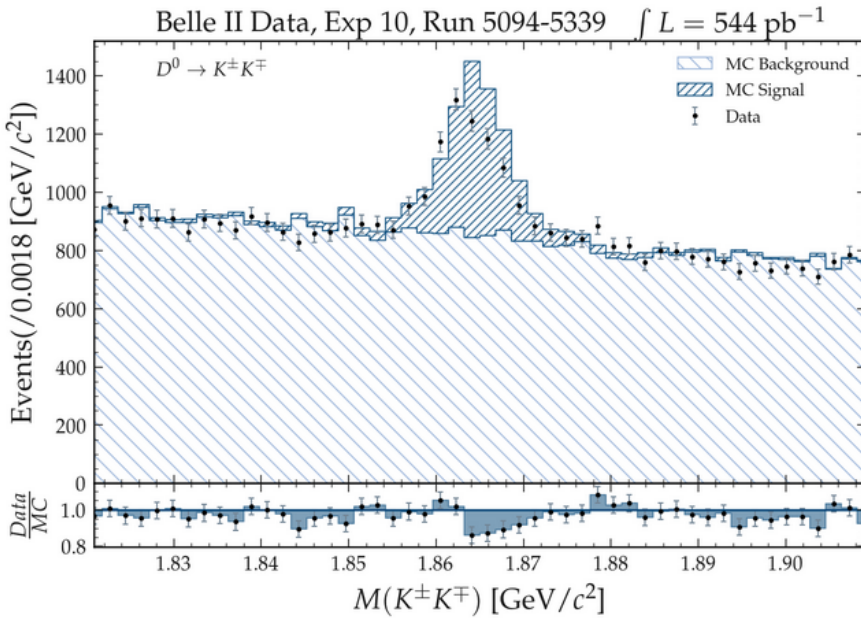


Figure V.43: Data/MC comparison of the  $K^\pm K^\mp$  invariant mass  $D^0$  reconstruction.

### V.5.4 Comparison of Kinematical $B^\pm$ Variables in MC and Data

For the final  $B^\pm$  list the  $M_{bc}$  and  $\Delta E$  distributions were compared for data and MC VIII.4.12. Fig. V.44 shows the  $\Delta E$  comparison after BCS and a selection on the  $M_{bc} > 5.27$  GeV signal region. As can be seen, the bin-by-bin yield for data is  $\approx 45\%$  less compared to MC. This overall discrepancy is observed for both signal and background region. Such an effect can only be generated by a global difference, as for example the *pionID* and *kaonID*, as also suggested by Fig. V.40 (a).

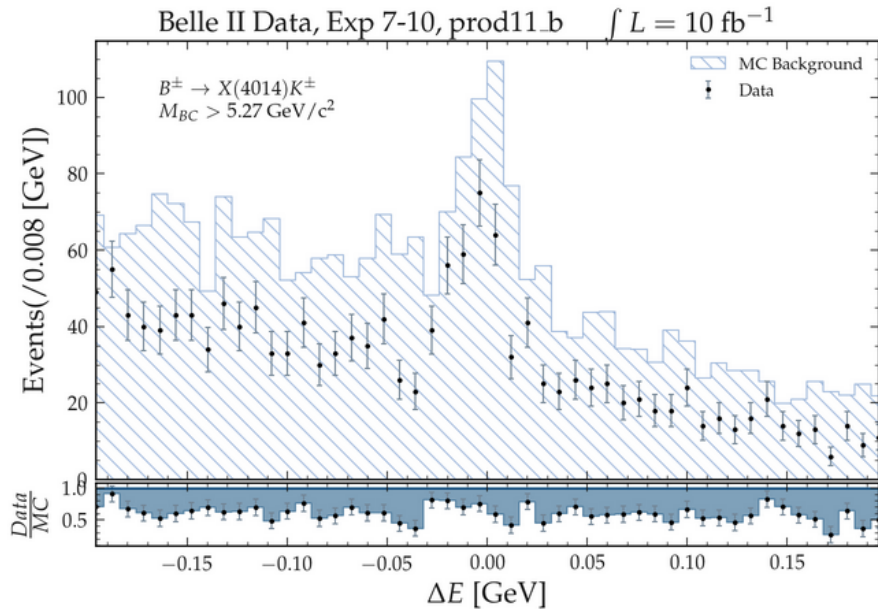


Figure V.44: Data/MC comparison of  $\Delta E$  for  $10 \text{ fb}^{-1}$  of Belle II data.

It should also be emphasized, that the data and MC for all steps before the final  $B$  meson yield are in very good agreement. In the next chapter, in Sec. VI.3, data and MC are compared for Belle, the predecessor experiment of Belle II. As will be seen, for Belle the situation is different from Belle II. Until a larger data set of around  $2 \text{ ab}^{-1}$  is available and the analysis is fully performed on real data, the crucial *kaonID* and *pionID* param-

eters for particle identification will be better understood and data and MC better calibrated. Since the statistical uncertainties are expected to be dominant, even when analyzing  $2 \text{ ab}^{-1}$  of data, the analysis of systematic errors, which would also include a well understood data/MC comparison, is not performed within this thesis.



$$V(r) = \frac{4}{3} \frac{\alpha_s}{r} + kr + \frac{32\pi\alpha_s}{9m_c^2} \delta_\sigma(r) \vec{S}_c \cdot \vec{S}_e$$

# Search for an Exotic Resonance at the $D^{*0} \bar{D}^{*0}$ Threshold in Charged $B$ Meson Decays at Belle

**T**HIS chapter aims on a search for the  $X(4014)$  resonance on the full  $711 \text{ fb}^{-1}$  Belle data set. The applied analysis strategy is similar to the one used for the Belle II simulation. At the end of the chapter, a possible improvement for a discovery with low data sets and/or small branching fractions, which was not exploited for the Belle II simulation but was proven to work on the reconstruction of the  $X(3872)$  reference channel in Belle data, is introduced. The whole simulation and analysis on Belle data is carried out with the b2bii framework.

## VI.1 Simulation of the $X(4014)$ at Belle Monte-Carlo

For the simulation of Belle signal MC, the same decay table as shown in Fig. V.4 is used. The generation and detector simulation is done within the final version of the Belle Analysis Framework (basf), while the reconstruction is performed within basf2 - the Belle II Analysis Framework. To reconstruct the MC simulated in basf, the data had to be converted with the b2bii framework for the analysis within basf2. This conversion was done online, i.e. during reconstruction with the same basf2 script as used for the Belle II simulation. The reconstruction steps for Belle MC and data are the same as in the Belle II simulation. For the selection variables a tighter  $pID$  selection of  $> 0.6$  for kaons and pions, is applied. Slightly different limits on the OCS for  $\pi^0$ ,  $D^0 \rightarrow K^\pm \pi^\mp \pi^0$ ,  $D^0 \rightarrow K^\pm \pi^\mp \pi^\pm \pi^\mp$  and  $X(4014)^1$  are applied.

<sup>1</sup>10 for  $\pi^0$  from  $D^0$ , 16 for  $\pi^0$  from  $X(4014)$ , 24 for  $D^0 \rightarrow K^\pm \pi^\mp \pi^\pm \pi^\mp$ , 25 for  $D^0 \rightarrow K^\pm \pi^\mp \pi^0$  and 35 for the  $X(4014)$ .

### VI.1.1 Comparison with the Belle II Simulation

Since it was already clear from the beginning, that a discovery of the X(4014) with the Belle data set is very unlikely, the simulation was not performed for all the width and branching fraction scenarios as taken into account for the Belle II simulation. Instead, the X(4014) was only simulated with a width of 0 MeV and the analysis was performed on a  $711 \text{ fb}^{-1}$  data set only. In this section, a comparison of the reconstruction efficiencies and purities between the Belle and Belle II simulation is made. All plots of the reconstructed intermediate state particles, as well as the fitting parameters, can be found in IX.1

In the following tables, Tab. VI.1 and Tab. VI.2, the most important parameters for the reconstruction of intermediate states,  $\pi^0$  and  $D^0$ , are listed. They show the fitted yield, the number of MCtruth matched candidates, the width and mean of the resonance, as well as the reconstruction and selection efficiency as defined in Eq. 1.

#### Comparison of reconstructed $\pi^0$

$\pi^0 \rightarrow \gamma\gamma$	Belle		Belle II	
	from $D^0$	from X(4014)	from $D^0$	from X(4014)
Fitted-Yield	58739	76143	116505	89717
MCtruth	86150	86178	117158	110425
Width [MeV]	4.3	6.63	5.6	8.14
Mass [MeV/ $c^2$ ]	134.9	135.6	132.5	132.4
$\eta_{reco}$ [%]	71.7	38.1	84.4	48.0
$\eta_{sel}$ [%]	8.7	16.8	10.9	19.2
<b>Changes in %</b>				
	from $D^0$		from X(4014)	
Width	+30		+23	
$\eta_{reco}$	+12.7		+9.9	
$\eta_{sel}$	+2.2		+2.4	

Table VI.1: Table summarizing the  $\pi^0$  parameters on signal MC of Belle (top) and Belle II (middle) and their changes in % (bottom). Positive changes are indicated in blue in a total data set of  $10^6$  events.

Comparison of reconstructed $D^0$					
$D^0 \rightarrow$	$K^\pm \pi^\mp$	$K^\pm \pi^\mp \pi^0$	$K \pi^\mp \pi^\pm \pi^\mp$	$K_S^0 \pi^\pm \pi^\mp$	$K^\pm K^\mp$
<b>Belle</b>					
Fitted-Yield	19858	20366	19097	9147	19280
MCTruth	21177	23941	22053	9683	20564
Width [MeV]	5.1	9.6	6.2	5.1	4.5
Mass [MeV/c <sup>2</sup> ]	1864.8	1864.3	1863.4	1864.8	1864.5
$\eta_{reco}$ [%]	64	20	31.9	29	61.4
$\eta_{sel}$ [%]	57.3	5.1	9.2	35.6	58.2
<b>Belle II</b>					
Fitted-Yield	17776	33947	11394	8076	15387
MCTruth	20258	33069	17615	9740	19050
Width [MeV]	4.6	9.0	4.0	4.5	3.8
Mass [MeV/c <sup>2</sup> ]	1864.3	1864.2	1864.0	1865.0	1864.2
$\eta_{reco}$ [%]	60.3	27.4	25.5	30.0	57.2
$\eta_{sel}$ [%]	55.1	5.9	8.1	38.2	55.2
<b>Changes in %</b>					
Width	-10	-6.3	-36	-12	-16
$\eta_{reco}$	-3.7	+7.4	-6.4	+1	-4.2
$\eta_{sel}$	-2.2	+0.8	-1.1	+2.6	-3

**Table VI.2:** Table summarizing the  $D^0$  parameters on signal MC of Belle (top) and Belle II (middle) and their changes in % (bottom). Positive changes are indicated in blue in a total data set of  $10^6$  events..

Summarized, it can be stated, that the overall reconstruction efficiency, purity and resolution for the reconstructed  $\pi^0$  and  $D^0$  states increases from Belle to Belle II MC. For some  $D^0$  channels, efficiency and purity are not increasing but decreasing which is most likely due to the very loose *particleID* selection in the Belle II case. For the Belle MC, a *kaonID* and *pionID* greater 0.6 was applied, while in the Belle II case those parameters were set to 0.1 and 0.05 respectively. The reason for that is the much better understood *particleID* for Belle, which is, in the Belle II case, still subject to investigation and optimization.

## VI.2 $B^\pm$ Reconstruction

After the final reconstruction of the  $B^\pm$  mesons, a best candidate selection, like in the Belle II case Eq. V.1, is applied. The  $\pi^0$  (6.63 MeV) and  $\Delta E$  (5.8 MeV) width, as well as the  $D^0$  width for the individual channels (IX.1.1.6 to IX.1.1.7) are taken from the Belle signal MC simulation IX.1. In Fig. VI.1, the invariant mass distribution of  $D^0\bar{D}^0\pi^0\pi^0$  in signal MC is shown. Since there were 100'000 simulated signal events, the reconstruction efficiency for the final  $B^\pm$  candidate list on Belle MC is 0.56 %. For the purity, a value of 6.8 % could be achieved. Compared to the Belle II simulation for a resonant  $X(4014)$  with  $\Gamma = 0$  MeV width, these numbers decrease  $\approx 48\%$  and  $\approx 40\%$  respectively.

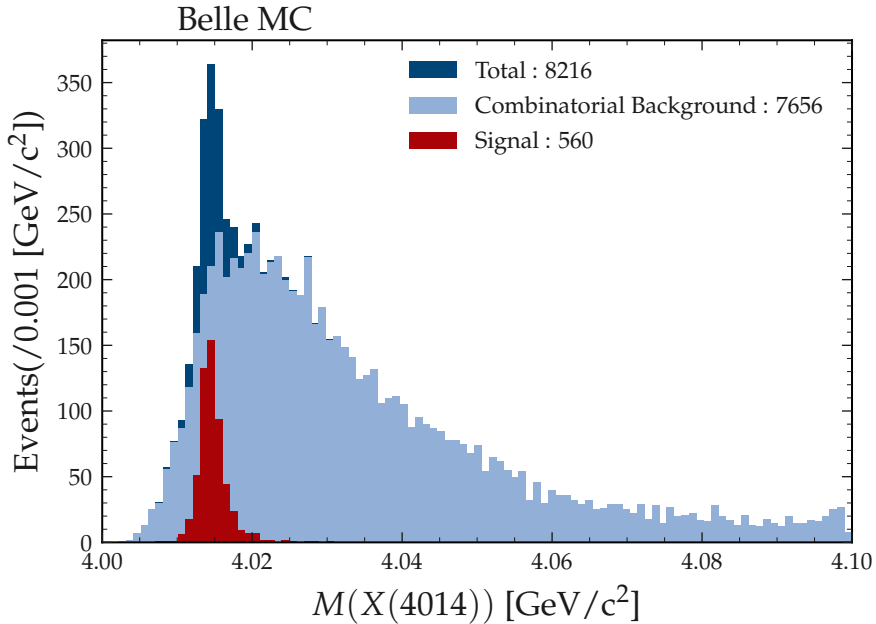


Figure VI.1:  $D^0\bar{D}^0\pi^0\pi^0$  invariant mass distribution for Belle signal MC after BCS.

After reconstruction of the signal MC, the generic Belle MC, corresponding to three times the recorded Belle on-resonance offline luminosity of  $711 \text{ fb}^{-1}$ , was reconstructed. Best candidates were selected with the same BCS as the signal MC. Final events are selected, like in the Belle II case, with a

$dq = M(X(4014)) - 2 \cdot M(D^0) - 2 \cdot M(\pi^0) < 40 \text{ MeV}/c^2$  constrained on the free energy in the  $X(4014)$  decay to suppress the non-resonant  $B^\pm$  decay, as well as a large fraction of the generic backgrounds.

Before exploiting the  $X(4014)$  analysis strategy on the full  $711 \text{ fb}^{-1}$  Belle data set, a data and MC comparison for the intermediate resonances and selection variables for Belle is made and the reconstruction strategy is verified on the  $X(3872)$  reference channel in Belle data.

### VI.3 Data and MC Comparison for Belle

To check whether a good agreement between the Belle data and MC is given, this section is dedicated to the comparison of data and MC for Belle. A comparison of final state particle variables, used for this analysis, as well as for all reconstructed intermediate resonances is made. At the end of the section, the  $\Delta E$  and  $M_{bc}$  variables in use to select the final  $X(4014)$  candidates are compared. The comparison plots for all variables are shown in the appendix under IX.2.

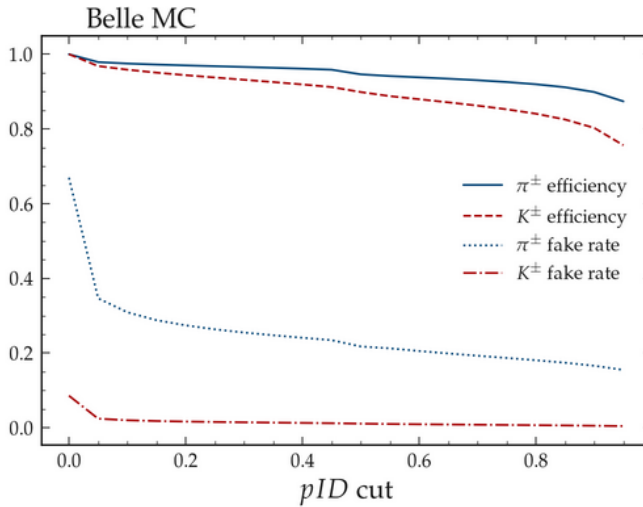


Figure VI.2: Efficiencies and fake-rates for  $K^\pm$  and  $\pi^\pm$  reconstruction with different values of *particleID*

The *particleID* selection criteria of  $kaonID > 0.6$  and  $pionID > 0.6$  were, like in the whole analysis, also used for the data/MC comparison. Fig. VI.2 shows the efficiencies and fake-rates for  $K^\pm$  and  $\pi^\pm$  reconstruction when demanding an increasing *particleID*. As one can observe, the efficiency is only slightly decreasing over a wide range of the *particleID*, while the fake-rate has a large drop above *particleID* > 0.1 and is then steadily decreasing. The efficiency in this case is defined as MCtruth-matched candidates surviving a certain *particleID* selection divided by the number of total reconstructed candidates. Fake-rate is defined as MCtruth matched candidates of the other, opponent particle type<sup>2</sup> kept after applying the *particleID* selection divided by the number of correct, demanded particles. Since Belle data and MC are not reprocessed anymore, the *particleID* is tuned to its final precision and the efficiencies of  $K^\pm/\pi^\pm$  reconstruction are not improving anymore. Both curves are above 80 % over the whole range of the *particleID* selection.

For all plots shown in this section the MC is scaled according to  $L_{Data}/L_{MC}$ , where  $L_{Data}$  is the offline measured data luminosity over a certain run range and  $L_{MC}$  is the calculated luminosity of reconstructed MC. To calculate those values, the MC samples, *uds*, *c $\bar{c}$* , *mixed* and *charged*, where reconstructed independently. The number of total events generated per reconstructed MC sample was taken to calculate  $L_{MC}$  via:

$$L_{MC}^i = \alpha_i \cdot N_{gen}^i$$

With  $i \in \{uds, c\bar{c}, mixed, charged\}$ ,  $N_{gen}$  the number of generated events per sample and  $\alpha$  the cross section factor in nb per sample<sup>3</sup>.

### VI.3.1 Comparison of Final State Particles in MC and Data

The final state reconstruction of  $K^\pm$  and  $\pi^\pm$  is performed with experiment 63, run 74 with an integrated luminosity of  $\int Ldt = 46.97 \text{ pb}^{-1}$ . In Fig. VI.3 the distribution of the *kaonID* for  $K^\pm$  and the impact parameter *d0* for  $\pi^\pm$  is shown as points with error-bars for data and a stacked histogram for MC. The inset plot shows the ratio of data/MC in each bin.

For both plots, as for all others in IX.2.1 and IX.2.2, the overall shape

---

<sup>2</sup>In case of  $K^\pm, \pi^\pm$  and vice versa.

<sup>3</sup> $\alpha_{uds} = 2.09, \alpha_{c\bar{c}} = 1.3, \alpha_{mixed} = 0.545, \alpha_{charged} = 0.545$

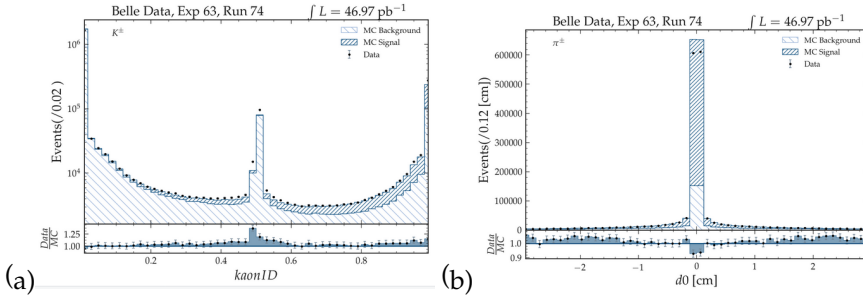


Figure VI.3: Data/MC comparison for  $kaonID$  of  $K^\pm$  (a) and  $d0$  for  $\pi^\pm$  (b).

seems to be in good agreement between data and MC. For higher values in  $kaonID$  (selection  $kaonID > 0.6$ ) the discrepancy between data and MC is less than 10 %. Over the whole range of  $d0$ , a maximum discrepancy of  $\approx 25$  % can be observed in the inset plot.

### VI.3.2 Comparison of $\pi^0$ in MC and Data

In Fig. VI.4 and VI.5, the comparison of the  $\gamma\gamma$  invariant mass spectrum for  $\pi^0$  candidates, stemming from  $D^0$  and  $X(4014)$  respectively is shown.

As can be seen from the plots in Fig. VI.4 and VI.5, the mass of the  $\pi^0$  is slightly shifted towards higher values for data. Apart from that, the overall shapes, as well as the number of candidates, are in good agreement between data and MC. In Tab. IX.1 and Tab. IX.3 of the appendix, the fit results of the data and MC fits to the  $\gamma\gamma$  invariant mass spectrum for  $\pi^0$  candidates stemming from  $D^0$  and  $X(4014)$  are shown respectively. The data/MC agreement is for both  $\pi^0$  reconstruction within a maximum of 10 % margin and therefore considered as good.

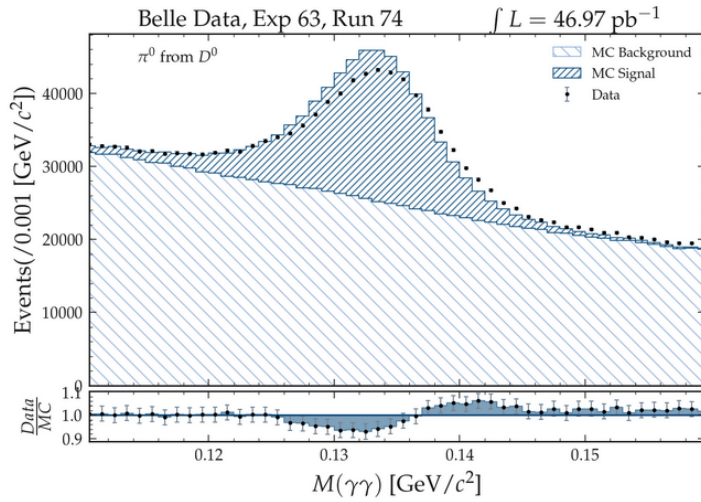


Figure VI.4: Data/MC comparison of the  $\gamma\gamma$  invariant mass for  $\pi^0$  candidates stemming from  $D^0$ .

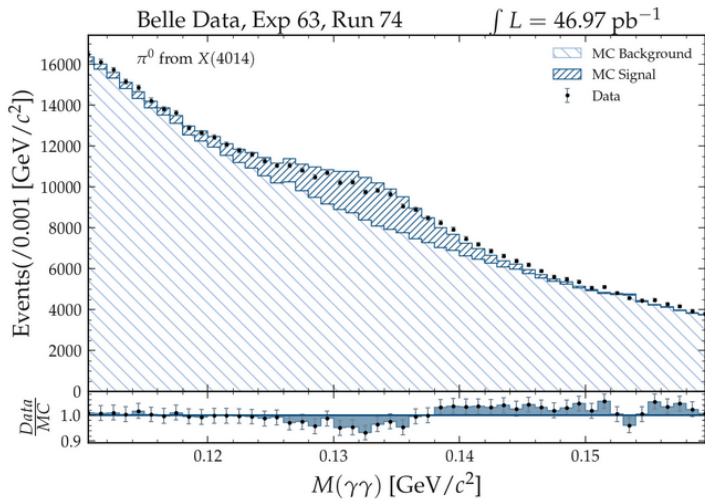


Figure VI.5: Data/MC comparison of the  $\gamma\gamma$  invariant mass for  $\pi^0$  candidates stemming from X(4014).

### VI.3.3 Comparison of $D^0$ in MC and Data

Comparing plots and fitting values of  $D^0$  candidates can be seen in Sec.IX.1.1.6 to IX.1.1.7. An example plot for the comparison between data and MC in the  $D^0 \rightarrow K^\pm \pi^\mp$  channel is shown in Fig. VI.6. The fitted values in IX.5, as well as for the other decays, are in good agreement when comparing data to MC. A maximum discrepancy of  $\approx 10\%$  per bin can be observed in the inset plot of Fig. VI.6 and for the other resonances in IX.1.1.6 to IX.1.1.7.

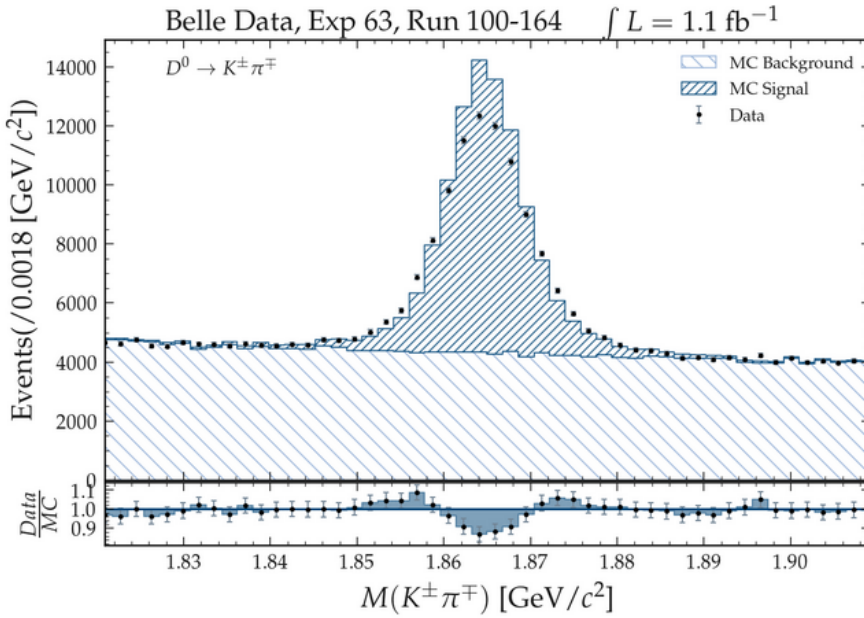


Figure VI.6: Data/MC comparison of the  $K^\pm \pi^\mp$  invariant mass  $D^0$  reconstruction.

### VI.3.4 Comparison of $B^\pm$ in MC and Data

For the final  $B^\pm$  list the  $M_{bc}$  and  $\Delta E$  distributions were compared for data and MC in IX.2.12 and IX.2.13, for the  $X(3872)$  and  $X(4014)$  respectively. Fig. VI.7 shows the  $\Delta E$  comparison after BCS and a selection on the  $M_{bc} > 5.27 \text{ GeV}/c^2$  and  $dq < 30 \text{ MeV}/c^2$  signal region and the  $M(D^0\bar{D}^0\pi^0) > 3.88 \text{ GeV}/c^2$  sidebands for the reconstruction of the  $X(3872)$ . As can be seen, the data fits the MC very well in almost all the bins. Thus a further analysis and fitting of the data is performed.

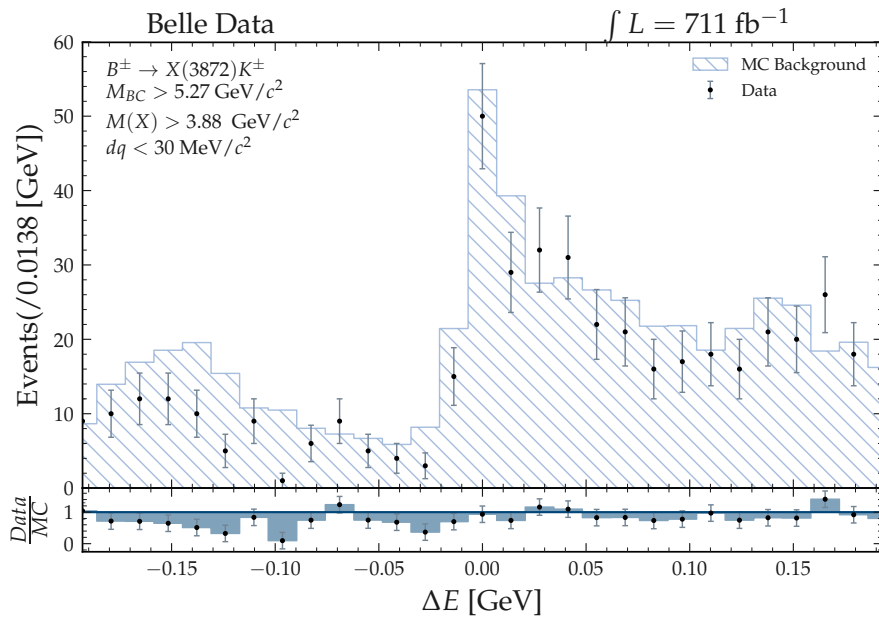


Figure VI.7: Data/MC comparison of  $\Delta E$  for  $711 \text{ fb}^{-1}$  of Belle data for the  $X(3872)$  reconstruction.

## VI.4 Exploiting the Reconstruction Strategy on the $X(3872) \rightarrow D^0 \bar{D}^0 \pi^0$ Reference Channel in *Belle Data.*

The  $X(3872) \rightarrow D^0 \bar{D}^0 \pi^0$  in  $B$  decays, was studied in Belle note 1006 from 2008 [100]. Since this channel is missing only one  $\pi^0$ , when comparing to the potential  $X(4014)$  decay, the decision was made to take it as reference channel and check the reconstruction and analysis strategy presented in this thesis. The authors of the Belle analysis were using the charged and neutral  $B$  decays, but only four  $D^0$  decays, namely  $K^\pm \pi^\mp$ ,  $K^\pm \pi^\mp \pi^\pm \pi^\mp$ ,  $K^\pm K^\mp$  and  $K_S^0 \pi^\pm \pi^\mp$ . A comparison of the extracted  $X(3872)$  properties in this work with the published numbers of the Belle paper will be given at the end of the section. For the analysis in this thesis, the reconstruction script was not optimized for  $X(3872)$ , instead, the exact same reconstruction, excluding the additional  $\pi^0$ , as for the  $X(4014)$  was used.

For signal events of the  $B^\pm \rightarrow X(3872)K^\pm$ , a peak in the invariant mass distribution, as well as in the  $M_{bc}$  and  $\Delta E$  distributions is expected. The signal region is therefore defined as  $M(D^0 \bar{D}^0 \pi^0) < 3.88 \text{ GeV}/c^2$ ,  $M_{bc} > 5.27 \text{ GeV}/c^2$ ,  $|\Delta E| < 12 \text{ MeV}$  and  $dq = M(D^0 \bar{D}^0 \pi^0) - 2 \cdot M(D^0) - M(\pi^0) < 30 \text{ MeV}/c^{24}$ .

Sec. IX.2.12 of the appendix shows all plots of the data/MC comparison for  $\Delta E$ ,  $M_{bc}$  and  $M(D^0 \bar{D}^0 \pi^0)$  for the sideband and signal region. In Fig. VI.8, the distributions for  $\Delta E$ ,  $M_{bc}$  and  $M(D^0 \bar{D}^0 \pi^0)$  are compared between data and MC. Data is shown as markers with errorbars and the generic MC background is indicated as blue striped histogram. MC is scaled according to  $711 \text{ fb}^{-1}$ . The inset plot shows the data/MC comparison per bin. Except of the signal region,  $|\Delta E| < 0.012 \text{ MeV}$ ,  $M_{BC} > 5.27 \text{ GeV}/c^2$  and  $M(D^0 \bar{D}^0 \pi^0) < 3.88 \text{ GeV}/c^2$ , the inset plots show good agreement between data and generic background. In the signal region a clear enhancement of data in all three distributions can be observed.

---

<sup>4</sup>Phase space in the decay is  $M(X(3872)) - 2 \cdot M(D^0) - M(\pi^0) = 10 \text{ MeV}/c^2$

Chapter VI. Search for an Exotic Resonance at the  $D^{*0}\bar{D}^{*0}$  Threshold in Charged B Meson Decays at Belle

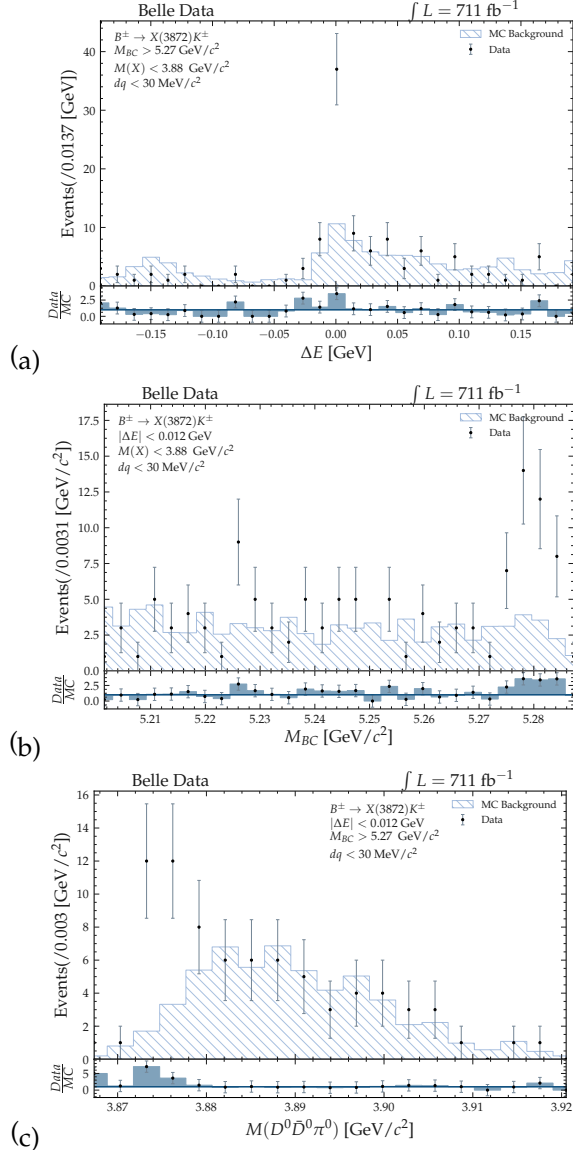


Figure VI.8: Data/MC comparison of  $\Delta E$  (a),  $M_{BC}$  (b) and  $M(D^0\bar{D}^0\pi^0)$  (c) in the  $X(3872)$  signal region for  $711 \text{ fb}^{-1}$  of Belle data.

VI.4. Exploiting the Reconstruction Strategy on the  
 $X(3872) \rightarrow D^0 \bar{D}^0 \pi^0$  Reference Channel in  
 Belle Data.

The MC components, signal, non-resonant, generic and combinatorial background, of the three distributions are then fitted individually and the shape parameters are extracted. Fitting functions are shown in the Tab. VI.3, the fit results and parameters are listed in the appendix IX.1.2.

	$\Delta E$	$M_{BC}$	$M(D^0 \bar{D}^0 \pi^0)$
Signal	Gauss	Gauss	Breit Wigner $\otimes$ Gauss
Non-resonant	Gauss	Gauss	Bif. Gauss
Generic	4 <sup>th</sup> polynomial	Argus	Bif. Gauss
Combinatoric	Gauss + Gauss	Gauss	Bif. Gauss + Gauss

Table VI.3: Fitting functions for the individual MC components and variables.

An example fit for the  $M_{BC}$  distribution of the generic background component, including the non-resonant  $B^\pm \rightarrow D^0 \bar{D}^0 \pi^0 K^\pm$  and  $B^\pm \rightarrow D^0 \bar{D}^0 K^\pm$  decays is shown in Fig. VI.9.

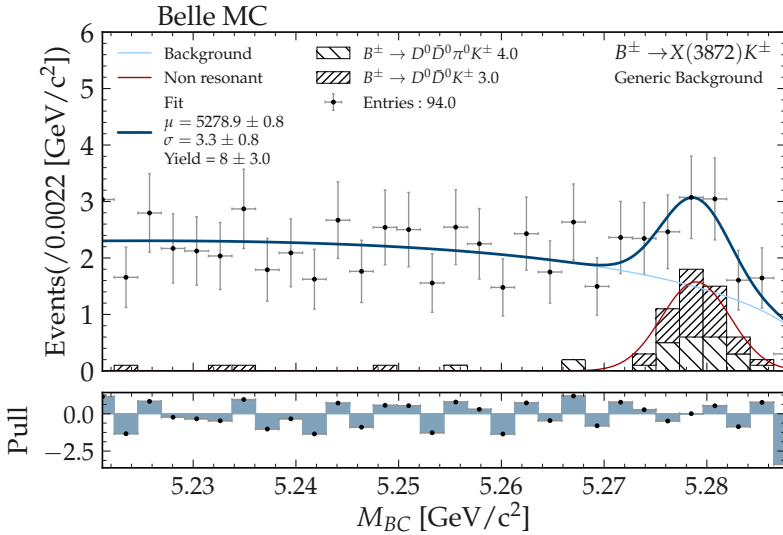


Figure VI.9: Fit to the  $M_{BC}$  distribution of the generic background component. In red, the fit to the non-resonant part is indicated. The stacked, dashed histogram shows the non-resonant MC contributions.

### VI.4.0.1 2D Fitting Strategy for Higher Signal Significance

Since for the signal decays a resonant structure in  $M(D^0\bar{D}^0\pi^0)$ ,  $M_{BC}$  and  $|\Delta E|$  is expected, all three distributions are fitted on data with an extended, unbinned, maximum-likelihood fit. For the  $\Delta E$  distribution, a one dimensional fit, only in  $\Delta E$ , is performed. The shape parameters for that fit were fixed to the ones extracted from the fits to the individual MC components shown in IX.1.2. The data for the fit are selected with:

- $dq < 30 \text{ MeV}/c^2$ ,
- $|M_{BC}| > 5.277 \text{ MeV}$ , and
- $M(D^0\bar{D}^0\pi^0) < 3.88 \text{ GeV}/c^2$

In Fig. VI.10, the fitted  $\Delta E$  distribution is shown. The blue, red and light blue lines show the total, signal and background fit respectively. The background MC is indicated as light blue area, statistical MC errors as black hashed overlays. Like expected, the fit has a narrow peak around 0 MeV. The signal yield contains  $20 \pm 6$  candidates, which is comparable with the one found in the Belle paper [100] of  $22 \pm 7.6$ .

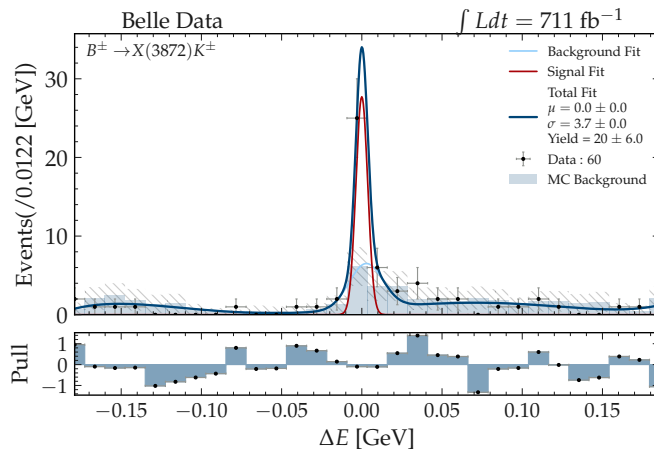


Figure VI.10: Fit to the  $\Delta E$  distribution for  $711 \text{ fb}^{-1}$  of Belle data. The blue line shows the total fit, red and light blue show the signal and background fit respectively. MC is shown as blue histogram with the statistical MC errors as black hashed overlays.

VI.4. Exploiting the Reconstruction Strategy on the  
 $X(3872) \rightarrow D^0 \bar{D}^0 \pi^0$  Reference Channel in  
Belle Data.

---

For the fit to the  $M_{BC}$  and  $M(D^0 \bar{D}^0 \pi^0)$  distributions, a 2D extended, unbinned maximum likelihood fit is performed. The fitted data set is selected with:

- $dq < 30 \text{ MeV}/c^2$ ,
- $|M_{BC}| > 5.27 \text{ MeV}$ , and
- $\Delta E < 12 \text{ MeV}$ .

A multidimensional fit is performed by multiplication of PDFs, describing the data shape for different variables. In case of two PDFs  $f_x(x; a)$  and  $f_y(y; b)$  in  $x$  and  $y$ , the two dimensional PDF can be written as:

$$f_{xy}(x, y; a, b) = f_x(x; a) \cdot f_y(y; b)$$

Since a necessary condition for a two-dimensional PDF is, that the variables ( $x$  and  $y$ ) are not correlated, and thus the PDFs  $f_x(x; a)$  and  $f_y(y; b)$  are orthogonal, the total PDF is properly normalized if  $f_x(x; a)$  and  $f_y(y; b)$  are normalized:

$$\begin{aligned} \int \int f_{xy}(x, y; a, b) dx dy &= \int \int f_x(x; a) \cdot f_y(y; b) dx dy \\ &= \int f_x(x; a) dx \int f_y(y; b) dy = 1 \end{aligned}$$

Due to the well defined normalization, the yields for the individual components of the backgrounds and the signal can be evaluated after the fit has converged. To check, whether the variables are uncorrelated, the Pearson product-moment correlation is calculated [107, p. 22]:

$$\rho_{xy} = \frac{\text{cov}[x, y]}{\sigma_x \sigma_y} \in [-1, 1] \begin{cases} \approx 1 : \text{positive correlated} \\ \approx 0 : \text{uncorrelated} \\ \approx -1 : \text{negative correlated} \end{cases}$$

With  $\text{cov}[x, y]$  being the covariance-matrix of the variables  $x$  and  $y$  and  $\sigma_i$  the standard deviation of the samples  $x$  and  $y$ . For the variables  $M_{BC}$  and  $M(D^0 \bar{D}^0 \pi^0)$ , a Pearson product moment of  $-0.048$  is extracted, which

*Chapter VI. Search for an Exotic Resonance at the  $D^{*0}\bar{D}^{*0}$  Threshold in Charged B Meson Decays at Belle*

---

is sufficiently small to treat the variables as uncorrelated and perform a two-dimensional fit.

The total, two-dimensional PDF is constructed from the functions listed in Tab. VI.3. For the signal component, the product can be written as:

$$S_{total} = (Breit - Wigner \otimes Gauss)_{M(X)} \times Gauss_{M_{BC}}$$

For the individual background components the product PDFs are expressed as:

$$B_{comb} = (Gauss + BifurGauss)_{M(X)} \times Gauss_{M_{BC}}$$

$$B_{non-reso} = BifurGauss_{M(X)} \times Gauss_{M_{BC}}$$

$$B_{generic} = BifurGauss_{M(X)} \times Argus_{M_{BC}}$$

The total background PDF can then be written as

$$B_{total} = N_{comb} \cdot B_{comb} + N_{non-reso} \cdot B_{non-reso} + B_{generic}$$

where  $N_{comb}$  and  $N_{non-reso}$  are the fractions of the combinatorial and the non-resonant background respectively. Since the sum of all three background components is normalized to one, the fraction of the generic background is implicitly given. The total PDF can now be constructed by adding  $S_{total}$  and  $B_{total}$  to

$$F_{total} = N_{signal} \cdot S_{total} + N_{background} \cdot B_{total}$$

with  $N_{signal}$  and  $N_{background}$  the number of fitted signal and background candidates respectively.

VI.4. Exploiting the Reconstruction Strategy on the  
 $X(3872) \rightarrow D^0 \bar{D}^0 \pi^0$  Reference Channel in  
 Belle Data.

The fit is then performed in 2 dimensions, namely  $M_{BC}$  and  $M(D^0 \bar{D}^0 \pi^0)$  over the whole range of the data set. The fitted PDF is then evaluated in the projection to  $M_{BC}$  and  $M(D^0 \bar{D}^0 \pi^0)$  with additional selections on the data **after the fit converged**, to illustrate a more pronounced signal peak, as can be already seen in the two-dimensional histogram of the fitted PDF in Fig. VI.11. The additional selections are : for the  $M_{BC}$  sample  $M(D^0 \bar{D}^0 \pi^0) < 3.88 \text{ GeV}/c^2$  and for the  $M(D^0 \bar{D}^0 \pi^0)$  sample  $M_{BC} > 5.277 \text{ GeV}/c^2$ .

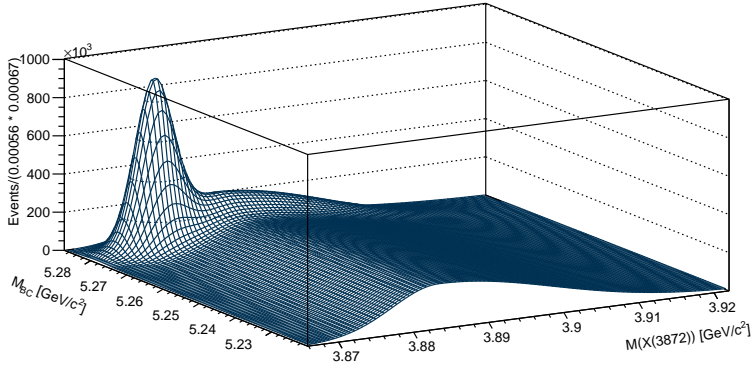


Figure VI.11: Two-dimensional histogram of the fitted 2D-PDF, with signal and background component,  $F_{total}$ , in  $M_{BC}$  and  $M(D^0 \bar{D}^0 \pi^0)$ . In Fig. IX.48, the fitted PDF with background component only is shown.

The total PDF is projected to the two axis,  $M(D^0 \bar{D}^0 \pi^0)$  and  $M_{BC}$ , in Fig. VI.12 (a) and (b) respectively. The plots show the total PDF as dark blue line, the signal PDF as red line and the background PDF as light blue line. The individual fits to the background components are indicated in dark blue (generic), blue (non-resonant) and light-blue (combinatoric). Generic background, indicated as stacked histogram, is split up in non-resonant  $B^\pm \rightarrow D^0 \bar{D}^0 \pi^0 X$  (  ) and  $B^\pm \rightarrow X$  (  ) origin, where  $X$  is a generic decay product. Data is shown as black dots with error-bars. The fit yields  $28 \pm 3$  events in the signal PDF with  $M(D^0 \bar{D}^0 \pi^0)$  peaking at  $\mu = 3874.4 \pm 1.1 \text{ MeV}/c^2$  and a width of  $2.62 \pm 0.7 \text{ MeV}/c^2$ . The significance of the fit is  $11.26 \sigma$ .

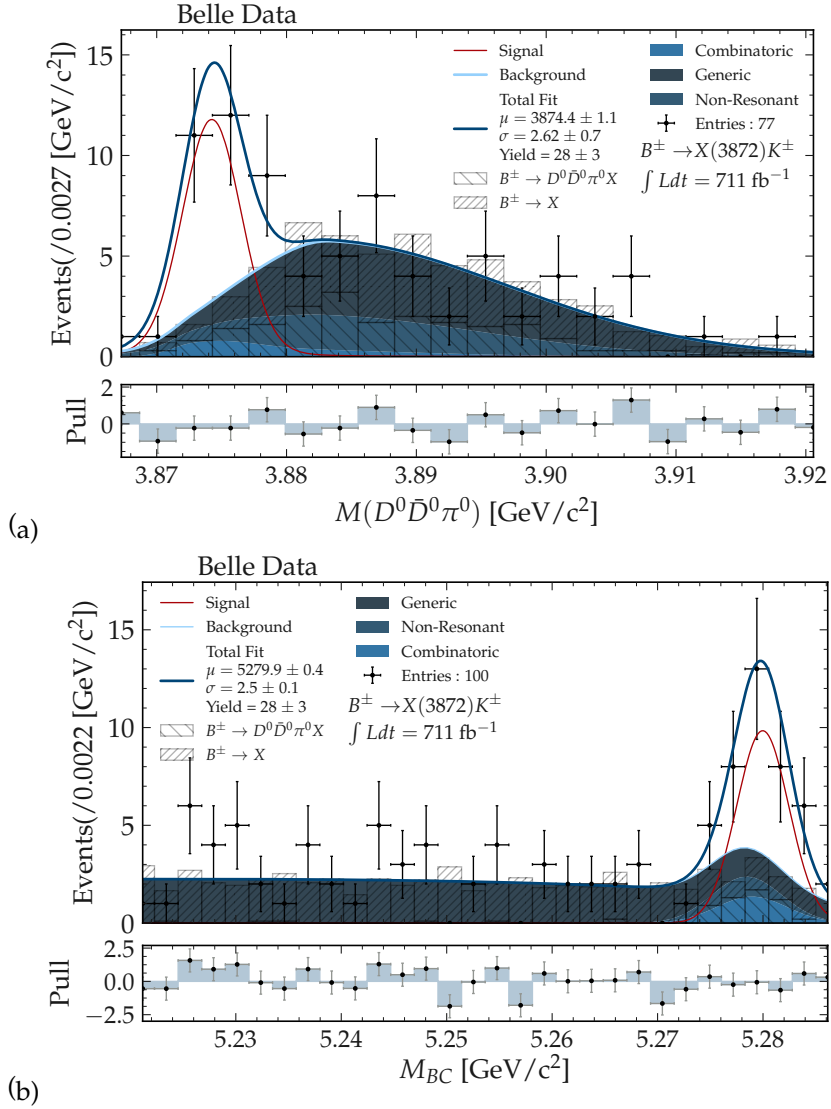


Figure VI.12: Projection of the two-dimensional fit in  $M(D^0\bar{D}^0\pi^0)$  (a) and  $M_{BC}$  (b).

### VI.4.1 Comparison of Extracted $X(3872)$ Properties with Published Numbers

With the presented reconstruction and fit strategy  $B^\pm \rightarrow X(3872)K^\pm$  was reconstructed with  $X(3872) \rightarrow D^0 \bar{D}^0 \pi^0$  and  $D^0 \rightarrow K^\pm \pi^\mp, K^\pm \pi^\mp \pi^0, K^\pm \pi^\mp \pi^\pm \pi^\mp, K_S^0 \pi^\pm \pi^\mp, K^\pm K^\mp$ . A two-dimensional fit in  $M_{BC}$  and  $M(D^0 \bar{D}^0 \pi^0)$  is performed yielding  $28 \pm 3$  candidates in the signal peak with a mass of  $M(X3872) = 3874.4 \pm 1.1 \text{ MeV}/c^2$ , a width of  $\sigma = 2.62 \pm 0.7 \text{ MeV}$  and a significance of  $11.26 \sigma$ . The extracted parameters and the branching fraction  $\mathcal{B}(B^\pm \rightarrow X(3872)K^\pm) \cdot \mathcal{B}(X(3872) \rightarrow D^0 \bar{D}^0 \pi^0)$  are now compared to published values from the PDG.

The branching fraction is calculated as:

$$\mathcal{B}(B^\pm \rightarrow X(3872)K^\pm) \cdot \mathcal{B}(X(3872) \rightarrow D^0 \bar{D}^0 \pi^0) = \frac{N_{sig}}{N_{B\bar{B}} \cdot 0.5 \cdot \epsilon \cdot (\sum \mathcal{B}_i)^2}$$

With  $N_{sig}$ , the number of fitted signal events,  $\epsilon = 0.716 \%$  the reconstruction efficiency on signal MC<sup>5</sup> and  $\mathcal{B}_i$  the branching fractions of the individual  $D^0$  decay channels. The number of  $B\bar{B}$  events,  $N_{B\bar{B}} = \int \mathcal{L} dt \cdot 1.1 \text{ nb}^{-1} = 782 \cdot 10^6$ , has to be multiplied by 0.5, since the reconstruction is performed only on the charged  $B$  mesons.  $1.1 \text{ nb}^{-1}$  corresponds to the branching fraction of  $e^+e^- \rightarrow Y(4S) \rightarrow B\bar{B}$ . In Tab. VI.4, the fitted parameters are listed and compared to the published PDG values of the  $X(3872)$ .

	$M(X(3872)) [\text{MeV}/c^2]$	$\sigma [\text{MeV}]$	$\mathcal{B} [10^{-4}]$
PDG <sup>a</sup>	3874.1	3.54	$1.0 \pm 0.4$
This work <sup>b</sup>	$3874.4 \pm 1.1$	$2.62 \pm 0.7$	$0.92 \pm 0.1$

**Table VI.4:** Comparison of the extracted  $X(3872)$  parameters from the fit with the values published in the PDG.

<sup>a</sup>For the mass and the width the average value of the three published measurements in the  $X(3872) \rightarrow D^0 \bar{D}^0 \pi^0$  mode are used.

<sup>b</sup>Errors include the statistical error **only**. In case of the branching fraction, the error is calculated with the signal yield plus its error: 31 events.

All values are in agreement with the ones published by the PDG. Since

<sup>5</sup>Number of MCtruth matched  $X(3872)$  candidates after the final selection divided by the number of generated events, 100000.

the  $B^\pm \rightarrow X(3872)K^\pm$  decay was used as a reference channel for the  $B^\pm \rightarrow X(4014)K^\pm$  analysis, it can be concluded, that the reconstruction and fitting strategy is working as expected.

## VI.5 Unblinding of Data in the $X(4014)$ Signal Region

As shown in Sec. VI.3 and IX.2.13, the data to MC comparison for the  $X(4014)$  reconstruction strategy is, within the errorbars, in good agreement. Until now only the data luminosity scaling factor is applied to the MC and no further factors like trigger efficiency or *particleID* efficiency is taken into account. The overall functionality of reconstruction, background suppression and fitting strategy was proven to work for the  $B^\pm \rightarrow X(3872)K^\pm$ ,  $X(3872) \rightarrow D^0\bar{D}^0\pi^0$  reference channel in Sec. VI.4. Given those results, the  $X(4014)$  signal region for  $711 \text{ fb}^{-1}$  of Belle data is unblinded in this section. The final selections, after BCS, are:

- $|\Delta E| < 12 \text{ MeV}$
- $M_{BC} > 5.274 \text{ GeV}/c^2$
- $dq = M(X4014) - 2 \cdot M(D^0) - 2 \cdot M(\pi^0) < 40 \text{ MeV}/c^2$

Fig. VI.14 shows the  $M(D^0\bar{D}^0\pi^0\pi^0)$  invariant mass distribution for the  $X(4014)$  signal region as defined above. Marker with errorbars show the data, luminosity scaled generic MC is illustrated as dashed blue histogram. Within the expected  $X(4014)$  mass region of  $4.01 < M(X(4014)) < 4.02 \text{ GeV}/c^2$ , no significant structure can be observed. This outcome was already anticipated by the results of the Belle II simulation in Sec. V.4.7. For a simulated data sample of  $711 \text{ fb}^{-1}$  the fitting showed now significant signal, even for scenarios where the branching fraction ( $10^{-4}$ ) and width (1.2 MeV) are comparable to the  $X(3872)$ . For the Belle simulation a reconstruction efficiency on signal MC of  $\approx 0.5 \%$  was achieved, which is about a factor of 2 smaller than the one computed for the Belle II simulation. To see a significant structure in the  $X(4014)$  mass region was therefore not expected. However, the region above  $4.02 \text{ GeV}/c^2$  and below  $4.03 \text{ GeV}/c^2$ , shows an enhancement in data compared to the generic MC.

## VI.5. Unblinding of Data in the X(4014) Signal Region

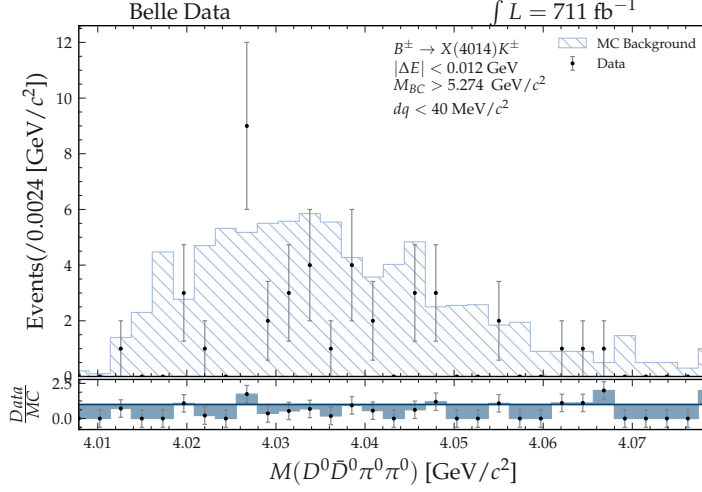


Figure VI.13: Data/MC comparison of the  $D^0\bar{D}^0\pi^0\pi^0$  invariant mass in the  $M_{BC}$ ,  $\Delta E$  and  $dq$  signal region.

Within the vicinity of that enhancement, another charmonium resonance, the X(4025), is located. This resonance was first observed by the BESIII experiment, as a charged state in 2014 [108]. Soon after the first observation, the BESIII collaboration published a second paper, in which the observation was made in a neutral decay  $X(4025) \rightarrow D^{*0}\bar{D}^{*0}$  [109]. Both observations were produced directly in  $e^+e^-$  collisions at a center of mass energy of  $\sqrt{s} = 4.23$  GeV.

The neutral X(4025) resonance is found to have a width of  $23.0 \pm 6$  MeV, which is much broader than the structure observed in Fig. VI.14. A reason for that could be the  $dq < 40$  MeV selection for a potential X(4014). For the X(4025) resonance a  $dq$  value of  $M(X4025) - 2 \cdot M(D^0) - 2 \cdot M(\pi^0) \approx 25$  MeV/ $c^2$  is expected. Thus, in addition to the  $|\Delta E| < 12$  MeV and  $M_{BC} > 5.274$  GeV/ $c^2$  selection, a value of  $dq < 100$  MeV/ $c^2$  was applied as selection cut for the  $D^0\bar{D}^0\pi^0\pi^0$  invariant mass data. If the structure is a true resonance, the  $\Delta E$  and  $M_{BC}$  distributions should also peak in the vicinity of that mass<sup>6</sup>.

<sup>6</sup>*Conditio sine qua non* - a necessary but not sufficient condition.

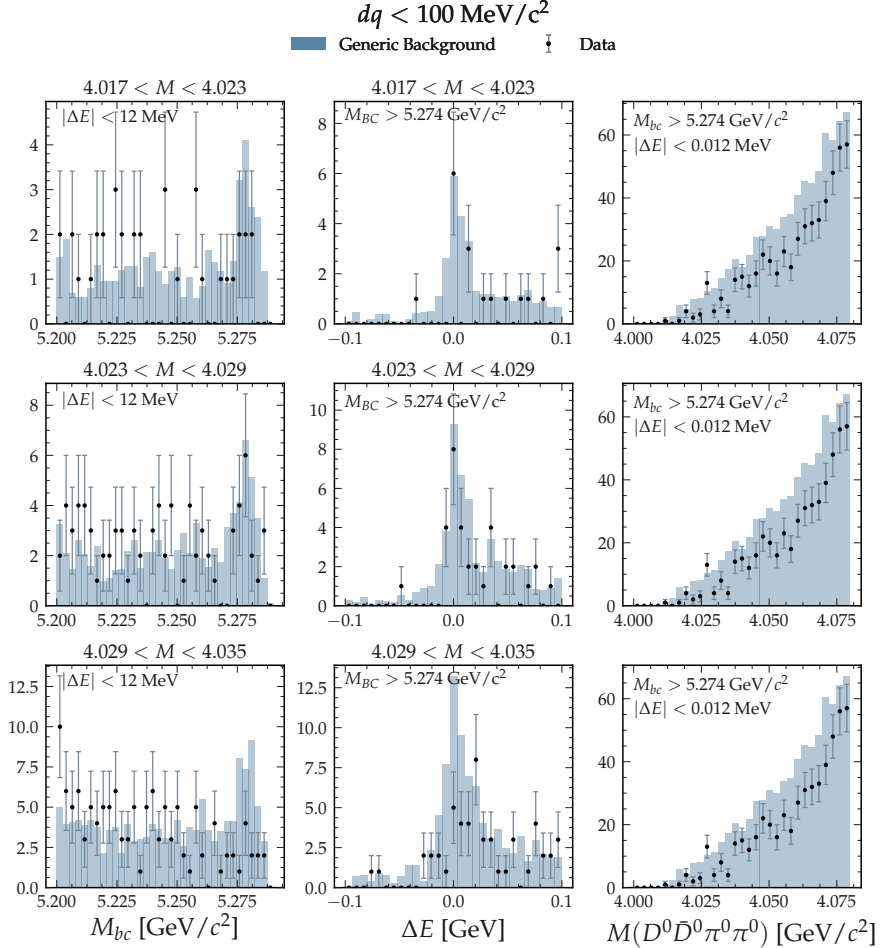


Figure VI.14: Plot matrix for  $M_{BC}$  (right),  $\Delta E$  (center) and  $M(D^0\bar{D}^0\pi^0\pi^0)$  (left). A common selection of  $dq < 100 \text{ MeV}/c^2$  is applied for all subplots. The left column for the invariant  $D^0\bar{D}^0\pi^0\pi^0$  is selected in the  $M_{BC} > 5.274 \text{ GeV}/c^2$  and  $\Delta E < 12 \text{ MeV}$  signal window. For the right column ( $M_{BC}$ ), a  $\Delta E < 12 \text{ MeV}$  and for the center column ( $\Delta E$ ) a  $M_{BC} > 5.274 \text{ GeV}/c^2$  selection is applied. From top to bottom the invariant  $D^0\bar{D}^0\pi^0\pi^0$  mass window is increased in bins of  $6 \text{ MeV}/c^2$ , starting at  $4.017 \text{ GeV}/c^2$ . Data is shown as black dots with errorbars, generic MC is indicated as blue histogram. The binning for the  $D^0\bar{D}^0\pi^0\pi^0$  plot is set to  $2.5 \text{ MeV}/c^2$ , which is close to the fitted  $X(3872)$  width from Fig. VI.12 (a).

The  $\Delta E$  and  $M_{BC}$  distributions are therefore sampled in  $D^0\bar{D}^0\pi^0\pi^0$  invariant mass bins of 6 MeV/c<sup>2</sup>. For the  $\Delta E$  sample the  $M_{BC}$  is forced to be greater than 5.274 GeV/c<sup>2</sup> and for the  $M_{BC}$  sample  $\Delta E$  is set to range from -12 to 12 MeV/c<sup>2</sup>. The sampling starts at 4.007 GeV/c<sup>2</sup> and increases, in three steps, to a maximum invariant mass of 4.035 GeV/c<sup>2</sup>. A plotting matrix of the sampling is shown in VI.14. The right column in this plot always shows the  $D^0\bar{D}^0\pi^0\pi^0$  invariant mass distribution in the  $\Delta E$  and  $M_{BC}$  signal region in bins of 2.5 MeV/c<sup>2</sup>, which is approximately the width of the fitted X(3872) resonance in Fig. VI.12.

In Fig. VI.14 the observed structure in the  $D^0\bar{D}^0\pi^0\pi^0$  invariant mass region of 4.023 to 4.029 GeV/c<sup>2</sup> is still enhanced compared to the rest of the distribution. One can also notice that  $\Delta E$  and  $M_{BC}$  have a peaking structure for that mass region, which fades when for both,  $\Delta E$  and  $M_{BC}$ , the invariant mass region is increasing to  $4.029 < M(D^0\bar{D}^0\pi^0\pi^0) < 4.035$  GeV/c<sup>2</sup>. For the  $M_{BC}$  distribution this also applies for the lower mass bin from  $4.017 < M(D^0\bar{D}^0\pi^0\pi^0) < 4.023$  GeV/c<sup>2</sup>.

The MC, indicated as light blue histogram in Fig. VI.14, is scaled to the data luminosity and does not correct any source of uncertainty like trigger efficiency or *particleID* efficiency. Only the generic MC is included. For the signal region invariant mass bin (the center row of Fig. VI.14) the data and MC seem to have good agreement in  $\Delta E$  and  $M_{BC}$ , while MC is a bit over represented in  $M(D^0\bar{D}^0\pi^0\pi^0)$ . For the other mass bins, MC and data do not match as good as in the signal region mass bin. Compared to the X(3872) data to MC comparison from Fig. VI.8, the data shows now significant enhancement over MC in the  $\Delta E$  and  $M_{BC}$  signal region.

The center row of Fig. VI.14 is examined a bit closer and a 2D fit in  $M_{BC}$  and  $M(D^0\bar{D}^0\pi^0\pi^0)$  is performed. For the  $M_{BC}$  distribution the sum of a Gaussian function and an Argus is used. The  $D^0\bar{D}^0\pi^0\pi^0$  invariant mass is fitted with a threshold function

$$t(M; p_0, p_1, p_2, \mu_0) = p_0 \cdot (M - \mu_0)^{p_1} * e^{p_2 \cdot (M - \mu_0)}$$

for the background and a Breit Wigner convoluted with a Gaussian for the peak. The background shape parameters,  $p_0$ ,  $p_1$ ,  $p_2$  and  $\mu_0$ , are taken from a fit to the generic background MC. For the peak-component of the

fit the resolution parameters of the Breit Wigner and the Gaussian are kept floating between 0 and 15 MeV. Since the fit should not be biased towards a certain peak position, the mean value  $\mu$  of the Breit Wigner was set floating between  $-\infty$  and  $\infty$ . When performing the fit for several initial Breit Wigner mean values,  $\mu$ , between 4.02 and 4.03 GeV/c<sup>2</sup>, the  $M_{BC}$ , as well as the  $M(D^0\bar{D}^0\pi^0\pi^0)$  PDF, are both showing a peaking structure. Outside of that range, no peaking structure are observed for both distributions.

Since a more detailed investigation on the significance of that enhancement needs more time, a dedicated signal MC study and tuning of the reconstruction strategy for a potential  $B^\pm \rightarrow X(4025)(D^0\bar{D}^0\pi^0\pi^0)K^\pm$  decay, it was not longer pursued within this thesis. Still, a closer look into that area could lead to more evidence for a resonant charmonium like structure around 4.025 GeV/c<sup>2</sup> and can be considered for future studies.



# Summary and Outlook

## VII.1 Alternative Output for the Belle II Pixel Detector DAQ

A feasibility study for an alternative data output routing for the Belle II PXD DAQ, via a 10 GbE shelf-switch was performed and tested. The firmware needed for this project, namely the `l1_combiner` IP-core, was developed and tested with an updated version for the EPICS and CSS slow control system, featuring new OPIs for the displaying of data rates and data flow. Due to missing DHH hardware on the sending side, two independent tests for data integrity and long term stability were successfully performed. No errors in the data transmission were seen and the incoming pixel pattern could be matched perfectly to the selected pattern, transmitted by the ONSSEN system. During the long time stability test, which was carried out for almost 3 days, no bit errors, link errors or framing errors occurred. The data and trigger rate showed no drops, indicating a smooth data taking at a maximum rate of 950 MB/s, which is about 30% more than required.

For a test on the final system at KEK in Japan, the receiving EVB2 must be modified to receive data on one cable and 8 links, instead of 32 cables and links. An additional feature, which could be introduced to the `l1_combiner`, is a re-framing of the four data packets received by the individual selector-AMC cards to one single frame transmitted to the EVB2. In that case, the receiving side just needs to wait until the final end of frame signal, instead of counting four end of frames, which, up to now, make up a full data packet from one selector-carrier. The final implementation into the Belle II DAQ system requires changes outside the ONSSEN system such as e.g. on the EVB2.

## VII.2 Search for an Exotic Resonance at the $D^{*0}\bar{D}^{*0}$ Threshold in Charged $B$ Meson Decays

The analysis part of this thesis splits up in two chapters, one covering the simulation of a potential  $X(4014)$  resonant partner state to the  $X(3872)$  at the  $D^{*0}\bar{D}^{*0}$  threshold, the other one covers the search of this state in Belle data and verifies a working reconstruction by using the  $X(3872)$  as a reference channel.

### VII.2.1 Simulation of a Resonant Structure at the $D^{*0}\bar{D}^{*0}$ threshold in $B$ decays at Belle II

A resonant structure, mimicking the potential  $X(4014)$  with a mass of  $M = 4014 \text{ MeV}/c^2$  and  $\text{spin} = 0$ , was simulated with 6 different widths of  $\Gamma = 0, 1.2, 3, 5, 7, 10 \text{ MeV}$  at the  $D^{*0}\bar{D}^{*0}$  threshold. A first simulation was performed with the decay  $B^\pm \rightarrow X(4014)K^\pm$  where  $X(4014)$  decays to  $D^{*0}\bar{D}^{*0}$ , which are reconstructed in the  $D^{*0} \rightarrow D^0\gamma$  and the  $D^{*0} \rightarrow D^0\pi^0$  channel. It was observed that, due to the relatively soft photon, the invariant mass distribution of the  $X(4014)$  becomes very broad, if no mass-vertex constrained fit is applied to the reconstructed  $D^{*0}$ s. In case of a mass-vertex constrained fit, possible entries below  $4014 \text{ MeV}/c^2$  in the invariant mass distribution of the  $X(4014)$  would be ruled out and thus, the resonance could not be observed if the pole would be slightly below the  $D^{*0}\bar{D}^{*0}$  threshold. Another strategy, skipping the  $D^{*0}$  reconstruction, and thus get rid of the mass-vertex constrained fit, was pursued and the  $X(4014)$  is reconstructed directly in  $D^0\bar{D}^0\pi^0\pi^0$ . The most crucial issues during reconstruction arise, when including the beam-backgrounds to the simulation. Due to the large number of generated photons, also the number of reconstructed  $\pi^0$  candidates, most dominantly in the low energetic regime, rises significantly. Since the  $\pi^0$  stemming from the  $X(4014)$  decay carry only a very low momentum, an energy selection of  $100 \text{ MeV}$  for photons would suppress almost all correctly reconstructed  $X(4014)$  candidates and thus bring the reconstruction efficiency to almost 0. Another way to suppress the high backgrounds, without losing a large fraction of the correct reconstructed  $\pi^0$  candidates, needed to be found. An Online Candidate Selection, which selected a number of "good"  $\pi^0$  per event, online, during reconstruction, was implemented. The OCS is based upon the decay angle of the first photon relative to the momentum of the  $\pi^0$  in the mothers rest frame. Since the  $\pi^0$  is an unpolarized

2-photon state, this distribution should be flat for correctly reconstructed  $\pi^0$ . In addition to the decay angle, also the center of mass momentum of the  $\pi^0$  is used. For each reconstructed  $\pi^0$  a  $\chi^2$ -function, combining those parameters, is introduced and the  $n$ -best candidates minimizing this function per event is kept. This method is also used to decrease the backgrounds for the  $D^0 \rightarrow K^\pm \pi^\mp \pi^0$  as well as the  $D^0 \rightarrow K^\pm \pi^\mp \pi^\pm \pi^\mp$  channels and the  $X(4014)$  itself. As a final reconstruction step, a Best Candidate Selection to the reconstructed  $B^\pm$  meson is applied, including the individual width of all  $D^0$  channels, the *particleID*, *dz* and *d0* of all final state  $K^\pm$  and  $\pi^\mp$ , the width of the  $\pi^0$  and a selection on the  $\Delta E$  distribution - which should peak at 0 for a correctly reconstructed  $B^\pm$  meson.

The whole reconstruction was performed for 6 different simulated width and 10 different assumed branching fractions,  $Br(B^\pm \rightarrow X(4014)K^\pm)$  of 0.1, 0.2, 0.3, 0.4, 0.5, 0.6, 0.7, 0.8, 0.9,  $1 \cdot 10^{-4}$ . The individual components of the reconstructed  $X(4014)$  invariant mass spectrum, for the different scenarios, are then fitted with an unbinned maximum likelihood fit and the shape parameters extracted. For the final, combined fits, the shape parameters are fixed and the total fit is applied to the total invariant mass spectrum for 3 different data sets of  $711 \text{ fb}^{-1}$ ,  $2 \text{ ab}^{-1}$  and  $14 \text{ ab}^{-1}$ . This procedure was performed once with a background fit to the sideband regions, leaving out the signal region (shape independent model), and once with a signal plus background fit over the full range (shape dependent model). The significance of the signal was calculated by comparing the observed events in the signal region with the expected events calculated from the background only fit to the sidebands, for the shape independent model, and by comparing the log-likelihood values of the signal plus background fit with the one from the background only fit over the full range for the shape dependent model. In total, 540 fits for the two different methods, each for combinations of 10 different branching fractions, 6 different generated width and 3 data sets were performed. The results are shown in discovery maps, which give rise to the discovery potential of different Belle II data sets for different scenarios of the  $X(4014)$  width and branching fraction. Already with a data set of  $2 \text{ ab}^{-1}$ , Belle II will have good chances to discover this resonance, if it exists. In general it can be stated, that for smaller branching fractions and larger width combinations, the discovery potential is massively decreasing, while for the opposite combination of larger branching fraction and smaller width, the discovery potential is significant.

## VII.2.2 Search for an Exotic Resonance at the $D^{*0}\bar{D}^{*0}$ Threshold in Charged $B$ Meson Decays at Belle

The Belle experiment, which was running from 1999 to 2010, collected a  $B\bar{B}$  data sample of  $\int Ldt = 711 \text{ fb}^{-1}$  - until now the worlds largest  $B\bar{B}$  sample. In Sec. VI, a search for a potential resonant structure at the  $D^{*0}\bar{D}^{*0}$  threshold in  $B^\pm \rightarrow D^0\bar{D}^0\pi^0\pi^0K^\pm$  was performed on that data set. The reconstruction strategy was taken from the one optimized on the Belle II simulation described in Sec. V. Apart from changes in the *particleID* selection, due to a well tuned particle identification for the Belle experiment, and different selection values for the online candidate selection, the reconstruction was not changed. In the Belle case, a  $X(4014) \rightarrow D^0\bar{D}^0\pi^0\pi^0$  signal MC with 100000 events was simulated and a reconstruction efficiency of  $\approx 0.5\%$ <sup>1</sup> was achieved.

Before unblinding the data in signal region, a data to MC comparison was performed and a reference channel was analyzed on data. The data MC comparison showed good agreement between data and data luminosity weighted MC when considering no additional error sources like trigger efficiency or *particleID* efficiency. For the reference channel the  $B^\pm \rightarrow X(3872)(D^0\bar{D}^0\pi^0)K^\pm$  channel was chosen, since it is only missing one  $\pi^0$  in the reconstruction, compared to the  $X(4014)$  decay. A comparison of data and MC for the final selection variables of the  $X(3872)$ , the beam constrained mass  $M_{BC}$  and  $\Delta E$ , was performed with a generic MC sample scaled to data luminosity for the full  $711 \text{ fb}^{-1}$  Belle data sample. Since the comparison showed a good agreement within the statistical errorbars, a fit to the  $D^0\bar{D}^0\pi^0$ ,  $\Delta E$  and  $M_{BC}$  distributions was performed.  $\Delta E$  was fitted with a unbinned maximum likelihood fit in the  $M_{BC} > 5.27 \text{ GeV}/c^2$ ,  $M(D^0\bar{D}^0\pi^0) < 3.88 \text{ GeV}/c^2$  and  $dq = M(X(3872)) - 2 \cdot M(D^0) - M(\pi^0) < 40 \text{ MeV}/c^2$  signal region. A signal yield of  $20 \pm 6$  candidates was fitted in the Gaussian signal peak. For the  $M_{BC}$  and  $D^0\bar{D}^0\pi^0$  distributions, a 2-dimensional fit was performed to increase the significance of the fitted peaks. For both variables the background was split up in a generic<sup>2</sup>, a combinatorial<sup>3</sup> and a non-resonant<sup>4</sup> component, which add up to the total background PDF. For the signal component a Gaussian function for the  $M_{BC}$  distribution and a

<sup>1</sup> 1/2 of the efficiency achieved for the Belle II simulation.

<sup>2</sup> Taken from the official Belle generic MC sample corresponding to 3 times the Belle data set.

<sup>3</sup> Candidates which do not satisfy the MCtruth selection on signal MC

<sup>4</sup>  $B^\pm \rightarrow D^0\bar{D}^0\pi^0K^\pm$  and  $B^\pm \rightarrow D^0\bar{D}^0K^\pm$  decays

Breit Wigner convoluted with a Gaussian function for the  $M(D^0\bar{D}^0\pi^0)$  component was used. The 2-dimensional unbinned extended maximum likelihood fit yields  $28 \pm 3$  signal candidates in the peak with a  $X(3872)$  mean and width of  $\mu = 3874.1 \pm 1.1 \text{ GeV}/c^2$  and  $\sigma = 2.62 \pm 0.7 \text{ MeV}$  respectively. When performing the fit without the signal PDF component and comparing the two log-likelihood values<sup>5</sup>, a significance of  $11.26 \sigma$  was achieved. The branching fraction  $\mathcal{B}(B^\pm \rightarrow X(3872)K^\pm) \cdot \mathcal{B}(X(3872) \rightarrow D^0\bar{D}^0\pi^0)$  was calculated as  $(0.92 \pm 0.1) \cdot 10^{-4}$ . As can be seen in Tab. VI.4, the fitted values and the calculated branching fraction are in good agreement with the values published in the PDG. The errors on all parameters only include the statistical error! Since the reconstruction and fitting strategy was proven to work for the  $B^\pm \rightarrow X(3872)(D^0\bar{D}^0\pi^0)K^\pm$  channel and the data MC comparison was in good agreement, the signal window for the  $X(4014)$  was opened. As could be already anticipated from the Belle II simulation, where the reconstruction efficiency was a factor 2 larger, no significant peak could be observed for the  $711 \text{ fb}^{-1}$  Belle data set. However, a structure around  $4025 \text{ MeV}/c^2$  was found in the  $D^0\bar{D}^0\pi^0\pi^0$  invariant mass spectrum. An investigation on the  $M_{BC}$  and  $\Delta E$  distributions for three different  $D^0\bar{D}^0\pi^0\pi^0$  mass regions was made. For a  $D^0\bar{D}^0\pi^0\pi^0$  invariant mass between  $4.023$  and  $4.029 \text{ MeV}/c^2$  the  $M_{BC}$  and the  $\Delta E$  distribution showed a peaking structure, which could be in agreement with the  $X(4025)$  resonance observed at BES III in neutral and charged  $D^*$  decays. Since the structure was, by eye, not significant enough and a more detailed investigation would have taken more time and another signal MC selection optimized for the  $X(4025)$ , it was not further pursued.

The work done in this thesis showed that for a larger Belle II data set ( $> 2 \text{ ab}^{-1}$ ) a search for the  $X(4014)$  resonance in  $D^0\bar{D}^0\pi^0\pi^0$  is feasible and could lead to an evidence or discovery, if the resonance has an advantageous width and branching fraction. The overall reconstruction and fitting strategy was performed for different scenarios of the  $X(4014)$  on Belle II MC and tested on Belle data with the  $B^\pm \rightarrow X(3872)(D^0\bar{D}^0\pi^0)K^\pm$  reference channel, where the fitted parameters showed good agreement with the published PDG values.

---

<sup>5</sup> $\sigma = \sqrt{2 \cdot (\ln(S+B) - \ln(B))}$

*Chapter VII. Summary and Outlook*

---

# Appendix A

**P**ART A of the appendix collects all fitting parameters and plots for the Belle II simulation performed in Chapter V of this thesis. The first section covers the fitting parameters of all intermediate resonances<sup>1</sup> and the parameters of the final fit. In the second section, plots and tables for the data/MC comparison, as explained in V.5, are presented.

## VIII.1 Fitting Parameters of Belle II Signal MC Fits

### VIII.1.1 Fits to Intermediate Resonances

#### VIII.1.1.1 $\pi^0$ from $D^0$

Function	Crystal Ball	Function	1 <sup>st</sup> order Chebychev
Events	$116505 \pm 1325$	Events	$959376 \pm 13482$
$\mu$	$0.13253 \pm 0.00009$	$a_0$	$-0.176 \pm 0.013$
$\sigma$	$0.00563 \pm 0.00021$		
$\alpha$	$1.05 \pm 0.19$		

(a) Signal Fit

(b) Background Fit

**Table VIII.1:** Fit parameters for the fit to the  $\gamma\gamma$  invariant mass distribution for  $\pi^0$  stemming from  $D^0$ . Signal (a), Background (b).

<sup>1</sup> $\pi^0$  and  $D^0$  plots are shown in sections V.2.3 and V.2.5 of Chapter V.

**VIII.1.1.2  $\pi^0$  from X(4014) Fit**

Function	Crystal Ball + Gaussian	Function	1 <sup>st</sup> order Chebychev
Events	$89717 \pm 5431$	Events	$797377 \pm 43776$
$\mu_{CB}$	$0.1331 \pm 0.0005$	$a_0$	$-0.5293 \pm 0.0915$
$\sigma_{CB}$	$0.0199 \pm 0.0012$	(b) Background Fit	
$\alpha$	$0.6435 \pm 0.4381$		
$\mu_G$	$0.1324 \pm 0.0009$		
$\sigma_G$	$0.0699 \pm 0.0062$		

(a) Signal Fit

**Table VIII.3:** Fit parameters for the fit to the  $\gamma\gamma$  invariant mass distribution for  $\pi^0$  stemming from X(4014). Signal (a), Background (b).

VIII.1.1.3  $D^0 \rightarrow K^\pm \pi^\mp$  Fit

Function	Gaussian + Gaussian	Function	1 <sup>st</sup> order Chebychev
Events	$17772 \pm 191$	Events	$22285 \pm 203$
$\mu_{G1}$	$1.8646 \pm 0.0001$	$a_0$	$-0.20353 \pm 0.01178$
$\sigma_{G1}$	$0.0028 \pm 0.0001$	(b) Background Fit	
$\mu_{G2}$	$1.8631 \pm 0.0004$		
$\sigma_{G2}$	$0.0081 \pm 0.0007$		
(a) Signal Fit			

Table VIII.5: Fit parameters for the fit to the  $K^\pm \pi^\pm$  invariant mass distribution for  $D^0$  reconstruction. Signal (a), Background (b).

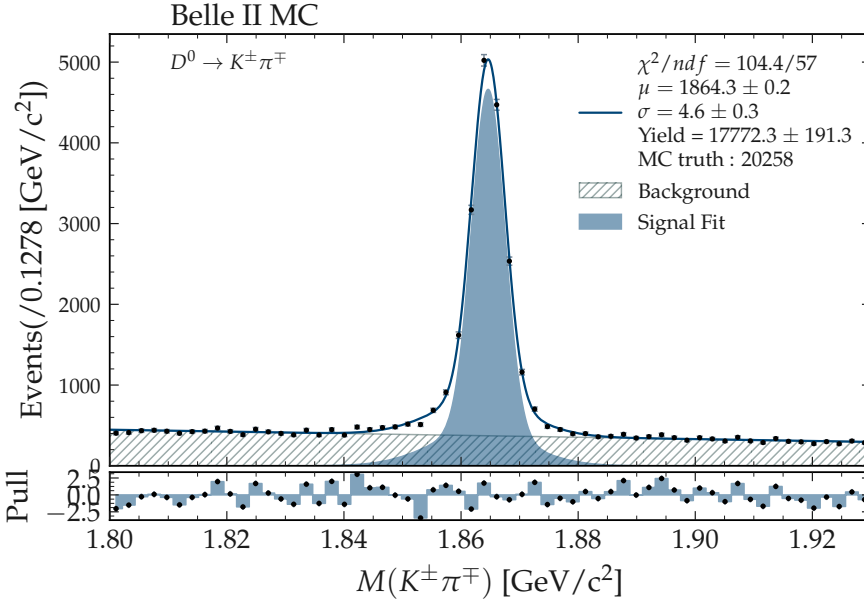


Figure VIII.1: Fit to the  $D^0$  invariant mass spectra for the  $K^\pm \pi^\mp$  decay channel.

VIII.1.1.4  $D^0 \rightarrow K^\pm \pi^\mp \pi^0$  Fit

Function	Crystal Ball + Gaussian	Function	2 <sup>nd</sup> order Chebychev
Events	$33947 \pm 907$	Events	$622781 \pm 7666$
$\mu_{CB}$	$1.8635 \pm 0.0017$	$a_0$	$-0.10838 \pm 0.00823$
$\sigma_{CB}$	$0.0043 \pm 0.0007$	$a_1$	$-0.02363 \pm 0.00748$
$\mu_G$	$1.8649 \pm 0.0159$	(b) Background Fit	
$\sigma_G$	$0.0127 \pm 0.0025$		

(a) Signal Fit

Table VIII.7: Fit parameters for the fit to the  $K^\pm \pi^\pm \pi^0$  invariant mass distribution for  $D^0$  reconstruction. Signal (a), Background (b).

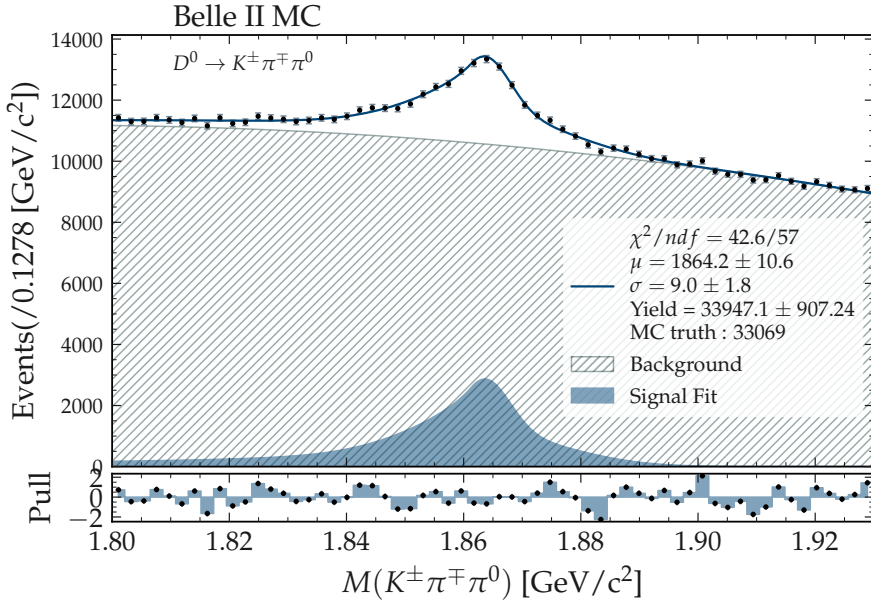


Figure VIII.2: Fit to the  $D^0$  invariant mass spectra for the  $K^\pm \pi^\mp \pi^0$  decay channel.

VIII.1.1.5  $D^0 \rightarrow K^\pm \pi^\mp \pi^\pm \pi^\mp$  Fit

Function	Gaussian + Gaussian	Function	2 <sup>nd</sup> order Chebychev
Events	$11394 \pm 447$	Events	$206957 \pm 508$
$\mu_{G1}$	$1.86366 \pm 0.00024$	$a_0$	$0.03473 \pm 0.00315$
$\sigma_{G1}$	$0.00496 \pm 0.00041$	$a_1$	$-0.03766 \pm 0.00424$
$\mu_{G2}$	$1.86434 \pm 0.00009$		
$\sigma_{G2}$	$0.00208 \pm 0.00047$		

(a) Signal Fit

(b) Background Fit

Table VIII.9: Fit parameters for the fit to the  $K^\pm \pi^\mp \pi^\pm \pi^\mp$  invariant mass distribution for  $D^0$  reconstruction. Signal (a), Background (b).

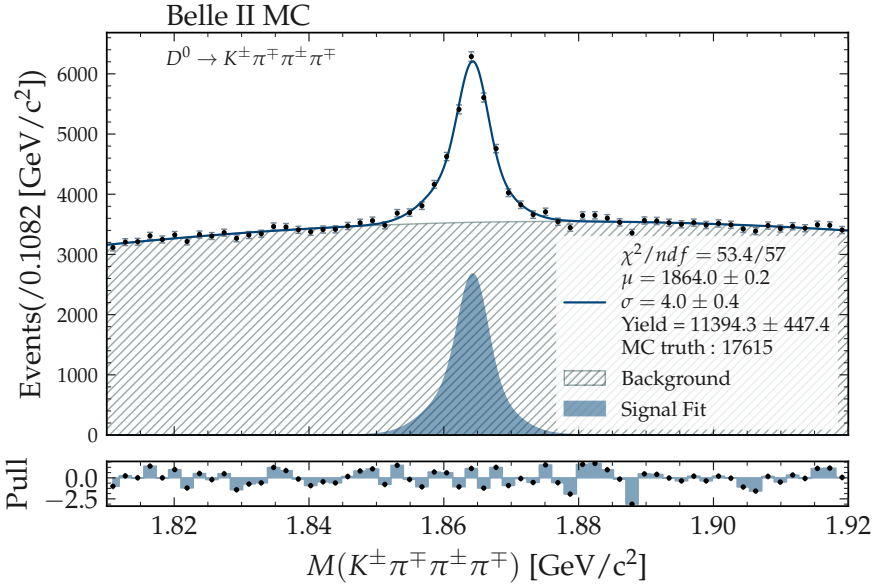


Figure VIII.3: Fit to the  $D^0$  invariant mass spectra for the  $K^\pm \pi^\mp \pi^\pm \pi^\mp$  decay channel.

VIII.1.1.6  $D^0 \rightarrow K_S^0 \pi^\pm \pi^\mp$  Fit

Function	Gaussian + Gaussian	Function	2 <sup>nd</sup> order Chebychev
Events	$8076 \pm 165$	Events	$20284 \pm 199$
$\mu_{G1}$	$1.86531 \pm 0.00008$	$a_0$	$-0.08519 \pm 0.01223$
$\sigma_{G1}$	$0.00256 \pm 0.00014$	$a_1$	$-0.08973 \pm 0.01647$
$\mu_{G2}$	$1.86449 \pm 0.00027$		
$\sigma_{G2}$	$0.00625 \pm 0.00064$		

(b) Background Fit

(a) Signal Fit

Table VIII.11: Fit parameters for the fit to the  $K_S^0 \pi^\pm \pi^\mp$  invariant mass distribution for  $D^0$  reconstruction. Signal (a), Background (b).

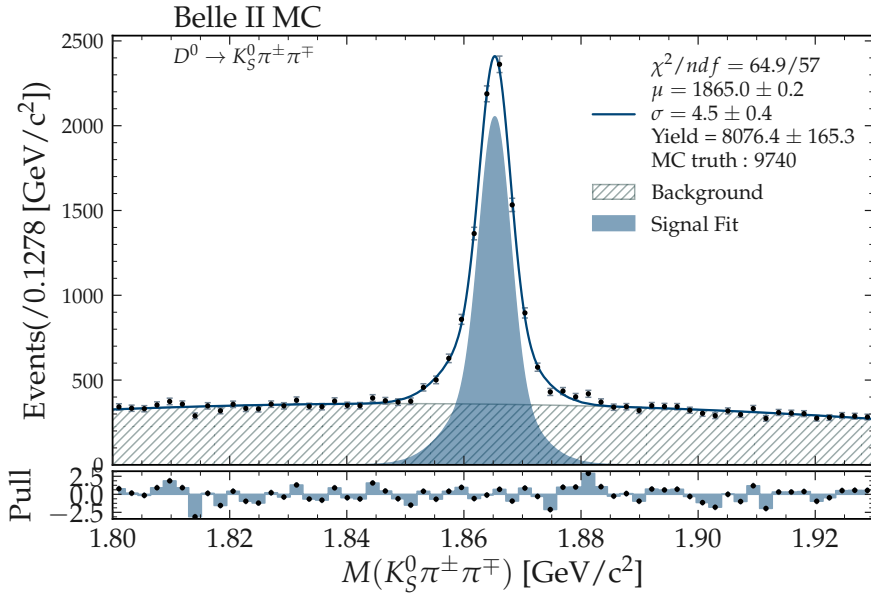


Figure VIII.4: Fit to the  $D^0$  invariant mass spectra for the  $K_S^0 \pi^\pm \pi^\mp$  decay channel.

VIII.1.1.7  $D^0 \rightarrow K^\pm K^\mp$  Fit

Function	Gaussian + Gaussian	Function	$2^{nd}$ order Chebychev
Events	$15387 \pm 516$	Events	$22278 \pm 244$
$\mu_{G1}$	$1.86433 \pm 0.00004$	$a_0$	$-0.13585 \pm 0.01169$
$\sigma_{G1}$	$0.00262 \pm 0.00007$	$a_1$	$-0.09437 \pm 0.01781$
$\mu_{G2}$	$1.86344 \pm 0.00041$		
$\sigma_{G2}$	$0.00697 \pm 0.00112$		

(a) Signal Fit

(b) Background Fit

Table VIII.13: Fit parameters for the fit to the  $K^\pm K^\pm$  invariant mass distribution for  $D^0$  reconstruction. Signal (a), Background (b).

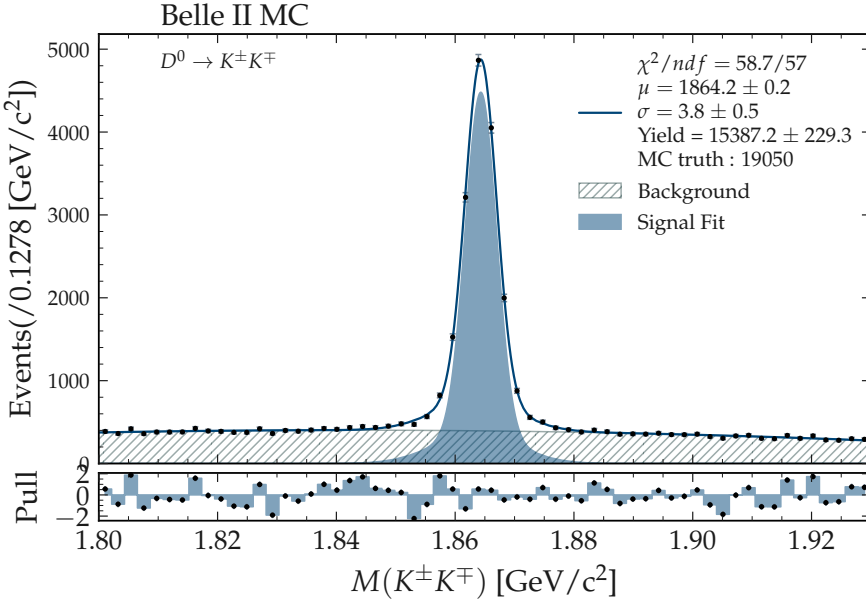


Figure VIII.5: Fit to the  $D^0$  invariant mass spectra for the  $K^\pm K^\mp$  decay channel.

## VIII.1.2 Fits to the $D^0$ Resonances Without PXD

### VIII.1.2.1 $D^0 \rightarrow K^\pm \pi^\mp$ Fit

Function	Gaussian + Gaussian	Function	1 <sup>st</sup> order Chebychev
Events	$7651 \pm 178$	Events	$22734 \pm 192$
$\mu_{G1}$	$1.86472 \pm 0.00004$	$a_0$	$-0.17872 \pm 0.01162$
$\sigma_{G1}$	$0.00293 \pm 0.00005$		
$\mu_{G2}$	$1.86280 \pm 0.00046$		
$\sigma_{G2}$	$0.00814 \pm 0.00061$		

(a) Signal Fit

(b) Background Fit

Table VIII.15: Fit parameters for the fit to the  $K^\pm \pi^\pm$  invariant mass distribution for  $D^0$  reconstruction **without PXD**. Signal (a), Background (b).

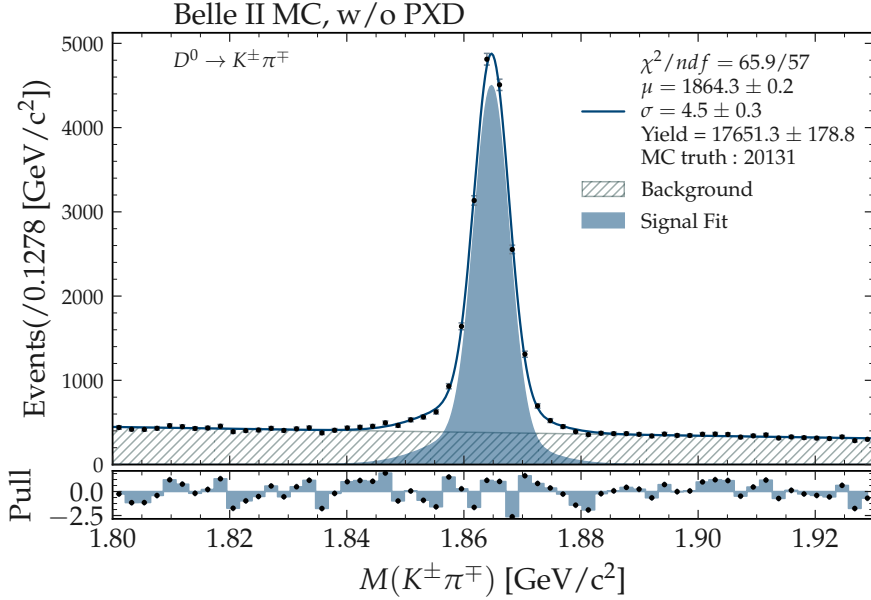


Figure VIII.6: Fit to the  $D^0$  invariant mass spectra for the  $K^\pm \pi^\mp$  decay channel.

VIII.1.2.2  $D^0 \rightarrow K^\pm \pi^\mp \pi^0$  Fit

Function	Crystal Ball + Gaussian	Function	$2^{nd}$ order Chebychev
Events	$38121 \pm 3336$	Events	$622533 \pm 2193$
$\mu_{CB}$	$1.86244 \pm 0.00501$	$a_0$	$-0.108915 \pm 0.065892$
$\sigma_{CB}$	$0.00779 \pm 0.00099$	$a_1$	$-0.012447 \pm 0.018927$
$\mu_G$	$1.86489 \pm 0.00129$		
$\sigma_G$	$0.01903 \pm 0.01419$		

(a) Signal Fit

(b) Background Fit

Table VIII.17: Fit parameters for the fit to the  $K^\pm \pi^\pm \pi^0$  invariant mass distribution for  $D^0$  reconstruction **without** PXD. Signal (a), Background (b).

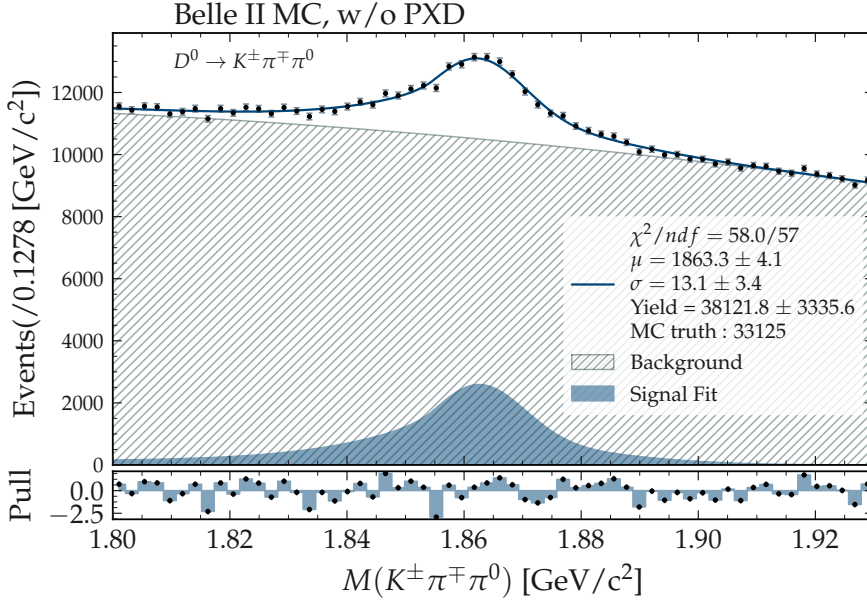


Figure VIII.7: Fit to the  $D^0$  invariant mass spectra for the  $K^\pm \pi^\mp \pi^0$  decay channel.

VIII.1.2.3  $D^0 \rightarrow K^\pm \pi^\mp \pi^\pm \pi^\mp$  Fit

Function	Gaussian + Gaussian	Function	2 <sup>nd</sup> order Chebychev
Events	11449 ± 554	Events	209417 ± 707
$\mu_{G1}$	1.865527 ± 0.002409	$a_0$	0.042724 ± 0.004115
$\sigma_{G1}$	0.006571 ± 0.002524	$a_1$	-0.023951 ± 0.005484
$\mu_{G2}$	1.863873 ± 0.000163		
$\sigma_{G2}$	0.002679 ± 0.000732		

(a) Signal Fit (b) Background Fit

Table VIII.19: Fit parameters for the fit to the  $K^\pm \pi^\mp \pi^\pm \pi^\mp$  invariant mass distribution for  $D^0$  reconstruction **without** PXD. Signal (a), Background (b).

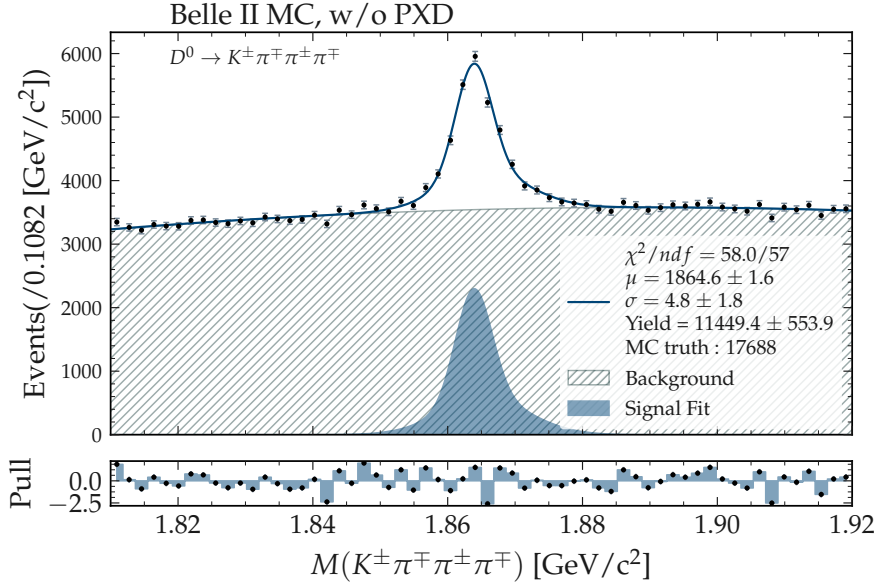


Figure VIII.8: Fit to the  $D^0$  invariant mass spectra for the  $K^\pm \pi^\mp \pi^\pm \pi^\mp$  decay channel.

VIII.1.2.4  $D^0 \rightarrow K_S^0 \pi^\pm \pi^\mp$  Fit

Function	Gaussian + Gaussian	Function	$2^{nd}$ order Chebychev
Events	$8611 \pm 216$	Events	$20736 \pm 242$
$\mu_{G1}$	$1.86525 \pm 0.00007$	$a_0$	$-0.0738 \pm 0.0122$
$\sigma_{G1}$	$0.00285 \pm 0.00011$	$a_1$	$-0.0431 \pm 0.0189$
$\mu_{G2}$	$1.86486 \pm 0.00036$		
$\sigma_{G2}$	$0.00858 \pm 0.00083$		

(a) Signal Fit

(b) Background Fit

Table VIII.21: Fit parameters for the fit to the  $K_S^0 \pi^\pm \pi^\pm$  invariant mass distribution for  $D^0$  reconstruction **without** PXD. Signal (a), Background (b).

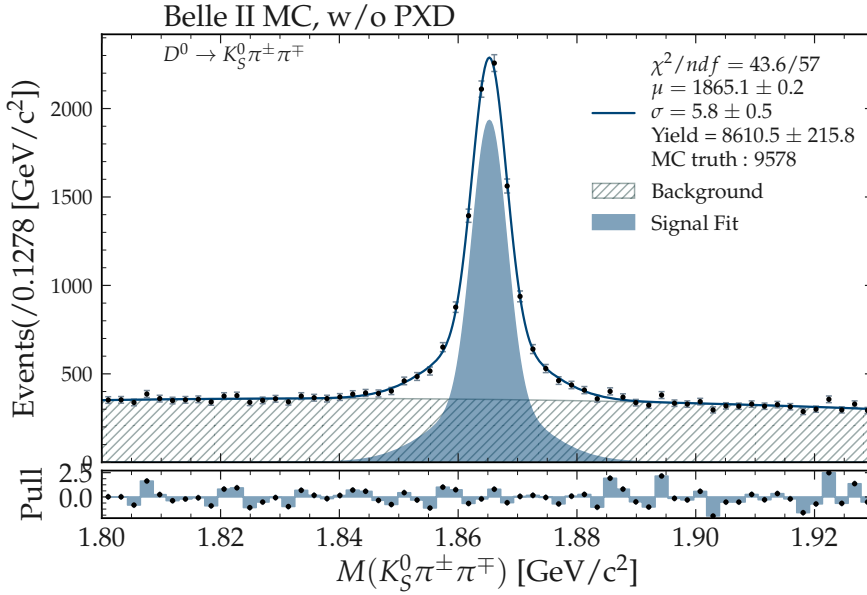


Figure VIII.9: Fit to the  $D^0$  invariant mass spectra for the  $K_S^0 \pi^\pm \pi^\mp$  decay channel.

VIII.1.2.5  $D^0 \rightarrow K^\pm K^\mp$  Fit

Function	Gaussian + Gaussian	Function	2 <sup>nd</sup> order Chebychev
Events	15734 ± 355	Events	20736 ± 242
$\mu_{G1}$	1.86305 ± 0.00059	$a_0$	-0.0738 ± 0.0122
$\sigma_{G1}$	0.00969 ± 0.00149	$a_1$	-0.0431 ± 0.0189
$\mu_{G2}$	1.86436 ± 0.00003		
$\sigma_{G2}$	0.00277 ± 0.00004		

(a) Signal Fit (b) Background Fit

Table VIII.23: Fit parameters for the fit to the  $K^\pm K^\pm$  invariant mass distribution for  $D^0$  reconstruction **without** PXD. Signal (a), Background (b).

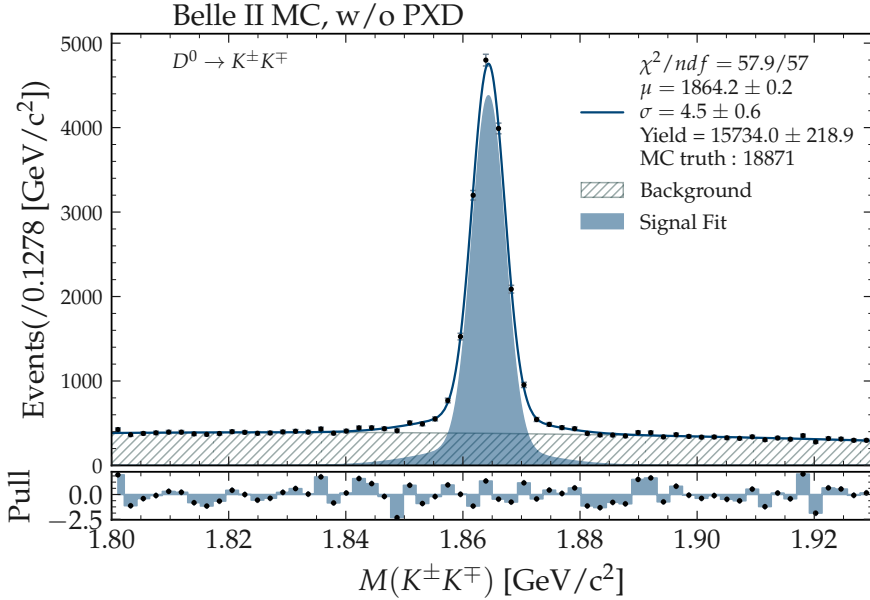


Figure VIII.10: Fit to the  $D^0$  invariant mass spectra for the  $K^\pm K^\mp$  decay channel.

### VIII.1.3 Fits to Variables of the Final $B^\pm$ Meson List

#### VIII.1.3.1 Fit to the $\Delta E$ Signal Distribution

Function	Gaussian + Gaussian
Events	$1971 \pm 46$
$\mu_{G1}$	$0.001304 \pm 0.000635$
$\sigma_{G1}$	$0.008361 \pm 0.001225$
$\mu_{G2}$	$0.000054 \pm 0.000218$
$\sigma_{G2}$	$0.004406 \pm 0.000349$

Table VIII.25: Fit parameters for the fit to the  $\Delta E$  distribution for  $B^\pm$  signal candidates.

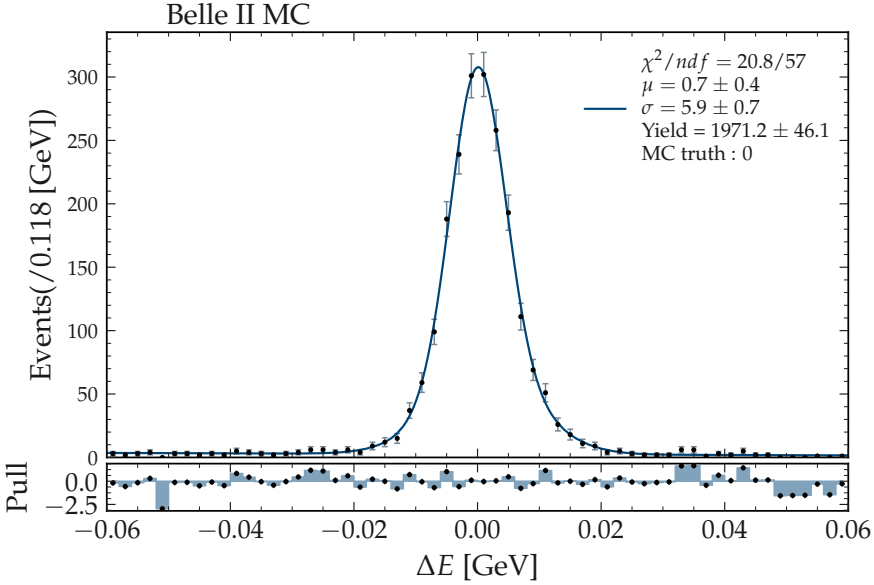


Figure VIII.11: Fitted  $\Delta E$  distribution of the MCtruth-matched  $B^\pm$  candidates for a simulated  $X(4014)$  width of 0 MeV.

VIII.1.3.2 Fit to the  $\Delta E$  Signal Distribution Without PXD

Function	Gaussian + Gaussian
Events	$1904 \pm 45$
$\mu_{G1}$	$0.00177 \pm 0.00068$
$\sigma_{G1}$	$0.00999 \pm 0.00002$
$\mu_{G2}$	$0.00026 \pm 0.00016$
$\sigma_{G2}$	$0.00439 \pm 0.00016$

Table VIII.26: Fit parameters for the fit to the  $\Delta E$  distribution for  $B^\pm$  signal candidates without the PXD in the reconstruction chain..

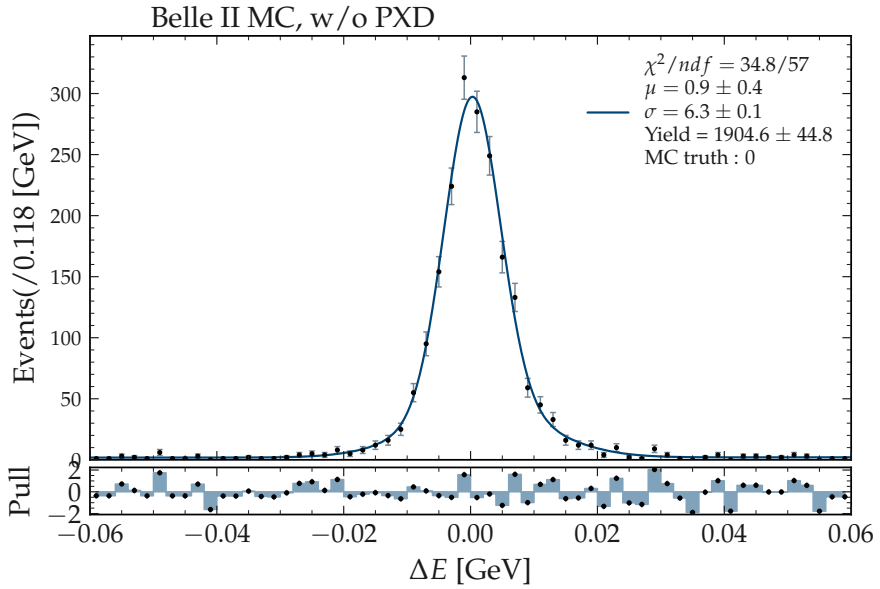


Figure VIII.12: Fitted  $\Delta E$  distribution of the MCtruth-matched  $B^\pm$  candidates for a simulated  $X(4014)$  width of 0 MeV without the PXD in the reconstruction chain.

VIII.1.3.3 Fits to the  $D^0\bar{D}^0\pi^0\pi^0$  Invariant Mass Signal Distribution

Generated width of the  $X(4014)$  :  $\Gamma = 0$  MeV

Function	Breit Wigner	Gaussian
Events	$1078 \pm 33$	
$\mu_{BW}$	$4.01422 \pm 0.00063$	
$\sigma_{BW}$	$0.00053 \pm 0.00083$	
$\mu_G$	$0.00017 \pm 0.00032$	
$\sigma_G$	$0.00144 \pm 0.00013$	

Table VIII.27: Fit parameters for the fit to the invariant mass distribution of the  $X(4014)$  signal candidates.

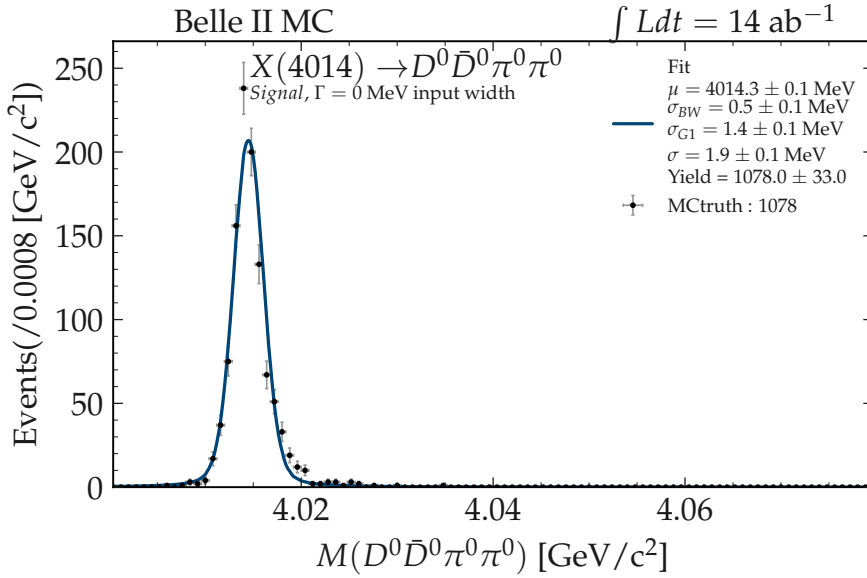


Figure VIII.13: Fitted invariant mass distribution of the MCtruth-matched  $X(4014)$  candidates for a simulated width of 0 MeV.

Generated width of the  $X(4014)$  :  $\Gamma = 1.2$  MeV

Function	Breit Wigner Gaussian
Events	$1066 \pm 33$
$\mu_{BW}$	$4.014223 \pm 0.000379$
$\sigma_{BW}$	$0.000219 \pm 0.000825$
$\mu_G$	$0.000514 \pm 0.000217$
$\sigma_G$	$0.001439 \pm 0.000235$

Table VIII.28: Fit parameters for the fit to the invariant mass distribution of the  $X(4014)$  signal candidates.

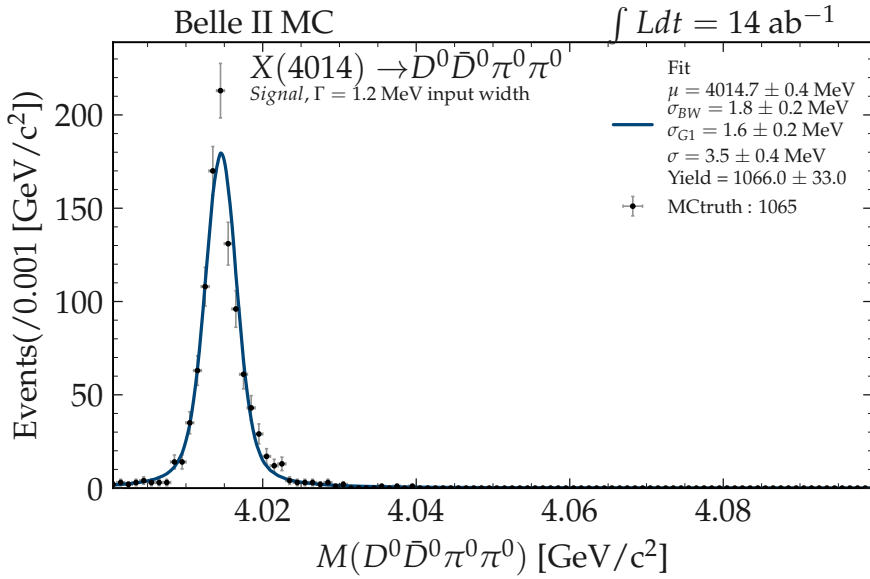


Figure VIII.14: Fitted invariant mass distribution of the MCtruth-matched  $X(4014)$  candidates for a simulated width of 1.2 MeV.

Generated width of the  $X(4014)$  :  $\Gamma = 3$  MeV

Function	Breit Wigner Gaussian
Events	$1038 \pm 32$
$\mu_{BW}$	$4.01421 \pm 0.00003$
$\sigma_{BW}$	$0.00030 \pm 0.00025$
$\mu_G$	$0.00044 \pm 0.00027$
$\sigma_G$	$0.00182 \pm 0.00026$

Table VIII.29: Fit parameters for the fit to the invariant mass distribution of the  $X(4014)$  signal candidates.

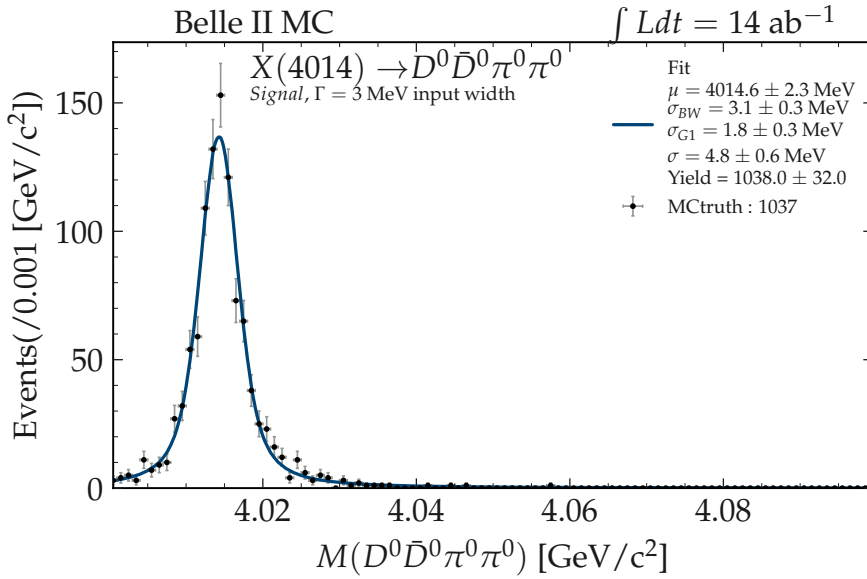


Figure VIII.15: Fitted invariant mass distribution of the MCtruth-matched  $X(4014)$  candidates for a simulated width of 3 MeV.

Generated width of the  $X(4014)$  :  $\Gamma = 5$  MeV

Function	Breit Wigner Gaussian
Events	$1058 \pm 33$
$\mu_{BW}$	$4.014025 \pm 0.000127$
$\sigma_{BW}$	$0.003411 \pm 0.000404$
$\mu_G$	$0.000019 \pm 0.000026$
$\sigma_G$	$0.003083 \pm 0.000316$

Table VIII.30: Fit parameters for the fit to the invariant mass distribution of the  $X(4014)$  signal candidates.

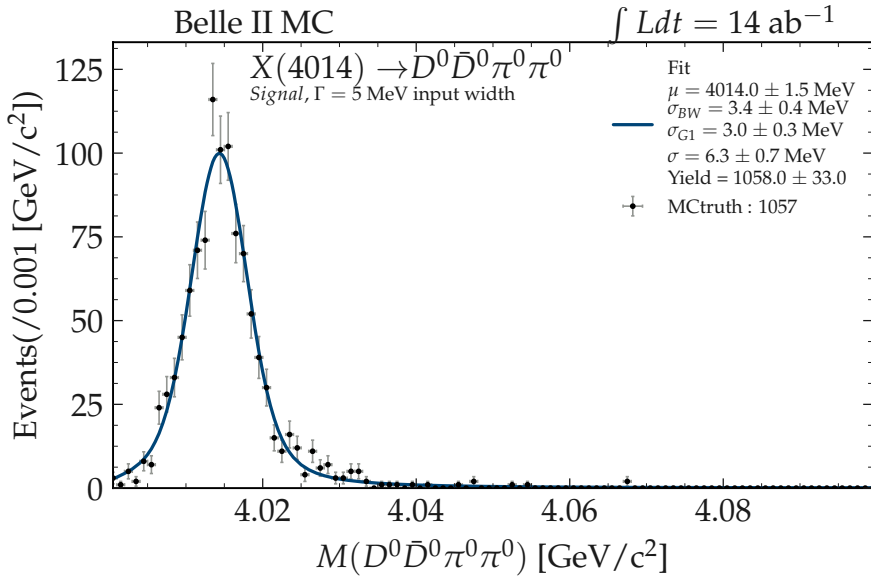


Figure VIII.16: Fitted invariant mass distribution of the MCtruth-matched  $X(4014)$  candidates for a simulated width of 5 MeV.

Generated width of the  $X(4014)$  :  $\Gamma = 7$  MeV

Function	Breit Wigner Gaussian
Events	$1025 \pm 32$
$\mu_{BW}$	$4.01432 \pm 0.00013$
$\sigma_{BW}$	$0.00461 \pm 0.00062$
$\mu_G$	$0.00026 \pm 0.00002$
$\sigma_G$	$0.00347 \pm 0.00041$

Table VIII.31: Fit parameters for the fit to the invariant mass distribution of the  $X(4014)$  signal candidates.

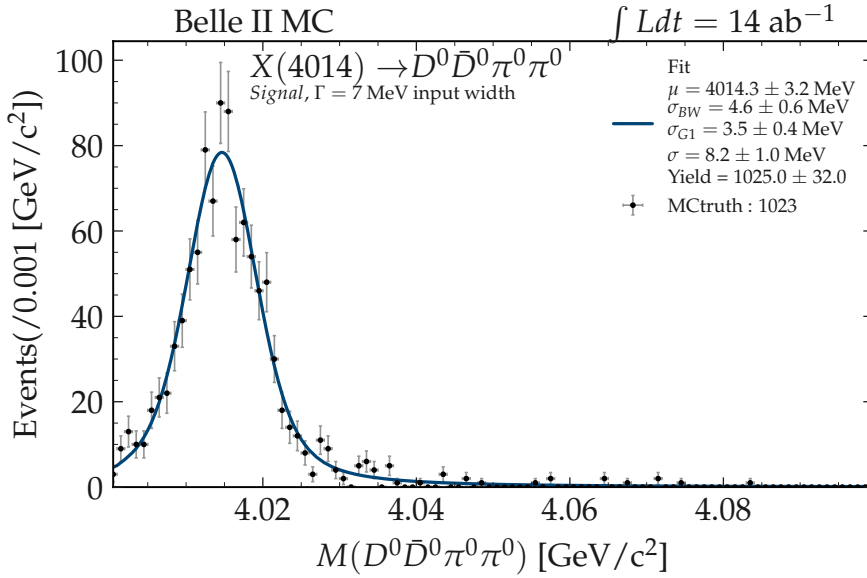


Figure VIII.17: Fitted invariant mass distribution of the MCtruth-matched  $X(4014)$  candidates for a simulated width of 7 MeV.

Generated width of the  $X(4014)$  :  $\Gamma = 10$  MeV

Function	Breit Wigner Gaussian
Events	$1036 \pm 32$
$\mu_{BW}$	$4.01444 \pm 0.00013$
$\sigma_{BW}$	$0.00864 \pm 0.00089$
$\mu_G$	$0.00031 \pm 0.00002$
$\sigma_G$	$0.00318 \pm 0.00062$

Table VIII.32: Fit parameters for the fit to the invariant mass distribution of the  $X(4014)$  signal candidates.

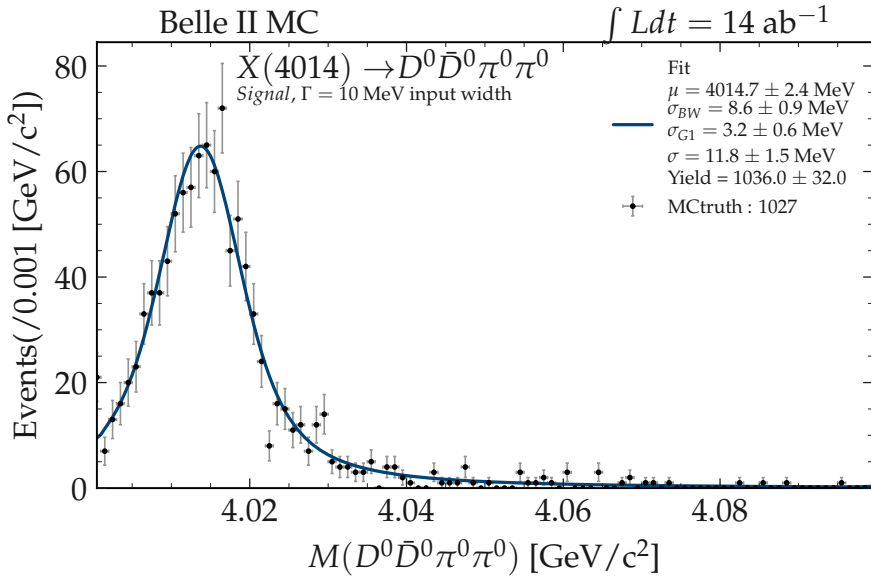


Figure VIII.18: Fitted invariant mass distribution of the MCtruth-matched  $X(4014)$  candidates for a simulated width of 10 MeV.

### VIII.1.4 Signal Event Estimation

	$711\text{fb}^{-1}$	$2\text{ab}^{-1}$	$11.2\text{ab}^{-1}$
$1.0 \cdot 10^{-4}$	5866	16500	115500
$0.9 \cdot 10^{-4}$	5279	14850	103950
$0.8 \cdot 10^{-4}$	4693	13200	92400
$0.7 \cdot 10^{-4}$	4106	11550	80850
$0.6 \cdot 10^{-4}$	3519	9900	69300
$0.5 \cdot 10^{-4}$	2933	8250	57750
$0.4 \cdot 10^{-4}$	2346	6600	46200
$0.3 \cdot 10^{-4}$	1760	4950	34650
$0.2 \cdot 10^{-4}$	1173	3300	23100
$0.1 \cdot 10^{-4}$	586	1650	11550

Figure VIII.19: Estimated number of signal events for the different branching fractions and simulated data sets.

### VIII.1.5 Invariant Mass Distributions of the $\Gamma = 3 \text{ MeV}$ Data Set

Stacked plots showing the combined  $D^0\bar{D}^0\pi^0\pi^0$  invariant mass distribution, including all different components, signal, generic background, combinatorial background and the non-resonant  $B^\pm \rightarrow D^{*0}\bar{D}^{*0}K^\pm$  decay, are shown in this section. The data set used for the plot below is generated with an expected  $X(4014)$  width of  $\Gamma = 3 \text{ MeV}$ , all branching fractions taken into account (0, 1.2, 3, 5, 7 and 10 MeV) are displayed.

Since there would be 18 plots of this kind, 6 for each integrated luminosity, an example for the  $\Gamma = 3 \text{ MeV}$  and  $\int Ldt = 2 \text{ ab}^{-1}$  scenario is given only.

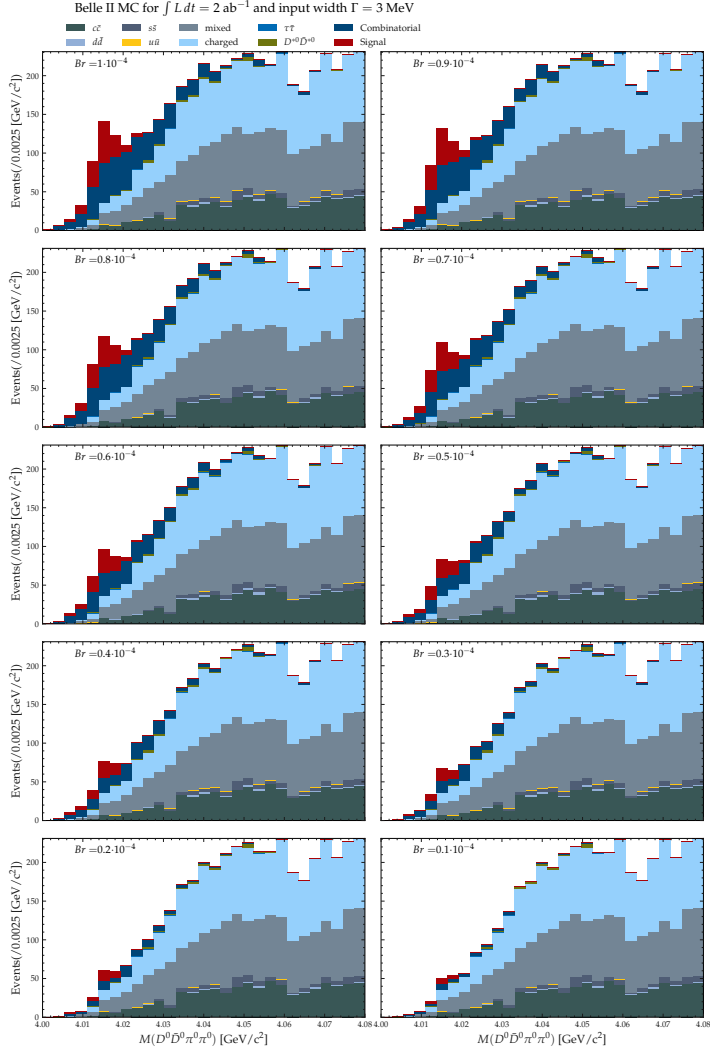


Figure VIII.20:  $M(X(4014))$  invariant mass distribution showing all components (signal, combinatoric background and generic backgrounds) of the final data set after BCS and selection of  $Q < 40 \text{ MeV}$ . The assumed signal width for the shown sample is  $\Gamma = 3 \text{ MeV}$ , branching fractions decrease in steps of  $0.1 \cdot 10^{-4}$  from the top left to bottom right plot.

### VIII.1.6 Fits to the Invariant Mass Distribution of the Combinatorial Background

Generated width of the  $X(4014)$  :  $\Gamma = 0$  MeV

Function	Bifurcated Gaussian + Gaussian
Events	$1965 \pm 120$
$\mu_{BG}$	$4.01375 \pm 0.00064$
$\sigma_{BG, left}$	$0.00306 \pm 0.00039$
$\sigma_{BG, right}$	$0.01915 \pm 0.00063$
$\mu_G$	$4.01988 \pm 0.00075$
$\sigma_G$	$0.00633 \pm 0.00045$

Table VIII.33: Fit parameters for the fit to the invariant mass distribution of the combinatorial background.

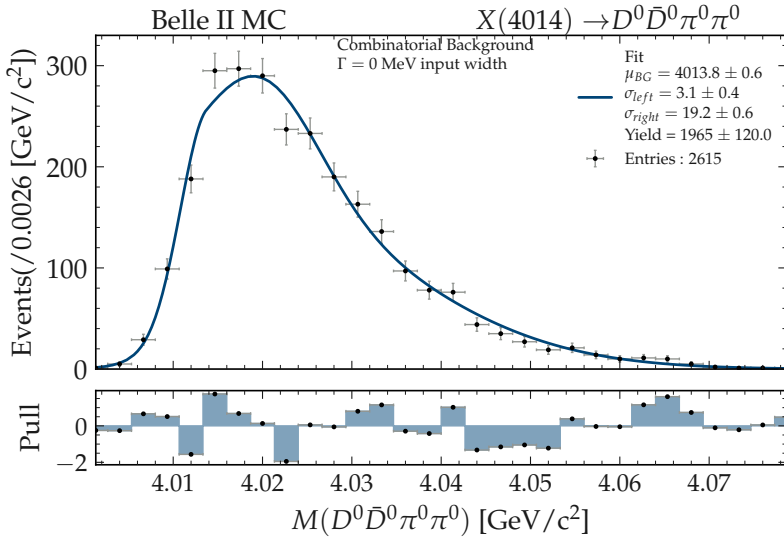


Figure VIII.21: Fitted invariant mass distribution of the combinatorial background contribution for a simulated  $X(4014)$  width of 0 MeV.

Generated width of the  $X(4014)$  :  $\Gamma = 1.2$  MeV

Function	Bifurcated Gaussian + Gaussian
Events	$2268 \pm 97$
$\mu_{BG}$	$4.0161 \pm 0.0004$
$\sigma_{BG, left}$	$0.0044 \pm 0.0002$
$\sigma_{BG, right}$	$0.0136 \pm 0.0008$
$\mu_G$	$4.0479 \pm 0.0074$
$\sigma_G$	$0.0167 \pm 0.0031$

Table VIII.34: Fit parameters for the fit to the invariant mass distribution of the combinatorial background.

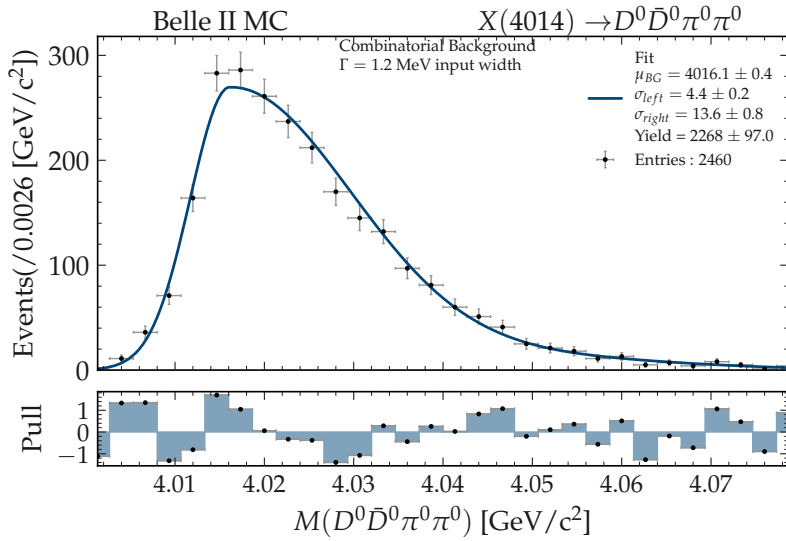


Figure VIII.22: Fitted invariant mass distribution of the combinatorial background contribution for a simulated  $X(4014)$  width of 1.2 MeV.

Generated width of the  $X(4014)$  :  $\Gamma = 3$  MeV

Function	Bifurcated Gaussian + Gaussian
Events	$2598 \pm 123$
$\mu_{BG}$	$4.01587 \pm 0.00047$
$\sigma_{BG, left}$	$0.00491 \pm 0.00029$
$\sigma_{BG, right}$	$0.01478 \pm 0.00081$
$\mu_G$	$4.05349 \pm 0.01673$
$\sigma_G$	$0.01843 \pm 0.00927$

Table VIII.35: Fit parameters for the fit to the invariant mass distribution of the combinatorial background.

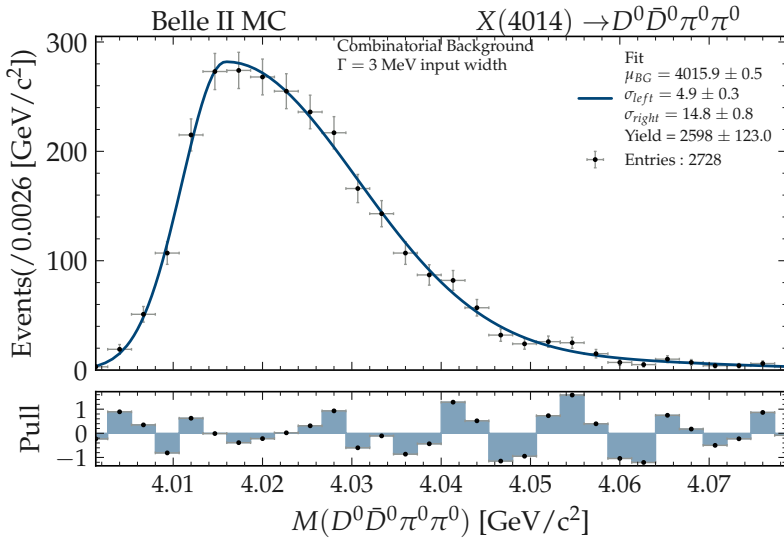


Figure VIII.23: Fitted invariant mass distribution of the combinatorial background contribution for a simulated  $X(4014)$  width of 3 MeV.

Generated width of the  $X(4014)$  :  $\Gamma = 5$  MeV

Function	Bifurcated Gaussian + Gaussian
Events	$2505 \pm 87$
$\mu_{BG}$	$4.01633 \pm 0.00053$
$\sigma_{BG, left}$	$0.00531 \pm 0.00032$
$\sigma_{BG, right}$	$0.01509 \pm 0.00086$
$\mu_G$	$4.05254 \pm 0.01452$
$\sigma_G$	$0.01709 \pm 0.00642$

Table VIII.36: Fit parameters for the fit to the invariant mass distribution of the combinatorial background.

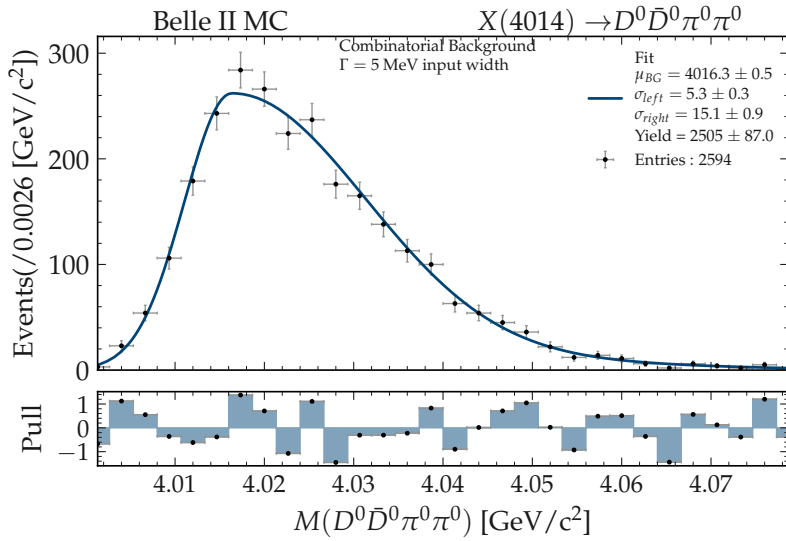


Figure VIII.24: Fitted invariant mass distribution of the combinatorial background contribution for a simulated  $X(4014)$  width of 5 MeV.

Generated width of the  $X(4014)$  :  $\Gamma = 7$  MeV

Function	Bifurcated Gaussian + Gaussian
Events	$1655 \pm 163$
$\mu_{BG}$	$4.01472 \pm 0.00111$
$\sigma_{BG, left}$	$0.00495 \pm 0.00059$
$\sigma_{BG, right}$	$0.02069 \pm 0.00092$
$\mu_G$	$4.02084 \pm 0.00091$
$\sigma_G$	$0.00762 \pm 0.00072$

Table VIII.37: Fit parameters for the fit to the invariant mass distribution of the combinatorial background.

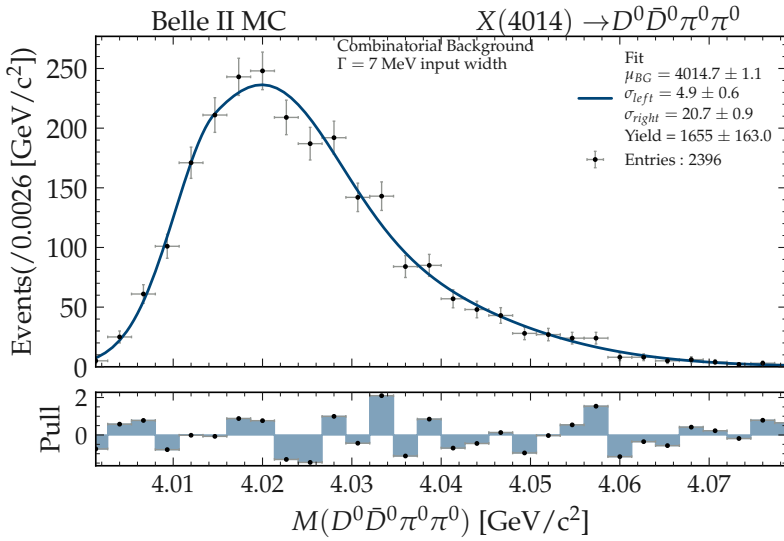


Figure VIII.25: Fitted invariant mass distribution of the combinatorial background contribution for a simulated  $X(4014)$  width of 7 MeV.

Generated width of the  $X(4014)$  :  $\Gamma = 10$  MeV

Function	Bifurcated Gaussian + Gaussian
Events	$1737 \pm 162$
$\mu_{BG}$	$4.01162 \pm 0.00075$
$\sigma_{BG, left}$	$0.00312 \pm 0.00057$
$\sigma_{BG, right}$	$0.02157 \pm 0.00089$
$\mu_G$	$4.02198 \pm 0.00081$
$\sigma_G$	$0.00833 \pm 0.00068$

Table VIII.38: Fit parameters for the fit to the invariant mass distribution of the combinatorial background.

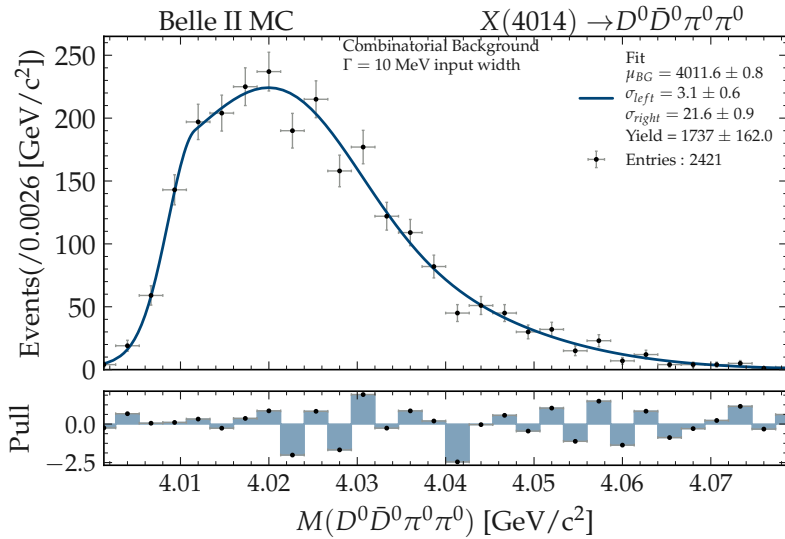


Figure VIII.26: Fitted invariant mass distribution of the combinatorial background contribution for a simulated  $X(4014)$  width of 10 MeV.

### VIII.1.7 Fit to the Invariant Mass Distribution of the Generic Background

Function	Bifurcated Gaussian
Events	$4053 \pm 64$
$\mu_{BG}$	$4.04365 \pm 0.00124$
$\sigma_{BG,left}$	$0.01354 \pm 0.00069$
$\sigma_{BG,right}$	$0.89950 \pm 0.45103$

Table VIII.39: Fit parameters for the fit to the invariant mass distribution of the generic background.

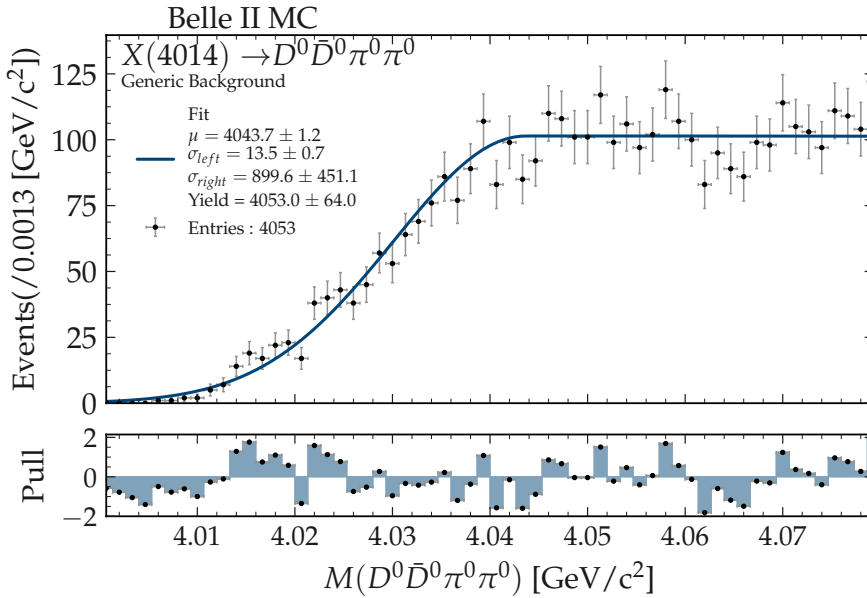


Figure VIII.27: Fitted invariant mass distribution of the generic background contribution.

## VIII.2 TOY MC Study

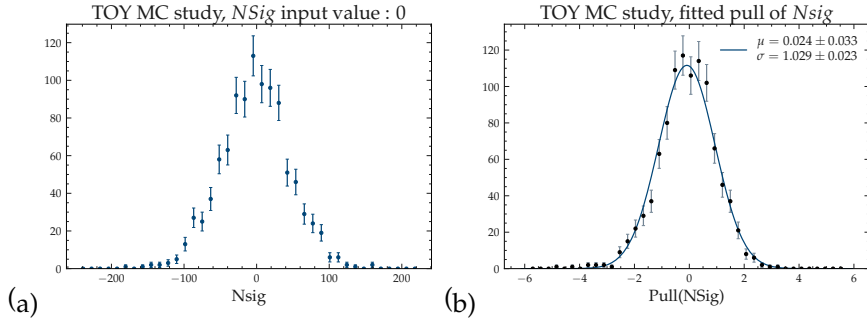


Figure VIII.28: Verification of an unbiased signal yield extraction for the total PDF with TOY-MC. Left plot (a) shows the distribution of the extracted signal yield. Left plot (b) shows the pull distribution. Fits were done on the 7 MeV width scenario. The input signal yield was chosen to be 0.

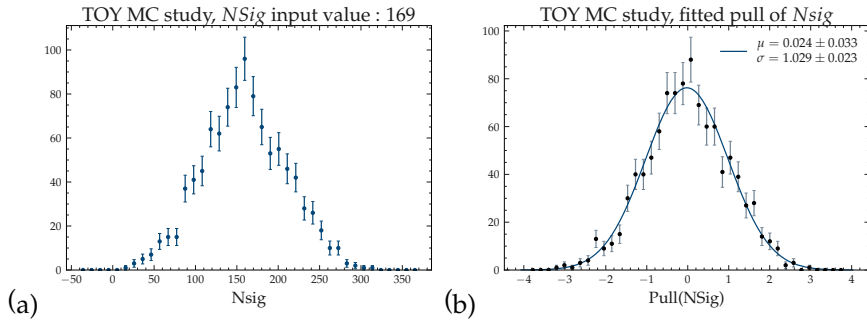


Figure VIII.29: Verification of an unbiased signal yield extraction for the total PDF with TOY-MC. Left plot (a) shows the distribution of the extracted signal yield. Left plot (b) shows the pull distribution. Fits were done on the 7 MeV width scenario. The input signal yield was chosen to be 169.

## VIII.3 Discovery Maps

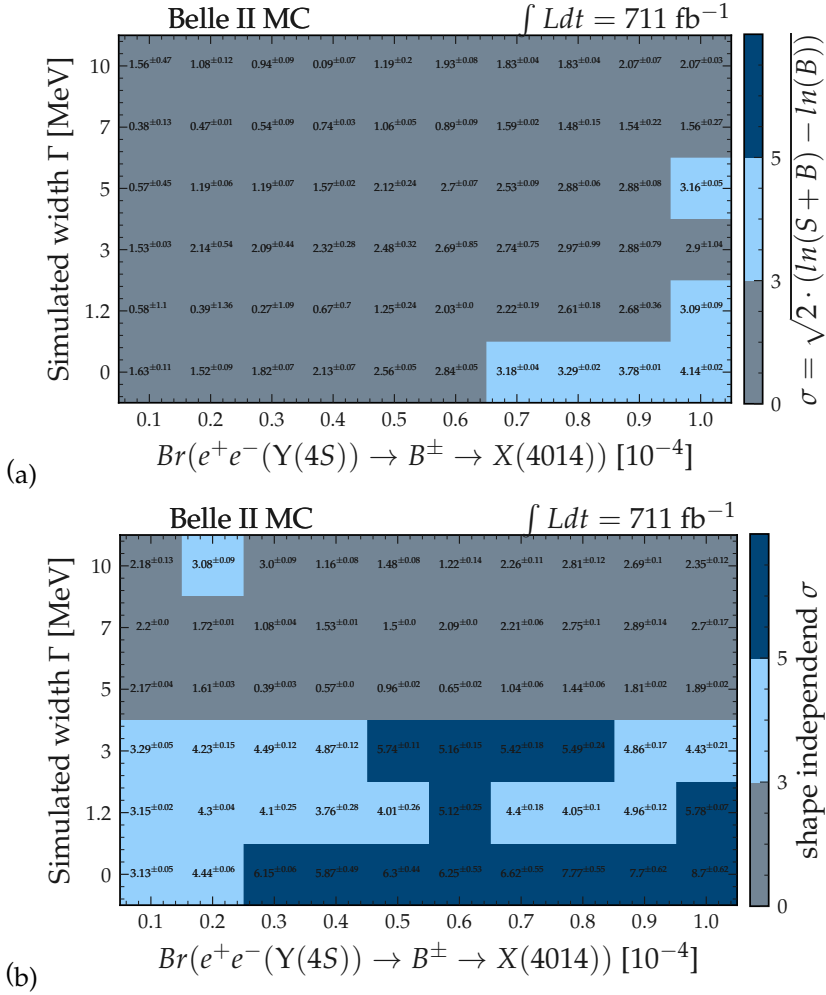


Figure VIII.30: Significance map of the  $711 \text{ fb}^{-1}$  data sample. Top (a) calculated with the shape dependent fitting model, bottom (b) calculated with the shape-independent model.

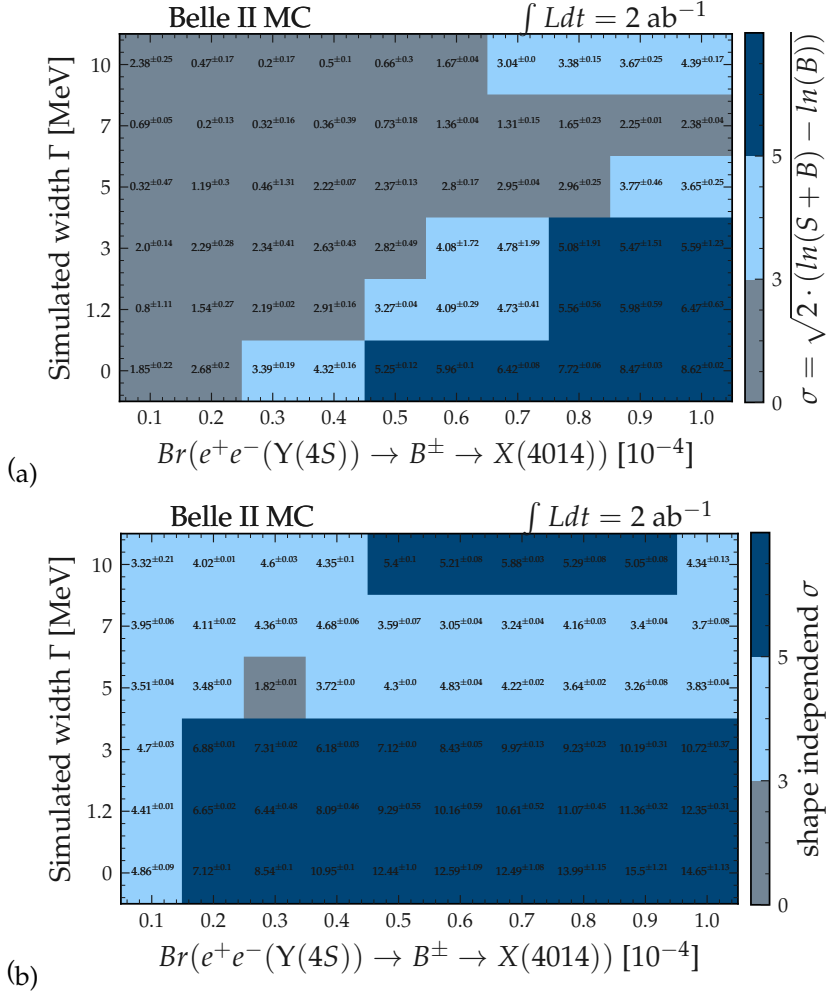


Figure VIII.31: Significance map of the  $2 \text{ ab}^{-1}$  data sample. Top (a) calculated with the shape dependent fitting model, bottom (b) calculated with the shape-independent model.

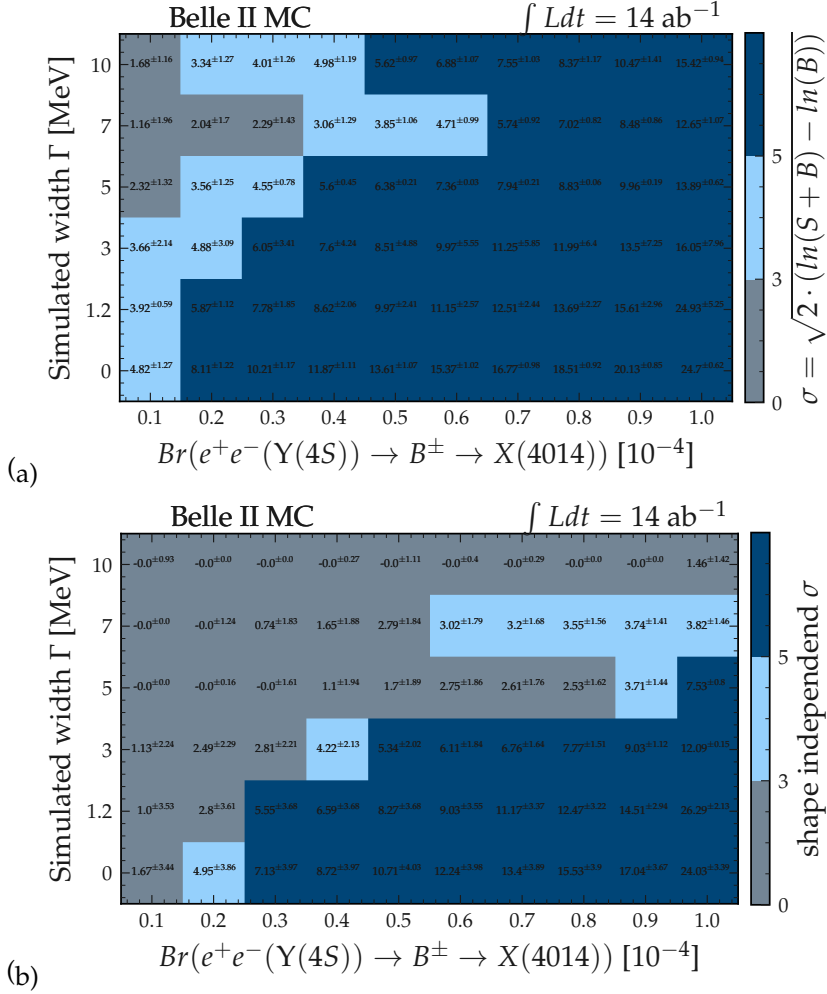


Figure VIII.32: Significance map of the  $14 \text{ ab}^{-1}$  data sample. Top (a) calculated with the shape dependent fitting model, bottom (b) calculated with the shape-independent model.

## VIII.4 Data/MC Comparison for Belle II

### VIII.4.1 $K^\pm$ Data/MC Comparison

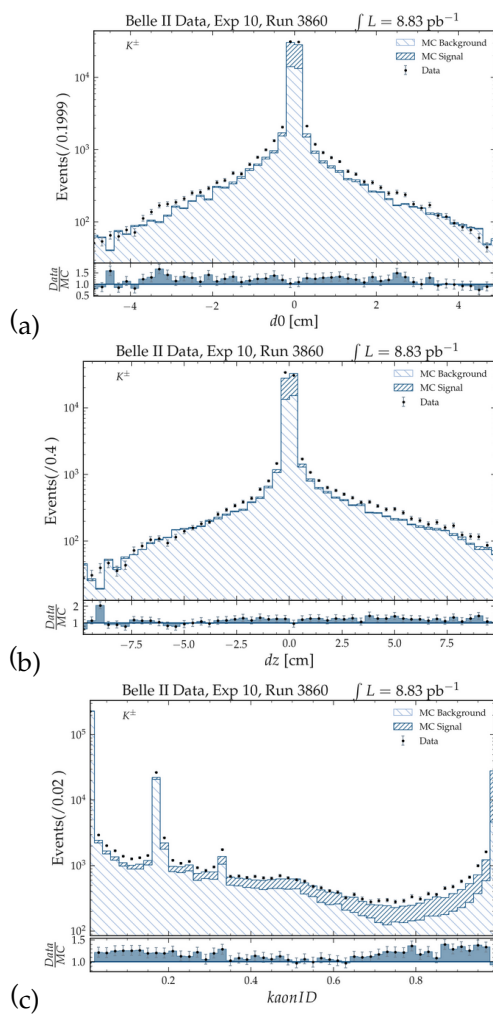
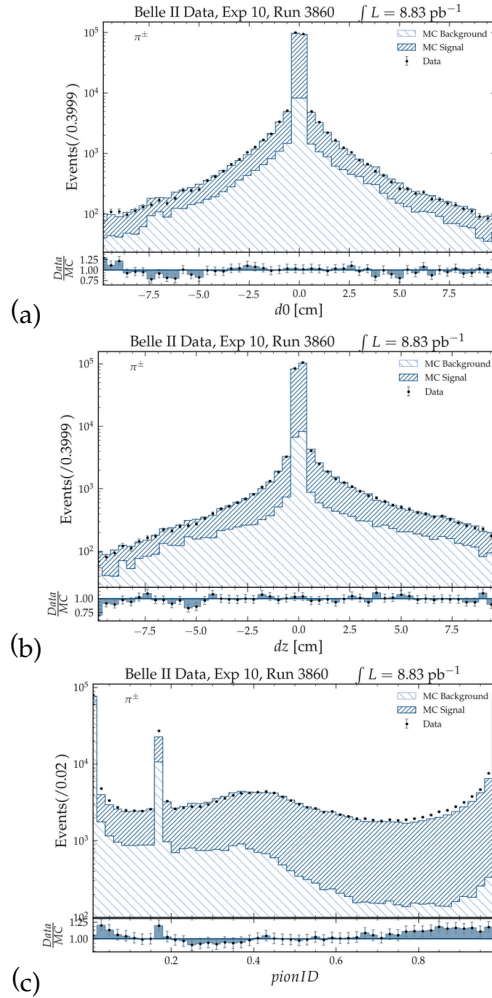


Figure VIII.33: Data/MC comparison for  $K^\pm$  variables  $d0$  (a),  $dz$  (b) and  $kaonID$  (c).

VIII.4.2  $\pi^\pm$  Data/MC ComparisonFigure VIII.34: Data/MC comparison for  $\pi^\pm$  variables  $d0$  (a),  $dz$  (b) and  $pionID$  (c).

### VIII.4.3 $K^\pm, \pi^\pm$ Efficiency and Fake Rate in Belle II MC

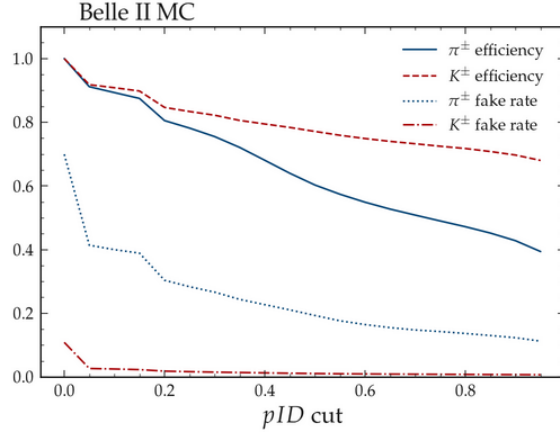


Figure VIII.35: Efficiencies and fake-rates for  $K^\pm$  and  $\pi^\pm$  reconstruction with different values of *particleID*

### VIII.4.4 $K_S^0$ Data/MC Comparison

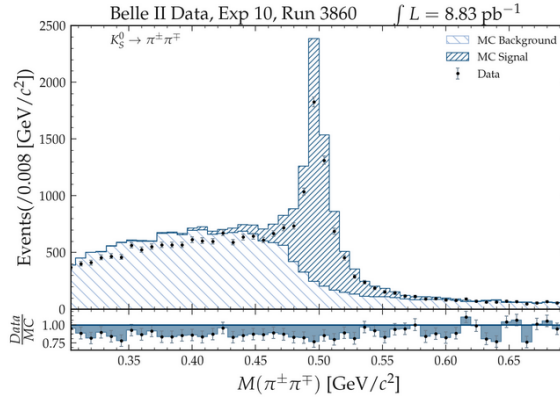


Figure VIII.36: Data/MC comparison for  $K_S^0$  reconstruction in  $8.83 \text{ pb}^{-1}$  of Belle II data.

VIII.4.5  $\pi^0$  from  $D^0$  Data/MC Comparison

	Data-fit	MC-fit
$\mu$	$131.6 \pm 4.4$	$133.6 \pm 0.0$
$\sigma$	$5.9 \pm 0.5$	$5.4 \pm 0.1$
$\chi^2/ndf$	92.2/47	59/47
Yield	$66813 \pm 1988$	$131596 \pm 4800$
MCtruth	75141	137667
Yield/ $\text{pb}^{-1}$	7567	8143
Y/MC	0.89	0.96

Table VIII.40: Fit parameters and results for the fit to the  $\gamma\gamma$  invariant mass distribution for data and MC in  $8.83 \text{ pb}^{-1}$ .

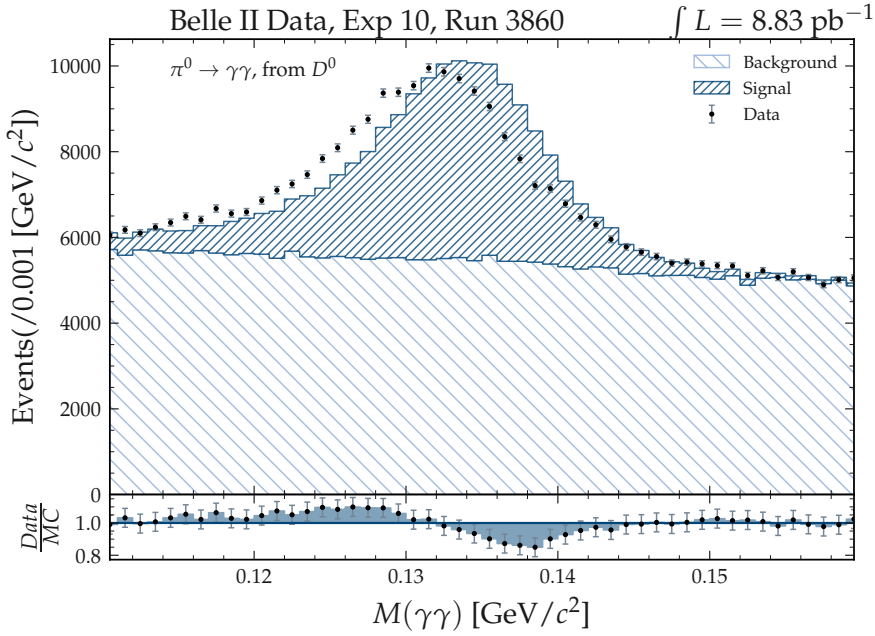


Figure VIII.37: Data/MC comparison of the  $\gamma\gamma$  invariant mass.

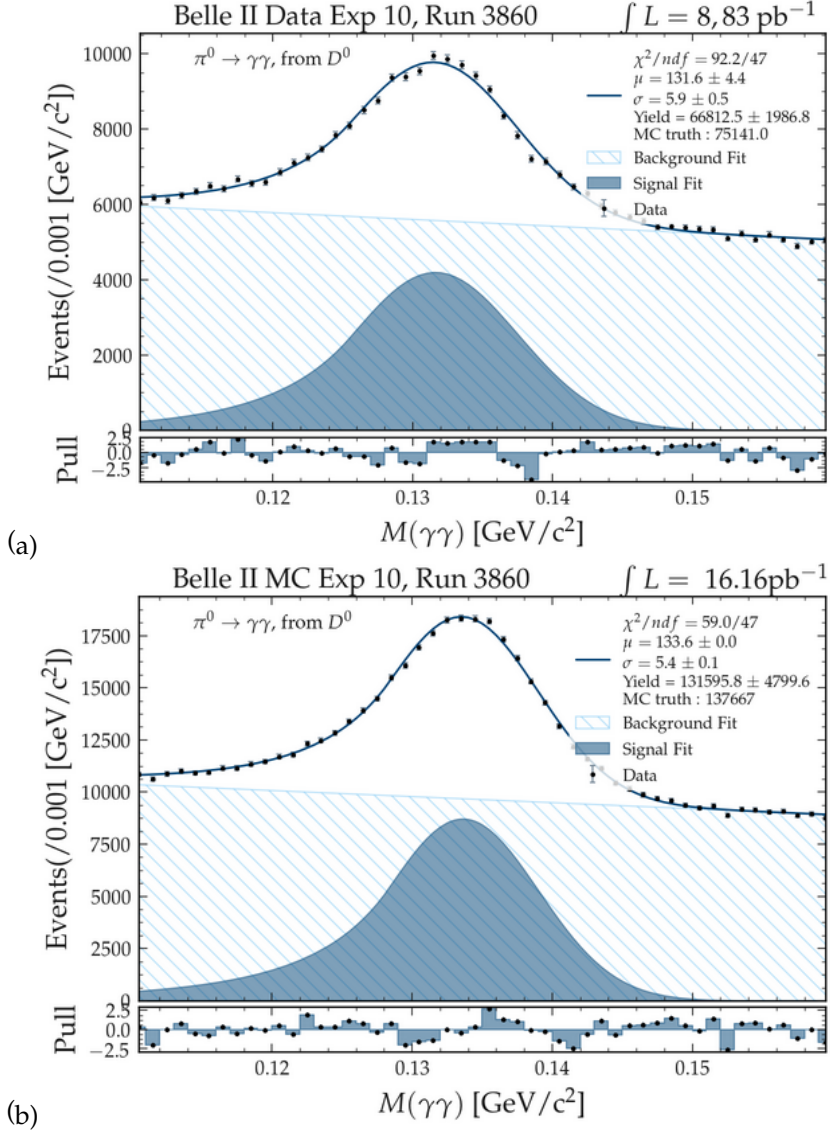


Figure VIII.38: Fits to the  $\gamma\gamma$  invariant mass in  $8.83 \text{ pb}^{-1}$  of Belle II data (a) and to MC corresponding to  $16.16 \text{ pb}^{-1}$  (b).

VIII.4.6  $\pi^0$  from  $X(4014)$  Data/MC Comparison

	Data-fit	MC-fit
$\mu$	$130 \pm 8.3$	$135.1 \pm 0.0$
$\sigma$	$8.5 \pm 3.2$	$4.9 \pm 0.0$
$\chi^2/ndf$	43.6/47	66.3/47
Yield	$6172 \pm 219$	$8250 \pm 171$
MCtruth	6734	12384
Yield/ $\text{pb}^{-1}$	699	511
Y/MC	0.92	0.67

Table VIII.41: Fit parameters and results for the fit to the  $\gamma\gamma$  invariant mass distribution for data and MC in  $8.83 \text{ pb}^{-1}$ .

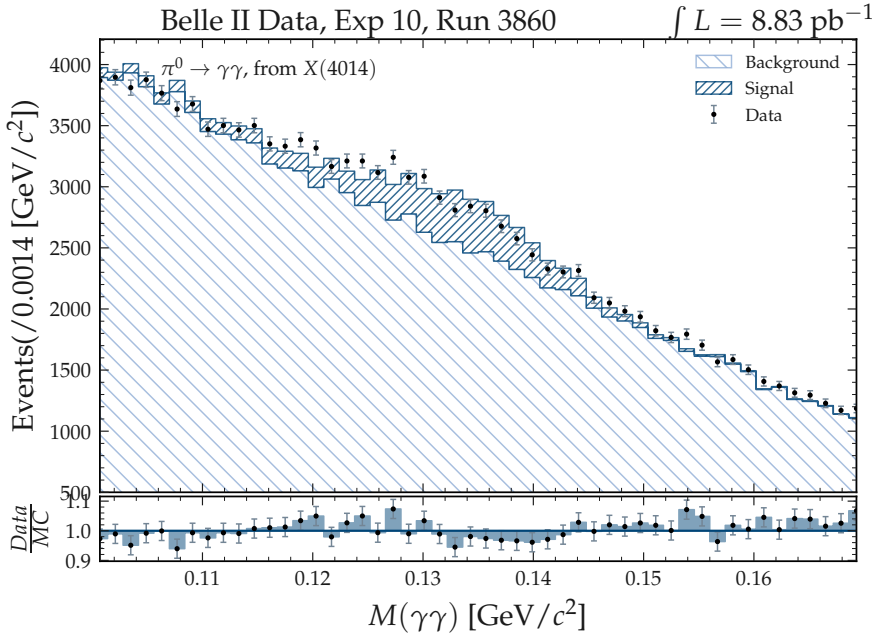


Figure VIII.39: Data/MC comparison of the  $\gamma\gamma$  invariant mass.

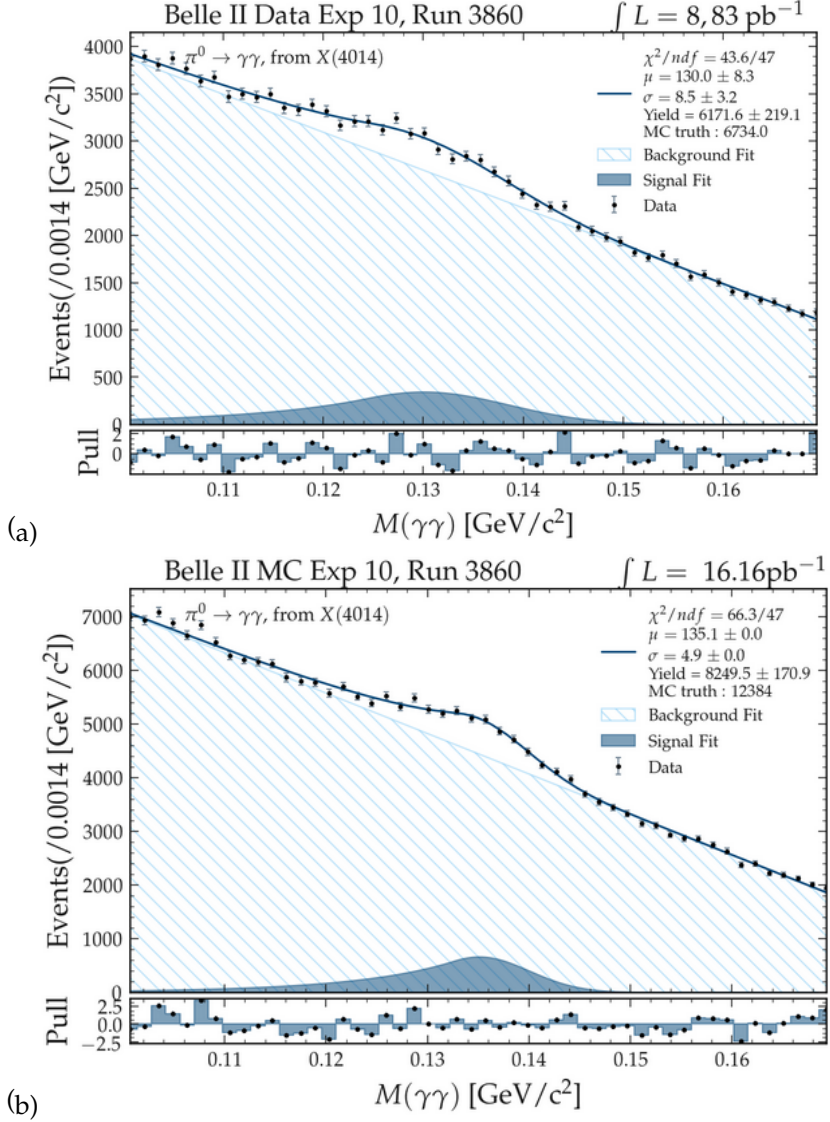


Figure VIII.40: Fits to the  $\gamma\gamma$  invariant mass in  $8.83 \text{ pb}^{-1}$  of Belle II data (a) and to MC corresponding to  $16.16 \text{ pb}^{-1}$  (b).

VIII.4.7  $D^0 \rightarrow K^\pm \pi^\mp$ 

	Data-fit	MC-fit
$\mu$	$1864.0 \pm 0.4$	$1864.4 \pm 0.1$
$\sigma$	$5.3 \pm 1.2$	$5.7 \pm 0.2$
$\chi^2/ndf$	32.8/47	62.2/47
Yield	$24348 \pm 1073$	$64156 \pm 440$
MCtruth	32070	66806
Yield/ $\text{pb}^{-1}$	45	57
Y/MC	0.67	0.96

Table VIII.42: Fit parameters and results for the fit to the  $K^\pm \pi^\mp$  invariant mass distribution for data and MC in  $8.83 \text{ pb}^{-1}$ .

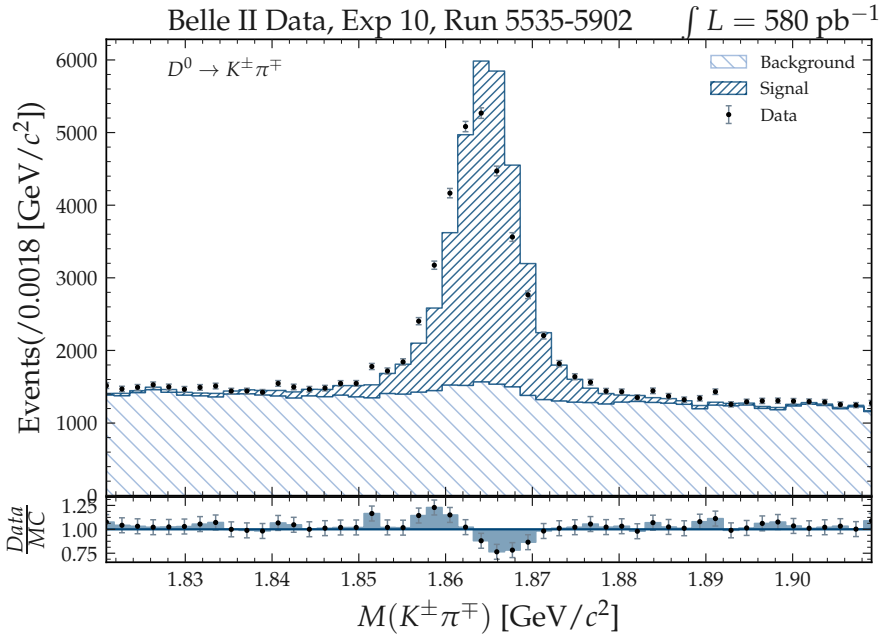


Figure VIII.41: Data/MC comparison of the  $K^\pm \pi^\mp$  invariant mass.

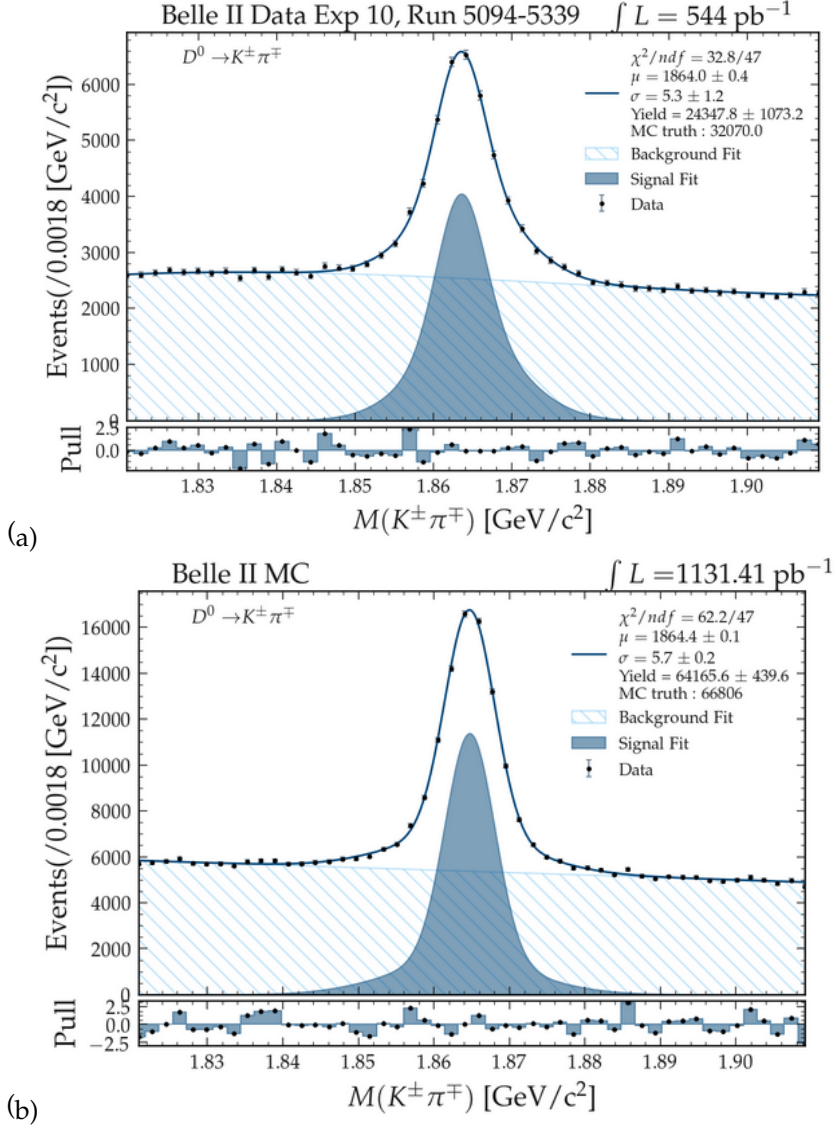


Figure VIII.42: Fits to the  $K^\pm \pi^\mp$  invariant mass in  $544 \text{ pb}^{-1}$  of Belle II data (a) and to MC corresponding to  $1131.41 \text{ pb}^{-1}$  (b).

VIII.4.8  $D^0 \rightarrow K^\pm \pi^\mp \pi^0$ 

	Data-fit	MC-fit
$\mu$	$1861.4 \pm 0.2$	$1863.4 \pm 0.9$
$\sigma$	$9.8 \pm 0.7$	$9.7 \pm 1.4$
$\chi^2/ndf$	41.4/47	37.2/47
Yield	$14159 \pm 302$	$38404 \pm 678$
MCtruth	15273	38693
Yield/ $\text{pb}^{-1}$	104	85
Y/MC	0.93	0.99

Table VIII.43: Fit parameters and results for the fit to the  $K^\pm \pi^\mp \pi^0$  invariant mass distribution for data and MC in  $8.83 \text{ pb}^{-1}$ .

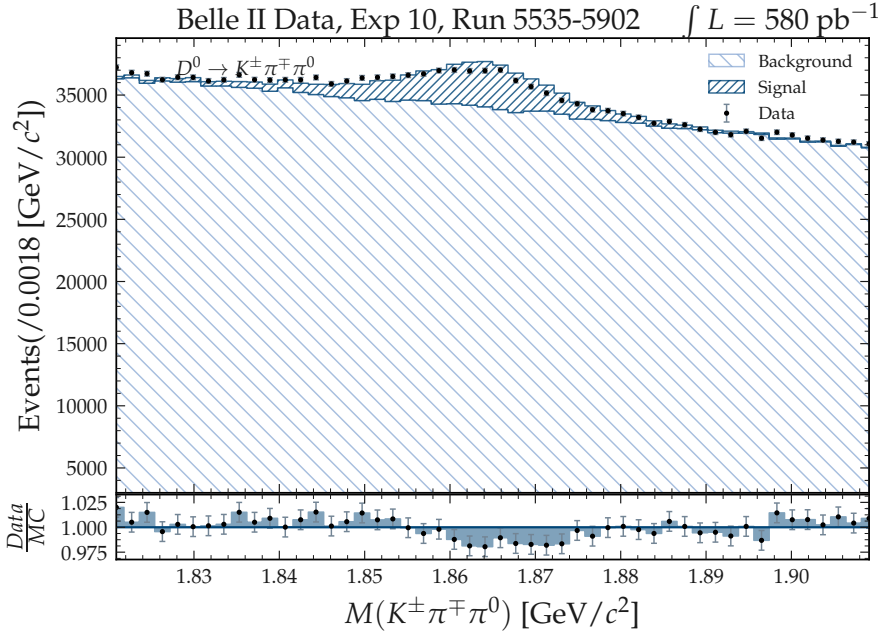


Figure VIII.43: Data/MC comparison of the  $K^\pm \pi^\mp \pi^0$  invariant mass.

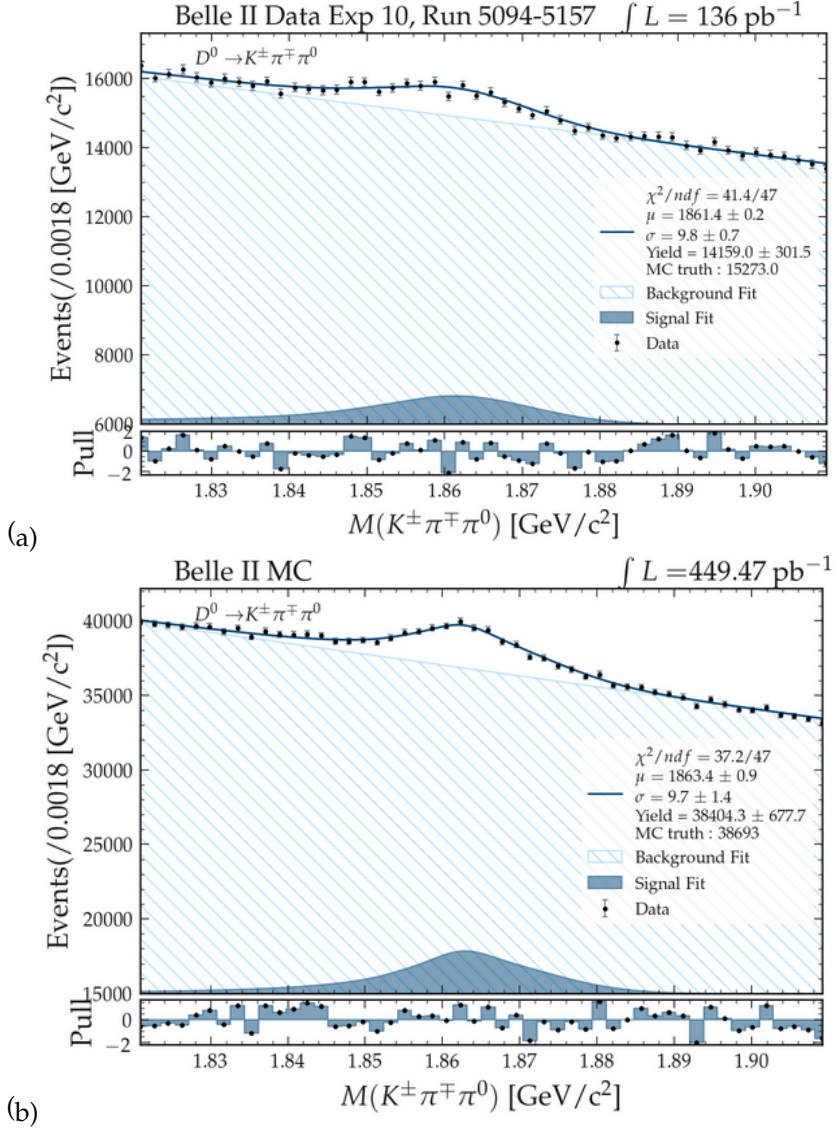


Figure VIII.44: Fits to the  $K^\pm \pi^\mp \pi^0$  invariant mass in  $136 \text{ pb}^{-1}$  of Belle II data (a) and to MC corresponding to  $499.47 \text{ pb}^{-1}$  (b).

VIII.4.9  $D^0 \rightarrow K^\pm \pi^\mp \pi^\pm \pi^\mp$ 

	Data-fit	MC-fit
$\mu$	$1863.8 \pm 0.2$	$1864.1 \pm 2.1$
$\sigma$	$4.2 \pm 0.0$	$5.6 \pm 0.8$
$\chi^2/ndf$	35.3/47	52.5/47
Yield	$17706 \pm 1246$	$67165 \pm 2444$
MCtruth	37537	78315
Yield/ $\text{pb}^{-1}$	33	59
Y/MC	0.47	0.86

Table VIII.44: Fit parameters and results for the fit to the  $K^\pm \pi^\mp \pi^\pm \pi^\mp$  invariant mass distribution for data and MC in  $8.83 \text{ pb}^{-1}$ .

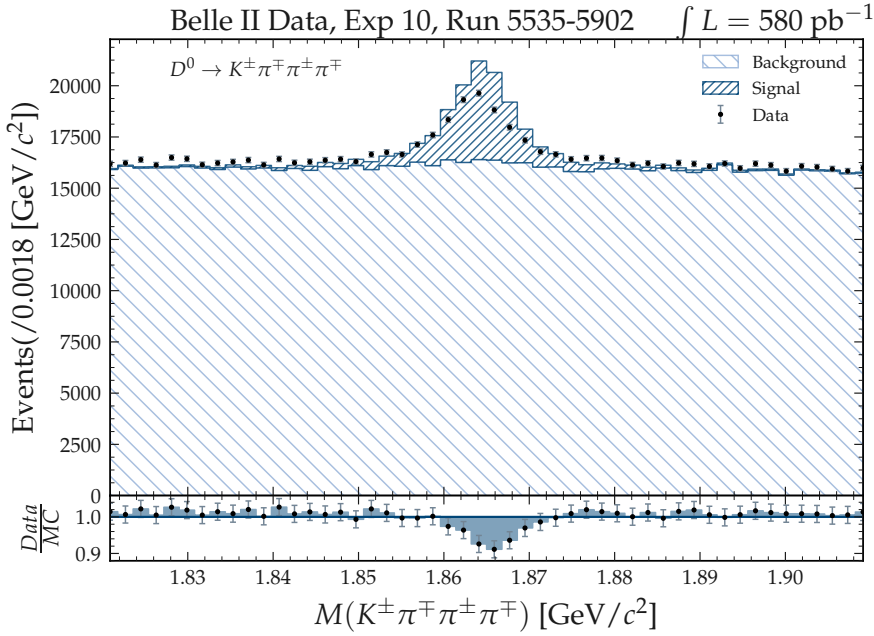


Figure VIII.45: Data/MC comparison of the  $K^\pm \pi^\mp \pi^\pm \pi^\mp$  invariant mass.

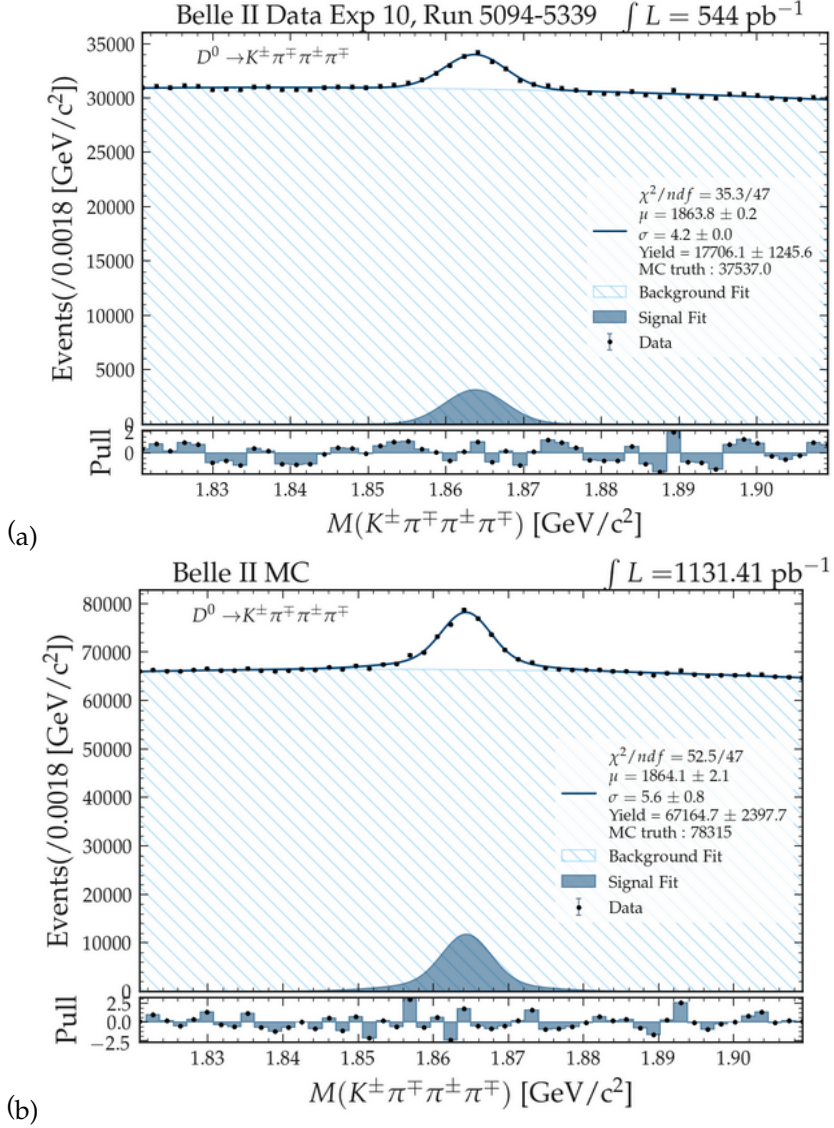


Figure VIII.46: Fits to the  $K^\pm \pi^\mp \pi^\pm \pi^\mp$  invariant mass in  $544 \text{ pb}^{-1}$  of Belle II data (a) and to MC corresponding to  $1131.41 \text{ pb}^{-1}$  (b).

VIII.4.10  $D^0 \rightarrow K_S^0 \pi^\pm \pi^\mp$ 

	Data-fit	MC-fit
$\mu$	$1864.4 \pm 0.9$	$1864.7 \pm 0.4$
$\sigma$	$5.3 \pm 0.7$	$5.0 \pm 0.6$
$\chi^2/ndf$	25.4/47	45.8/47
Yield	$6021 \pm 630$	$17517 \pm 75$
MCtruth	8813	18377
Yield/ $\text{pb}^{-1}$	11	15
Y/MC	0.68	0.95

Table VIII.45: Fit parameters and results for the fit to the  $K_S^0 \pi^\pm \pi^\mp$  invariant mass distribution for data and MC in  $8.83 \text{ pb}^{-1}$ .

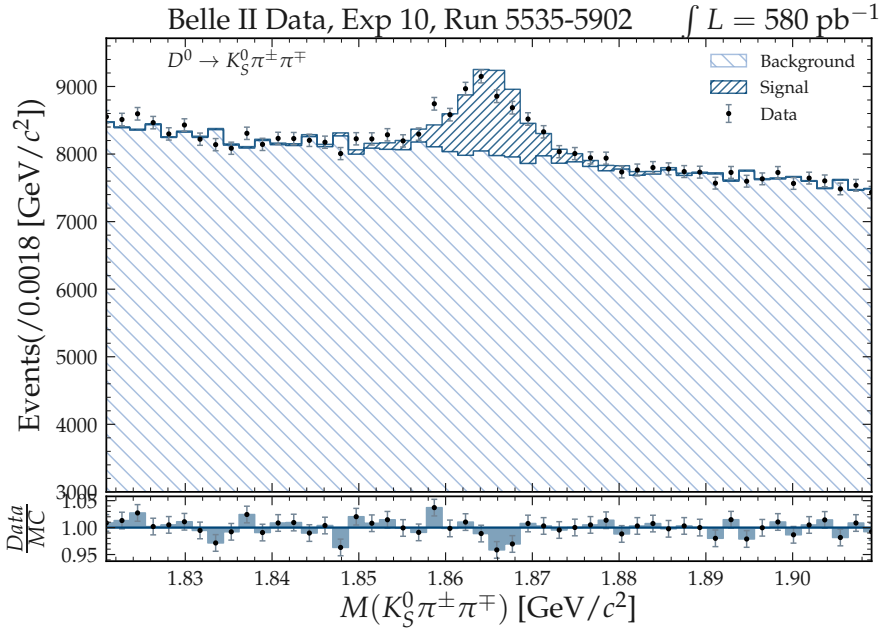


Figure VIII.47: Data/MC comparison of the  $K_S^0 \pi^\pm \pi^\mp$  invariant mass.

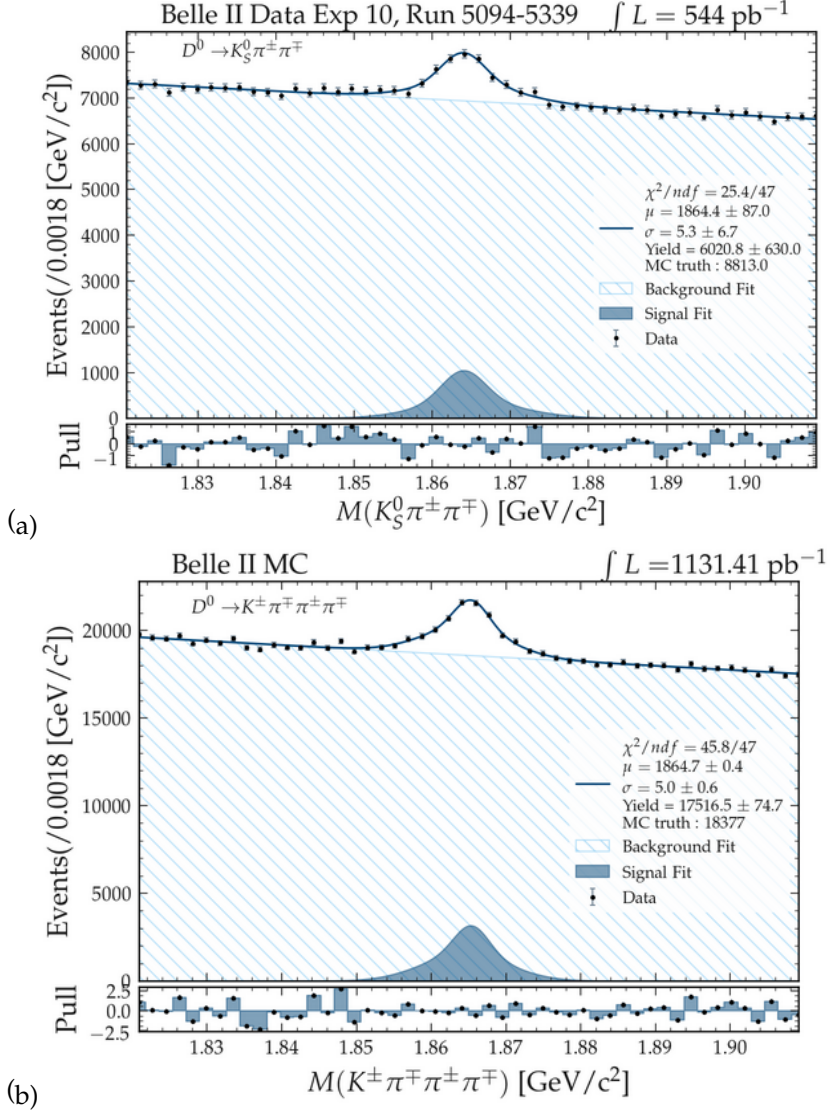


Figure VIII.48: Fits to the  $K_S^0 \pi^+ \pi^-$  invariant mass in  $544 \text{ pb}^{-1}$  of Belle II data (a) and to MC corresponding to  $1131.41 \text{ pb}^{-1}$  (b).

VIII.4.11  $D^0 \rightarrow K^\pm K^\mp$ 

	Data-fit	MC-fit
$\mu$	$1864.1 \pm 0.2$	$1864.2 \pm 0.1$
$\sigma$	$6.5 \pm 1.2$	$4.8 \pm 1.5$
$\chi^2/ndf$	32.6/47	36.8/47
Yield	$2820 \pm 224$	$6119 \pm 314$
MCtruth	3294	6864
Yield/ $\text{pb}^{-1}$	5	5
Y/MC	0.86	0.89

Table VIII.46: Fit parameters and results for the fit to the  $K^\pm K^\mp$  invariant mass distribution for data and MC in  $8.83 \text{ pb}^{-1}$ .

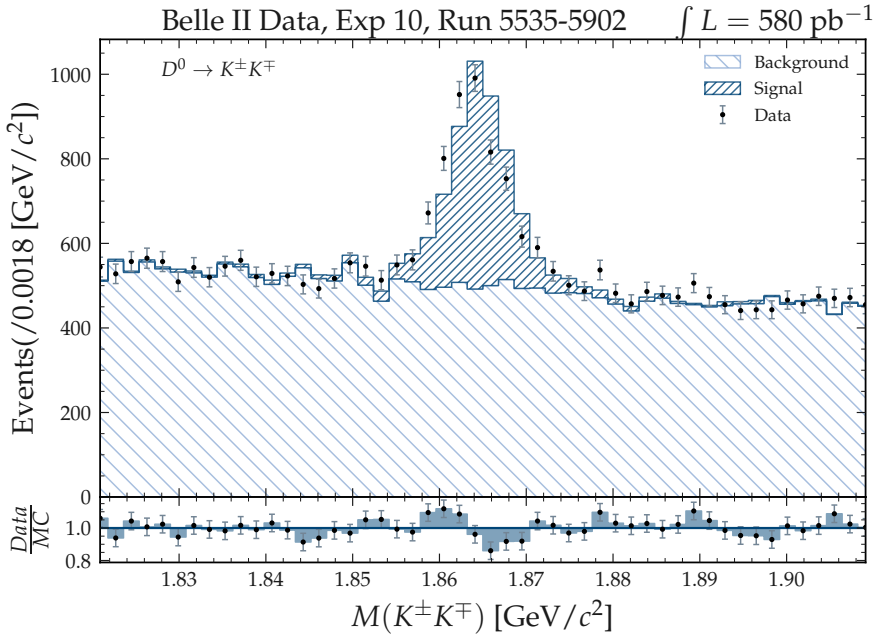


Figure VIII.49: Data/MC comparison of the  $K^\pm K^\mp$  invariant mass.

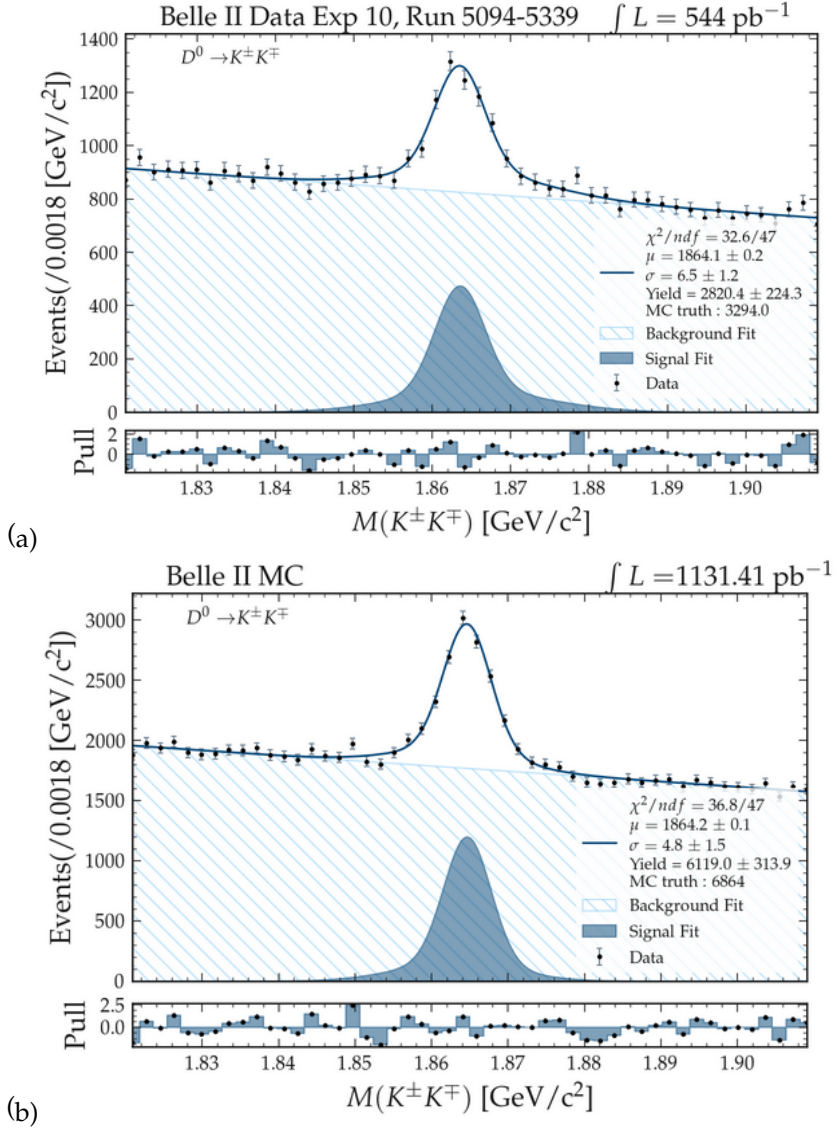


Figure VIII.50: Fits to the  $K^\pm K^\mp$  invariant mass in  $544 \text{ pb}^{-1}$  of Belle II data (a) and to MC corresponding to  $1131.41 \text{ pb}^{-1}$  (b).

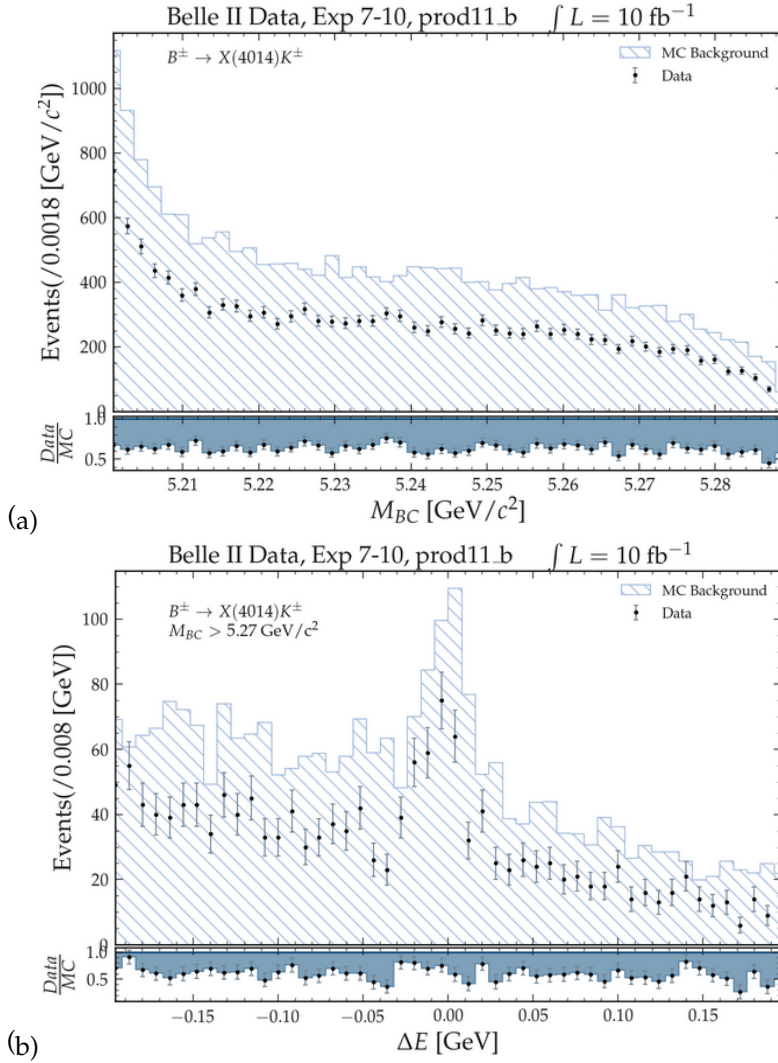
VIII.4.12  $B^\pm$  List Variables

Figure VIII.51: Data/MC comparison for  $M_{BC}$  (a) and  $\Delta E$  (b), for  $10 \text{ fb}^{-1}$  of Belle II data.



# Appendix B

**P**ART B of the appendix collects all fitting parameters and plots for the Belle analysis performed in Chapter VI of this thesis. The first section covers the fitting parameters of all intermediate resonances and the parameters of the final fit. In the second section, plots and tables for the data/MC comparison, as explained in VI.3, are presented.

## IX.1 Fitting Parameters to Belle Signal MC Fits

### IX.1.1 Fits to Intermediate Resonances

#### IX.1.1.1 $\pi^0$ from $D^0$

Function	Crystal Ball	Function	1 <sup>st</sup> order Chebychev
Events	$58739 \pm 17260$	Events	$1732583 \pm 1729$
$\mu$	$0.1349 \pm 0.0006$	$a_0$	$-0.3422 \pm 0.0312$
$\sigma$	$0.0043 \pm 0.0006$		
$\alpha$	$1.77 \pm 2.49$		

(a) Signal Fit

(b) Background Fit

Table IX.1: Fit parameters for the fit to the  $\gamma\gamma$  invariant mass distribution for  $\pi^0$  stemming from  $D^0$ . Signal (a), Background (b).

IX.1.1.2  $\pi^0$  from X(4014) Fit

Function	Crystal Ball	Function	$e^x + 1^{st}$ order Chebychev
Events	$76143 \pm 8889$	Events	$532007 \pm 8907$
$\mu_{CB}$	$0.1356 \pm 0.0001$	$a_0$	$-0.72 \pm 0.04$
$\sigma_{CB}$	$0.0066 \pm 0.0004$	$c$	$-38.34 \pm 1.66$
$\alpha$	$1.42 \pm 0.12$		

(a) Signal Fit

(b) Background Fit

Table IX.3: Fit parameters for the fit to the  $\gamma\gamma$  invariant mass distribution for  $\pi^0$  stemming from X(4014).Signal (a), Background (b).

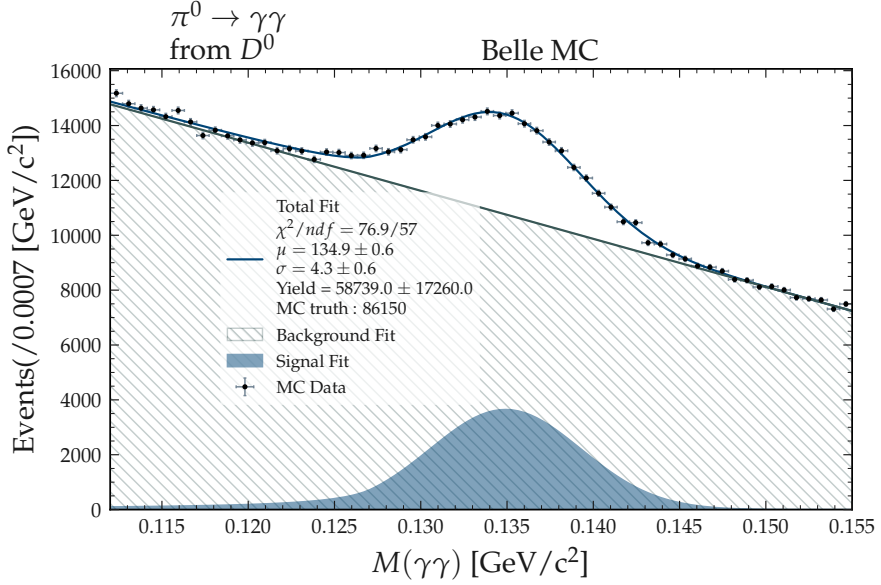
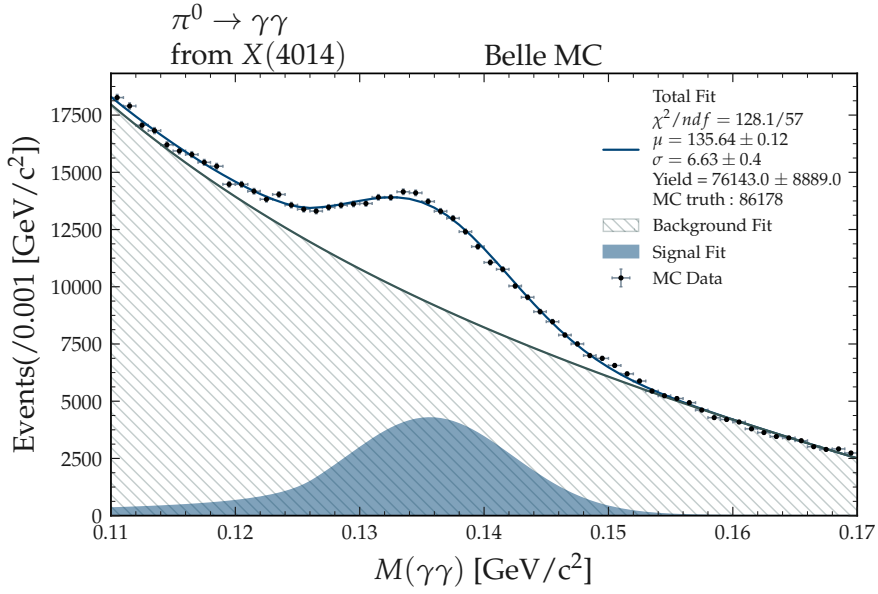


Figure IX.1: Fit to the  $\gamma\gamma$  invariant mass spectrum for  $\pi^0$  from  $D^0$ .

Figure IX.2: Fit to the  $\gamma\gamma$  invariant mass spectrum for  $\pi^0$  from X(4014).

IX.1.1.3  $D^0 \rightarrow K^\pm \pi^\mp$  Fit

Function	Gaussian + Gaussian	Function	1 <sup>st</sup> order Chebychev
Events	$19858 \pm 195$	Events	$19754 \pm 188$
$\mu_{G1}$	$1.8647 \pm 0.0001$	$a_0$	$-0.1542 \pm 0.0127$
$\sigma_{G1}$	$0.0038 \pm 0.0001$		
$\mu_{G2}$	$1.8654 \pm 0.0005$		
$\sigma_{G2}$	$0.0080 \pm 0.0005$		

(a) Signal Fit

(b) Background Fit

Table IX.5: Fit parameters for the fit to the  $K^\pm \pi^\pm$  invariant mass distribution for  $D^0$  reconstruction. Signal (a), Background (b).

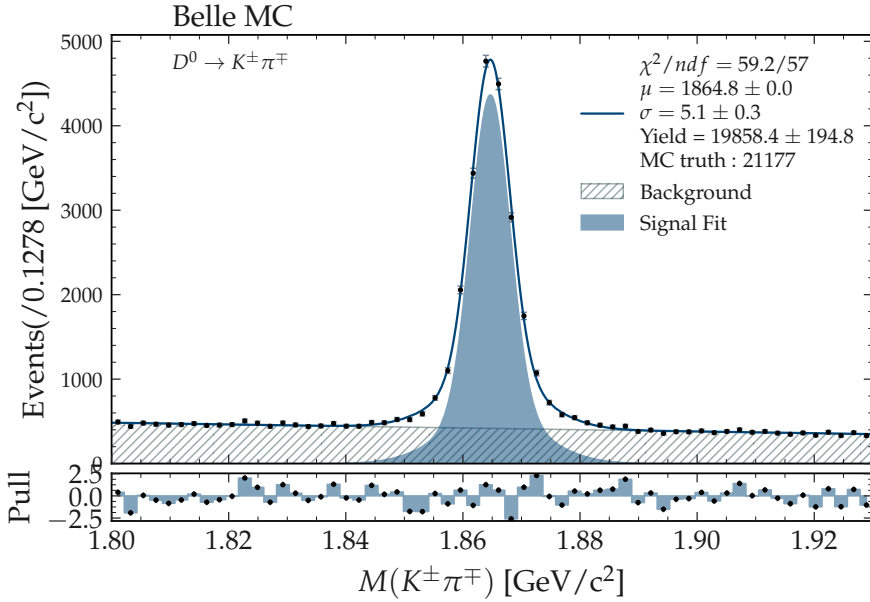


Figure IX.3: Fit to the  $D^0$  invariant mass spectra for the  $K^\pm \pi^\mp$  decay channel.

IX.1.1.4  $D^0 \rightarrow K^\pm \pi^\mp \pi^0$  Fit

Function	Crystal Ball + Gaussian	Function	$2^{nd}$ order Chebychev
Events	$20365 \pm 2799$	Events	$572881 \pm 1503$
$\mu_{CB}$	$1.8642 \pm 0.0008$	$a_0$	$-0.1219 \pm 0.0011$
$\sigma_{CB}$	$0.0099 \pm 0.0001$	$a_1$	$-0.0336 \pm 0.0035$
$\alpha$	$1.2348 \pm 0.0274$		
$\mu_G$	$1.8656 \pm 0.0017$		
$\sigma_G$	$0.0026 \pm 0.0172$		

(a) Signal Fit

(b) Background Fit

Table IX.7: Fit parameters for the fit to the  $K^\pm \pi^\pm \pi^0$  invariant mass distribution for  $D^0$  reconstruction. Signal (a), Background (b).

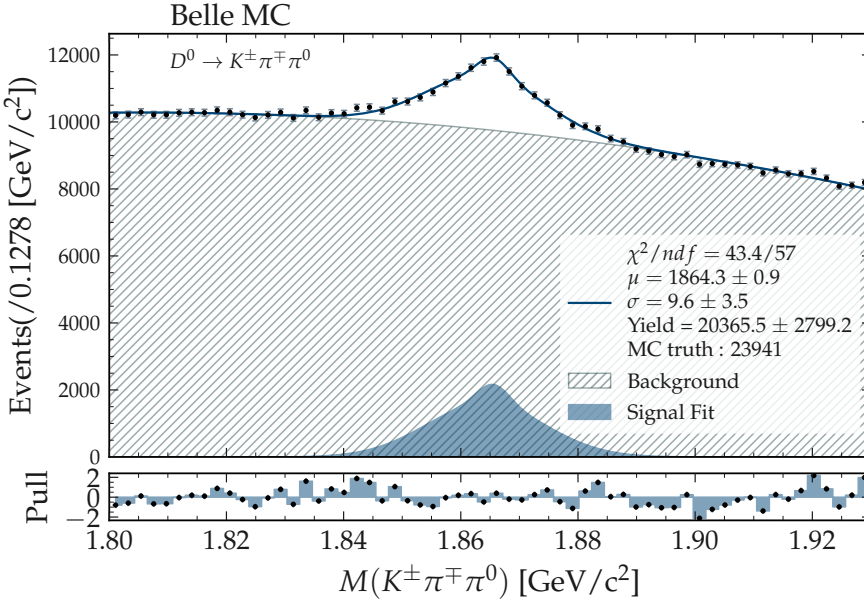


Figure IX.4: Fit to the  $D^0$  invariant mass spectra for the  $K^\pm \pi^\mp \pi^0$  decay channel.

IX.1.1.5  $D^0 \rightarrow K^\pm \pi^\mp \pi^\pm \pi^\mp$  Fit

Function	Gaussian + Gaussian	Function	2 <sup>nd</sup> order Chebychev
Events	19097 ± 441	Events	186298 ± 581
$\mu_{G1}$	1.86327 ± 0.00005	$a_0$	0.0261 ± 0.0043
$\sigma_{G1}$	0.00299 ± 0.00005		
$\mu_{G2}$	1.86499 ± 0.00034		
$\sigma_{G2}$	0.00757 ± 0.00047		

(a) Signal Fit

(b) Background Fit

Table IX.9: Fit parameters for the fit to the  $K^\pm \pi^\pm \pi^\pm \pi^\mp$  invariant mass distribution for  $D^0$  reconstruction. Signal (a), Background (b).

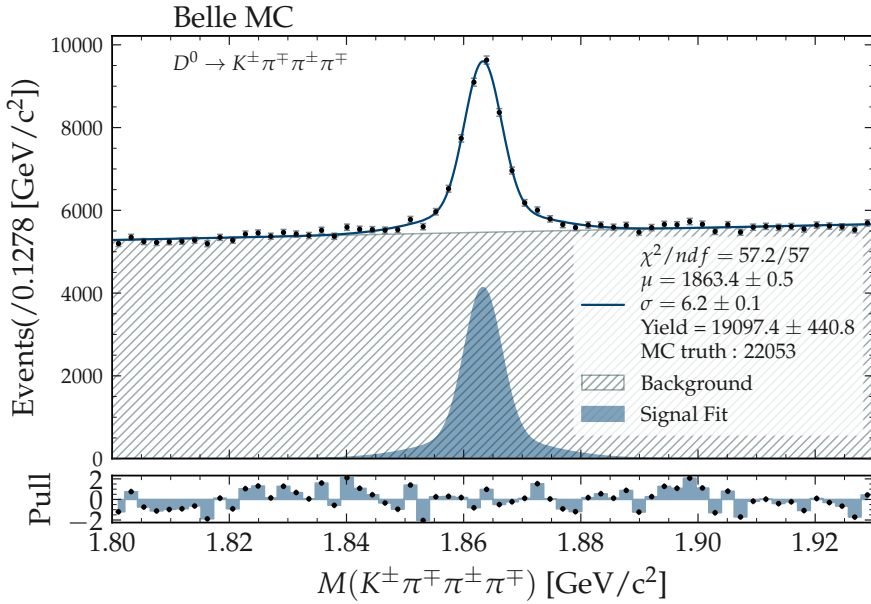


Figure IX.5: Fit to the  $D^0$  invariant mass spectra for the  $K^\pm \pi^\mp \pi^\pm \pi^\mp$  decay channel.

IX.1.1.6  $D^0 \rightarrow K_S^0 \pi^\pm \pi^\mp$  Fit

Function	Gaussian + Gaussian	Function	1 <sup>st</sup> order Chebychev
Events	$9147 \pm 232$	Events	$15315 \pm 190$
$\mu_{G1}$	$1.86499 \pm 0.00012$	$a_0$	$-0.07636 \pm 0.01418$
$\sigma_{G1}$	$0.00868 \pm 0.00104$		
$\mu_{G2}$	$1.86423 \pm 0.00005$		
$\sigma_{G2}$	$0.00279 \pm 0.00010$		

(a) Signal Fit

(b) Background Fit

Table IX.11: Fit parameters for the fit to the  $K_S^0 \pi^\pm \pi^\pm$  invariant mass distribution for  $D^0$  reconstruction. Signal (a), Background (b).

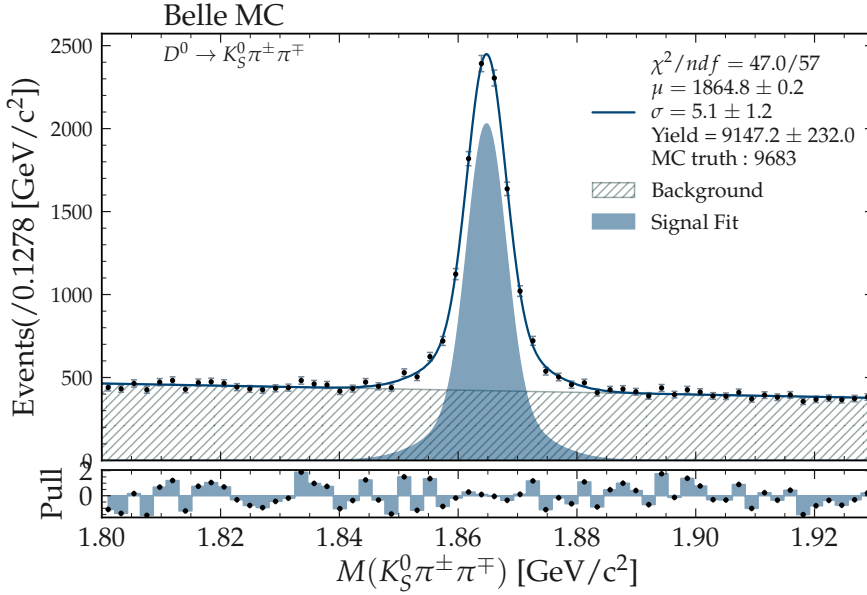


Figure IX.6: Fit to the  $D^0$  invariant mass spectra for the  $K_S^0 \pi^\pm \pi^\mp$  decay channel.

IX.1.1.7  $D^0 \rightarrow K^\pm K^\mp$  Fit

Function	Gaussian + Gaussian	Function	1 <sup>st</sup> order Chebychev
Events	$19280 \pm 201$	Events	$14928 \pm 182$
$\mu_{G1}$	$1.86499 \pm 0.00001$	$a_0$	$-0.1146 \pm 0.0146$
$\sigma_{G1}$	$0.00777 \pm 0.00083$		
$\mu_{G2}$	$1.86439 \pm 0.00004$		
$\sigma_{G2}$	$0.00310 \pm 0.00007$		

(a) Signal Fit

(b) Background Fit

Table IX.13: Fit parameters for the fit to the  $K^\pm K^\pm$  invariant mass distribution for  $D^0$  reconstruction. Signal (a), Background (b).

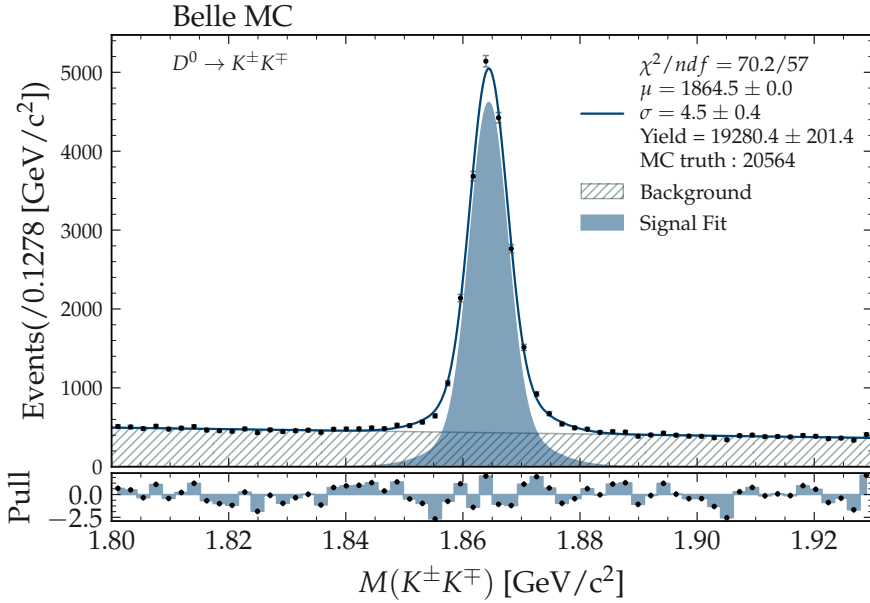


Figure IX.7: Fit to the  $D^0$  invariant mass spectra for the  $K^\pm K^\mp$  decay channel.

## IX.1.2 Fits to Variables of the Final $B^\pm$ Meson List for the $X(3872)$ Analysis

### IX.1.2.1 Fit to the $\Delta E$ Signal MC Distribution

Function	Gaussian
Events	$729 \pm 0$
$\mu_G$	$0.00055 \pm 0.00034$
$\sigma_G$	$0.00511 \pm 0.00018$

Table IX.15: Fit parameters for the fit to the  $\Delta E$  distribution for  $B^\pm$  background candidates.

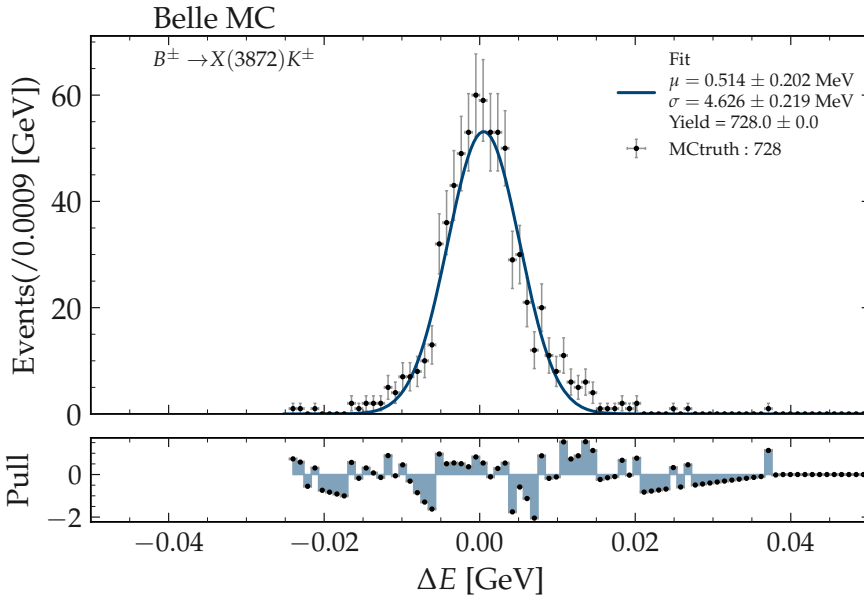


Figure IX.8: Fitted  $\Delta E$  distribution of the  $X(3872)$  signal MC  $B^\pm$  candidates.

IX.1.2.2 Fit to the  $M_{BC}$  Signal MC Distribution

Function	Gaussian + Argus
Events	$1036 \pm 0$
$\mu_G$	$5.27797 \pm 0.00008$
$\sigma_G$	$0.00248 \pm 0.00006$
$argpar$	$-3.85 \pm 1.16$

Table IX.16: Fit parameters for the fit to the  $M_{BC}$  distribution for the X(3872) signal MC.

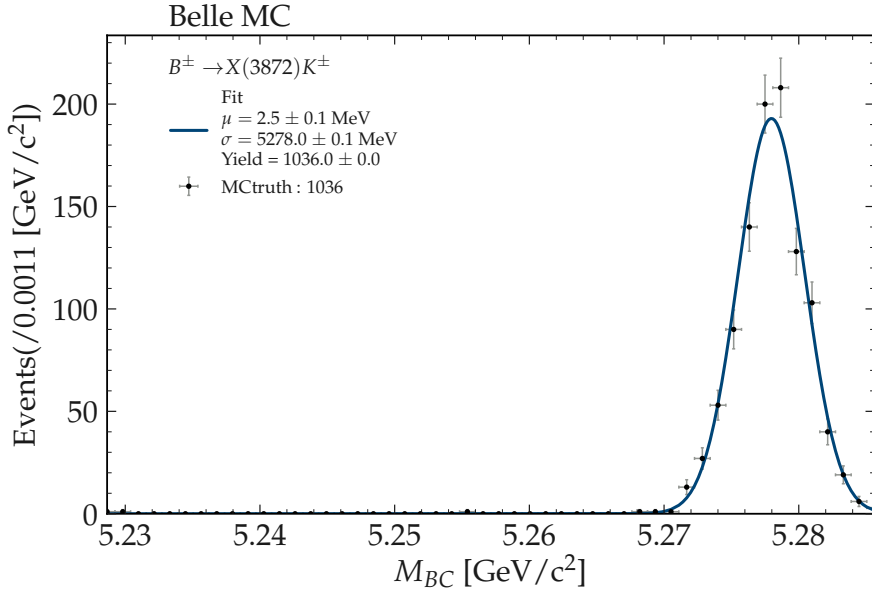
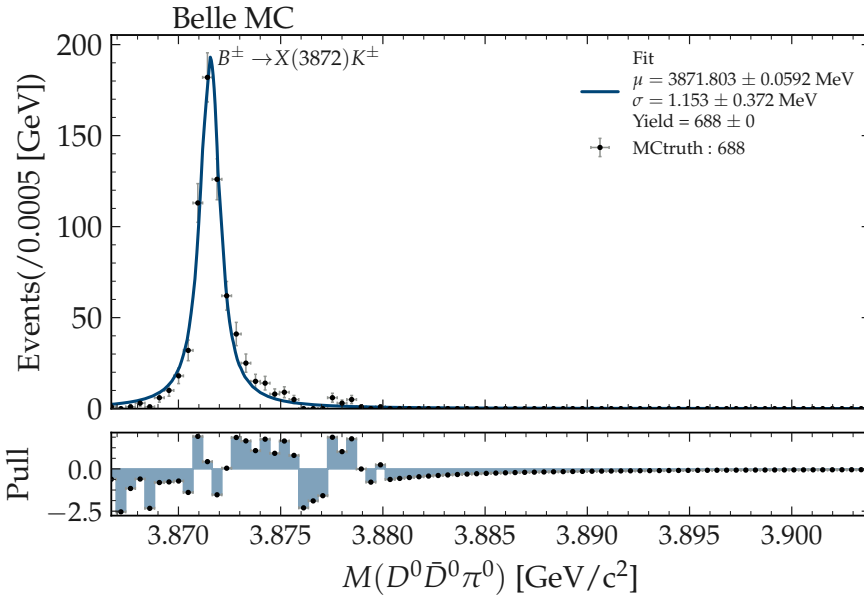


Figure IX.9: Fitted  $M_{BC}$  distribution of the X(3872) signal MC.

IX.1.2.3 Fit to the MCtruth-matched  $X(3872)$  Invariant Mass Signal MC Distribution

Function	Breit Wigner * Gaussian
Events	$688 \pm 0$
$\mu_{BW}$	$3.87148 \pm 0.00006$
$\sigma_{BW}$	$0.00011 \pm 0.00007$
$\mu_G$	$0.00032 \pm 0.00029$
$\sigma_G$	$0.00011 \pm 0.00031$

Table IX.17: Fit parameters for the fit to the MCtruth-matched  $X(3872)$  invariant mass distribution for signal MC.Figure IX.10: Fitted MCtruth-matched  $X(3872)$  invariant mass distribution for signal MC.

IX.1.2.4 Fit to the  $\Delta E$  Combinatorial Background Distribution

Function	Gaussian + Gaussian
Events	$472 \pm 0.6$
$\mu_{G1}$	$0.0057 \pm 0.0023$
$\sigma_{G1}$	$0.0138 \pm 0.0016$
$\mu_{G2}$	$0.0006 \pm 0.0004$
$\sigma_{G2}$	$0.0061 \pm 0.0006$

Table IX.18: Fit parameters for the fit to the  $\Delta E$  combinatorial background distribution.

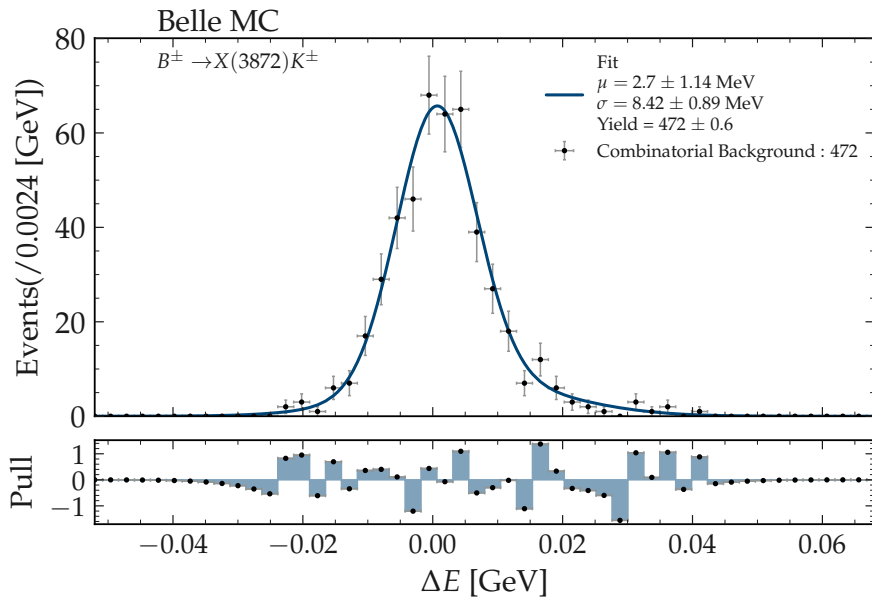
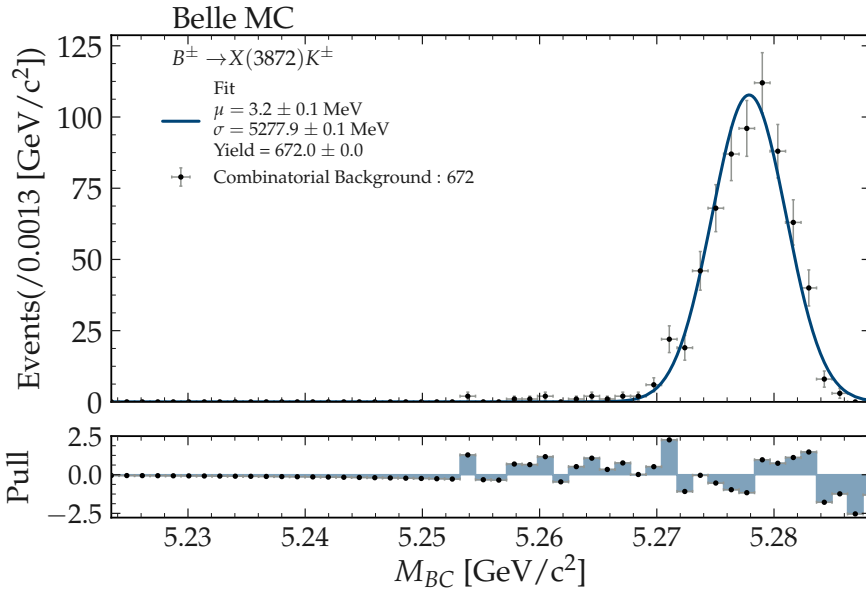


Figure IX.11: Fitted  $\Delta E$  combinatorial background distribution.

IX.1.2.5 Fit to the  $M_{BC}$  Combinatorial Background Distribution

Function	Gaussian
Events	$672 \pm 0.0$
$\mu_G$	$5.2779 \pm 0.0001$
$\sigma_G$	$0.0032 \pm 0.0001$

Table IX.19: Fit parameters for the fit to the  $M_{BC}$  combinatorial background distribution.Figure IX.12: Fitted  $M_{BC}$  combinatorial background distribution.

**IX.1.2.6 Fit to the  $X(3872)$  Combinatorial Background Invariant Mass Distribution**

Function	Bifurcated Gaussian plus Gaussian
Events	$688 \pm 0$
$\mu_{BG}$	$3.8718 \pm 0.0008$
$\sigma_{BG,left}$	$0.0018 \pm 0.0006$
$\sigma_{BG,right}$	$0.0013 \pm 0.0007$
$\mu_G$	$3.8721 \pm 0.0007$
$\sigma_G$	$0.0028 \pm 0.0005$

Table IX.20: Fit parameters for the fit to the  $X(3872)$  combinatorial invariant mass distribution.

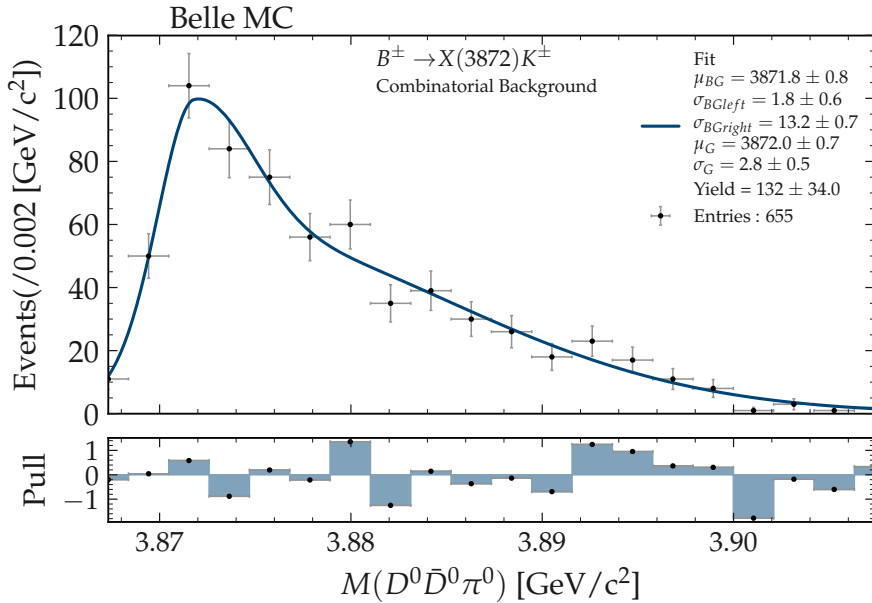
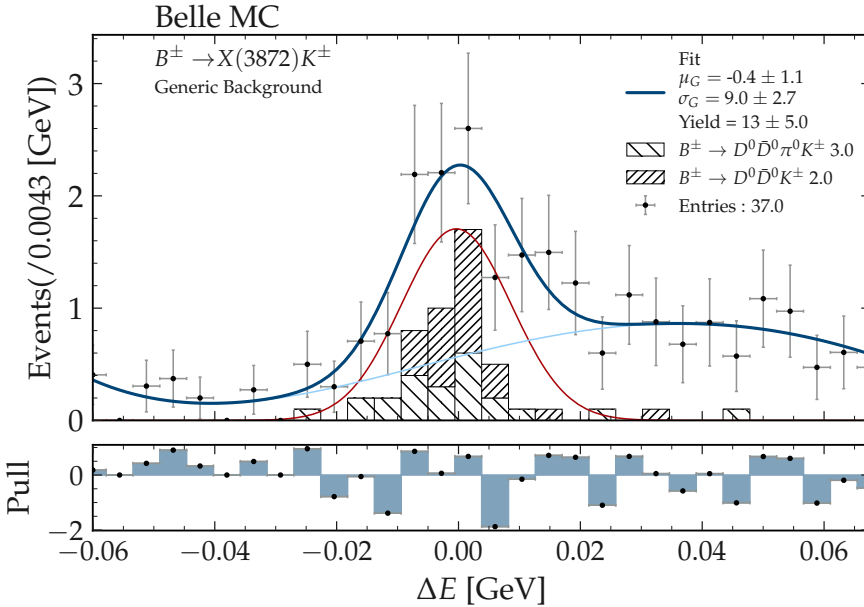


Figure IX.13: Fitted  $X(3872)$  combinatorial background invariant mass distribution.

IX.1.2.7 Fit to the  $\Delta E$  of the Generic Background (Including Non-Resonant)

Function	Gaussian plus 4 <sup>rd</sup> order polynomial
Events	$37 \pm 1$
$\mu_G$	$-0.00036 \pm 0.0011$
$\sigma_G$	$0.0089 \pm 0.0027$
$a_0$	$0.511 \pm 1.722$
$a_1$	$-0.132 \pm 1.251$
$a_2$	$-0.384 \pm 1.343$
$a_2$	$0.068 \pm 1.265$

Table IX.21: Fit parameters for the fit to the  $\Delta E$  distribution of the generic background.Figure IX.14: Fitted  $\Delta E$  distribution for generic background.

**IX.1.2.8 Fit to the  $M_{BC}$  Distribution of the Generic Background (Including Non-Resonant)**

Function	Gaussian plus Argus
Events	$94 \pm 1$
$\mu_G$	$5.2789 \pm 0.0814$
$\sigma_G$	$0.0033 \pm 0.0008$
$argpar$	$-19.65 \pm 80.93$

Table IX.22: Fit parameters for the fit to the  $M_{BC}$  distribution of the generic background.

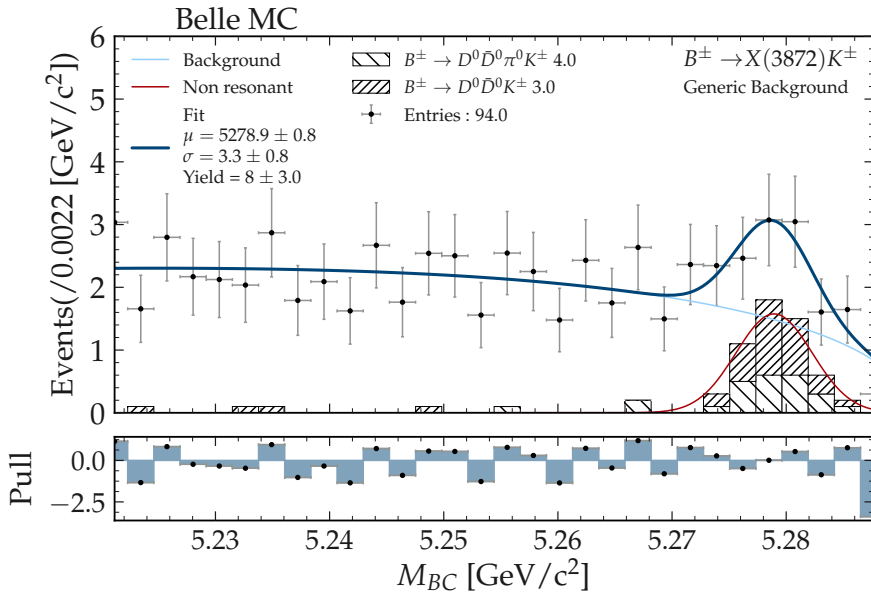
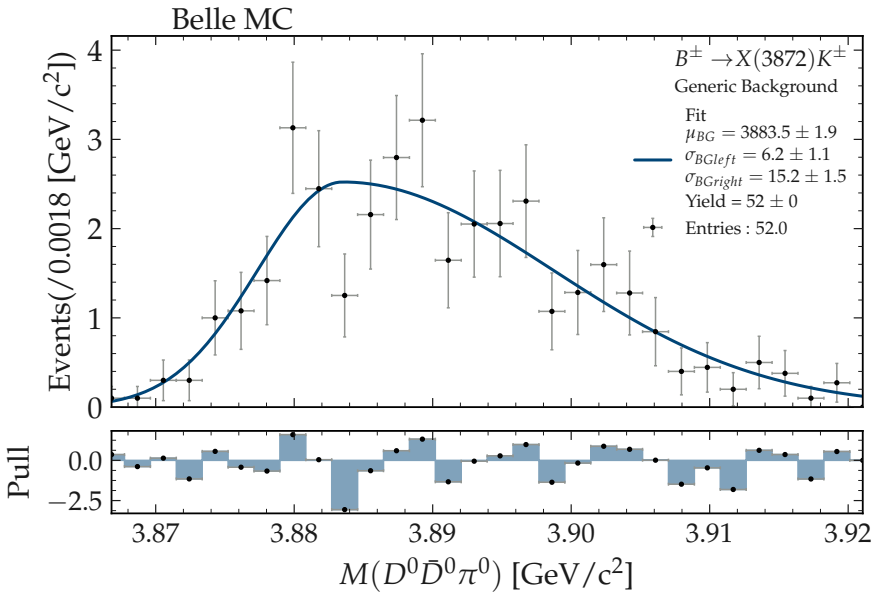


Figure IX.15: Fitted  $M_{BC}$  distribution of the generic background.

IX.1.2.9 Fit to the  $M(D^0\bar{D}^0\pi^0)$  Invariant Mass Distribution of the Generic Background

Function	Bifurcated Gaussian
Events	$52 \pm 0$
$\mu_{BG}$	$3.8835 \pm 0.0018$
$\sigma_{BG,left}$	$0.0062 \pm 0.0011$
$\sigma_{BG,right}$	$0.0152 \pm 0.0015$

Table IX.23: Fit parameters for the fit to the  $M(D^0\bar{D}^0\pi^0)$  invariant mass distribution of the generic background.Figure IX.16: Fitted  $M(D^0\bar{D}^0\pi^0)$  invariant mass distribution of the generic background.

**IX.1.2.10 Fit to the  $M(D^0\bar{D}^0\pi^0)$  Invariant Mass Distribution of the Non-Resonant Background**

Function	Bifurcated Gaussian
Events	$21 \pm 0$
$\mu_{BG}$	$3.8829 \pm 0.0021$
$\sigma_{BG,left}$	$0.0071 \pm 0.0018$
$\sigma_{BG,right}$	$0.0130 \pm 0.0014$

Table IX.24: Fit parameters for the fit to the  $M(D^0\bar{D}^0\pi^0)$  invariant mass distribution of the non-resonant background.

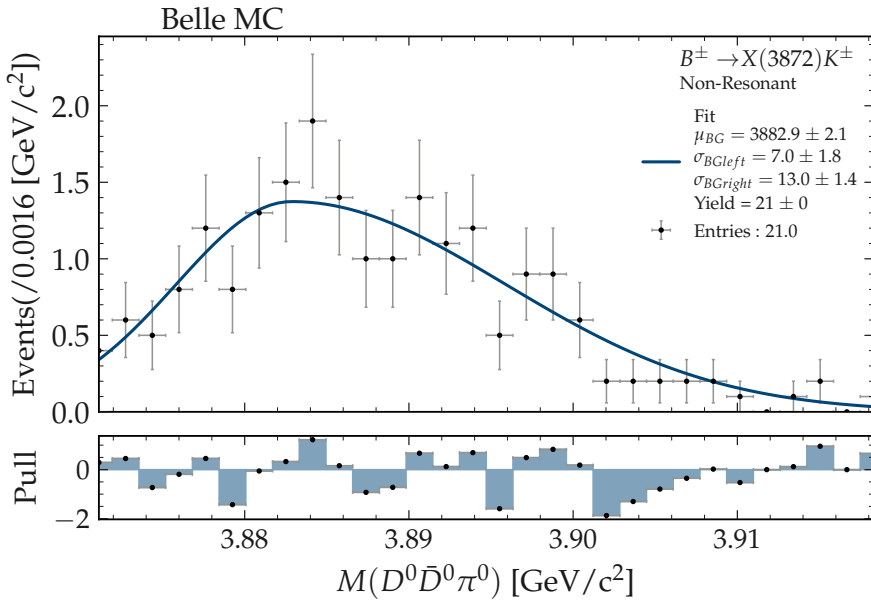


Figure IX.17: Fitted  $M(D^0\bar{D}^0\pi^0)$  invariant mass distribution of the non-resonant background.

## IX.2 Data/MC Comparison for Belle

### IX.2.1 $K^\pm$ Data/MC Comparison

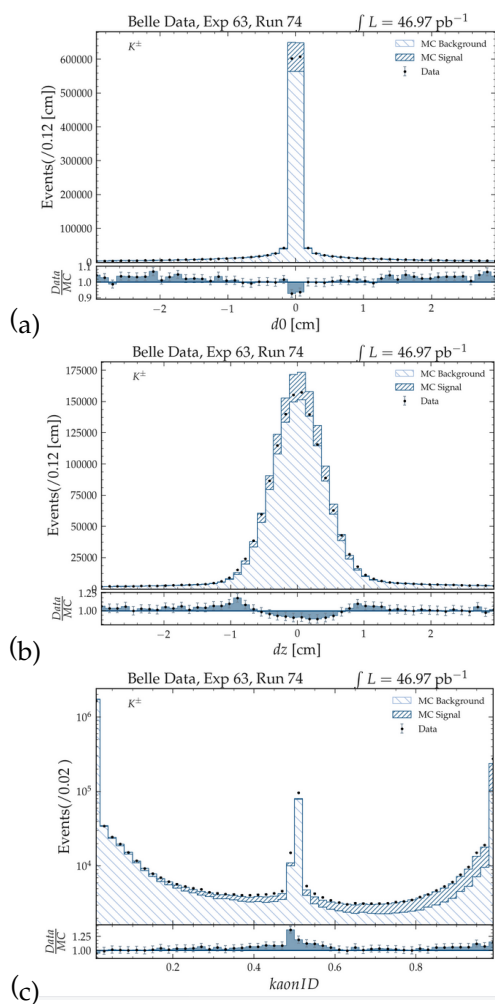


Figure IX.18: Data/MC comparison for  $K^\pm$  variables  $d0$  (a),  $dz$  (b) and  $kaonID$  (c).

## IX.2.2 $\pi^\pm$ Data/MC Comparison

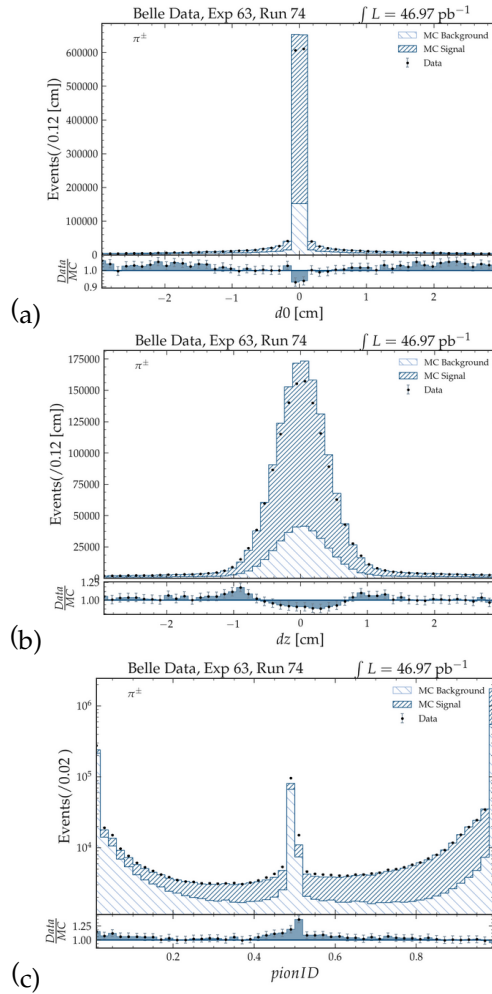


Figure IX.19: Data/MC comparison for  $\pi^\pm$  variables  $d0$  (a),  $dz$  (b) and  $pionID$  (c).

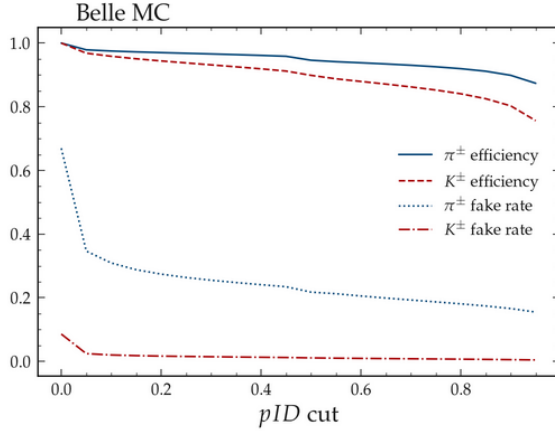
IX.2.3  $K^\pm, \pi^\pm$  Efficiency and Fake Rate in Belle MC

Figure IX.20: Efficiencies and fake-rates for  $K^\pm$  and  $\pi^\pm$  reconstruction with different values of  $particleID$

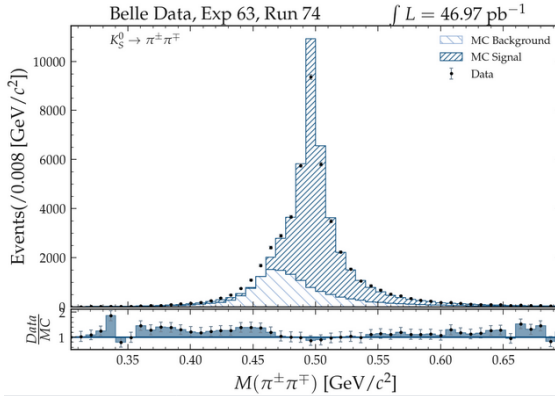
IX.2.4  $K_S^0$  Data/MC Comparison

Figure IX.21: Data/MC comparison for  $K_S^0$  reconstruction in  $46.97 \text{ pb}^{-1}$  of Belle data.

### IX.2.5 $\pi^0$ from $D^0$ Data/MC Comparison

	Data-fit	MC-fit
$\mu$	$133.8 \pm 0.0$	$133.1 \pm 0.0$
$\sigma$	$4.6 \pm 1.2$	$4.2 \pm 0.0$
$\chi^2/ndf$	67.2/47	92.3/47
Yield	$230180 \pm 740$	$1643448 \pm 5140$
MCtruth	268180	1841436
Yield/ $\text{pb}^{-1}$	4901	4350
Y/MC	0.86	0.89

Table IX.25: Fit parameters and results for the fit to the  $\gamma\gamma$  invariant mass distribution for data and MC in  $46.97 \text{ pb}^{-1}$ .

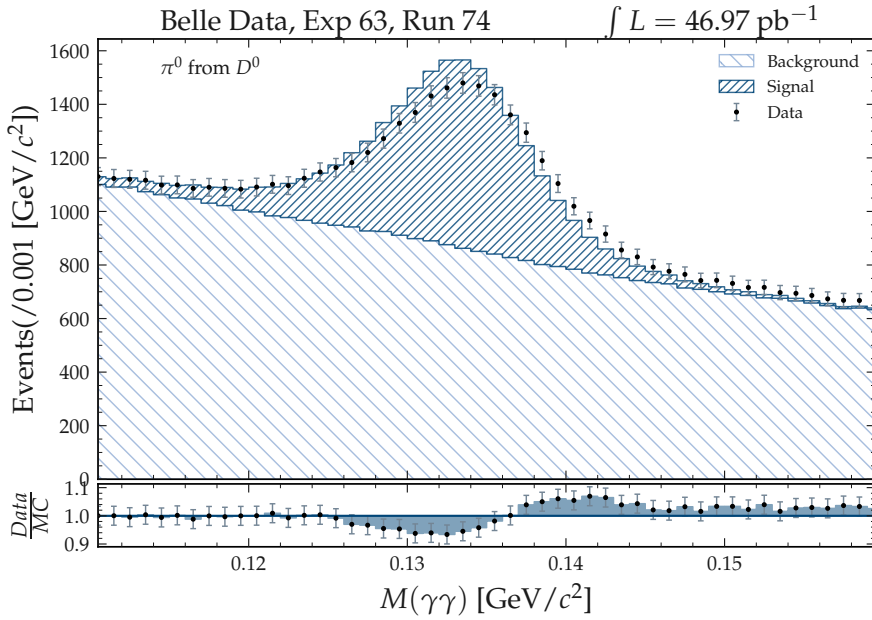


Figure IX.22: Data/MC comparison of the  $\gamma\gamma$  invariant mass.

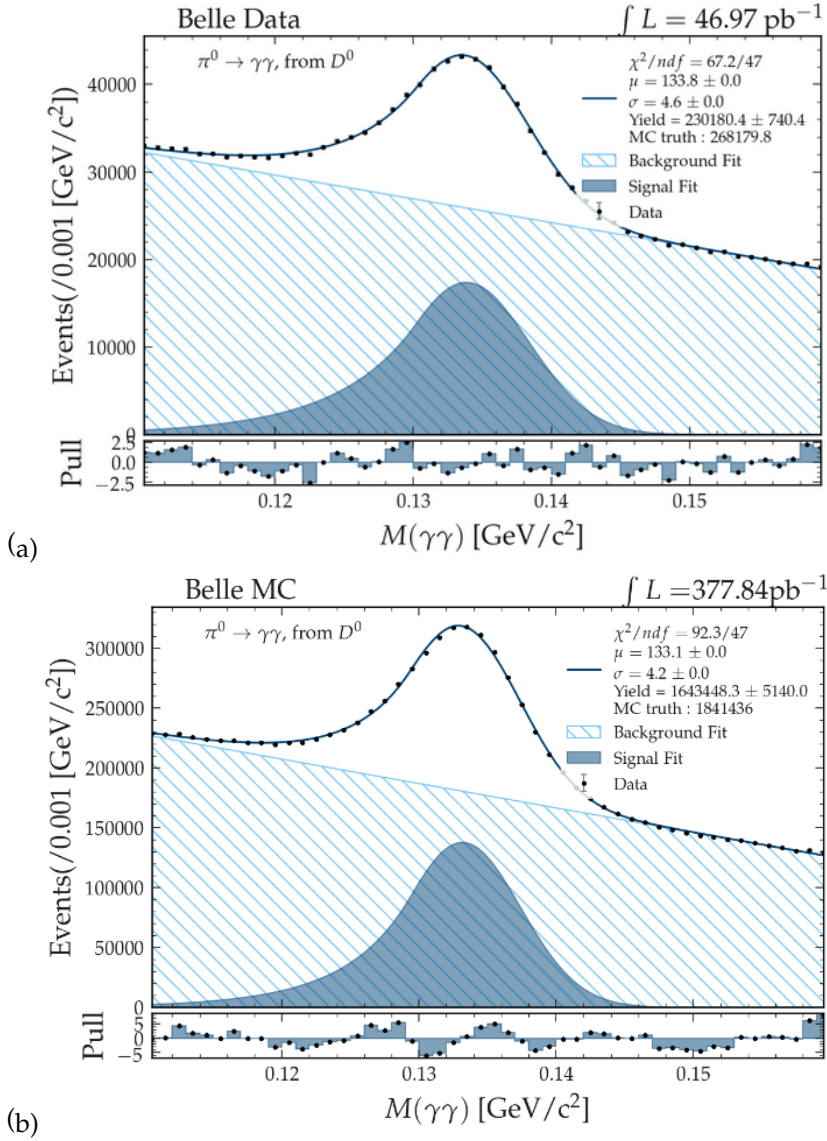


Figure IX.23: Fits to the  $\gamma\gamma$  invariant mass in  $46.97 \text{ pb}^{-1}$  of Belle data (a) and to MC corresponding to  $377.84 \text{ pb}^{-1}$  (b).

### IX.2.6 $\pi^0$ from $X(4014)$ Data/MC Comparison

	Data-fit	MC-fit
$\mu$	$133.3 \pm 0.2$	$131.9 \pm 0.1$
$\sigma$	$6.4 \pm 0.6$	$6.0 \pm 0.1$
$\chi^2/ndf$	48.5/47	195.4/47
Yield	$27379 \pm 6576$	$201465 \pm 1280$
MCtruth	33542	250814
Yield/ $\text{pb}^{-1}$	583	533
Y/MC	0.82	0.8

Table IX.26: Fit parameters and results for the fit to the  $\gamma\gamma$  invariant mass distribution for data and MC in  $46.97 \text{ pb}^{-1}$ .

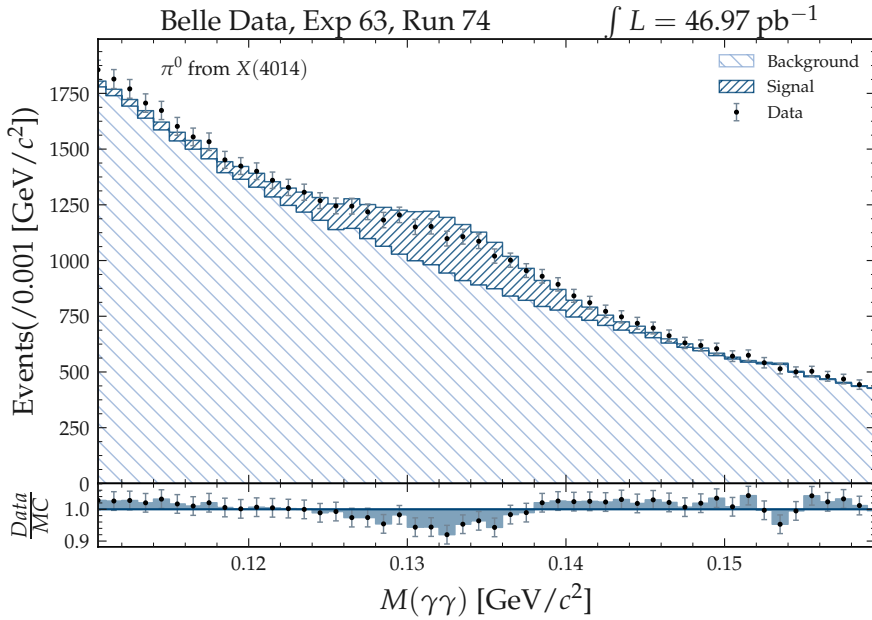


Figure IX.24: Data/MC comparison of the  $\gamma\gamma$  invariant mass.

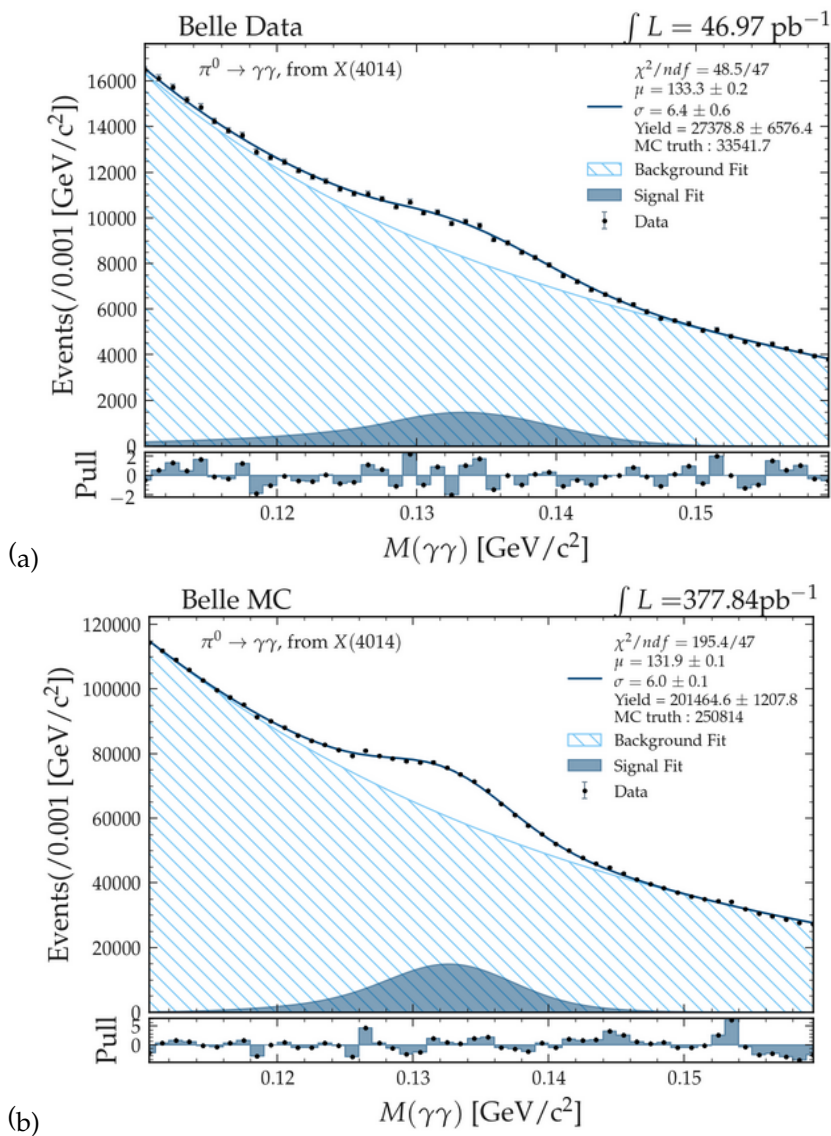


Figure IX.25: Fits to the  $\gamma\gamma$  invariant mass in  $46.97 \text{ pb}^{-1}$  of Belle data (a) and to MC corresponding to  $377.84 \text{ pb}^{-1}$  (b).

IX.2.7  $D^0 \rightarrow K^\pm \pi^\mp$

	Data-fit	MC-fit
$\mu$	$1864.8 \pm 0.1$	$1864.8 \pm 0.0$
$\sigma$	$6.2 \pm 0.1$	$6.0 \pm 0.0$
$\chi^2/ndf$	$36.2/47$	$85.6/47$
Yield	$58833 \pm 922$	$115314 \pm 2762$
MCtruth	65356	120178
Yield/ $\text{pb}^{-1}$	53	57
Y/MC	0.9	0.95

Table IX.27: Fit parameters and results for the fit to the  $K^\pm \pi^\mp$  invariant mass distribution for data and MC in  $1103.53 \text{ pb}^{-1}$ .

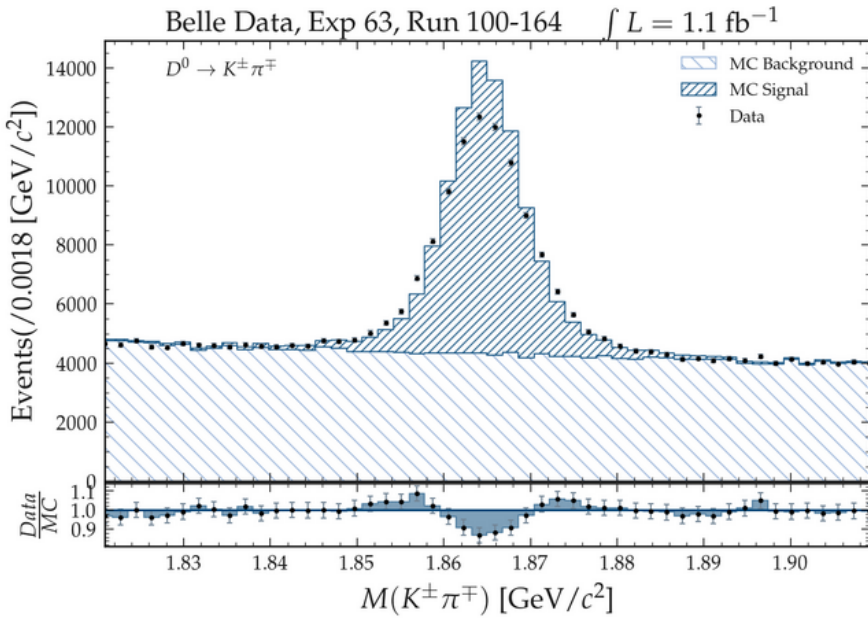


Figure IX.26: Data/MC comparison of the  $K^\pm \pi^\mp$  invariant mass.

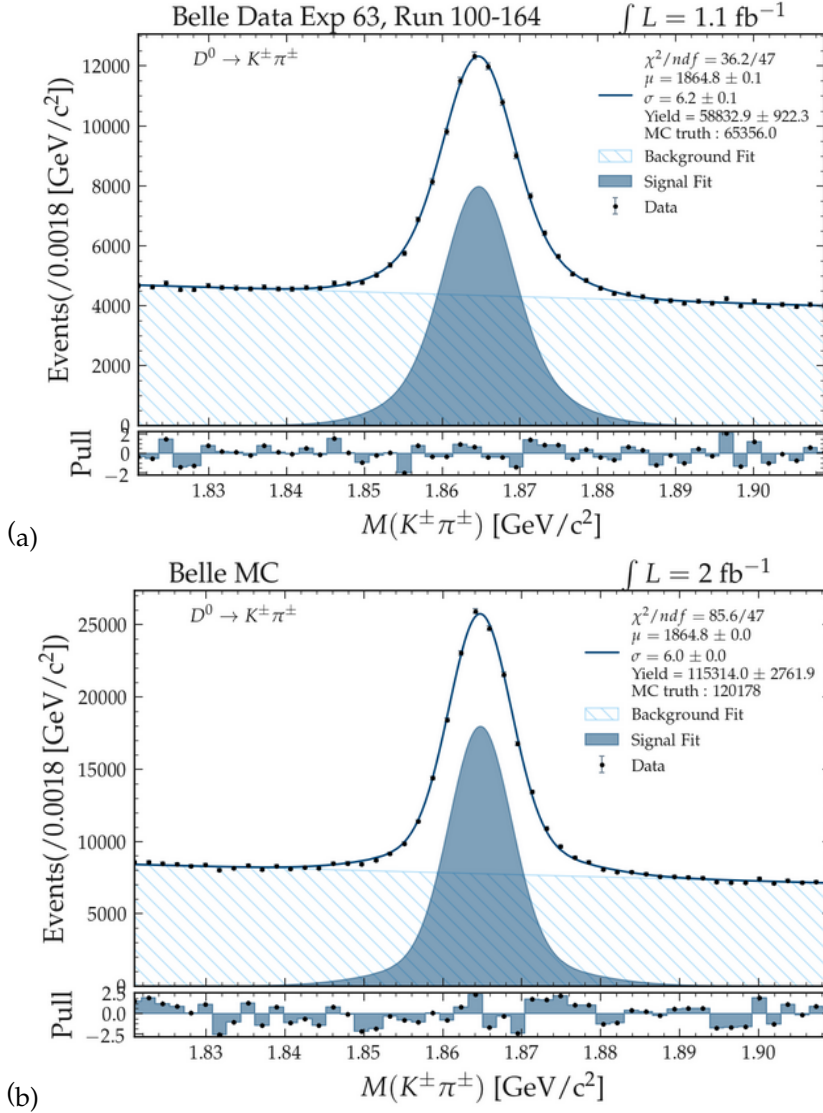


Figure IX.27: Fits to the  $K^\pm \pi^\mp$  invariant mass in  $1.1 \text{ fb}^{-1}$  of Belle data (a) and to MC corresponding to  $2 \text{ fb}^{-1}$  (b).

IX.2.8  $D^0 \rightarrow K^\pm \pi^\mp \pi^0$

	Data-fit	MC-fit
$\mu$	$1867.7 \pm 0.6$	$1864.1 \pm 0.2$
$\sigma$	$8.6 \pm 0.0$	$9.3 \pm 1.5$
$\chi^2/ndf$	68.4/47	60.2/47
Yield	$64733 \pm 2466$	$186918 \pm 2466$
MCtruth	86752	168033
Yield/ $\text{pb}^{-1}$	56	93
Y/MC	0.75	1.11

Table IX.28: Fit parameters and results for the fit to the  $K^\pm \pi^\mp \pi^0$  invariant mass distribution for data and MC in  $1103.53 \text{ pb}^{-1}$ .

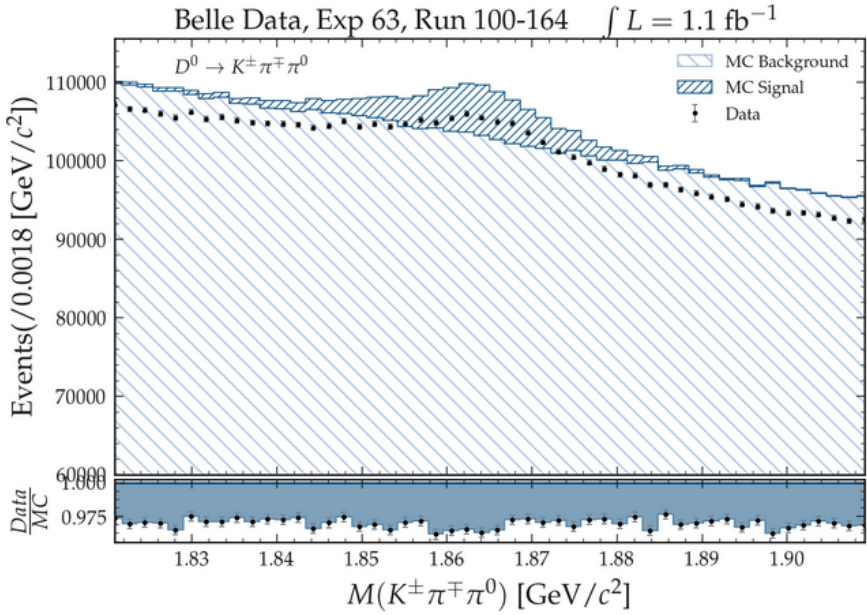


Figure IX.28: Data/MC comparison of the  $K^\pm \pi^\mp \pi^0$  invariant mass.

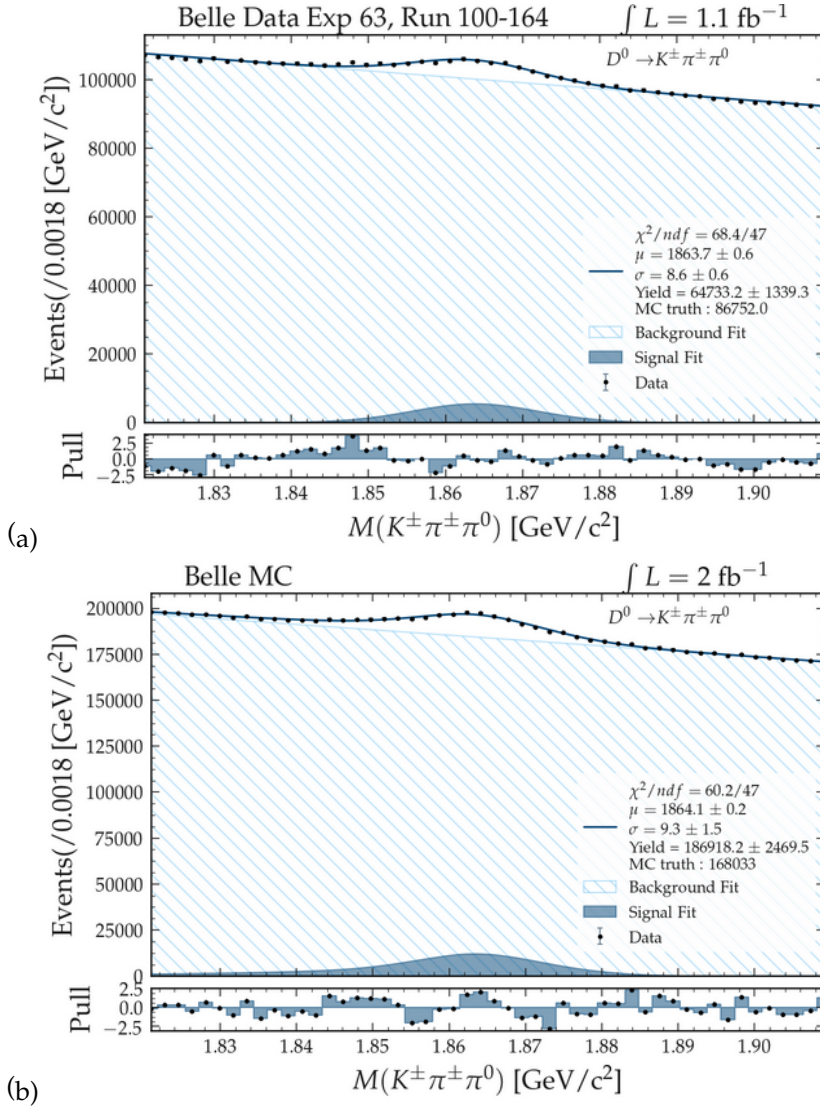


Figure IX.29: Fits to the  $K^\pm \pi^\mp \pi^0$  invariant mass in  $1.1 \text{ fb}^{-1}$  of Belle data (a) and to MC corresponding to  $2 \text{ fb}^{-1}$  (b).

IX.2.9  $D^0 \rightarrow K^\pm \pi^\mp \pi^\pm \pi^\mp$

	Data-fit	MC-fit
$\mu$	$1863.1 \pm 0.1$	$1864.0 \pm 0.3$
$\sigma$	$6.3 \pm 0.0$	$6.1 \pm 0.2$
$\chi^2/ndf$	42.4/47	39.1/47
Yield	$74456 \pm 1365$	$134256 \pm 1145$
MCtruth	71260	134296
Yield/ $\text{pb}^{-1}$	67	67
Y/MC	0.90	1.04

Table IX.29: Fit parameters and results for the fit to the  $K^\pm \pi^\mp \pi^\pm \pi^\mp$  invariant mass distribution for data and MC in  $1103.53 \text{ pb}^{-1}$ .

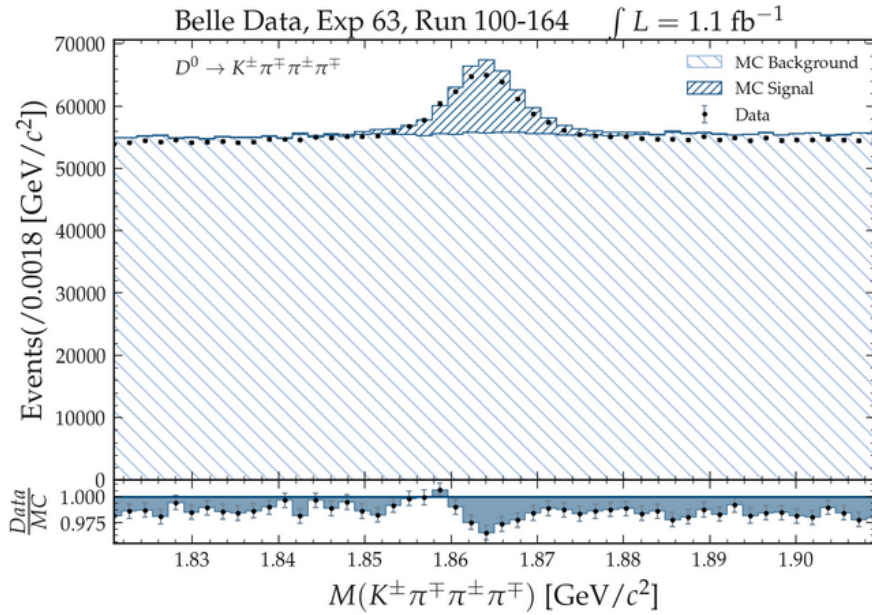


Figure IX.30: Data/MC comparison of the  $K^\pm \pi^\mp \pi^\pm \pi^\mp$  invariant mass.

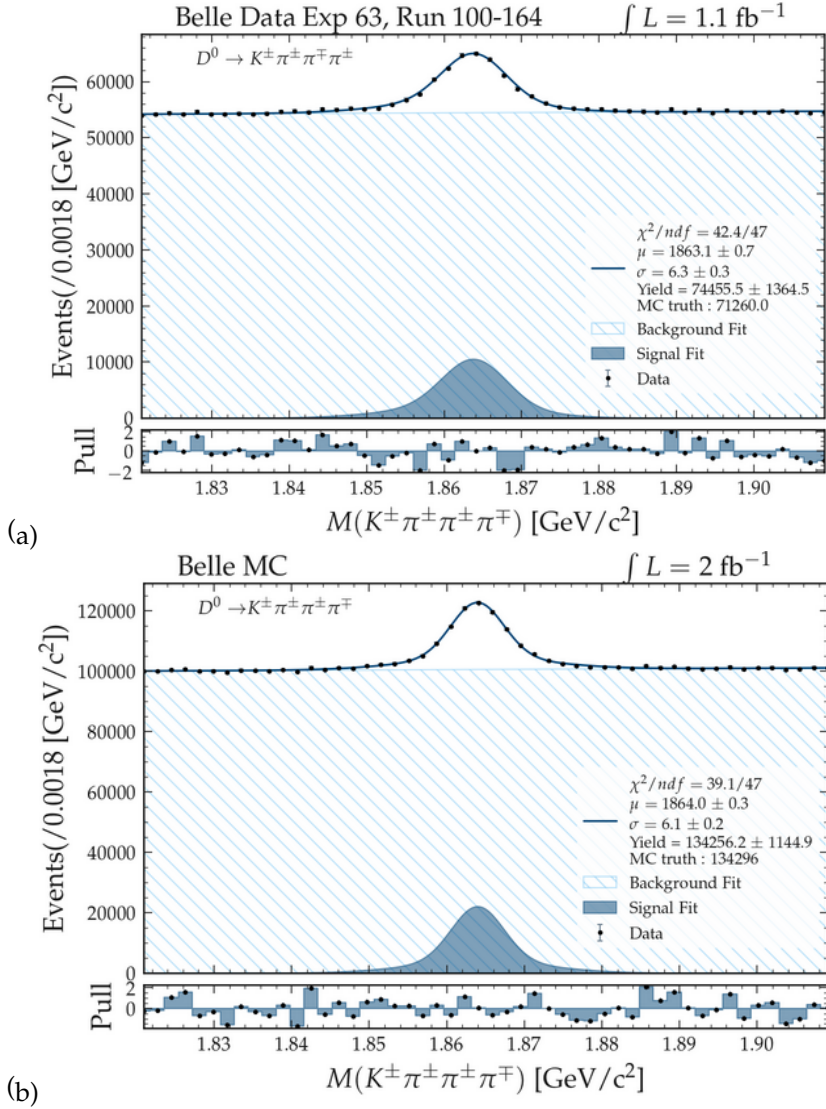


Figure IX.31: Fits to the  $K^\pm \pi^\mp \pi^\pm \pi^\mp$  invariant mass in  $1.1 \text{ fb}^{-1}$  of Belle data (a) and to MC corresponding to  $2 \text{ fb}^{-1}$  (b).

IX.2.10  $D^0 \rightarrow K_S^0 \pi^\pm \pi^\mp$

	Data-fit	MC-fit
$\mu$	$1865.0 \pm 0.1$	$1865.0 \pm 0.1$
$\sigma$	$5.2 \pm 0.4$	$5.1 \pm 0.2$
$\chi^2/ndf$	51.4/47	42.2/47
Yield	$16439 \pm 1499$	$34248 \pm 1631$
MCtruth	19460	36581
Yield/ $\text{pb}^{-1}$	15	17
Y/MC	0.84	0.94

Table IX.30: Fit parameters and results for the fit to the  $K_S^0 \pi^\pm \pi^\mp$  invariant mass distribution for data and MC in  $1103.53 \text{ pb}^{-1}$ .

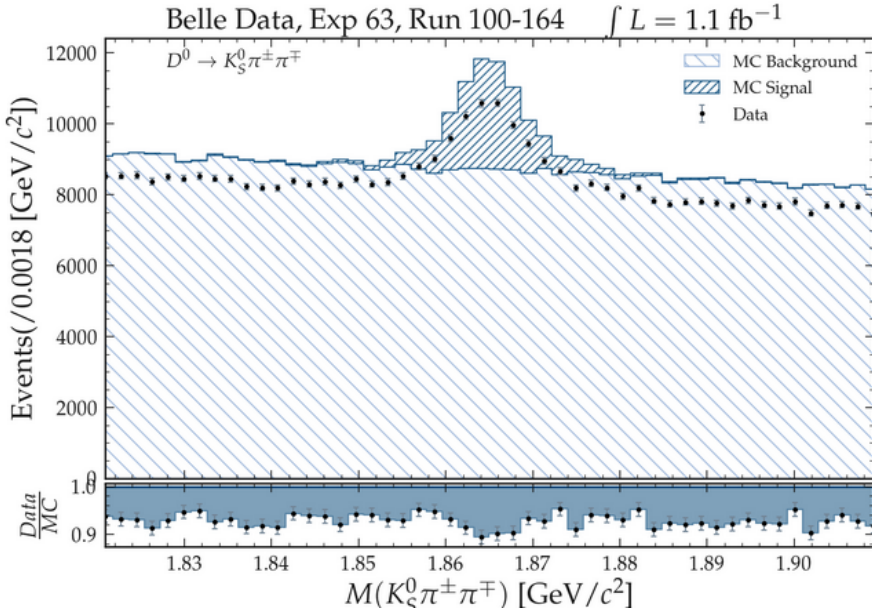


Figure IX.32: Data/MC comparison of the  $K_S^0 \pi^\pm \pi^\mp$  invariant mass.

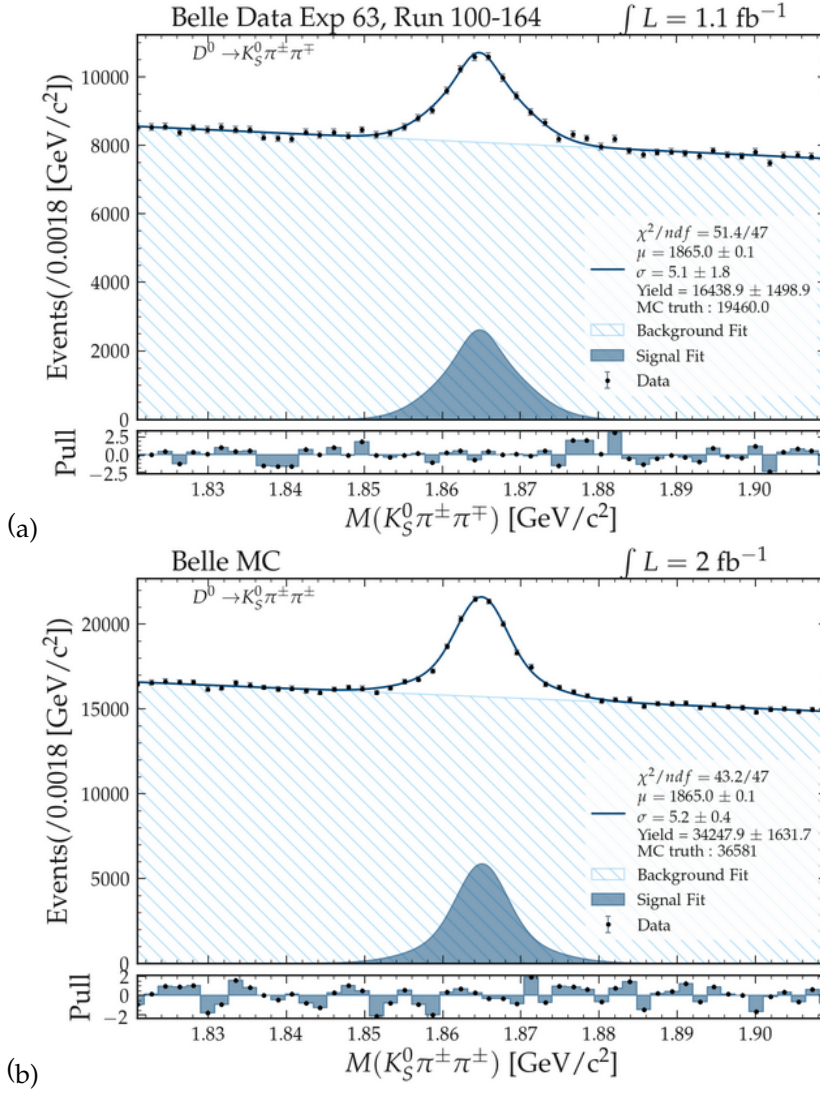


Figure IX.33: Fits to the  $K_S^0 \pi^\pm \pi^\mp$  invariant mass in  $1.1 \text{ fb}^{-1}$  of Belle data (a) and to MC corresponding to  $2 \text{ fb}^{-1}$  (b).

IX.2.11  $D^0 \rightarrow K^\pm K^\mp$

	Data-fit	MC-fit
$\mu$	$1864.1 \pm 0.1$	$1864.4 \pm 0.8$
$\sigma$	$6.0 \pm 0.5$	$5.7 \pm 0.1$
$\chi^2/ndf$	55.8/47	41.5/47
Yield	$6064 \pm 242$	$10666 \pm 504$
MCtruth	5873	10996
Yield/ $\text{pb}^{-1}$	5	5
Y/MC	1.03	0.97

Table IX.31: Fit parameters and results for the fit to the  $K^\pm K^\mp$  invariant mass distribution for data and MC in  $1103.53 \text{ pb}^{-1}$ .

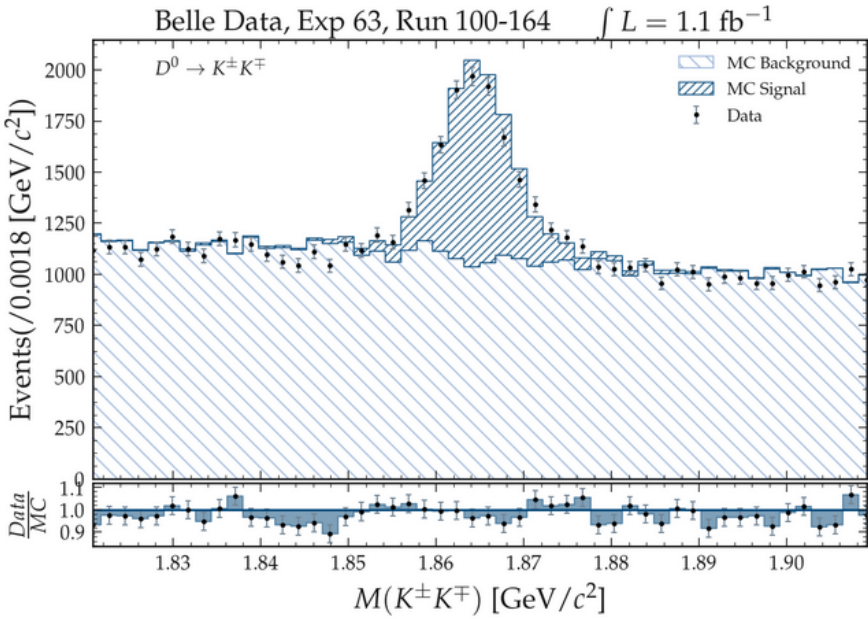


Figure IX.34: Data/MC comparison of the  $K^\pm K^\mp$  invariant mass.

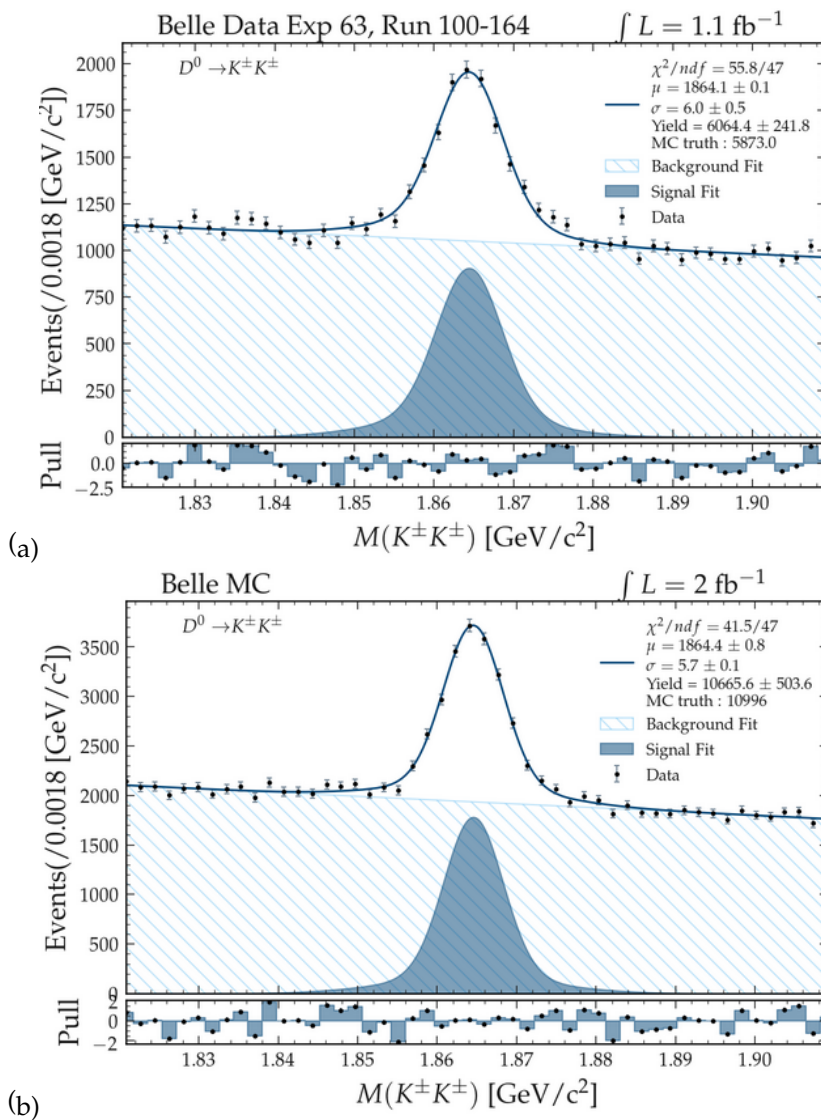


Figure IX.35: Fits to the  $K^\pm K^\mp$  invariant mass in  $1.1 \text{ fb}^{-1}$  of Belle data (a) and to MC corresponding to  $2 \text{ fb}^{-1}$  (b).

### IX.2.12 $B^\pm$ List Variables for the $X(3872)$ Decay

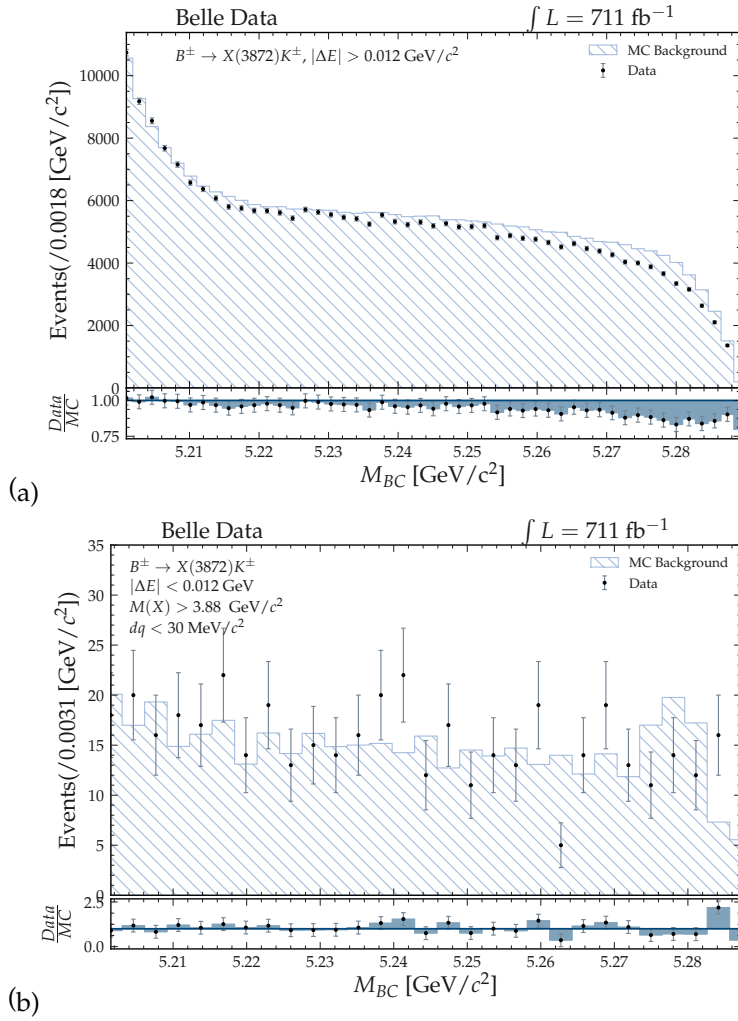
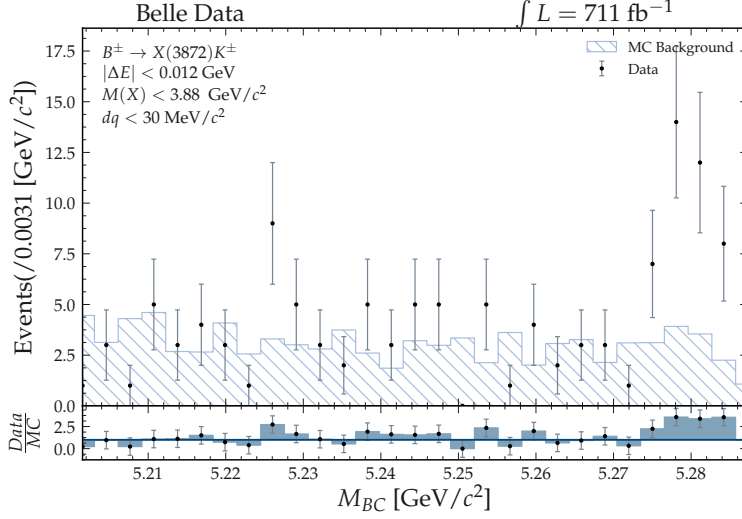
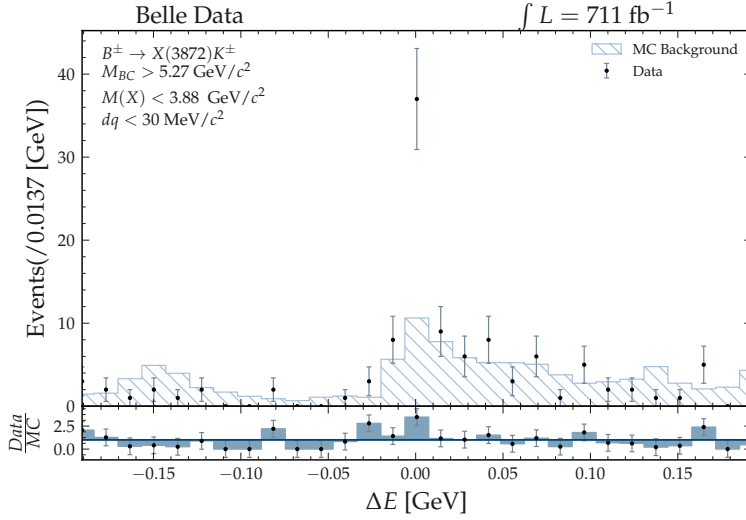


Figure IX.36: Data/MC comparison for  $M_{BC}$  in the sideband region (a) and in a semi signal region with all selections except  $M(X(3872)) < 3.88 \text{ GeV}/c^2$ .


 Figure IX.37: Data/MC comparison for  $M_{BC}$  in final signal region.

 Figure IX.38: Data/MC comparison for  $\Delta E$  in final signal region.

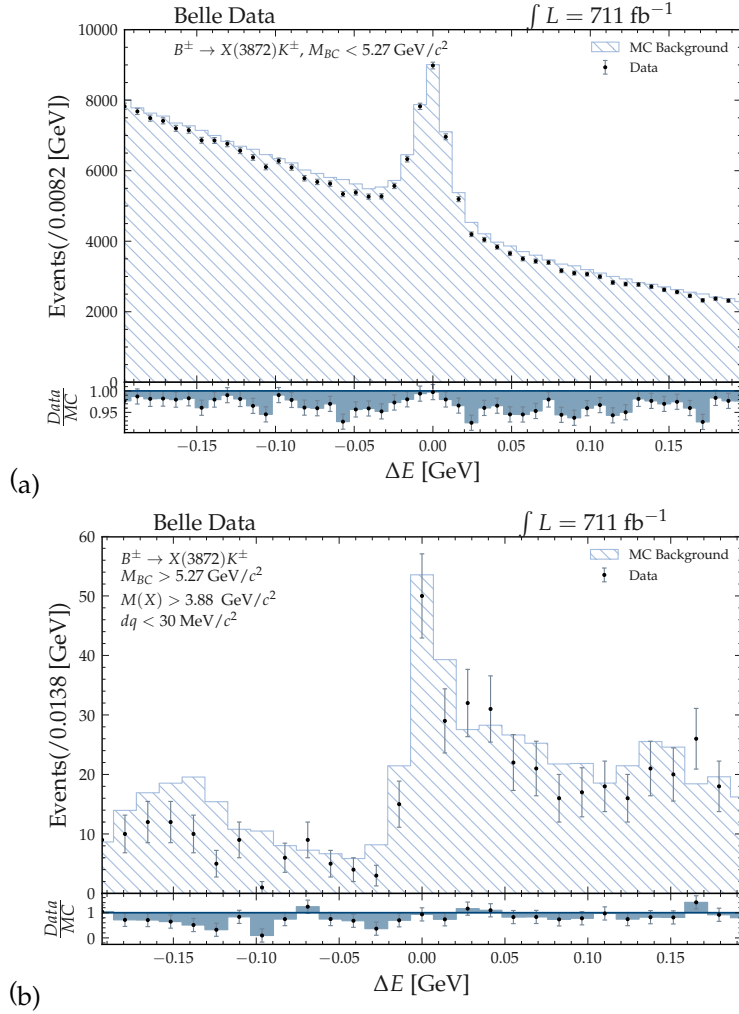


Figure IX.39: Data/MC comparison for  $\Delta E$  in the sideband region (a) and in a semi signal region with all selections except  $M(X(3872)) < 3.88 \text{ GeV}/c^2$  and  $M_{BC} > 5.27 \text{ GeV}/c^2$ .

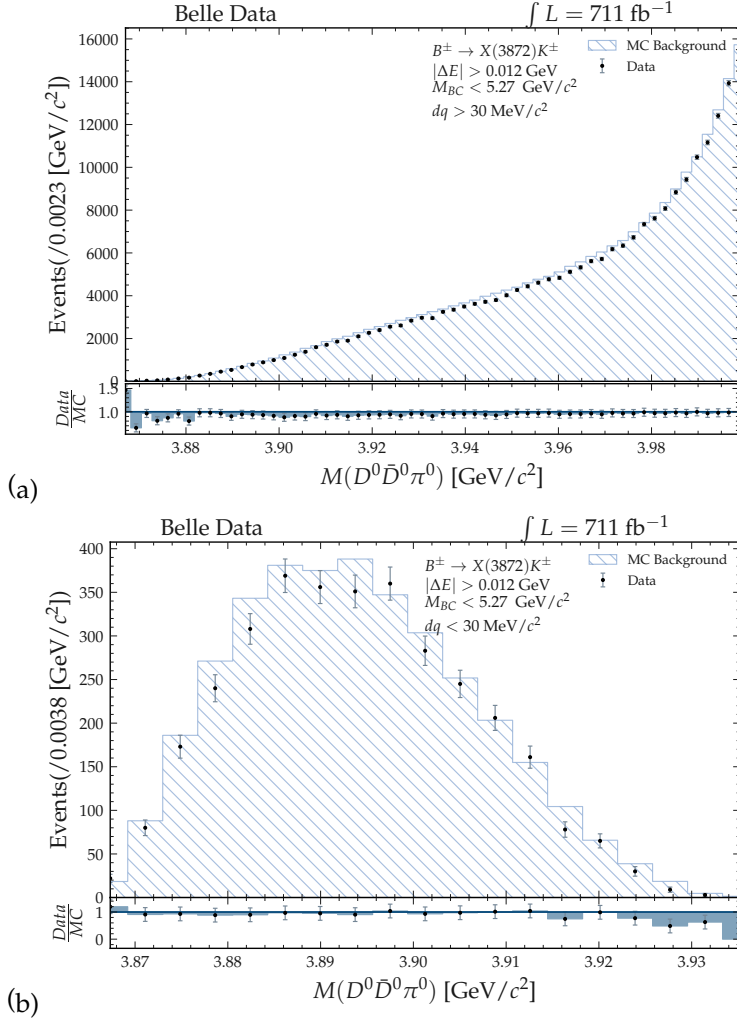


Figure IX.40: Data/MC comparison for  $M(X(3872))$  in the sideband region (a) and in a semi signal region with all selections except  $\Delta E < 12 \text{ MeV}$ .

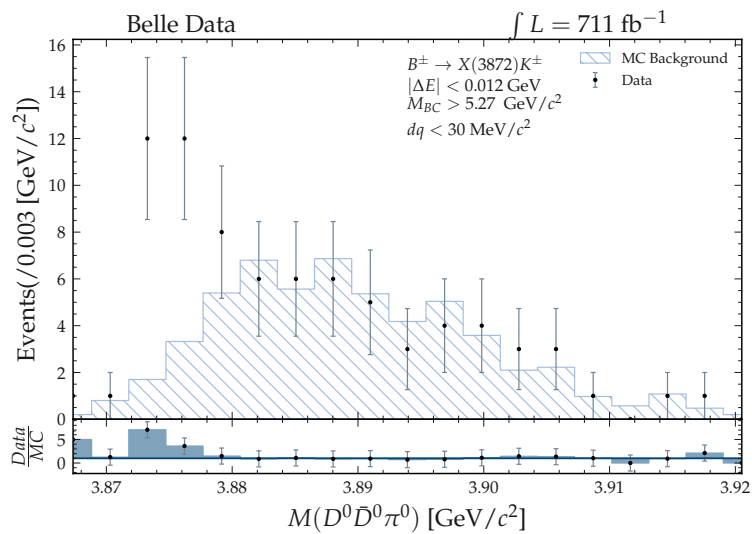


Figure IX.41: Data/MC comparison for  $M(X(3872))$  in final signal region.

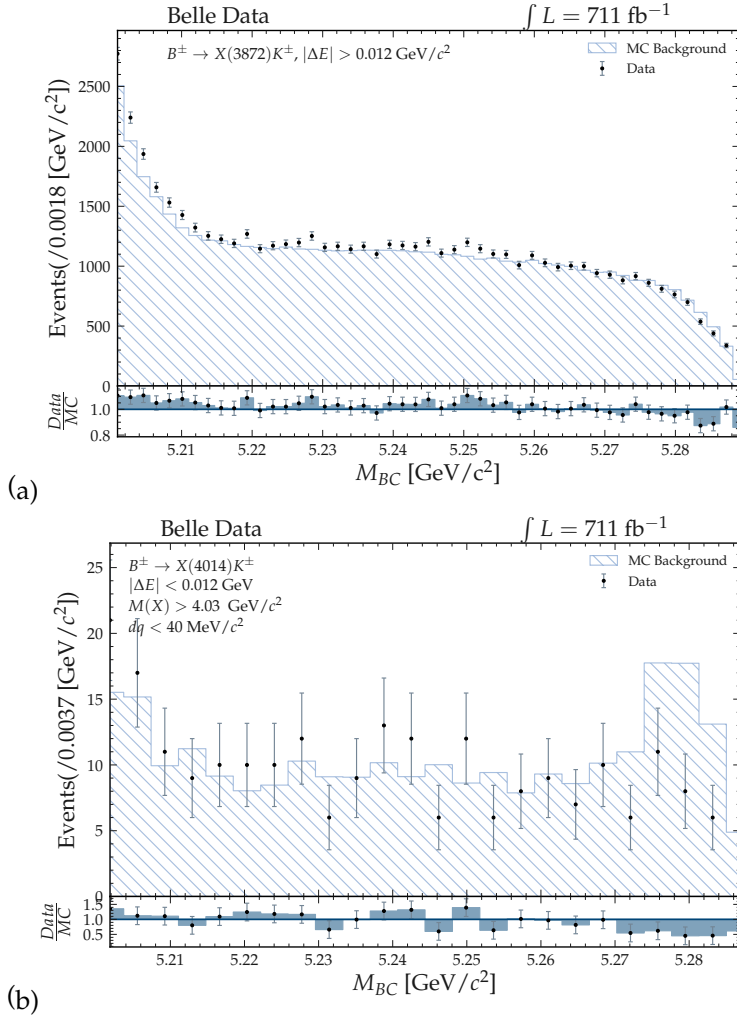
IX.2.13  $B^\pm$  List Variables for the  $X(4014)$  Decay

Figure IX.42: Data/MC comparison for  $M_{BC}$  in the sideband region (a) and in a semi signal region with all selections except  $M(X(4014)) < 4.03 \text{ GeV}/c^2$ .

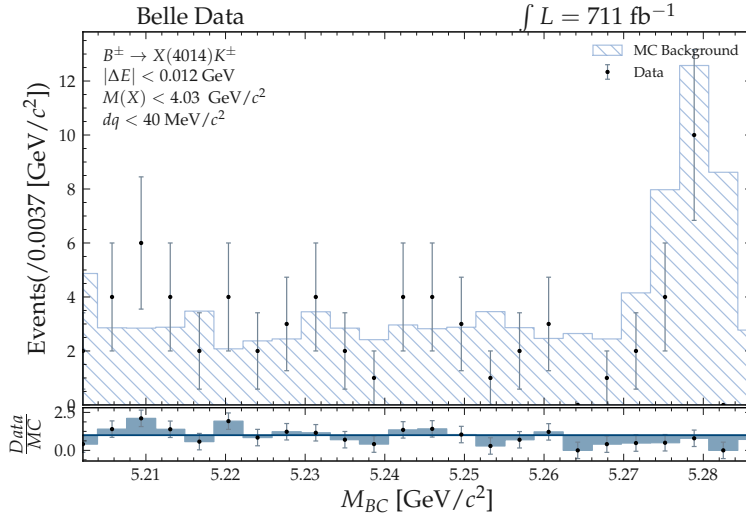


Figure IX.43: Data/MC comparison for  $M_{BC}$  in final signal region.

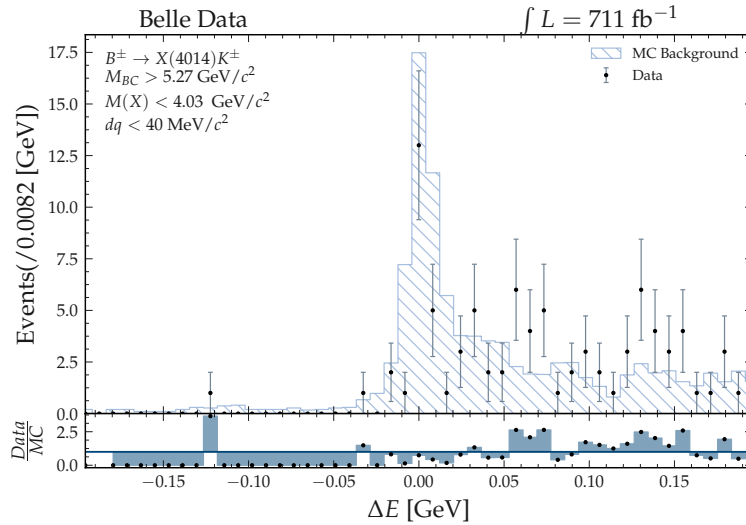


Figure IX.44: Data/MC comparison for  $\Delta E$  in final signal region.

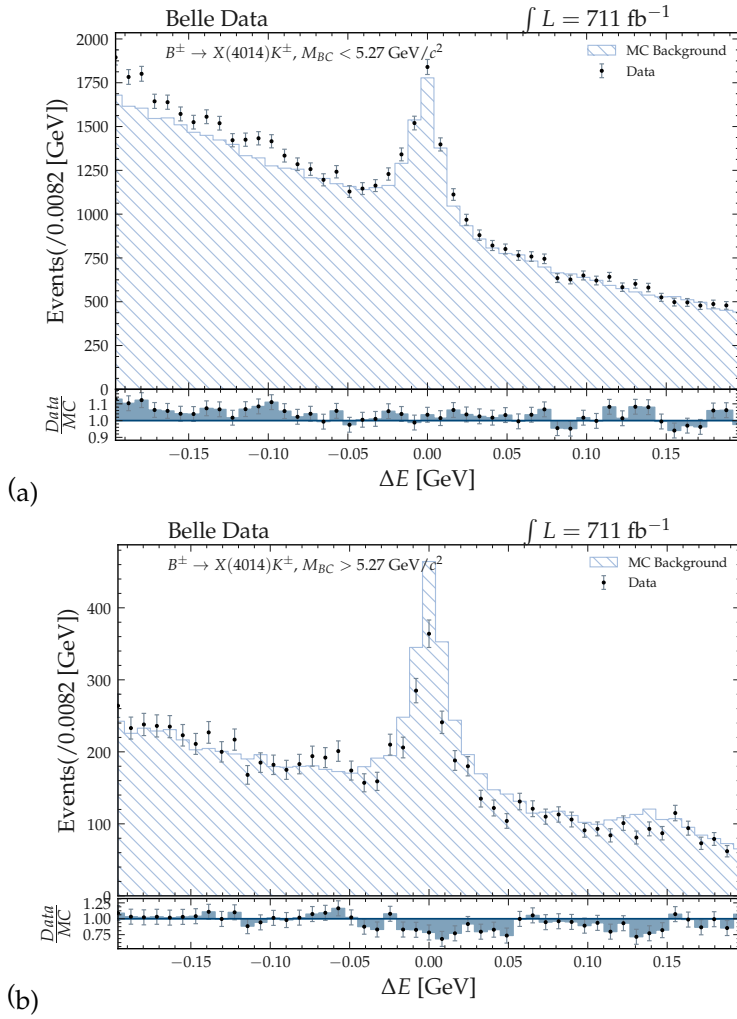


Figure IX.45: Data/MC comparison for  $\Delta E$  in the sideband region (a) and in a semi signal region with all selections except  $M(X(4014)) < 4.03 \text{ GeV}/c^2$ .

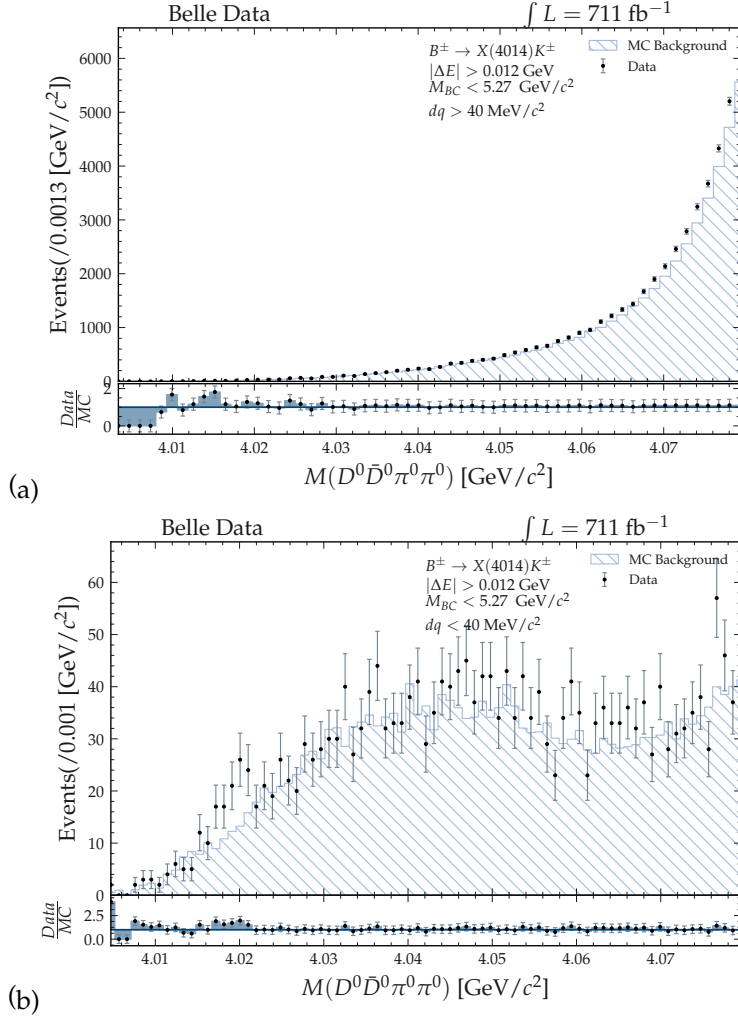


Figure IX.46: Data/MC comparison for  $M(X(4014))$  in the sideband region (a) and in a semi signal region with all selections except  $\Delta E < 12 \text{ MeV}$  and  $M_{BC} > 5.27 \text{ GeV}/c^2$ .

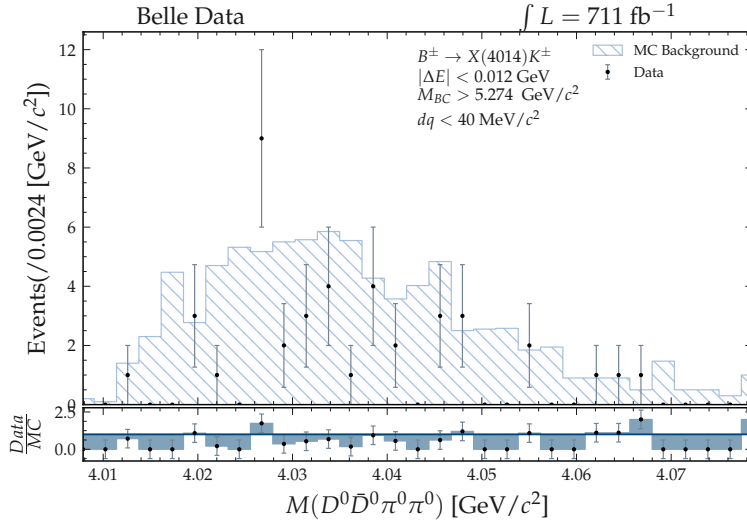


Figure IX.47: Data/MC comparison for the invariant  $M(X(4014))$  in final signal region.

### IX.3 $X(3872)$ 2D Fit PDF

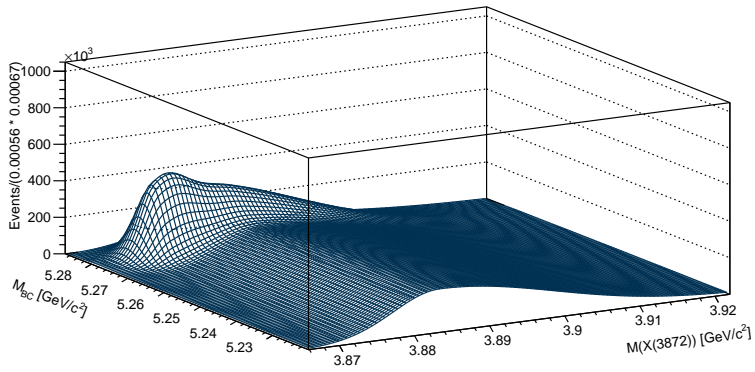


Figure IX.48: Two-dimensional histogram of the fitted 2D-PDF in  $M_{BC}$  and  $M(X(3872))$  with background component only.

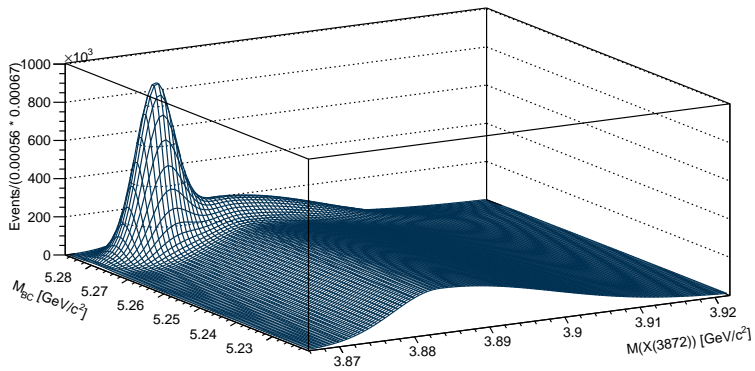
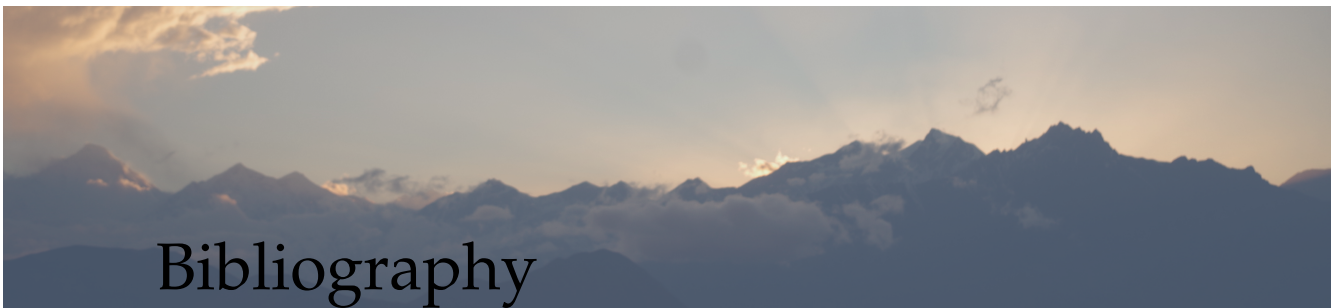


Figure IX.49: Two-dimensional histogram of the fitted 2D-PDF with signal and background component,  $F_{total}$ , in  $M_{BC}$  and  $M(D^0\bar{D}^0\pi^0)$ .



# Bibliography

- [1] C. N. Yang and R. L. Mills, *Conservation of Isotopic Spin and Isotopic Gauge Invariance*, Phys. Rev. **96** (Oct, 1954) 191–195.  
<https://link.aps.org/doi/10.1103/PhysRev.96.191>.
- [2] S. L. Glashow, *Partial-symmetries of weak interactions*, Nuclear Physics **22** (1961) no. 4, 579 – 588. <http://www.sciencedirect.com/science/article/pii/0029558261904692>.
- [3] S. Weinberg, *A Model of Leptons*, Phys. Rev. Lett. **19** (1967) 1264–1266.
- [4] F. H. et al., *Search for elastic muon-neutrino electron scattering*, Physics Letters B **46** (1973) no. 1, 121 – 124. <http://www.sciencedirect.com/science/article/pii/0370269373904942>.
- [5] W. Pauli, *Relativistic Field Theories of Elementary Particles*, Rev. Mod. Phys. **13** (Jul, 1941) 203–232.  
<https://link.aps.org/doi/10.1103/RevModPhys.13.203>.
- [6] S. L. Glashow, J. Iliopoulos, and L. Maiani, *Weak Interactions with Lepton-Hadron Symmetry*, Phys. Rev. D **2** (Oct, 1970) 1285–1292.  
<https://link.aps.org/doi/10.1103/PhysRevD.2.1285>.
- [7] M. Tanabashi et al., Particle Data Group, *Review of Particle Physics*, Phys. Rev. **D98** (2018) no. 3, 030001.
- [8] M. Thomson, *Modern Particle Physics*. Cambridge University Press, 2013.
- [9] S. K. Choi et al., Belle, *Observation of a narrow charmonium - like state in exclusive  $B^\pm \rightarrow K^\pm \pi^+ \pi^- J/\psi$  decays*, Phys. Rev. Lett. **91** (2003) 262001, [arXiv:hep-ex/0309032](https://arxiv.org/abs/hep-ex/0309032) [hep-ex].

- [10] B. Aubert, R. Barate, and Boutigny, BABAR Collaboration, *Study of the  $B^- \rightarrow J/\psi K^- \pi^+ \pi^-$  decay and measurement of the  $B^- \rightarrow X(3872)K^-$  branching fraction*, Phys. Rev. D **71** (Apr, 2005) 071103. <https://link.aps.org/doi/10.1103/PhysRevD.71.071103>.
- [11] M. Ablikim, M. N. Achasov, and X. C. Ai, BESIII Collaboration, *Observation of  $e^+e^- \rightarrow \gamma X(3872)$  at BESIII*, Phys. Rev. Lett. **112** (Mar, 2014) 092001. <https://link.aps.org/doi/10.1103/PhysRevLett.112.092001>.
- [12] M. Kobayashi and T. Maskawa, *CP-Violation in the Renormalizable Theory of Weak Interaction*, Progress of Theoretical Physics **49** (02, 1973) 652–657, <https://academic.oup.com/ptp/article-pdf/49/2/652/5257692/49-2-652.pdf>. <https://doi.org/10.1143/PTP.49.652>.
- [13] CMS, *Search for the rare decay  $B_s^0 \rightarrow \mu^+ \mu^-$  at the LHC with the CMS and LHCb experiments: Combination of LHC results of the search for  $B_s \rightarrow \mu^+ \mu^-$  decays*, .
- [14] I. Bigi and A. Sanada, *Notes on the observability of CP violations in B decays*, Nuclear Physics B **193** (1981) no. 1, 85 – 108. <http://www.sciencedirect.com/science/article/pii/0550321381905198>.
- [15] M. Röhrken, *Time-Dependent CP Violation Measurements*. Springer, Cham, 2014.
- [16] A. Einstein, B. Podolsky, and N. Rosen, *Can Quantum-Mechanical Description of Physical Reality Be Considered Complete?*, Phys. Rev. **47** (May, 1935) 777–780. <https://link.aps.org/doi/10.1103/PhysRev.47.777>.
- [17] R. Abe, H. Aihara, G. Alimonti, Y. Asano, A. Bakich, E. Banas, A. Bozek, T. Browder, J. Dragic, C. Everton, C. Fukunaga, A. Gordon, H. Guler, J. Haba, K. Hara, T. Hara, N. Hastings, M. Hazumi, E. Heenan, T. Higuchi, T. Hojo, H. Ishino, G. Iwai, P. Jalocho, J. Kaneko, P. Kapusta, T. Kawasaki, K. Korotuschenko, J. S. Lange, Y. Li, D. Marlow, T. Matsubara, H. Miyake, L. Moffitt, G. Moloney, S. Mori, Y. Nagshima, T. Nakadaira, T. Nakamura, Z. Natkaniec, S. Okuno, S. Olsen, W. Ostrowicz, H. Palka, L. Peak, M. Rozanska, J. Ryuko, M. Sevir, K. Shimada, K. Sumisawa, S. Stanic, R. Stock, S. Swain, H. Tagomori, H. Tajima, S. Takahashi, F. Takasaki,

- 
- N. Tamura, J. Tanaka, M. Tanaka, G. Taylor, T. Tomura, K. Trabelsi, T. Tusboyama, Y. Tsujita, G. Varner, K. Varvell, H. Yamamoto, Y. Watanabe, Y. Yamada, M. Yokoyama, H. Zhao, and D. Zontar, *Performance of the BELLE silicon vertex detector*, IEEE Transactions on Nuclear Science **48** (2001) no. 4, 997–1001.
- [18] K. Abe, K. Abe, R. Abe, I. Adachi, B. S. Ahn, H. Aihara, M. Akatsu, G. Alimonti, K. Asai, M. Asai, and et al., *Observation of Large CP Violation in the Neutral B Meson System*, Physical Review Letters **87** (Aug, 2001) .  
<http://dx.doi.org/10.1103/PhysRevLett.87.091802>.
- [19] B. Aubert, D. Boutigny, J.-M. Gaillard, A. Hicheur, Y. Karyotakis, J. P. Lees, P. Robbe, V. Tisserand, A. Palano, G. P. Chen, and et al., *Observation of CP Violation in the B Meson System*, Physical Review Letters **87** (Aug, 2001) .  
<http://dx.doi.org/10.1103/PhysRevLett.87.091801>.
- [20] A. J. Bevan, B. Golob, T. Mannel, S. Prell, B. D. Yabsley, H. Aihara, F. Anulli, N. Arnaud, T. Aushev, M. Beneke, and et al., *The Physics of the B Factories*, The European Physical Journal C **74** (Nov, 2014) .  
<http://dx.doi.org/10.1140/epjc/s10052-014-3026-9>.
- [21] L. Wolfenstein, *Parametrization of the Kobayashi-Maskawa Matrix*, Phys. Rev. Lett. **51** (Nov, 1983) 1945–1947.  
<https://link.aps.org/doi/10.1103/PhysRevLett.51.1945>.
- [22] I. Adachi, H. Aihara, D. M. Asner, V. Aulchenko, and Aushev, The Belle Collaboration, *Precise Measurement of the CP Violation Parameter  $\sin 2\phi_1$  in  $B^0 \rightarrow (c\bar{c})K^0$  Decays*, Phys. Rev. Lett. **108** (Apr, 2012) 171802.  
<https://link.aps.org/doi/10.1103/PhysRevLett.108.171802>.
- [23] J. Charles, A. Höcker, H. Lacker, S. Laplace, F. R. Le Diberder, J. Malclés, J. Ocariz, M. Pivk, and L. Roos, *CP violation and the CKM matrix: assessing the impact of the asymmetric B factories*, The European Physical Journal C **41** (May, 2005) 1–131.  
<http://dx.doi.org/10.1140/epjc/s2005-02169-1>.
- [24] E. Eichten, K. Gottfried, T. Kinoshita, K. D. Lane, and T. M. Yan, *Charmonium: The model*, Phys. Rev. D **17** (Jun, 1978) 3090–3117.  
<https://link.aps.org/doi/10.1103/PhysRevD.17.3090>.
-

- [25] T. Barnes, S. Godfrey, and E. S. Swanson, *Higher charmonia*, *Physical Review D* **72** (Sep, 2005) .  
<http://dx.doi.org/10.1103/PhysRevD.72.054026>.
- [26] N. Brambilla, S. Eidelman, C. Hanhart, A. Nefediev, C.-P. Shen, C. E. Thomas, A. Vairo, and C.-Z. Yuan, *The XYZ states: experimental and theoretical status and perspectives*, *arXiv:1907.07583* [hep-ex].
- [27] K. G. Wilson, *Confinement of quarks*, *Phys. Rev. D* **10** (Oct, 1974) 2445–2459.  
<https://link.aps.org/doi/10.1103/PhysRevD.10.2445>.
- [28] L. Liu, G. Moir, M. Peardon, S. M. Ryan, C. E. Thomas, P. Vilaseca, J. Dudek, R. G. Edwards, B. Joó, D. G. Richards, and F. the Hadron Spectrum Collaboration, *Excited and exotic charmonium spectroscopy from lattice QCD*, *Journal of High Energy Physics* **2012** (2012) 1–33.
- [29] M. Ablikim, M. N. Achasov, X. C. Ai, O. Albayrak, D. J. Ambrose, F. F. An, Q. An, J. Z. Bai, R. Baldini Ferroli, Y. Ban, and et al., *Observation of a Charged Charmoniumlike Structure in  $e^+e^- \rightarrow J/\psi$  at  $\sqrt{s}=4.26\text{ GeV}$* , *Physical Review Letters* **110** (Jun, 2013) .  
<http://dx.doi.org/10.1103/PhysRevLett.110.252001>.
- [30] M. Ablikim et al., BESIII, *Observation of a Charged Charmoniumlike Structure in  $e^+e^- \rightarrow \pi^+\pi^- J/\psi$  at  $\sqrt{s} = 4.26\text{ GeV}$* , *Phys. Rev. Lett.* **110** (2013) 252001, *arXiv:1303.5949* [hep-ex].
- [31] X. L. Wang et al., Belle, *Observation of Two Resonant Structures in  $e^+e^- \rightarrow \pi^+\pi^-\psi(2S)$  via Initial State Radiation at Belle*, *Phys. Rev. Lett.* **99** (2007) 142002, *arXiv:0707.3699* [hep-ex].
- [32] Z.-Y. Zhou, Z. Xiao, and H.-Q. Zhou, *Could the  $X(3915)$  and the  $X(3930)$  Be the Same Tensor State?*, *Phys. Rev. Lett.* **115** (2015) no. 2, 022001, *arXiv:1501.00879* [hep-ph].
- [33] B. Aubert et al., BaBar, *Evidence of a broad structure at an invariant mass of  $4.32\text{- GeV}/c^2$  in the reaction  $e^+e^- \rightarrow \pi^+\pi^-\psi_{2S}$  measured at BaBar*, *Phys. Rev. Lett.* **98** (2007) 212001, *arXiv:hep-ex/0610057* [hep-ex].
- [34] M. Voloshin, *Charmonium*, *Progress in Particle and Nuclear Physics* **61** (Oct, 2008) 455–511.  
<http://dx.doi.org/10.1016/j.pnnp.2008.02.001>.

- 
- [35] S. Dubynskiy and M. Voloshin, *Hadro-charmonium*, Physics Letters B **666** (Sep, 2008) 344–346. <http://dx.doi.org/10.1016/j.physletb.2008.07.086>.
- [36] M. B. Voloshin, *Zc(3900)—what is inside?*, Physical Review D **87** (May, 2013). <http://dx.doi.org/10.1103/PhysRevD.87.091501>.
- [37] L. Maiani, A. D. Polosa, and V. Riquer, *A theory of X and Z multiquark resonances*, Physics Letters B **778** (Mar, 2018) 247–251. <http://dx.doi.org/10.1016/j.physletb.2018.01.039>.
- [38] P. C. Wallbott, G. Eichmann, and C. S. Fischer, *X(3872) as a four-quark state in a Dyson-Schwinger/Bethe-Salpeter approach*, Physical Review D **100** (Jul, 2019). <http://dx.doi.org/10.1103/PhysRevD.100.014033>.
- [39] T. Barnes, F. Close, and F. de Viron, *QQG hybrid mesons in the MIT bag model*, Nuclear Physics B **224** (1983) no. 2, 241 – 264. <http://www.sciencedirect.com/science/article/pii/0550321383900044>.
- [40] T. Barnes, F. E. Close, and E. S. Swanson, *Hybrid and conventional mesons in the flux tube model: Numerical studies and their phenomenological implications*, Physical Review D **52** (Nov, 1995) 5242–5256. <http://dx.doi.org/10.1103/PhysRevD.52.5242>.
- [41] S. Cotanch and F. Llanes-Estrada, *Relativistic many-body approach to exotic and charmed hybrid mesons*, Nuclear Physics A **689** (2001) no. 1, 481 – 484. <http://www.sciencedirect.com/science/article/pii/S0375947401008867>. European Few-Body Problems in Physics.
- [42] R. Oncala and J. Soto, *Heavy quarkonium hybrids: Spectrum, decay, and mixing*, Physical Review D **96** (Jul, 2017). <http://dx.doi.org/10.1103/PhysRevD.96.014004>.
- [43] J. J. Dudek, *The lightest hybrid meson supermultiplet in QCD*, Phys. Rev. D **84** (Oct, 2011) 074023. <https://link.aps.org/doi/10.1103/PhysRevD.84.074023>.
- [44] N. A. Trnqvist, *From the deuteron to deusons, an analysis of deuteronlike meson-meson bound states*, Zeitschrift fr Physik C Particles and Fields **61** (Sep, 1994) 525–537. <http://dx.doi.org/10.1007/BF01413192>.
-

- [45] F. kun Guo, C. Hanhart, U.-G. Meißner, Q. Wang, Q. Zhao, and B. song Zou, *Hadronic molecules*, 2017.
- [46] F.-K. Guo, C. Hanhart, U.-G. Meißner, Q. Wang, Q. Zhao, and B.-S. Zou, *Hadronic molecules*, *Reviews of Modern Physics* **90** (Feb, 2018) . <http://dx.doi.org/10.1103/RevModPhys.90.015004>.
- [47] V. MATHIEU, N. KOICHELEV, and V. VENTO, *THE PHYSICS OF GLUEBALLS*, *International Journal of Modern Physics E* **18** (Jan, 2009) 1–49. <http://dx.doi.org/10.1142/S0218301309012124>.
- [48] D. Bugg, *Reinterpreting several narrow “resonances” as threshold cusps*, *Physics Letters B* **598** (Sep, 2004) 8–14. <http://dx.doi.org/10.1016/j.physletb.2004.07.047>.
- [49] R. Aaij, C. Abellan Beteta, B. Adeva, M. Adinolfi, C. Adrover, A. Affolder, Z. Ajaltouni, J. Albrecht, F. Alessio, and et al., *Observation of  $X(3872)$  production in  $pp$  collisions at  $\sqrt{s} = 7$  TeV*, *The European Physical Journal C* **72** (May, 2012) . <http://dx.doi.org/10.1140/epjc/s10052-012-1972-7>.
- [50] T. Aushev, N. Zwahlen, I. Adachi, H. Aihara, A. M. Bakich, V. Balagura, A. Bay, K. Belous, V. Bhardwaj, M. Bischofberger, and et al., *Study of the  $B \rightarrow X(3872)(\rightarrow D^{*0}D^0)K$  decay*, *Physical Review D* **81** (Feb, 2010) . <http://dx.doi.org/10.1103/PhysRevD.81.031103>.
- [51] B. Aubert, M. Bona, D. Boutigny, Y. Karyotakis, J. P. Lees, V. Poireau, X. Prudent, V. Tisserand, A. Zghiche, J. G. Tico, and et al., *Study of resonances in exclusive  $B$  decays to  $D^*D^*K$* , *Physical Review D* **77** (Jan, 2008) . <http://dx.doi.org/10.1103/PhysRevD.77.011102>.
- [52] R. Aaij et al., LHCb, *Determination of the  $X(3872)$  meson quantum numbers*, *Phys. Rev. Lett.* **110** (2013) 222001, arXiv:1302.6269 [hep-ex].
- [53] S.-K. Choi, S. L. Olsen, K. Trabelsi, I. Adachi, H. Aihara, K. Arinstein, D. M. Asner, T. Aushev, A. M. Bakich, E. Barberio, and et al., *Bounds on the width, mass difference and other properties of  $X(3872) \rightarrow \pi^+\pi^-J/\Psi$  decays*, *Physical Review D* **84** (Sep, 2011) . <http://dx.doi.org/10.1103/PhysRevD.84.052004>.

- 
- [54] J. Nieves and M. Pavón Valderrama, *Heavy quark spin symmetry partners of the  $X(3872)$* , *Physical Review D* **86** (Sep, 2012) .  
<http://dx.doi.org/10.1103/PhysRevD.86.056004>.
- [55] C. Hidalgo-Duque, J. Nieves, and M. P. Valderrama, *Light flavor and heavy quark spin symmetry in heavy meson molecules*, *Physical Review D* **87** (Apr, 2013) . <http://dx.doi.org/10.1103/PhysRevD.87.076006>.
- [56] M. Cleven, F.-K. Guo, C. Hanhart, Q. Wang, and Q. Zhao, *The Nature of Near-Threshold XYZ States*, *Proceedings of the 10th International Workshop on the Physics of Excited Nucleons (NSTAR2015)* (May, 2016) . <http://dx.doi.org/10.7566/JPSCP.10.010017>.
- [57] N. A. Tornqvist, *From the deuteron to deusons, an analysis of deuteron-like meson meson bound states*, *Z. Phys. C* **61** (1994) 525–537,  
[arXiv:hep-ph/9310247](http://arxiv.org/abs/hep-ph/9310247).
- [58] D. Ebert, R. Faustov, and V. Galkin, *Masses of heavy tetraquarks in the relativistic quark model*, *Physics Letters B* **634** (Mar, 2006) 214–219.  
<http://dx.doi.org/10.1016/j.physletb.2006.01.026>.
- [59] F. Okiharu, H. Suganuma, and T. T. Takahashi, *Detailed analysis of the tetraquark potential and flip-flop in  $SU(3)$  lattice QCD*, *Physical Review D* **72** (Jul, 2005) . <http://dx.doi.org/10.1103/PhysRevD.72.014505>.
- [60] J. S. Lange, *XYZ states : experimental observation of new narrow states with heavy quarks*, 2013.
- [61] L. Maiani, F. Piccinini, A. D. Polosa, and V. Riquer, *Diquark-antidiquark states with hidden or open charm and the nature of  $X(3872)$* , *Physical Review D* **71** (Jan, 2005) .  
<http://dx.doi.org/10.1103/PhysRevD.71.014028>.
- [62] M. Shifman, A. Vainshtein, and V. Zakharov, *QCD and resonance physics. theoretical foundations*, *Nuclear Physics B* **147** (1979) no. 5, 385 – 447. <http://www.sciencedirect.com/science/article/pii/0550321379900221>.
- [63] G. Breit and E. Wigner, *Capture of Slow Neutrons*, *Phys. Rev.* **49** (Apr, 1936) 519–531.  
<https://link.aps.org/doi/10.1103/PhysRev.49.519>.
-

- [64] T. J. Burns, F. Piccinini, A. D. Polosa, and C. Sabelli, *The2+assignment for the X(3872)*, Physical Review D **82** (Oct, 2010) .  
<http://dx.doi.org/10.1103/PhysRevD.82.074003>.
- [65] N. V. Drenska, R. Faccini, and A. D. Polosa, *Exotic hadrons with hidden charm and strangeness*, Physical Review D **79** (Apr, 2009) .  
<http://dx.doi.org/10.1103/PhysRevD.79.077502>.
- [66] H. Georgi, *An effective field theory for heavy quarks at low energies*, Physics Letters B **240** (1990) no. 3, 447 – 450. <http://www.sciencedirect.com/science/article/pii/037026939091128X>.
- [67] S. Godfrey and N. Isgur, *Mesons in a relativized quark model with chromodynamics*, Phys. Rev. D **32** (Jul, 1985) 189–231.  
<https://link.aps.org/doi/10.1103/PhysRevD.32.189>.
- [68] B.-Q. Li, C. Meng, and K.-T. Chao, *Coupled-channel and screening effects in charmonium spectrum*, Phys. Rev. D **80** (Jul, 2009) 014012.  
<https://link.aps.org/doi/10.1103/PhysRevD.80.014012>.
- [69] L. Maiani, F. Piccinini, A. D. Polosa, and V. Riquer, *Diquark-antidiquark states with hidden or open charm and the nature of X(3872)*, Phys. Rev. D **71** (Jan, 2005) 014028.  
<https://link.aps.org/doi/10.1103/PhysRevD.71.014028>.
- [70] T. Abe et al., Belle-II, *Belle II Technical Design Report*, arXiv:1011.0352 [physics.ins-det].
- [71] W. Neeser, M. Bocker, P. Buchholz, P. Fischer, P. Holl, J. Kemmer, P. Klein, H. Koch, M. Locker, G. Lutz, H. Matthay, L. Struder, M. Trimpl, J. Ulrici, and N. Wermes, *The DEPFET pixel BIOSCOPE*, Nuclear Science, IEEE Transactions on **47** (June, 2000) 1246–1250.
- [72] A. Moll, *Comprehensive study of the background for the Pixel Vertex Detector at Belle II*. PhD thesis, Munich U., 2015.  
<https://edoc.ub.uni-muenchen.de/19106>.
- [73] S. Rummel and L. Andricek, *The DEPFET active pixel sensor for vertexing at ILC and Super KEKB*, Nuclear Instruments and Methods in Physics Research Section A: Accelerators, Spectrometers, Detectors and Associated Equipment **623** (2010) no. 1, 189 – 191. <http://www.sciencedirect.com/science/article/pii/S0168900210004766>. 1st

---

International Conference on Technology and Instrumentation in Particle Physics.

- [74] H. Krüger, *Front-end electronics for DEPFET pixel detectors at SuperBelle (BELLE II)*, Nuclear Instruments and Methods in Physics Research Section A: Accelerators, Spectrometers, Detectors and Associated Equipment **617** (2010) no. 1, 337 – 341. <http://www.sciencedirect.com/science/article/pii/S0168900209019470>. 11th Pisa Meeting on Advanced Detectors.
- [75] M. Lemarenko, T. Hemperek, H. Krüger, M. Koch, F. Lüticke, C. Marinas, and N. Wermes, *Test results of the Data Handling Processor for the DEPFET Pixel Vertex Detector*, Journal of Instrumentation **8** (jan, 2013) C01032–C01032. <https://doi.org/10.1088/2F1748-0221/2F8/2F01/2Fc01032>.
- [76] J. Knopf, P. Fischer, C. Kreidl, and I. Peric, *A 256 channel 8-Bit current digitizer ASIC for the Belle-II PXD*, Journal of Instrumentation **6** (jan, 2011) C01085–C01085. <https://doi.org/10.1088/2F1748-0221/2F6/2F01/2Fc01085>.
- [77] A. A. Watson, *The discovery of Cherenkov radiation and its use in the detection of extensive air showers*, Nuclear Physics B - Proceedings Supplements **212-213** (Mar, 2011) 13–19. <http://dx.doi.org/10.1016/j.nuclphysbps.2011.03.003>.
- [78] M. Y. et al., *RPC systems for BELLE detector at KEKB*, Nuclear Instruments and Methods in Physics Research Section A: Accelerators, Spectrometers, Detectors and Associated Equipment **456** (2000) no. 1, 109 – 112. <http://www.sciencedirect.com/science/article/pii/S0168900200009736>. Proceedings of the 5th Int. Workshop on Resistive Plate Chambers and Related Detectors.
- [79] T. Aushev, D. Besson, K. Chilikin, R. Chistov, M. Danilov, P. Katrenko, R. Mizuk, G. Pakhlova, P. Pakhlov, V. Rusinov, and et al., *A scintillator based endcap KL and muon detector for the Belle II experiment*, Nuclear Instruments and Methods in Physics Research Section A: Accelerators, Spectrometers, Detectors and Associated Equipment **789** (Jul, 2015) 134–142. <http://dx.doi.org/10.1016/j.nima.2015.03.060>.

- [80] R. Frühwirth, *Application of Kalman filtering to track and vertex fitting*, Nuclear Instruments and Methods in Physics Research Section A: Accelerators, Spectrometers, Detectors and Associated Equipment **262** (1987) no. 2, 444 – 450. <http://www.sciencedirect.com/science/article/pii/0168900287908874>.
- [81] M. Nakao, *Timing distribution for the Belle II data acquisition system*, Journal of Instrumentation **7** (jan, 2012) C01028–C01028. <https://doi.org/10.1088/1748-0221/7/01/C01028>.
- [82] D. Sun, Z. Liua, J. Zhao, and H. Xu, *Belle2Link: A Global Data Readout and Transmission for Belle II Experiment at KEK*, Physics Procedia **37** (2012) 1933 – 1939. <http://www.sciencedirect.com/science/article/pii/S1875389212019104>. Proceedings of the 2nd International Conference on Technology and Instrumentation in Particle Physics (TIPP 2011).
- [83] T. Higuchi et al., *Development of a PCI based data acquisition platform for high intensity accelerator experiments*, eConf **C0303241** (2003) TUGT004, arXiv:hep-ex/0305088 [hep-ex].
- [84] R. Itoh, T. Higuchi, M. Nakao, S. Y. Suzuki, and S. Lee, *Data Flow and High Level Trigger of Belle II DAQ System*, IEEE Transactions on Nuclear Science **60** (Oct, 2013) 3720–3724.
- [85] D. Levit, I. Konorov, S. Paul, and D. Greenwald, *FPGA based data read-out system of the Belle II pixel detector*, IEEE Trans. Nucl. Sci. **62** (2015) no. 3, 1033–1039, arXiv:1406.3864 [physics.ins-det]. [7097505(2014)].
- [86] X. Inc., *Aurora 8B/10B Protocol Specification*, 2014. [https://www.xilinx.com/support/documentation/ip\\_documentation/aurora\\_8b10b\\_protocol\\_spec\\_sp002.pdf](https://www.xilinx.com/support/documentation/ip_documentation/aurora_8b10b_protocol_spec_sp002.pdf).
- [87] F. Bernlochner, B. Deschamps, J. Dingfelder, C. Marinas, and C. Wessel, *Online Data Reduction for the Belle II Experiment using DATCON*, EPJ Web Conf. **150** (2017) 00014, arXiv:1709.00612 [hep-ex].
- [88] A. S. Hassanein, S. Mohammad, M. Sameer, and M. E. Ragab, *A Survey on Hough Transform, Theory, Techniques and Applications*, ArXiv **abs/1502.02160** (2015) .

- 
- [89] T. Geßler, *Development of FPGA-Based Algorithms for the Data Acquisition of the Belle II Pixel Detector*. PhD thesis, Giessen U., 2015. <http://docs.belle2.org/record/416>.
- [90] J. Zhao, Z. Liu, H. Xu, W. Gong, K. Wang, H. Lin, F. Guo, W. Kuehn, T. Gessler, C. Wang, Z. Liu, and F. Deng, *A general xTCA compliant and FPGA based data processing building blocks for trigger and data acquisition system*, in *2014 19th IEEE-NPSS Real Time Conference*, pp. 1–4. May, 2014.
- [91] T. Kuhr, C. Pulvermacher, M. Ritter, T. Hauth, and N. Braun, *The Belle II Core Software*, *Computing and Software for Big Science* 3 (Nov, 2018). <http://dx.doi.org/10.1007/s41781-018-0017-9>.
- [92] I. A. et al., *ROOT — A C++ framework for petabyte data storage, statistical analysis and visualization*, *Computer Physics Communications* 180 (2009) no. 12, 2499 – 2512. <http://www.sciencedirect.com/science/article/pii/S0010465509002550>. 40 YEARS OF CPC: A celebratory issue focused on quality software for high performance, grid and novel computing architectures.
- [93] R. Kalman, *A new approach to linear filtering and prediction problems*” *transaction of the asme journal of basic*, 1960.
- [94] M. Gelb, T. Keck, M. Prim, H. Atmacan, J. Gemmler, R. Itoh, B. Kronenbitter, T. Kuhr, M. Lubej, F. Metzner, C. Park, S. Park, C. Pulvermacher, M. Ritter, and A. Zupanc, *B2BII: Data Conversion from Belle to Belle II*, *Computing and Software for Big Science* 2 (Nov, 2018) 9. <https://doi.org/10.1007/s41781-018-0016-x>.
- [95] X. Inc., *LocalLink User Interface page*, . [http://www.xilinx.com/aurora/aurora\\_member/sp006.pdf](http://www.xilinx.com/aurora/aurora_member/sp006.pdf).
- [96] EPICS, *Experimental Physics and Industrial Control System (EPICS)*, . <https://epics-controls.org/>.
- [97] CSS, *Control System Studio*, . <http://controlsystemstudio.org/>.
- [98] D. J. Lange, *The EvtGen particle decay simulation package*, *Nucl. Instrum. Meth. A* 462 (2001) 152–155.
- [99] S. Agostinelli et al., *Geant4-a simulation toolkit*, *Nuclear Instruments and Methods in Physics Research A* 506 (2003) 250–303.
-

- [100] T. A. N. Zwahlen, *Study of  $B \rightarrow X(3872)(DD^*)K$* , BELLE-NOTE-1006-v09.
- [101] F.-K. Guo, C. Hidalgo-Duque, J. Nieves, and M. Pavón Valderrama, *Consequences of heavy-quark symmetries for hadronic molecules*, *Physical Review D* **88** (2013) no. 5, .  
<http://dx.doi.org/10.1103/PhysRevD.88.054007>.
- [102] M. Tanabashi, K. Hagiwara, K. Hikasa, K. Nakamura, Y. Sumino, F. Takahashi, J. Tanaka, K. Agashe, G. Aielli, C. Amsler, M. Antonelli, D. M. Asner, H. Baer, S. Banerjee, R. M. Barnett, T. Basaglia, C. W. Bauer, J. J. Beatty, V. I. Belousov, J. Beringer, S. Bethke, A. Bettini, H. Bichsel, O. Biebel, K. M. Black, E. Blucher, O. Buchmuller, V. Burkert, M. A. Bychkov, R. N. Cahn, M. Carena, A. Ceccucci, A. Cerri, D. Chakraborty, M.-C. Chen, R. S. Chivukula, G. Cowan, O. Dahl, G. D'Ambrosio, T. Damour, D. de Florian, A. de Gouvêa, T. DeGrand, P. de Jong, G. Dissertori, B. A. Dobrescu, M. D'Onofrio, M. Doser, M. Drees, H. K. Dreiner, D. A. Dwyer, P. Eerola, S. Eidelman, J. Ellis, J. Erler, V. V. Ezhela, W. Fetscher, B. D. Fields, R. Firestone, B. Foster, A. Freitas, H. Gallagher, L. Garren, H.-J. Gerber, G. Gerbier, T. Gershon, Y. Gershtein, T. Gherghetta, A. A. Godizov, M. Goodman, C. Grab, A. V. Gritsan, C. Grojean, D. E. Groom, M. Grünewald, A. Gurtu, T. Gutsche, H. E. Haber, C. Hanhart, S. Hashimoto, and Hayato, Particle Data Group, *Review of Particle Physics*, *Phys. Rev. D* **98** (2018) 030001.  
<https://link.aps.org/doi/10.1103/PhysRevD.98.030001>.
- [103] T. A. N. Zwahlen, *Study of  $B \rightarrow X(3872)(D^*D)K$* , Belle Note #1006 (v9), July 2008.
- [104] T. Aushev et al., Belle, *Study of the  $B \rightarrow X(3872)(D^{*0}\bar{D}^0)K$  decay*, *Phys. Rev. D* **81** (2010) 031103, [arXiv:0810.0358](https://arxiv.org/abs/0810.0358) [hep-ex].
- [105] S.-K. Choi et al., Belle, *Bounds on the width, mass difference and other properties of  $X(3872) \rightarrow \pi^+ \pi^- J/\psi$  decays*, *Phys. Rev. D* **84** (2011) 052004, [arXiv:1107.0163](https://arxiv.org/abs/1107.0163) [hep-ex].
- [106] T. Ferber and P. Urquijo, *Overview of the Belle II Physics Generators*, .
- [107] O. Behnke, K. Kroninger, G. Schott, and T. Schorner-Sadenius, *Data Analysis in High Energy Physics: A Practical Guide to Statistical Methods*. Wiley-VCH, 1st ed., 2013.

- [108] M. Ablikim, M. Achasov, O. Albayrak, D. Ambrose, F. An, Q. An, J. Bai, R. Baldini Ferroli, Y. Ban, J. Becker, and et al., *Observation of a Charged Charmoniumlike Structure in  $e^+e^- \rightarrow (D^*D^{\mp})_{\pm}$  at  $s=4.26\text{ GeV}$* , Physical Review Letters **112** (Apr, 2014) .  
<http://dx.doi.org/10.1103/PhysRevLett.112.132001>.
- [109] M. Ablikim, M. Achasov, X. Ai, O. Albayrak, M. Albrecht, D. Ambrose, A. Amoroso, F. An, Q. An, J. Bai, and et al., *Observation of a Neutral Charmoniumlike State  $Z_c(4025)0$  in  $e^+e^- \rightarrow (D^*D^{\mp})00$* , Physical Review Letters **115** (Oct, 2015) .  
<http://dx.doi.org/10.1103/PhysRevLett.115.182002>.



